Springer Tracts in Civil Engineering

T. G. Sitharam
Ravi S. Jakka
Sreevalsa Kolathayar *Editors*

Advances in Earthquake Geotechnics

Springer

Springer Tracts in Civil Engineering

Springer Tracts in Civil Engineering (STCE) publishes the latest developments in Civil Engineering - quickly, informally and in top quality. The series scope includes monographs, professional books, graduate textbooks and edited volumes, as well as outstanding PhD theses. Its goal is to cover all the main branches of civil engineering, both theoretical and applied, including:

- Construction and Structural Mechanics
- Building Materials
- Concrete, Steel and Timber Structures
- Geotechnical Engineering
- Earthquake Engineering
- Coastal Engineering; Ocean and Offshore Engineering
- Hydraulics, Hydrology and Water Resources Engineering
- Environmental Engineering and Sustainability
- Structural Health and Monitoring
- Surveying and Geographical Information Systems
- Heating, Ventilation and Air Conditioning (HVAC)
- Transportation and Traffic
- Risk Analysis
- Safety and Security

Indexed by Scopus

To submit a proposal or request further information, please contact:
Pierpaolo Riva at Pierpaolo.Riva@springer.com (Europe and Americas) Wayne Hu at wayne.hu@springer.com (China)

T. G. Sitharam · Ravi S. Jakka ·
Sreevalsa Kolathayar
Editors

Advances in Earthquake Geotechnics

Springer

Editors
T. G. Sitharam
Indian Institute of Technology Guwahati
Guwahati, Assam, India

Sreevalsa Kolathayar
Department of Civil Engineering
National Institute of Technology Karnataka
Surathkal, Karnataka, India

Ravi S. Jakka
Department of Earthquake Engineering
Indian Institute of Technology Roorkee
Roorkee, Uttarakhand, India

ISSN 2366-259X ISSN 2366-2603 (electronic)
Springer Tracts in Civil Engineering
ISBN 978-981-19-3329-5 ISBN 978-981-19-3330-1 (eBook)
https://doi.org/10.1007/978-981-19-3330-1

This Springer imprint is published by the registered company Springer Nature Singapore Pte Ltd.
The registered company address is: 152 Beach Road, #21-01/04 Gateway East, Singapore 189721, Singapore

Preface

This book volume contains the state-of-the-art contributions from invited speakers of the 7th International Conference on Recent Advances in Geotechnical Earthquake Engineering and Soil Dynamics, 2021 (7ICRAGEE). This book serves as 2nd keynote volume of 7ICRAGEE. 1st Keynote volume titled 'Latest Developments in Geotechnical Earthquake Engineering and Soil Dynamics' has been published in Springer Transactions in Civil and Environmental Engineering in the year 2021.

We thank all the staff of Springer for their full support and cooperation at all the stages of the publication of this book. We do hope that this book will be beneficial to students, researchers and professionals working in the field of Geotechnical Earthquake Engineering and Soil Dynamics. The comments and suggestions from the readers and users of this book are most welcome.

Guwahati, India — T. G. Sitharam
Roorkee, India — Ravi S. Jakka
Surathkal, India — Sreevalsa Kolathayar

Acknowledgements

We (editors) thank all the invited speakers of 7th International Conference on Recent Advances in Geotechnical Earthquake Engineering and Soil Dynamics, 2021 (7ICRAGEE), who have contributed articles to this book. We could bring this volume out in time only due to the invited authors' timely contribution and cooperation. The editors also thank and acknowledge the service of the anonymous reviewers for their valuable time and efforts.

Contents

About the Editors

Prof. T. G. Sitharam is Director of Indian Institute of Technology Guwahati, Assam, since July 2019. He is a member of the Science and Engineering Research Board (SERB), Established through an Act of Parliament: SERB Act 2008, Department of Science and Technology, Government of India. He is Senior Professor in the Department of Civil Engineering, Indian Institute of Science (IISc), Bangalore, and served IISc for more than 27 years. He was Chairman of the Board of Governors at IIT Guwahati during 2019–2020 for more than a year. He was the former Chairman, Research Council, CSIR-CBRI (Central Building Research Institute, Roorkee). He is holding the position of Director (additional charge) of Central Institute of Technology, Kokrajhar, Assam (A Deemed to be University), since May 2021. Over the last 35 years, he has carried out research and development in the area of geotechnical and infrastructure engineering, seismic microzonation and soil dynamics, geotechnical earthquake engineering and has developed innovative technologies in the area of earth sciences, leading to about 500 technical papers, 20 books with Google scholar H-index of 47 and I-10 index 137 with more than 7175 citations. He has guided 40 Ph.D. students and 35 Master's Students. He was listed in the world's top 2% of scientists for the most-cited research scientists in various disciplines by Stanford University in 2020. Again his name appeared in the top 2% of scientists IN Elsevier by Stanford University in 2021. His broad area of research falls into Geotechnical Infrastructure engineering, earth sciences, hydrology, seismology, and natural hazards. He has carried out seismic microzonation of many urban centers in India, and he is an authority on seismic microzonation and site effects. Presently, he is the President of the Indian Society of Earthquake Technology, and he was the chairman of the 7th International conference on recent advances in geotechnical earthquake engineering and soil dynamics held in July 2021. He is the chief editor of the International Journal of Geotechnical Earthquake Engineering, (IJGEE), PA, USA since 2010. He is Editor-in-chief, Springer Transactions in Civil and Environmental Engg series, Book Series, Singapore. He is Fellow of ASCE, Fellow of

ICE (UK), Diplomat of Geotechnical Engineering (D.Ge.) from Academy of GeoProfessionals, ASCE, Fellow of IGS, ISET, ISES, and many other Societies. He is also a certified professional engineer and a chartered engineer from the Institution of Engineers.

Prof. Ravi S. Jakka is working as Associate Professor in the Department of Earthquake Engineering, Indian Institute of Technology, Roorkee, and serving as Editor to the International Journal of Geotechnical Earthquake Engineering and ISET Journal of Earthquake Technology. He graduated in Civil Engineering from Andhra University Engineering College in the year 2001. He has obtained masters and doctorate degrees from IIT Delhi in the years 2003 and 2007, respectively. His areas of interest are Dynamic Site Characterization, Soil Liquefaction, Seismic Slope Stability of Dams, Landslides, Foundations and Seismic Hazard Assessment. He has published over 100 articles in reputed international journals and conferences. He has supervised over 35 Masters Dissertations and 7 Ph.D. thesis, while he is currently guiding 10 Ph.D. Thesis. He has received prestigious DAAD and National Doctoral fellowships. He has obtained University Gold Medal from Andhra University. He also received the "Young Geotechnical Engineer Best Paper Award" from the Indian Geotechnical Society. He was instrumental in the development of the Earthquake Early Warning System for northern India, a prestigious national project. He was also Organizing Secretary to 7th International Conference on Recent Advances in Geotechnical Earthquake Engineering.

Prof. Sreevalsa Kolathayar pursued M.Tech from IIT Kanpur, Ph.D. from Indian Institute of Science (IISc), and served as International Research Staff at UPC BarcelonaTech Spain. He is presently Assistant Professor in the Department of Civil Engineering, National Institute of Technology Karnataka, Surathkal, India. Dr. Sreevalsa has authored five books, edited 16 book volumes, and published 100 research papers. He is Associate Editor of two International Journals and acted as a reviewer for many. His research interests include seismic hazard assessment, local site effects, disaster risk reduction, earth reinforcement, and water geotechnics. He is currently Secretary Indian chapter of the International Association for Coastal Reservoir Research (IACRR) and Executive Committee Member of the Indian Society of Earthquake Technology (ISET). In 2017, The New Indian Express honored Dr. Sreevalsa with South India's Most Inspiring Young Teachers Award. He is the recipient of the ISET DK Paul Research Award from the Indian Society of Earthquake Technology (ISET) in 2018. He is on the roster of two technical committees of ASCE Geo-Institute. Dr. Sreevalsa received the "IEI Young Engineers Award" by The Institution of Engineers (India), in recognition of his contributions in the field of Civil Engineering. He served as Organizing Secretary to the 7th International Conference on Recent Advances in Geotechnical Earthquake Engineering.

Risks and Vulnerabilities in the Design, Construction, and Operation of Offshore Wind Turbine Farms in Seismic Areas

Subhamoy Bhattacharya, Domenico Lombardi, Athul Prabhakaran, Harsh K. Mistry, Surya Biswal, Muhammad Aleem, Sadra Amani, Ganga Prakhya, Sachin Jindal, Joshua Macabuag, and Zhijian Qiu

1 Introduction

The United Nations recently declared that we are facing a grave climate emergency, and this is one of the grand technological challenges in our times. Continuous ocean and atmospheric warming, heat waves, and rising sea levels are some of the most common manifestations of climate change. One of the pathways to reduce emission is to decarbonize energy sources. A practical way to achieve a net-zero target is to run the country mostly on electricity produced from renewable sources without burning much fossil fuel. Offshore Wind farms have evolved as one of the scalable technologies to produce power. These relatively new technologies are also being constructed in seismic areas like Taiwan, Japan, China, and the United States. There

S. Bhattacharya (✉)
Chief Scientific Officer, University of Surrey, Guildford, UK
e-mail: S.Bhattacharya@surrey.ac.uk

D. Lombardi · H. K. Mistry
The University of Manchester, Manchester, UK

A. Prabhakaran
University of California (San Diego), La Jolla, California, USA

S. Biswal · M. Aleem · S. Amani · S. Jindal
University of Surrey, Guildford, UK

G. Prakhya
Sir Robert McAlpine, Birmingham, UK

J. Macabuag
Chief Product Officer, OWF-PRA (A University of Surrey spin-out), Guildford, UK

S. Bhattacharya
OWF-PRA (A University of Surrey spin-out), Guildford, UK

Z. Qiu
Xiamen University, Xiamen, China

T. G. Sitharam et al. (eds.), *Advances in Earthquake Geotechnics*, Springer Tracts in Civil Engineering, https://doi.org/10.1007/978-981-19-3330-1_1

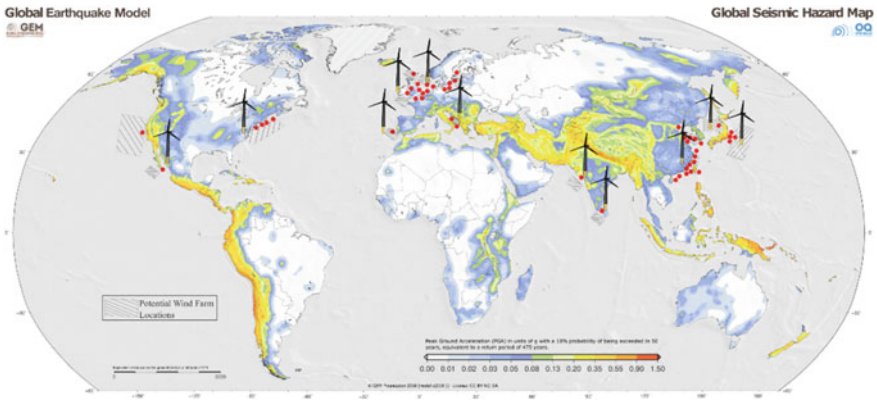

Fig. 1 Global Seismic Hazard Map showing the PGA and possible locations of offshore wind farm adapted from GEM project. **Base map source (GEM model)** (Bhattacharya et al. 2021a)

are plans to construct in other seismic countries such as India, Italy, Greece, Turkey, etc. Figure 1 shows a world map showing the potential locations of offshore wind along with the global seismic hazard map.

Offshore wind turbines are relatively new structures, and their construction in seismic areas is in its infancy. Therefore, codes of practice/best practice guidelines are not fully developed. As a result, the seismic design of offshore wind turbine (OWT) structure is uncertain, fragmentary, and often borrowed from methods adopted for Nuclear Power Plant design or building design. The aim of the keynote lecture at the conference is, therefore:

(A) To discuss the challenges in the analysis and design of these structures with emphasis on the foundations.
(B) To provide rational guidelines on the main issues concerning the risk and vulnerabilities of offshore wind farm.

1.1 Offshore Wind Farm

Offshore Wind farms are a collection of turbines with a substation and cables to transmit electricity to the onshore grid. Figure 2 shows a typical layout of an offshore wind farm for a grounded system where the different components are shown. Readers are referred to Chap. 1 of Bhattacharya (2019) for important details.

To de-risk an offshore wind farm for seismic conditions, we need to assess the vulnerability of all the main components:

(1) Offshore Wind Turbines structures,
(2) Inter array and export cables,
(3) Substation structure.

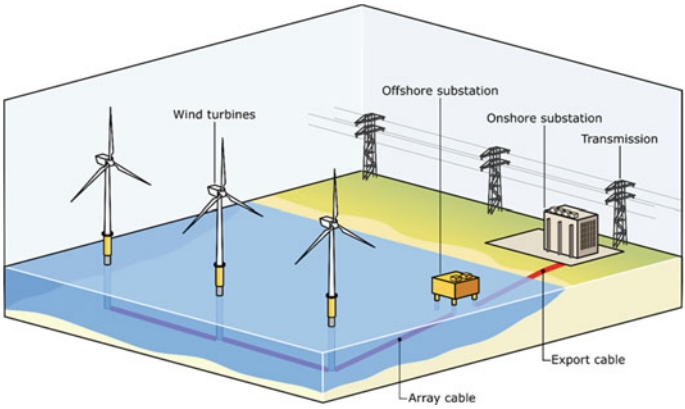

Fig. 2 Layout of an offshore windfarm (grounded system)

Figure 3 shows a range of offshore wind turbine structures currently used or planned to be used, and they are classified into grounded systems and floating systems. Typically, for water depth less than 60 m, it is expected grounded systems will be used and they are types 1–5 in the figure.

Offshore Wind Turbines are relatively new structures, and it is important to list the performance requirements for these systems for uninterrupted energy production. Table 1 lists the various requirements of offshore wind turbine systems keeping in mind the seismic hazards. It must be appreciated that offshore wind farms should

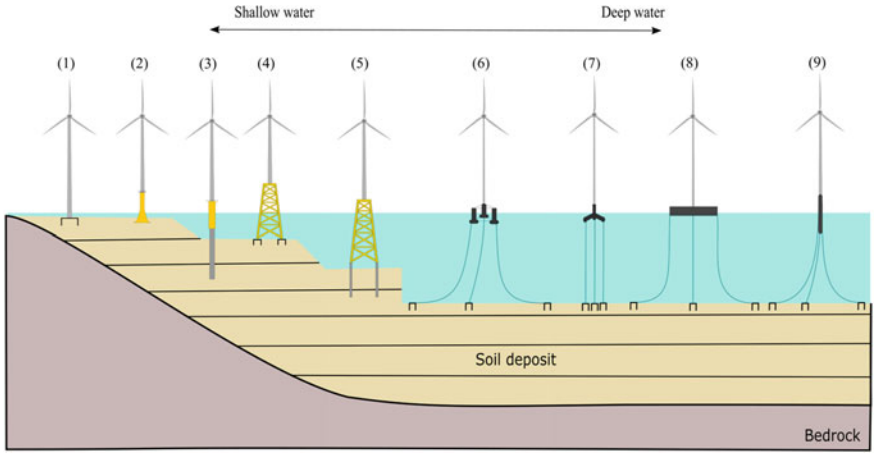

Fig. 3 Types of systems depending on water depths. Types of foundation [(1) Suction Bucket/Caisson, (2) Gravity-Based Foundation, (3) Monopile, (4) jacket on suction caisson, (5) jacket on monopile, (6) Semi-Submersible, (7) tension leg platform (TLP), (8) barge, (9) spar

Table 1 Examples of Offshore Wind Turbines with high consequences of failure where seismic design might need to be considered

Factor influencing the probability of exceedance	Typical example
Economic impact	(a) Permanent tilting of the whole wind turbines beyond repair (Fig. 6). The consequence of tilting is the loss of the investment. This is an example of ULS (Ultimate Limit State) (b) Tilt of the overall structure within the allowable limit (SLS criteria satisfied—e.g., tilt <0.5–0.75°) but the blade cracked. The blade needs a replacement and, therefore, a huge unplanned cost. In addition, energy production halted for a substantial amount of time (c) RNA acceleration exceeded the allowable limit damaging some components of the electronics. Repair would cost together with loss of energy production (d) Large-scale Wind farms in the coastal areas and with no power production will have a national economic impact
Impact on post-earthquake relief	Loss of power production could impact the rescue effort and recovery
Structural integrity	(a) Limit on blade deflection and not to hit the tower during earthquakes; see Fig. 5 (b) Tilting of the tower will enhance P-delta moment causing more fatigue damage leading to early end of life

remain operational even after a major earthquake so that rescue operations (if necessary) can be carried out.

It may be noted that Table 1 is by no means exhaustive, and further work is underway to describe these and bring out the criteria for seismic design. The majority of offshore wind turbines are supported on monopiles, and it is important to discuss the SLS criteria of this particular foundation. One of the important design aspects of monopile-supported wind turbines is the allowable tilt. The current allowable tilt is 0.5–0.75 degrees, and this requirement is still valid for both mainshocks and aftershocks. The possible reasons for stricter SLS are shown schematically in Fig. 4, and the readers are referred to Chap. 3 of Bhattacharya (2019) for further details. Increased tilt may result in reduced blade-tower collision, increased wear and tear of bearings, increased foundation loads (Fig. 5).

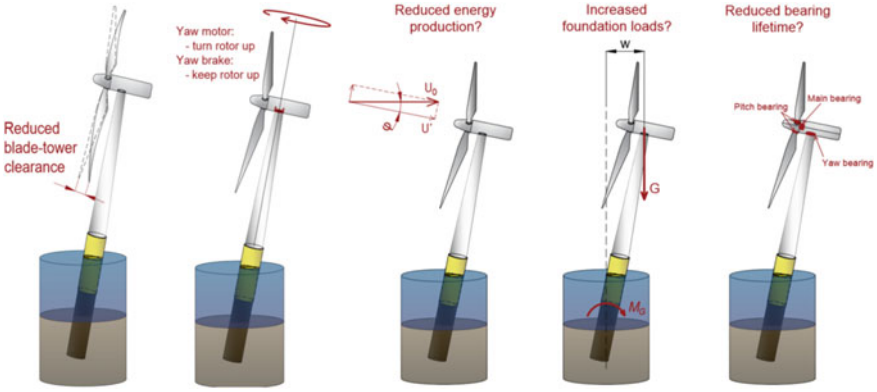

Fig. 4 Aspects governing the SLS requirements for monopile foundation

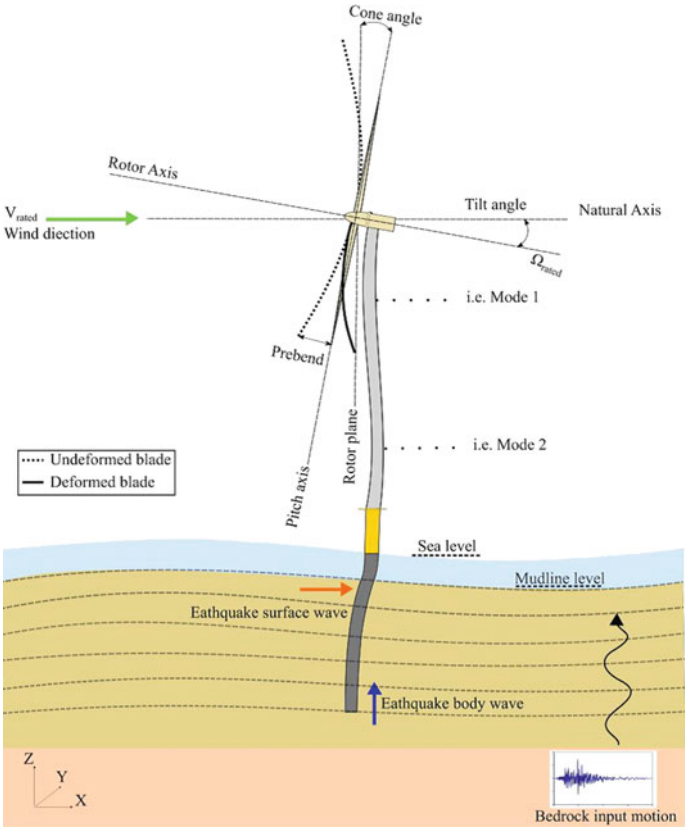

Fig. 5 Deflection of the blade and blade-tower interaction during seismic loading

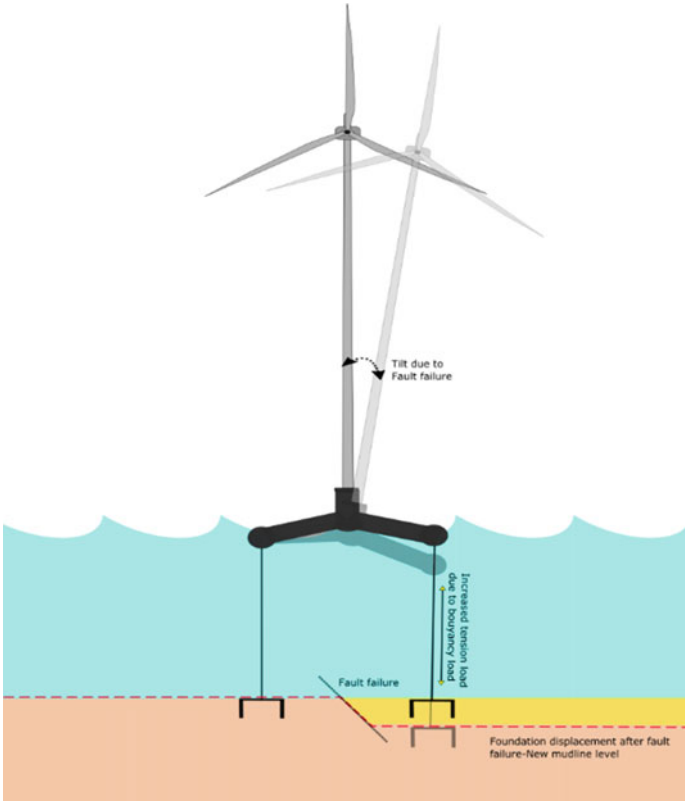

Fig. 6 Effect of support settlement for TLP foundations (Bhattacharya et al. 2021b)

1.2 Seismic Risks to an Offshore Wind Farm

Seismic hazards to an offshore wind farm can be numerous. Alati et al. (2015), Bhattacharya (2019), Bhattacharya et al. (2019), Kementzetzidis et al. (2019), Ali et al. (2020), Bhattacharya et al. (2021), and Bhattacharya et al. (2022) list necessary steps in a seismic risk evaluation:

(a) Identification of potential seismic hazards at the site and must include cascading events.
(b) Effect of large fault movements (i.e., subduction fault) can lead to rupture of the cables or embedded anchoring for floating systems. Figure 6 shows a schematic diagram explaining the situation taking into consideration a TLP system.
(c) Ground shaking with no-liquefaction of the subsurface. This includes inertial effects on the structure and will induce inertial bending moment on the foundation piles. Due to kinematic interaction, additional bending moments will be induced if the ground is layered with contrasting stiffness.

(d) Shaking of the ground together with liquefaction of the subsurface. Liquefaction may lead to a large unsupported pile length and will elongate the natural vibration period of the whole structure. One of the significant risks is the tilting of the foundation due to liquefaction. The ground may liquefy quickly or take time and is a function of the ground profile and type of input motion. In such scenarios, the transient effects of liquefaction need to be considered, as it will affect the bending moment in the piles.
(e) If there is a tsunami risk, the effect must be considered together with the ground shaking and liquefaction.
(f) Earthquakes may cause submarine landslides, and the potential impact must be considered.
(g) The effect of earthquake sequence such as Foreshock + Mainshock + Aftershock need to be evaluated.

1.3 Codes of Practices for Seismic Design of Offshore Wind Turbines

OWT consists of a long slender tower with a top-heavy fixed mass (Nacelle) and a heavy rotating mass. The structure is constantly exposed to variable environmental wind and wave loads. These relatively new structures can also be characterized as an inverted pendulum (with a substantial mass concentrated in the upper 3rd of the tower), and guidelines for designing such special structures are not explicitly mentioned in current codes of practices.

Eurocode 8 mainly focuses on buildings and bridges, and at present, it is of interest to review some clauses. Eurocode 8 (Part 1) (EC8, 2003) states that special structures such as offshore structures are beyond the scope. Clauses/Guidelines of EC8 are divided into principles (P) and application rules. Principles are identified by P after the clause number and cover items for which no alternative is permitted. Application rules are recommended methods of achieving the Principles, but alternative rules may also be used.

Other codes of practice for the seismic design, such as novel structures or guidelines for their certification (e.g., DNV/Risø, 2002; Germanischer Lloyd, 2005; DNV, 2014; IEC 2009) are not fully developed nor validated as the installation of offshore wind farms in earthquake-prone countries is in its relative infancy and is expanding rapidly. Often, specific requirements are borrowed from the guidelines developed for the petroleum and natural gas industries (ISO 19901-2:2017). Furthermore, the existing codes of practice on seismic design are mostly developed for conventional structures, and their applicability to offshore wind turbines needs to be verified and validated. However, analysis and design must be carried out to support the *energy-transition* initiatives to understand the vulnerability under seismic loading.

The required performance is to reduce operational expenditure (OPEX) following an earthquake and not to enhance capital expenditure (CAPEX), avoiding over-conservativism unnecessarily.

2 Challenges in Seismic Design

The analysis and design of foundations for offshore wind turbines is challenging due to complex load conditions arising from the environmental loads (i.e., wind, wave, currents). In seismic areas, there are additional loads due to the phenomena and processes discussed in the earlier section. Figure 7 shows a schematic diagram of the environmental loads acting on a typical offshore wind turbine, which must be carried by the foundations and transferred to the adjacent soil. There are four main environmental loads: wind, wave, 1P (rotor frequency), and 2P/3P (blade passing frequency) loads whose waveform is also shown in Fig. 7 for a monopile foundation. The salient characteristics of these loads are summarized as follows:

(a) Wind and wave result in a different offset of amplitude, frequency, and the number of cycles applied to the foundation. Figure 7 shows a schematic representation of the frequency of these loads together with the frequency intervals corresponding to the three possible design choices: Soft-Soft, Soft-Stiff, and Stiff-Stiff.
(b) Wind and the wave loads are random in both space and time and therefore are better described statistically through probability distributions, mean values, and standard deviation.
(c) Wave and wind load act in two different directions, which give rise to the so-called wind-wave misalignment.
(d) 1P loading is caused by mass and aerodynamic imbalances of the rotor, and hence the forcing frequency equals the rotational frequency of the rotor.

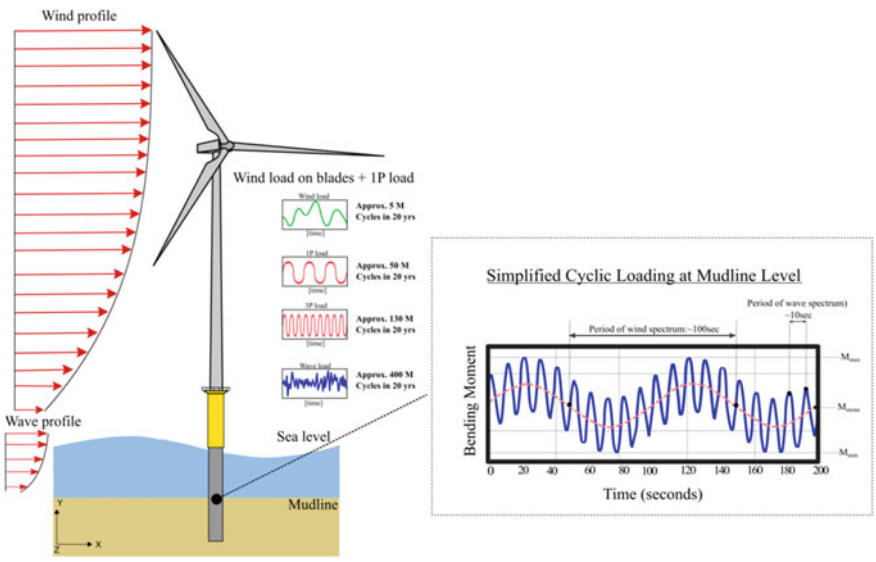

Fig. 7 Load complexity with an approximate number of cycles for 20 years assumed lifetime

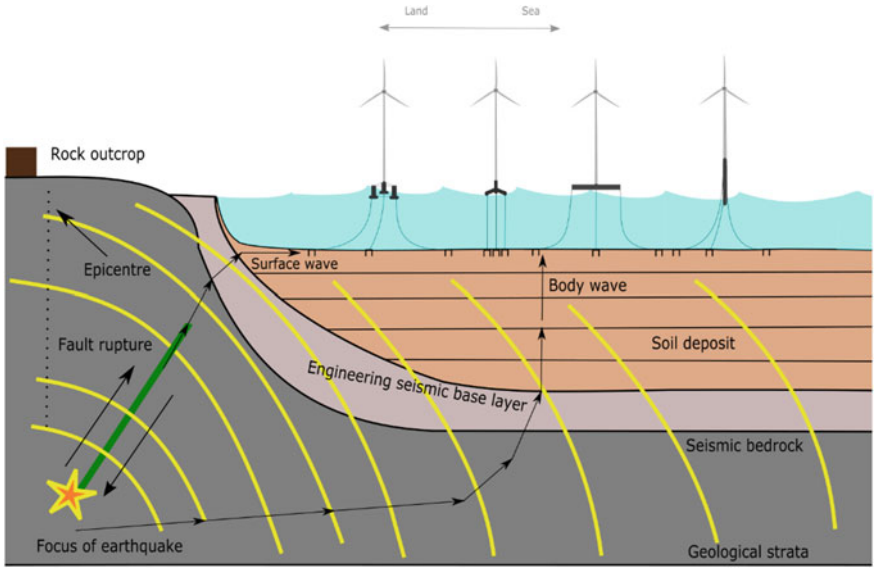

Fig. 8 Schematic of fault rupture to site response for Floating Offshore Turbines

(e) 2P/3P loading is caused by the blade shadowing effect and wind shear (i.e., the change in wind speed with height above the ground), and rotational sampling of turbulence. Its frequency is 2 or 3 times the 1P frequency for two and three-bladed turbines, respectively.

Figure 8 shows additional design considerations in seismic areas, and the different processes/mechanisms are schematically shown for floating systems. To assess the performance of wind turbines as laid out in Table 1, it is necessary to carry out a dynamic analysis for which time history of motions is required. From Fig. 8, the generation of input motion for a given site depends on the seismotectonics of the area. This includes faulting pattern, the site's distance from earthquake source, wave path, the geology of the area, etc. This can be done using either synthetic (artificially generated) or recorded ground motion from previous earthquakes (unscaled records). Intuitively, it also appears that a grounded system will provide a higher response to RNA when compared with floating systems.

3 Issues in Seismic Analysis

The main issues that must be addressed in the design process of an offshore wind turbine are summarized as follows:

(a) Definition of return periods (T_R) for different hazard levels considering that the design lifetime for offshore wind turbines is typically 25–30 years.

(b) Assessment of the seismic hazard at the given site.
(c) Definition of the Design Response Spectra at different hazard levels.
(d) Selection of strong motions for time-history analysis.
(e) Definition of the load combination criteria considering wind, wave, earthquake (multi-directional), and the control system.
(f) Explicit performance requirements (limit states) at different hazard levels

This section of the paper discusses each of the points above.

3.1 Design Return Period

Large seismic events are low probability but high-risk for offshore wind farms, given their value (typically $0.75bN–$1.25bN for 500 MW). The typical Return Period (T_R) of large earthquakes is hundreds to thousands of years. Currently, offshore wind turbines are designed for a lifespan of 25–30 years, with a possible extension of up to 5 years. Therefore, it is imperative to quantify and mitigate seismic risk over their lifetime.

Most standards currently use the 475 years return period, corresponding to a 10% probability of exceedance in 50 years. The time window of 50 years refers to the lifespan of a typical structure/infrastructure. This calculation assumes the earthquake occurrence as Homogeneous Poisson Process (HPP), and, therefore, the time between seismic events is exponentially distributed. If the time window of 50 years is shortened to 25 years, an event with a 475-year return period has an approximately 5% probability of exceedance.

For an OWT, depending on client requirements (e.g., low OPEX cost), different limit states need to be considered. For example, due to the high replacement costs, the structural integrity of the blades should be guaranteed following an earthquake. Therefore, besides the essential requirements of collapse prevention (i.e., CO, the collapse of foundation, or structural failure of the tower), there must also be another criterion of the integrity of critical components (e.g., blades) based on the economic impact.

Codes of practice often consider the previous aspect through the analysis of the consequences of failure. EC8 [Part 1] recommends two levels, one preventing the ultimate limit state (ULS) and other the serviceability limit state (SLS) as follows: (a) No collapse (ULS) representing 10% exceedance probability in 50 years, i.e., 475-year return period; (b) Damage limitation – 10% exceedance probability in 10 years, i.e., 95-year return period.

In designing traditional structures, if a particular seismic code is adopted, it is inherently assumed that structures, during their lifetime, will be subjected to some form of damage under extreme events to dissipate energy to satisfy some performance criteria. In the case of inhabited structures, it will allow occupants/users a safe evacuation. In the case of offshore wind turbines, these limits cannot be accepted in their current form. Therefore, customized requirements for offshore wind farms may be

necessary and must be agreed upon with the client in a contract. Table 1 provides a few examples of typical requirements but is by no means exhaustive.

Based on the lifetime of the structure, seismic hazard levels can be explicitly defined. The return periods for these hazard levels can then be obtained from Seismic Hazard Analysis (SHA).

3.2 Seismic Hazard Analysis (Ground-Motion Parameter and Fault Displacement)

3.2.1 DSHA and PSHA for Ground-Motion Parameters

A seismic hazard analysis (SHA) provides the probability of exceeding a certain ground-motion intensity parameter, typically peak-ground acceleration or spectral acceleration, or fault displacement in a given seismotectonic condition. There are two main types of SHA: (i) Probabilistic Seismic Hazard Analysis (PSHA) and (ii) Deterministic Seismic Hazard Assessment (DSHA). The two types of hazard assessment share similar inputs, namely, seismic catalog, seismic source, and ground-motion models. However, they also differ in some fundamental respects, most notably in the treatment of uncertainties and the characterization of the hazard. The main steps of a typical PSHA are illustrated in Fig. 9 and can be summarized as follows (Cornell, 1968; McGuire, 2004).

Step 1—Definition of seismic source models: It compiles an earthquake catalog that lists all known historical and instrumented earthquakes in the study region. The catalog is used to build the seismic source model that defines the spatial distribution of all the seismic sources that contribute to the hazard at the site.

Step 2—Definition of earthquake recurrence law: This step also relies on the earthquake catalog and defines the rate of earthquake occurrence for each seismic source defined in Step 1. The Gutenberg-Richter (GR) recurrence law is often adopted for the recurrence model. As the GR law may produce unrealistically large earthquakes, it is often truncated to the maximum possible magnitude that the seismic source can produce.

Step 3—Definition of ground-motion models: It consists of quantifying the intensity of the earthquake in terms of parameters of engineering interest, such as peak-ground acceleration (PGA), spectral accelerations, spectral velocities, etc. These are computed based on empirical ground-motion prediction equations (GMPEs), evaluated from a regression analysis of a large set of records. Although different GMPEs have been developed and are available for regions of different seismicity, all provide the distribution of a ground-motion parameter (Intensity measure) as a function of several independent variables such as the earthquake magnitude, the source-to-site distance, the faulting mechanism, and the geotechnical parameters that characterize the soil conditions at the site. Given the inherent randomness of the seismic process

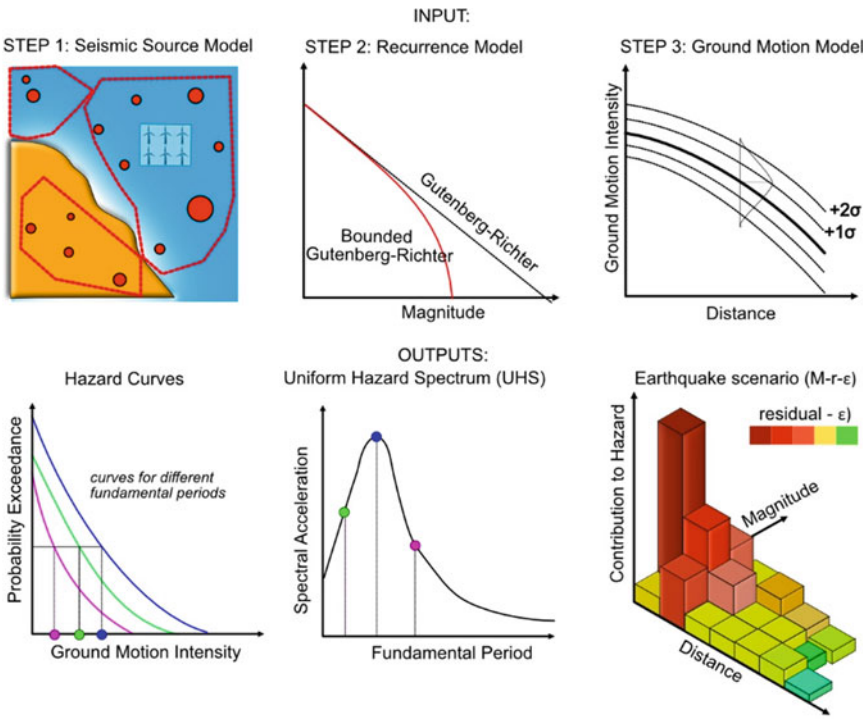

Fig. 9 3-step procedure for probabilistic seismic hazard assessment (PSHA) and typical outputs

and the epistemic uncertainty in the models, multiple GMPEs are usually adopted for SHA using a logic tree with appropriate weights.

The output of a typical PSHA is often presented using a suite of curves, known as seismic hazard curves, which represent the average annual rate of exceedance of a given ground-motion intensity measure for different vibration periods. Since the earthquake occurrence is modeled as a Poisson process, the average annual rate, λ, can be expressed in terms of the probability of exceedance, P, and time, t, such that

$$\lambda = \frac{-\ln(1-P)}{t} \tag{1}$$

from which it follows that a probability of exceedance of 10% (P = 0.1) in 50 years (T = 50) corresponds to an average annual rate of 0.002 or return period (which is its inverse, i.e., $1/\lambda$) of approximately 475 years.

The PSHA results can be used to plot the spatial distribution of the hazard, such as in hazard maps, or compute the ordinates of the Uniform Hazard Spectrum (UHS). Since the PSHA "aggregates" different earthquake scenarios, the resulting hazard cannot be associated with any real earthquake scenarios. The disaggregation analysis enables identifying a "fictitious" seismic scenario, expressed in terms of

magnitude-distance-residual, which provides the greatest contribution to the hazard. This scenario is often used for the selection of ground-motion records compatible with the estimated hazard.

The deterministic approach, DSHA, can be seen as a special case of the PSHA, where only the most dangerous scenario is considered. This is the so-called worst-case scenario, defined in magnitude and source-to-site distance regardless of its likelihood of occurrence. It is worth noting that both methodologies present limitations based on the simplifying assumption they rely upon and the degree of subjectivity involved in the process.

Deterministic seismic hazard analysis can be easily performed and may be suitable in the early stages of an offshore wind farm project (e.g., feasibility study, preliminary design) and if the wind farm is to be built in a low- to-medium-seismicity area. From the catalog of historical seismic events, it is possible to identify the maximum magnitude and the minimum distance of the farm location from the potential seismic sources. Subsequently, using ground-motion prediction equations (GMPEs) suitable for the specific case study. Using the probability of exceedance agreed with the Wind Farm Developer, it is possible to define the hazard that is suitable for design purposes.

It is important to state that PSHA is critical for Nuclear Power Plants due to other far-reaching consequences, and in low-seismic wind farm locations, such type of analysis may have a lower cost-benefit ratio. The readers are referred to Yawson and Lombardi (2018) for an example of PSHA for a low-seismic country such as the UK.

3.2.2 Probabilistic Fault Displacement Hazard Assessment

Similar to the PSHA described in Sect. 3.2.1, one can compute the displacement induced by the fault rupture at the surface. It is worth noting that this is different from the displacement generated by the propagation of seismic waves through the sediments as it is directly caused by the fault rupture. Hence, the probabilistic approach needs to be modified in order to include the probability of slip exceedance given that an earthquake of strikes the site. Figure 10 presents a flow chart for the probabilistic fault displacement hazard assessment for an offshore site. The steps are as follows:

(1) The first step is to identify the site and determine the mean annual occurrence rate λ_m and distribution of magnitude occurrence f(m) from parameter of the Gutenberg-Richter law (GR law). The distribution f(m) is normally truncated to a maximum magnitude M_{max}.

(2) The second step requires the definition of fault displacement prediction equation that substitute the ground-motion prediction equation used in the conventional PSHA. The fault displacement prediction equation depends on the style of faulting, e.g., reverse, normal and strike-slip. As not all fault rupture will propagate to the surface, it is required to determine the probability of occurrence of a slip given a magnitude m; this is expressed by the conditional probability function P(*slip*|*m*).

(3) Then, the probability of exceedance of a given level of displacement P($D >$ *d*|*m*) can be computed as the product of P(*slip*|*m*) and the convolution of the

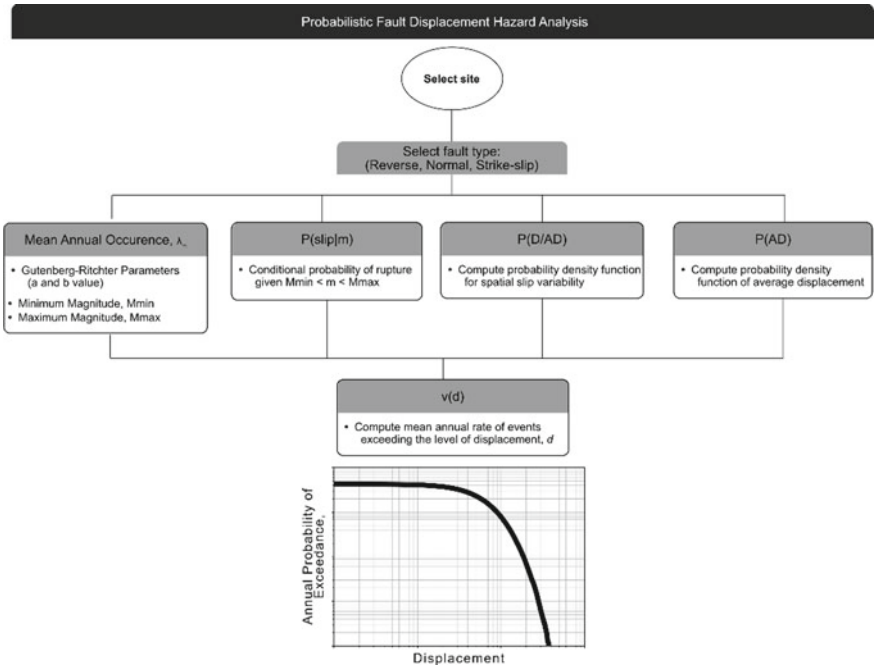

Fig. 10 Probabilistic fault rupture hazard analysis

probability density function of the fault displacement D, normalized by the average displacement AD, i.e., P(D/AD), and probability density function of the average displacement P(AD).

(4) Finally, the annual rate of events exceeding a given fault displacement $\nu(d)$ can be computed from the integral:

$$\nu(d) = \lambda_m \int_{M_{min}}^{M_{max}} f(m) P(D > d|m) dm$$

3.3 Choosing the Response Spectra

The dynamic modal analysis with response spectrum is an accepted procedure used to evaluate the structural response of many structural typologies (Zhao et al., 2020). In the context of Offshore Wind turbine design, there are broadly three types of response spectrum that can be used:

(a) The response spectrum of a single record. It shows the maximum response acceleration of a family of single degree of freedom (SDOF) structures with different periods and prescribed damping.

(b) Uniform Hazard Spectra (UHS) is the main product of the PSHA and can be calculated for different return periods. This is a horizontal spectrum and not directional dependent. Vertical UHS can also be produced. UHS is site-specific and does not take into account the energy dissipation due to allowable structural damage.

(c) Code-based standard Response Spectrum is readily available in most codes of practice (for example, EC8 or IBC). The code-based response spectrum is generally just a functional smooth form (Malhotra, 2006) and can be completely defined if its parameters have been calculated using PSHA. Code-based response spectra are available for both horizontal and vertical directions. The spectrum can be customized to incorporate the response reduction factor (R) to reflect the extent of energy dissipation and ductility. Traditionally, these code-based response spectra have only been defined for onshore or near-shore environments and cannot be readily used for an offshore site.

It must be mentioned that the code-specified elastic spectrum is just a normalization of the uniform hazard spectrum (UHS) that is obtained from the PSHA. A response spectrum can also be derived from a DSHA, and normalization can also be done on this spectrum. Figure 11 shows an example from a site to illustrate the above description.

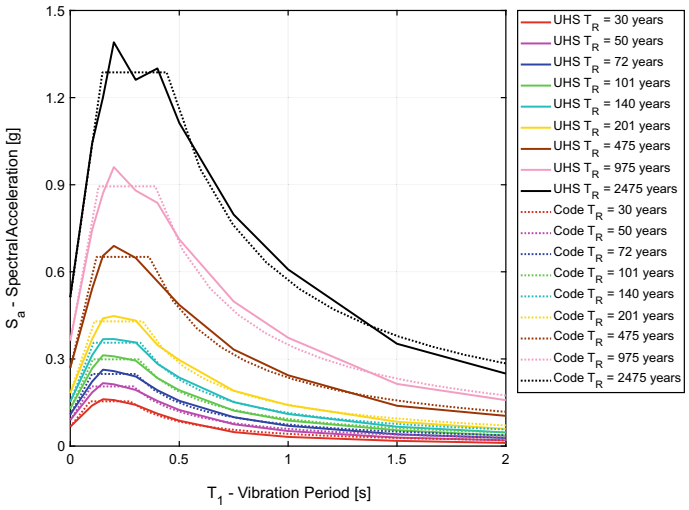

Fig. 11 Example of UHS and its regularization for several return periods

3.4 Ground-Motion Selection for Time-History Analyses

Two methods are generally used for selecting ground motions: (a) Scenario-based methods and (b) Response-spectrum-matching-based methods.

Earthquake scenarios are defined by the seismotectonic features such as magnitude, distance, local site conditions, typology of the fault mechanisms. All these parameters may influence the spectral content of the ground-motion records. Two potential approaches are possible for scenario-based selection. If DSHA is used, it is required to define a design critical earthquake scenario for a given site considering the characteristics of the earthquake rupture of the identified fault. On the other hand, if PSHA analysis is performed, it must utilize the seismic disaggregation results from the PSHA. If multiple scenarios have significant contributions to the hazard, multiple scenarios should be examined (De Risi et al., 2018).

On the other hand, Response spectrum matching methods are based on matching the amplitude of spectral ordinates, and therefore the method attempts to match both the ground-motion intensity and frequency content. The target response spectrum is often the design code spectrum (Iervolino et al., 2010). This selection method is based on the comparison of a candidate response spectrum with the target response spectrum. The matching is usually calculated using as a reference the differences between the spectral ordinates of the reference spectrum and the spectrum of the candidate ground motion. Such a difference is usually evaluated over a vibration period range. This period range should ideally cover the relevant vibration periods of the offshore wind turbine structure under scrutiny. In this regard, Eurocode 8 suggests a range of 0.2 times to 2 times the first vibration period. Furthermore, EC8 suggests that the average spectrum of 7 records needs to be larger than 90% of the target spectrum, which avoids underestimation. A further upper-bound criterion can also be implemented to avoid dispersion of the results.

Ideally, the target spectrum should be site-specific, and, therefore, the uniform hazard spectrum is desirable. It may be noted that different earthquake scenarios govern different parts of the uniform hazard spectrum. For example, moderate events at short distances tend to be dominant at shorter vibration periods, whereas large events at far distances tend to be more critical for longer vibration periods. Furthermore, when UHS is used as the target spectrum, candidate records having similar spectral ordinates for the entire period range tend to be extreme. Thus, forcing an input motion to match the UHS may result in excessively conservative and unrealistic ground motions.

To resolve this issue, a different approach for obtaining hazard consistent ground motions utilizing the Conditional Mean Spectrum (CMS) (Baker, 2011) was proposed. The CMS approach is a combination of scenario-based and spectral-matching methods. In this method, a suite of ground motions is scaled to match the CMS, the mean response spectrum conditioned at a target spectral acceleration value at the period of the structure. To control the dispersion, confidence intervals are generally adopted around the conditional mean spectrum.

Practically, it is hard to find natural records that can match a specific target spectrum. There are a couple of possible solutions in such cases: (a) Natural records from real events can be scaled to reach the matching. This scaling factor should not be excessively high, otherwise unrealistic, combinations of amplitude and frequency contents may be obtained (Luco & Bazzurro, 2007); (b) Time-histories can be simulated to obtain stochastic ground motions matching the hazard spectrum.

More recently, as highlighted by Zhang and Zheng (2020), strong motion records at offshore sites may have different spectral signatures compared to similar motion recorded onshore, particularly at longer periods. The differences are most significant in the vertical component of motion attributed to the high-frequency suppression due to the overlying ocean. Therefore, further work is required to ensure if conventual attenuation relationships developed using data largely recorded at onshore sites are applicable to their offshore counterparts.

3.5 Combination of Seismic Actions with Wind and Wave

As presented in Fig. 12, different loads may act on a monopile-supported wind turbine system. There will be an overturning moment for a monopile type of foundation due to the combination of wind and wave load, which is generally asymmetric and can be one way. Seismic action will increase the lateral load and add the operational load due to normal or emergency braking. If the ground is liquefiable, lateral load-carrying capacity will be lost, leading to a permanent tilt, and is discussed later in the paper. Figure 12 identifies different stages so that engineering calculations can be carried out.

(a) Stage 1 represents the standard calculations necessary for non-seismic locations. There will be minimum and maximum moment and will depend on turbine size, water depth, wind, and wave characteristics. Further details can be found in Jalbi et al. (2019).

(b) Stage 2 represents the arrival of the seismic waves and the onset of the control mechanism of the turbine to reduce overall damage or OPEX cost. It is likely that a normal or emergency brake may be applied depending on whether the turbine is idling (not connected to the grid) or parked or in power generation mode. The loading in this stage will comprise of inertia load together with the braking load. To obtain a conservative estimate of the lateral load and moment at Stage 2, the braking and inertia loads may be added to the load in Stage 1.

(c) In liquefiable deposits, as the earthquake progresses, the ground would progressively liquefy in a top-down fashion, and the moment carrying capacity of the foundation may reduce drastically. The enhanced unsupported length of monopile due to liquefaction coupled with seismic and other operational loads may lead to the potential failure of OWT structure based on ULS (Ultimate Limit State) or SLS (Serviceability Limit State).

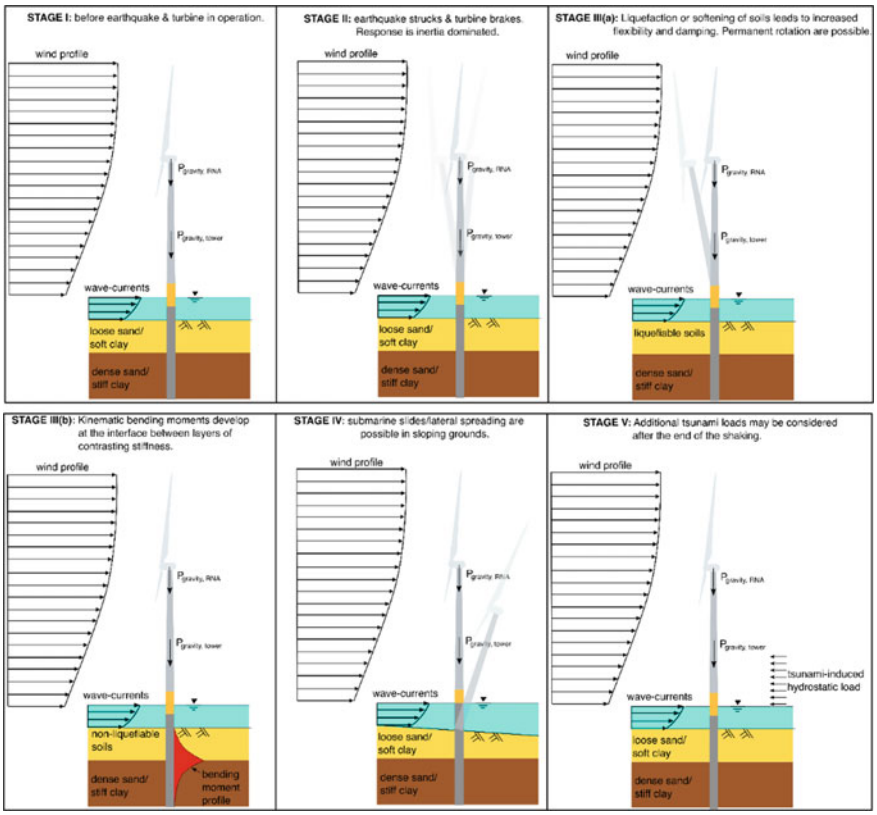

Fig. 12 Schematic diagram of the load cases

(d) If the ground is non-liquefiable, in layered deposits, there may be high kinematic bending moments.
(e) If there are submarine landslides, extra lateral loads may be applied to the foundation.
(f) In Tsunami risk areas, there may be additional loads due to hydrodynamic loads.

4 Effect of Soil Liquefaction on Monopile: Reduction in Capacity and Permanent Tilt

Offshore wind farms are increasingly being constructed in areas of potentially liquefiable soil (Bhattacharya and Goda, 2016). Moreover, young offshore deposits are particularly vulnerable to soil liquefaction, during strong shaking. Soil liquefaction results in stages where the supporting ground behaves as a heavy fluid, resulting in a

loss of lateral and vertical resistance. Further, upward artesian flow due to excess pore pressure generation can result in high buoyant forces that can result in cable floatation, if not accounted for in the design. Figure 13 presents a simplified sketch to plot the capacity of the foundation in two stages: No-Liquefaction (Pre-liquefaction) and Maximum Liquefaction (Post-Liquefaction). In the same plot, the load cases can also be shown. The effect of soil liquefaction is the loss of lateral and moment resisting capacity of the foundation as shown in Amani et al. (2022). Such simplified estimates of capacity using pre- and post-liquefaction properties can help in the preliminary sizing of foundations for offshore wind farms. Once, resistance (capacity) is estimated, the action (demand) on the foundation using several load cases can be used to schematically estimate the margin of safety according to Aleem et al. (2022).

During earthquakes, soil deposits often liquefy top-down. The upper layers lose strength, and the liquefaction front progressively travels to deeper layers as highlighted by Scott (1986). Therefore, as presented in Fig. 14, it is expected that with progressive liquefaction, the foundation capacity will reduce in stages.

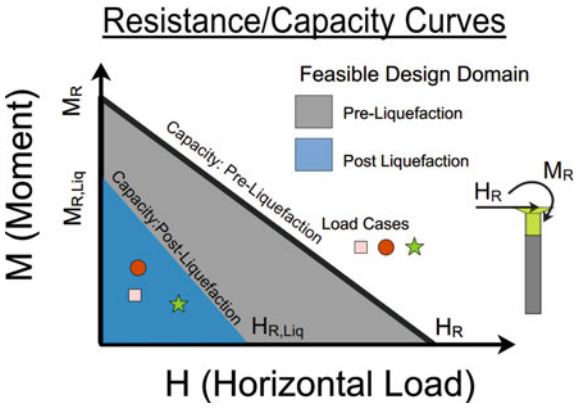

Fig. 13 Schematic diagram showing the demand and capacity

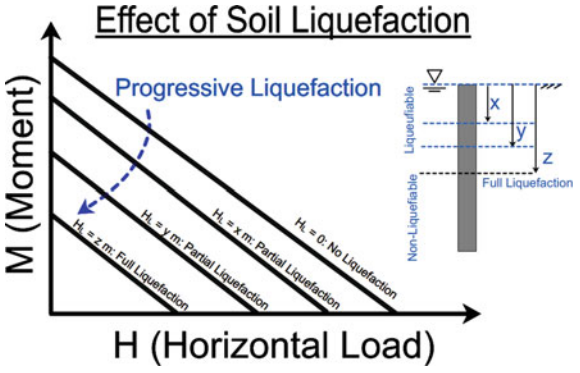

Fig. 14 Capacity envelopes following progressive liquefaction

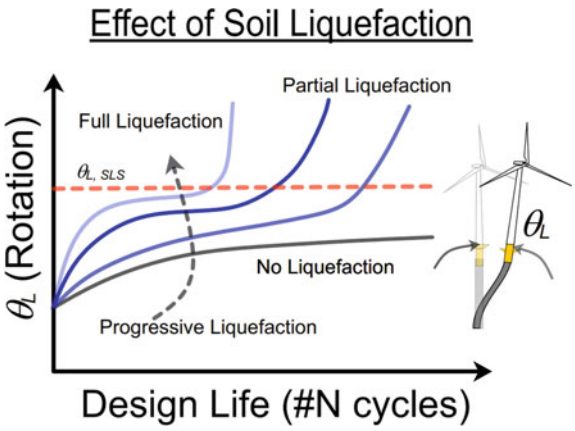

Fig. 15 Accumulation of tilt at pile head during progressive liquefaction

Therefore, considering the design life of the wind farm and tolerable risk, a probabilistic assessment can be performed for liquefaction triggering potential, thereby reducing the requirement for expensive ground remediation measures.

An additional hazard due to loss of foundation capacity is the accumulated tilt of the system. As shown in Fig. 15, pre-Liquefaction, the ground offers sufficient resistance (capacity) to prevent excessive tilt of the superstructure. However, strong shaking can result in high inertial demands at the hub level, resulting in large moments on the mudline. These demands can lead to tilting of the foundation which can be exacerbated by soil liquefaction and additional long-term loading, if not corrected. It is noted that appropriate soil constitutive models such as Lombardi and Bhattacharya (2014, 2016), Lombardi et al. (2017), and Dash et al. (2017) must be used to model soil-pile interaction after liquefaction.

5 Offshore Substations

For a wind farm to be operable and producing energy after a seismic event, all the essential components (cables, turbines, and offshore substation) must also be operating. Offshore substations systems serve to collect and transmit the power generated from multiple turbines in the wind farm. Electricity generated from the turbines is transported through submarine cables and collected at a common substation. The substation is then connected to the grid, transferring the generated power onshore, see Fig. 2 for the layout. Therefore, characterization of the seismic resilience of offshore substations is crucial, when designing windfarms. In general, offshore substations are top-heavy structures similar to offshore rigs from the oil and natural gas industry. However, substations have acceleration-sensitive non-structural components which require detailed seismic design. Figure 16 shows two photos of offshore substa-

tions supported on monopile and jacket. The weight of the top side of the substation depends on the type of transformers. DC-type transformers are normally heavier than AC transformers. Figure 17 details an analysis of a 600 MW offshore substation structure, with an approximate weight of 40MN. A water depth of 70 m was assumed with a 50-year wave height of 15 m at a period of 10 s.

Fig. 16 Photographs of offshore substations. *Source* http://www.trianel-borkum.de/en/kraftwerk/converter-platform/ and https://commons.wikimedia.org/wiki/File:Offshore-132kv-Substation.jpg

Fig. 17 Analysis of offshore substation structure

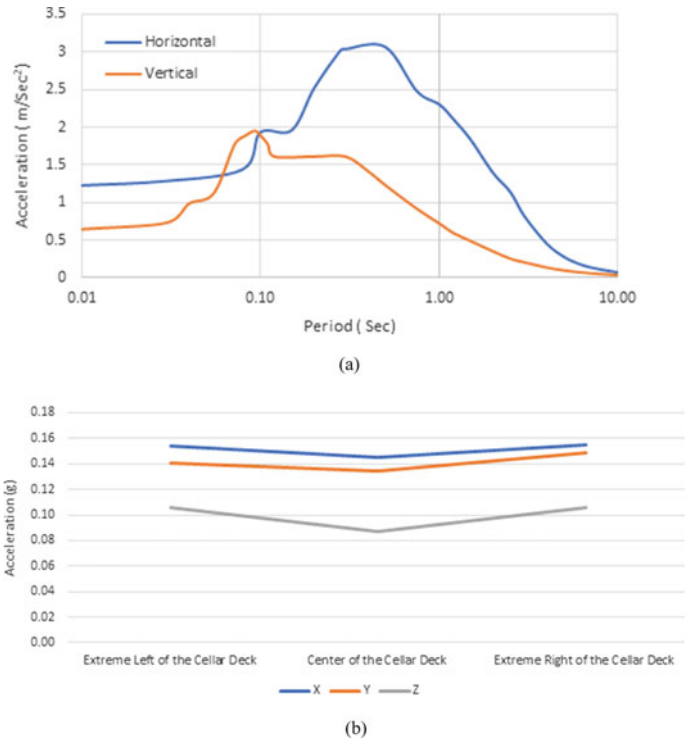

Fig. 18 **a** Typical offshore substation structure. **b** Acceleration response at deck of the platform

The structure is analyzed using the response spectrum method, using the horizontal and vertical spectra presented in Fig. 18a. The analysis results are presented in Fig. 18b. Further detailed characterization requires time-history analyses with appropriate constitutive models to account for material non-linearity within the structural elements.

However, it must be noted that the design of each component of the wind farm: Turbines, offshore substation, and cables are done separately and therefore, the design may not be risk consistent, i.e., each structure may not be explicitly designed using the same set of ground motions selected at a specific hazard level.

6 Performance-Based Design and Risk Modeling

Conventional design (Load and Resistance Factor Design) of offshore turbines is performance-based, however with limited consideration to the explicit performance of the system. Performance-based design frameworks, such as that by the Pacific

Earthquake Engineering Research Center (PEER), supersede existing design methodologies, explicitly characterizing system performance, risk, and associated loss of function.

Offshore wind farms serve as lifeline structures, necessitating their need to remain functional post-seismic events. Further, costs incurred during times of zero output can significantly affect the agencies involved. Therefore, the operation of the group of wind turbines, and associated structures, including power stations and underwater cables, is critical. Further, explicit considerations toward satisfying performance limits enable greater transparency, bringing together stakeholders in the design stage. Figure 19 presents a preliminary workflow drawn from the PEER PBEE methodology, designed to compute the associated risk for wind farms post-earthquakes. Each step has been explained in the previous sections. Such a framework allows designers to estimate potential downtimes at different hazard levels systematically.

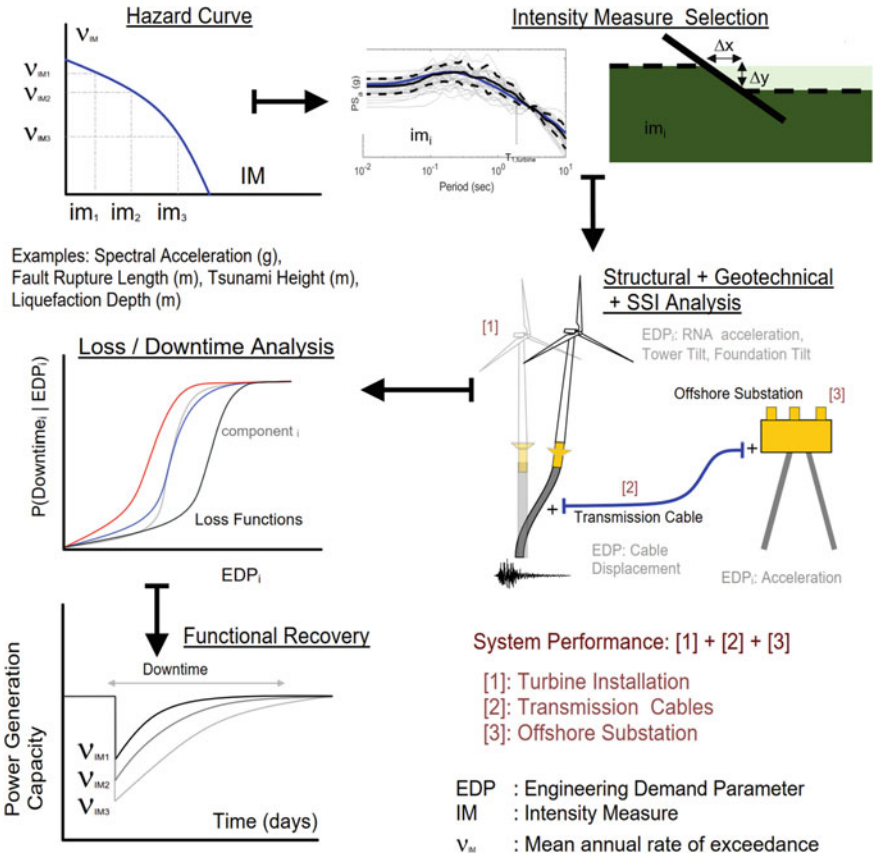

Fig. 19 Workflow for functional recovery analysis

The sensitivity of non-structural components in wind farms necessitates performance-based design. Further, the proposed framework can also look at other seismic hazards apart from ground shaking, including fault rupture, soil liquefaction, and seismically induced landslides.

EERI (2009) highlights the need to shift the existing prescriptive design paradigm toward functional recovery to obtain "better than code" seismic designs, where explicit considerations are made toward the loss of functionality of the structure post-earthquakes. Currently, the existing PBEE framework is predominantly used to study buildings and bridge structures. Therefore, more work is necessary for each step of this process while adopting the framework for the design of offshore wind farms, particularly given their short lifespan. Further work in the area should look at estimates of the loss and fragility functions for turbines, power station, and cables.

6.1 Approaches to RISK Modeling for Offshore Wind Farms

In catastrophe risk modeling, the seismic risk can be computed by convoluting seismic hazard, exposure, and vulnerability. For a typical offshore wind farm, as mentioned earlier, the seismic hazard includes:

1. Ground shaking: effect induced by propagation of body waves.
2. Liquefaction: loss of bearing capacity of soil caused by excess pore water pressure development.
3. Fault displacement: propagation of fault rupture at the surface. This is usually classified in primary and distributed faulting.
4. Submarine landslide: loss of stability of sloping grounds.
5. Tsunami: sudden large surges of water, reaching heights above 30 m.

Exposure components

The exposure component includes information related to the different assets operating in an offshore wind plant; these can be classified into generation assets (e.g., turbine) and transmission assets (e.g., cables, substations). The information included in the exposure model can be diverse but they normally include: geographical location (i.e., Latitude and Longitude), structural and non-structural characteristics, and economic data, including replacement costs, insured costs, etc.

The vulnerability model comprises fragility functions and loss functions. The fragility functions define the probability of exceeding a set of damage states given an intensity measure. One of the intellectual tasks is the relevant damage states that need to be identified for both generation and transmission assets. The loss functions define the probability distribution of loss for each damage state. The seismic risk assessment can be performed following one of the following approaches:

Method–1: Intensity-based approach: Hazard is computed in terms of an earthquake intensity measure. This can be expressed in terms of either spectral accelerations or displacement, or suite of accelerograms that have been selected and scaled for consistency with the design spectrum. The output is expressed in terms of annual probability of loss for a given intensity measure.

Method–2: Scenario-based assessment: This provides intensity parameters for one or more earthquake scenario, each of which is defined by the pair magnitude-distance. The chosen earthquake scenario often corresponds to the so-called worst-case scenario, although this may not be appropriate for offshore wind farms whose assets are largely unmanned. The output is expressed in terms of annual probability of loss for a given scenario (i.e., pair magnitude-distance).

Method–3: Time-based assessment: Wherein the ground-shaking hazard is determined through probabilistic seismic hazard analysis where all possible earthquake scenarios that might affect the study area are considered within a probabilistic framework. The time-based assessment is normally adopted by cat models used in the (re)insurance industry. The output is expressed in terms of annual probability of loss for a selected asset and/or a portfolio of assets.

7 Discussion and Conclusions

The available methods for the design of offshore Wind Turbine structures in seismically active areas are largely based on codes intended for ordinary buildings and critical facilities, such as Nuclear Power Plants. However, there are important differences between wind turbines and these structures as the former are designed for a significantly shorter life span and are predominantly unmanned. Therefore, it is questionable whether the available seismic provisions should be extended to design wind farms in seismic areas. It is argued that the entire design process is driven by the overall performance of the turbine, and the safety of the individual components (e.g., blades, gearboxes, etc.), whose failure may lead to prolonged downtimes and expensive reparation costs. Considering the relatively lifespan for which offshore wind turbines are typically designed, it is questionable whether a detailed PSHA is required to define the seismic hazard at the site. Furthermore, the paucity of recorded strong-ground-motion data at offshore sites introduces additional challenges and uncertainties in the seismic hazard estimates. The paper summarizes the various analysis and design issues.

References

Alati, N., Failla, G., & Arena, F. (2015). Seismic analysis of offshore wind turbines on bottom-fixed support structures. *Philosophical Transactions of the Royal Society A, 373*(2035), 20140086.

Aleem, M., Bhattacharya, S., Cui, L., Amani, S., Salem, A. R., & Jalbi, S. (2022). Load utilisation (LU) ratio of monopiles supporting offshore wind turbines: Formulation and examples from European Wind Farms. *Ocean Engineering, 248*, 110798. https://doi.org/10.1016/j.oceaneng.2022.110798

Ali, A., De Risi, R., Sextos, A., Goda, K., & Chang, Z. (2020). Seismic vulnerability of offshore wind turbines to pulse and non-pulse records. *Earthquake Engineering & Structural Dynamics, 49*(1), 24–50.

Amani, S., Prabhakaran, A., & Bhattacharya, S. (2022). Design of monopiles for offshore and nearshore wind turbines in seismically liquefiable soils: Methodology and validation. *Soil Dynamics and Earthquake Engineering, 157*, 107252. https://doi.org/10.1016/j.soildyn.2022.107252

Baker, J. W. (2011). Conditional mean spectrum: Tool for ground-motion selection. *Journal of Structural Engineering, 137*(3), 322–331.

Bhattacharya, S. (2019). *Design of foundations for offshore wind turbines*. Wiley.

Bhattacharya, S., Goda, K. (2016). Use of offshore wind farms to increase seismic resilience of Nuclear Power Plants. *Soil Dynamics and Earthquake Engineering*, *80*, 65–68. (Jan 2016). https://doi.org/10.1016/j.soildyn.2015.10.001.

Bhattacharya, S., Orense, R. P., & Lombardi, D. (2019). *Seismic design of foundations: Concepts and applications*. Text book, ICE Publications.

Bhattacharya, S., Amani, S., Prabhakaran, A., & Macabuag, J. (2022). Hazard considerations in the vulnerability assessment of offshore wind farms in seismic zones. *Earthquake Engineering and Resilience, 1*(1), 88–109. https://doi.org/10.1002/eer2.11

Bhattacharya, S., Biswal, S., Aleem, M., Amani, S., Prabhakaran, A., Prakhya, G., Lombardi, D., & Mistry, H. K. (2021a). Seismic design of offshore wind turbines: good, bad and unknowns. *Energies, 14*(12), 3496. https://doi.org/10.3390/en14123496

Bhattacharya, S., Biswal, S., Aleem, M., Amani, S., Prabhakaran, A., Prakhya, G., Lombardi, D., Mistry, H. K. (2021b). Seismic design of offshore wind turbines. In *The 17th World Conference on Earthquake Engineering 2021*, Sendai, Japan.

Bhattacharya, S., Lombardi, D., Amani, S., Aleem, M., Prakhya, G., Adhikari, S., Aliyu, A., Alexander, N., Wang, Y., Cui, L., Jalbi, S. (2021). Physical modelling of offshore wind turbine foundations for TRL (technology readiness level) studies. *Journal of Marine Science and Engineering, 9*(6), 589. https://doi.org/10.3390/jmse9060589

Cornell, C. A. (1968). Engineering seismic risk analysis. *Bulletin of the Seismological Society of America, 58*(5), 1583–1606.

Dash, S., Rouholamin, M., Lombardi, D., & Bhattacharya, S. (2017). A practical method for construction of py curves for liquefiable soils. *Soil Dynamics and Earthquake Engineering, 97*, 478–481.

De Risi, R., Bhattacharya, S., & Goda, K. (2018). Seismic performance assessment of monopile-supported offshore wind turbines using unscaled natural earthquake records. *Soil Dynamics and Earthquake Engineering, 109*, 154–172.

DNV. (2017). Det Norske Veritas. Design of offshore wind turbine structures. Offshore Standard DNV-OS-J101 (p. 238). https://www.dnvgl.com/.

DNV/Risø. (2002). Guidelines for design of wind turbines (2nd ed.) Copenhagen, Denmark: Det Norske Veritas and Wind Energy Department, Risø National Laboratory

EC8 (2003) CEN. Eurocode 8: Design of structures for earthquake resistance—Part 1: General rules, seismic actions and rules for buildings. Final draft. prEN 1998–1. Brussels.

EERI. (2019): Functional recovery: A conceptual framework with policy options. White Paper. https://www.eeri.org/images/archived/wp-content/uploads/EERI-Functional-Recovery-Conceptual-Framework-White-Paper-201912.pdf/.

Germanischer, G. L. (2005). *Guideline for the certification of offshore wind turbines*. Hamburg.

IEC, International Electrotechnical Commission. (2009). IEC 61400*3: Wind turbines–Part 3: Design requirements for offshore wind turbines, 3rd ed. ISO 19901-2:2017. (Petroleum and

natural gas industries—Specific requirements for offshore structures—Part 2: Seismic design procedures and criteria).

Iervolino, I., Galasso, C., & Cosenza, E. (2010). REXEL: Computer aided record selection for code-based seismic structural analysis. *Bulletin of Earthquake Engineering, 8*(2), 339–362.

Jalbi, S., Arany, L., Salem, A., Cui, L., & Bhattacharya, S. (2019). A method to predict the cyclic loading profiles (one-way or two-way) for monopile supported offshore wind turbines. *Marine Structures, 63*, 65–83. https://doi.org/10.1016/j.marstruc.2018.09.002

Kementzetzidis, E., Corciulo, S., Versteijlen, W. G., & Pisanò, F. (2019). Geotechnical aspects of offshore wind turbine dynamics from 3D non-linear soil-structure simulations. *Soil Dynamics and Earthquake Engineering, 120*, 181–199.

Lombardi, D., Bhattacharya, S., & Wood, D. M. (2013). Dynamic soil–structure interaction of monopile supported wind turbines in cohesive soil. *Soil Dynamics and Earthquake Engineering, 49*, 165–180.

Lombardi, D., & Bhattacharya, S. (2014). Modal analysis of pile-supported structures during seismic liquefaction. *Earthquake Engineering & Structural Dynamics*, *43*(1), 119–138.

Lombardi, D., & Bhattacharya, S. (2016). Evaluation of seismic performance of pile-supported models in liquefiable soils. *Earthquake Engineering & Structural Dynamics, 45*(6), 1019–1038.

Lombardi, D., Dash, S. R., Bhattacharya, S., Ibraim, E., Muir Wood, D., & Taylor, C. A. (2017). Construction of simplified design p–y curves for liquefied soils. *Géotechnique, 67*(3), 216–227.

Luco, N., & Bazzurro, P. (2007). Does amplitude scaling of ground motion records result in biased nonlinear structural drift responses? *Earthquake Engineering & Structural Dynamics, 36*(13), 1813–1835.

Malhotra, P. K. (2006). Smooth spectra of horizontal and vertical ground motions. *Bulletin of the Seismological Society of America, 96*(2), 506–518.

McGuire, R. K. (2004). MNO-10, Seismic hazard and risk analysis (pp. 240). Earthquake Engineering Research Institute.

Pagani, M., et al. (2020) The 2018 version of the Global Earthquake Model: Hazard component. *Earthquake Spectra*, *36*(1_suppl), 226–251. (Oct 2020). https://doi.org/10.1177/8755293020931866.

Scott, R. F. (1986). Solidification and Consolidation of a Liquefied Sand Column. *Soils and Foundations, 26*(4), 23–31.

Yawson, P. Y., & Lombardi, D. (2018). Probabilistic seismic risk assessment of nuclear reactor in a hypothetical UK site. *Soil Dynamics and Earthquake Engineering, 113*, 278–285.

Zhang, Q., & Zheng, X. Y. (2020). Temporal and spectral characteristics of seismic ground motions: Offshore versus onshore. *Marine Structures, 74*, 102812.

Zhao, M., Gao, Z., Wang, P., & Du, X. (2020). Response spectrum method for seismic analysis of monopile offshore wind turbine. *Soil Dynamics and Earthquake Engineering, 136*, 106212.

Numerical Modelling of Basin Effects on Earthquake Ground Motions in Kutch Basin

A. Boominathan and R. Vijaya

1 Introduction

On 26 January 2001 at 8.46 am, one of the deadliest earthquakes struck Kutch region, located in the western part of India and caused 20,000 fatalities and an economic loss of around 5 billion USD. After the devastating earthquake, the Indian seismic code was revised and the Kutch region that is located in one of the wealthiest and prosperous states in India–Gujarat, was placed under seismic zone 5 (highest seismic risk). It is noted from the past seismic history that the basin effects have played a crucial role in the damage distribution of Kutch region. The site response studies carried out in the Kutch region by various authors after the 2001 Bhuj earthquake, revealed significant spatial variation of strong motion and high site amplification was observed at certain regions (Mandal et al., 2005, 2008; Malagnini et al., 2006; Sawada et al., 2001). The site amplification inferred by various researchers in Kutch Basin shows a relatively large variability owing to the negligence of subsurface geometry inclusion. Though the field studies indicate enough evidence of basin effect, there are no detailed numerical studies on the site response of Kutch Basin carried out. In the present study a sincere attempt is made to study the basin effects in Kutch region through development of numerical models of Kutch Basin. The complicated wave propagation phenomenon that occurs in the basin in multidimensions and modifies the ground motion characteristics significantly across the basin surface is termed as basin effect. Though there are enough evidences of basin effect on ground motion modification available from 1985 Michoacan earthquake in Mexico Basin (Flores-Estrella et al., 2007), 1994 Northridge earthquake in Los Angeles Basin (Graves, 1995), 1995 Hyogo-Ken Nanbu earthquake in Kobe Basin (Pitarka et al., 1997), 2001 Bhuj earthquake in Kutch Basin, etc., it is not transferred yet to the building design codes and provisions due to the lack of sufficient research and computational

A. Boominathan (✉) · R. Vijaya
Indian Institute of Technology Madras, Chennai, India
e-mail: boomi@iitm.ac.in

T. G. Sitharam et al. (eds.), *Advances in Earthquake Geotechnics*, Springer Tracts in Civil Engineering, https://doi.org/10.1007/978-981-19-3330-1_2

power. In the present study, the Kutch region is modelled in two different domains, using two different numerical tools. Initially a three-dimensional simplified model is developed to analyse the effect of basin. Later, a two-dimensional typical Kutch Basin model is developed and the best model to examine the seismic behaviour of Kutch Basin is arrived. Finally, a comprehensive parametric study is carried out using the developed model to assess the seismic response of generic basin.

2 Basin Effects

Basin effect refers to the influence of two- or three-dimensional sedimentary basin structures on ground motions. The basin effects were noticed initially by Hanks (1975) during the analysis of data recorded in San Fernando Valley during the 1971 San Fernando earthquake. However, the basin effect became a critical issue only after the 1985 Michoacan earthquake, in which the surface motion was significantly modified due to the effects of basins in Mexico City (Bard et al., 1988). The peak ground acceleration recorded at the station SCT located in Mexico city 400 km away from the epicentre was found to be larger than that at the Campos station located nearby the epicentre. Even inside the city, a huge variation in the intensity of ground motion was observed between the stations SCT and UNAM located at different parts of the Mexico Basin. The peak ground acceleration at SCT station is found to be five times higher than that of UNAM station and spectral acceleration at the period of 2 s at SCT is about 10 times greater than at UNAM (Semblat & Pecker, 2009). Later, the damage pattern observed during 1988 Armenia earthquake, 1994 Northridge Earthquake, 1995 Kobe Earthquake, 1995 Dinar earthquake and 1999 Kocaeli earthquake also reflected the multidimensional effects of the basin on ground motion.

The spatial variation of the surface ground motion on basins has been investigated through analysis of recorded data by various researchers (Kawase & Aki, 1989; Graves, 1995; Davis et al., 2000). The studies showed that the lateral heterogeneity of the sedimentary basins is the leading cause for the significant amplification of the seismic wave. The complicated wave scattering phenomena such as wave trapping, basin edge effects, wave focussing and double resonance, occurring due to the multidimensional effect of the basin are found to play a significant role in ground motion modification (Narayan & Kamal, 2015; Semblat et al., 2002). The 2D and 3D numerical simulation of an earthquake is then carried out in valleys and basins across the world to study the multidimensional basin effect. The studies on site amplification for the typical basins by various numerical methods showed a variation of amplification from a factor of 1–6 along the surface of the basin (Frankel, 1993; Olsen, 2000; Smerzini et al., 2011). Thus, the observed damage patterns and the numerical analysis revealed that incorporation of multidimensional basin effects is crucial in the hazard assessment and the seismic design of structures.

There are several basins in India, such as Kutch Basin, Indo-Gangetic Basin, Brahmaputra Basin and Talchir Basin which are located in regions of highest seismic

risk. The basin amplification factors are developed for the Indo-Gangetic region by various numerical approaches (Bajaj & Anbazhagan, 2019; Bagchi & Raghukanth, 2017). However, very limited studies are carried out on the multidimensional effect of the basin on ground motion characteristics and the structural response in the Indian context. Most of the civilisations and cities are developed along the river basins and the majority of the growing population is migrating towards these cities leading to huge development in real estate and infrastructure. Therefore, it is essential to analyse the multidimensional effect of the basin through site response analysis and incorporate the basin factor in seismic code. The Gujarat state, one of the wealthiest states in the country has three basins in the state namely Kutch, Cambay and Narmada, amongst which the Kutch Basin has experienced several moderate to major intra-plate earthquakes in a span of 200 years (Rajendran & Rajendran, 2001). The 2001 Bhuj earthquake that occurred in the Kutch region had a devastating effect and the aftershocks continued for a decade. The severe damage caused during the 2001 Bhuj earthquake in the regions 350 km away from the epicentre demonstrated the influence of nature and geometry of the subsurface soil in the local modification of the seismic ground motions (Narayan & Sharma, 2004).

3 Kutch Basin: Seismotectonic Setting and Strong Motion Instrumentation

All the rift basins in the Gujarat state, namely, the Kutch Basin, the Cambay Basin and the Narmada Basin, are formed due to reactivated movements along the major Precambrian trends. The Kutch Basin, distinguished by highlands and the plains which are the areas of uplifts and the basins, respectively, has the typical geometry of an asymmetric rift basin inclined towards the South. The rifting of Kutch Basin commenced during the late Triassic breakup of the Gondwanaland and terminated during the late Cretaceous pre-collision stage of the Indian plate. During the post-collision compressive regime of the Indian plate, the Kutch rift Basin became a shear zone with strike-slip movements along the sub-parallel rift faults. This faulting formed a series of half grabens/basins successively from north to south. The Kutch Mainland fault became the active principal fault and the epicentres of two big earthquakes including the aftershock hypocentre of 2001 Bhuj earthquake are located in this zone. The structural axis of the basin descends southwest as indicated by sediment thickness; the thicknesses of sediment range from less than 500 m in the north to over 4000 m in the south and from 200 m in the east to over 2500 m in the west (Biswas, 2005). The Kutch Basin consists of Tertiary rocks in the periphery and Quaternary sediments deposited in the basin.

After the 2001 Bhuj earthquake, the aftershock activity had been very intensive and was continuing with occasional occurrences of M 3 and M 4 aftershocks in the Kutch region. The National Geophysical Research Institute deployed an array of network consisting of three-component broadband sensors and accelerographs

to monitor these aftershocks. Even after five years of the mainshock, aftershock of moderate intensity M 5.6 occurred on 6 April 2006. Using this strong motion data, the sediment thickness is also estimated based on the travel time difference between the S and Sp waves and from the velocity model obtained from geophysical surveys.

4 3D Seismic Analysis of Kutch Basin by Spectral Element Method

The Kutch Basin in India extending from latitude 23.00° N to 23.85° S and longitude 69.55° E to 70.85° W, as reported by Mandal (2006), is considered in this study. 3D numerical modelling of the study region is carried out using spectral element code SPEED (Mazzieri et al., 2013), to analyse the effects of basin on the ground motion amplification and structural response. The dimensions of the numerical model are based on the data described in the following. The maximum sediment thickness estimated in Kutch Basin is 1.534 km, hence a basin depth of 1.5 km is considered. As the highest frequency of aftershocks occurred at focal depth of 20–30 km and 2001 Bhuj earthquake at 25 km (Mandal et al., 2005), the depth of the half space is taken as 30 km. The basin extends for approximately 250 km in the E–W and 150 km in the N–S direction; however, the sediment thickness data for 150 km in the E–W and 90 km in the N–S direction in the basin reported by Mandal (2006) is considered for modelling basin geometry. Thus, computational domain of size 200 km × 140 km × 30 km, within which lies a simplified rectangular basin of size 150 km × 90 km × 1.5 km, is adopted for the analysis. A geometric layout of the 3D model used in the study is shown in Fig. 1.

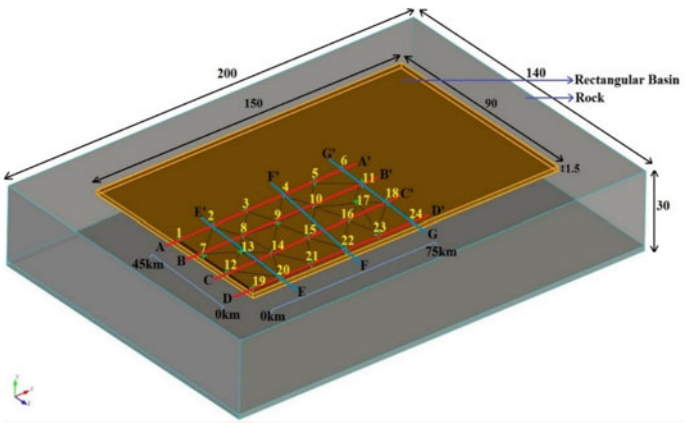

Fig. 1 3D simplified model of Kutch Basin along with the surface of monitored points (not to scale) (Vijaya et al., 2020)

The entire computational domain is discretised using hexahedral elements. For accurate wave propagation, 5 grid points per minimum wavelength is considered (Paolucci et al., 2016). The soil in the basin is modelled as a linear visco-elastic medium characterised by average density (ρ) and shear wave velocity (Vs). The shear wave velocity of Kutch region measured by Multichannel Analysis of Surface waves (MASW) and PS-logging methods is found to vary from 200 m/s at the surface to 800 m/s at the depth of 60 m (Sairam et al., 2019). Based on the measured shear wave velocity of the region, the average Vs value of 500 and 1000 m/s is adopted for the soil and rock, respectively. The values of compressional wave velocity (Vp), damping (Q) and density (ρ) are calculated from the shear wave velocity. Poisson's ratio is assumed to be 0.2 and 0.15 for the fine dense sandy soil and rock, respectively, as per the literature (Sairam et al., 2019). Absorbing boundary conditions are implemented along the sides by considering the local P3 paraxial condition, proposed by Stacey (1988). A second ricker wavelet with maximum frequency 1 Hz is used as the input motion at the bottom. Simulation is performed at Virgo Cluster available at IIT Madras using 124 parallel processors. The single simulation for the basin was carried out at total computational time of about 90 h. More details on the 3D modelling of the Kutch Basin can be found in Vijaya et al. (2018, 2020).

From the 3D ground response analysis of the simplified Kutch Basin acceleration time history is obtained at 24 different points on the basin surface, as shown in Fig. 1. These 24 points are located along four cross sections A–A′, B–B′, C–C′, and D–D′ (marked red in Fig. 1) in the longitudinal direction (E–W) and three cross sections E–E′, F–F′, and G–G′ (marked blue in Fig. 1) in the transverse direction (N–S). Due to symmetry, only one-fourth of the basin surface is monitored. The horizontal component of acceleration time history obtained at section A–A′ and D–D′ is presented in Fig. 2.

It can be seen from the figure that multiple peaks are occurring near the basin edge and the number of peaks reduces as we move towards the centre of the basin. It was also found that the number of peaks in cross-sectional C–C′ and D–D′ are comparatively higher than that of sections A–A′ and B–B′. The reason for the higher number of peaks near the edges is attributed to the surface waves generated by interference of body waves and reflected waves from the edges, implying the basin edge effect. There are a lesser number of peaks towards the centre due to the dampening of surface waves with distance. The duration of ground motion is observed to be comparatively longer near the edges than the basin centre due to the locally generated surface waves. Similar observation is also reported by Pitilakis et al. (2004) based on the field observation studies carried out at EUROSEISTEST site located in northern Greece.

The snapshots of horizontal ground velocity at various time instants (T) are shown in Fig. 3 to examine the crucial role played by the multiple basin edges and trapping of waves in three dimensions.

The peak ground velocity (PGV) observed near the edges and centre of the basin, associated with surface waves and trapped waves, respectively, are marked in the figure as rectangular bands. At T = 30 s the surface waves are generated at the edges and at later time instants (T = 50, 75 s) the waves travel from the edges towards the

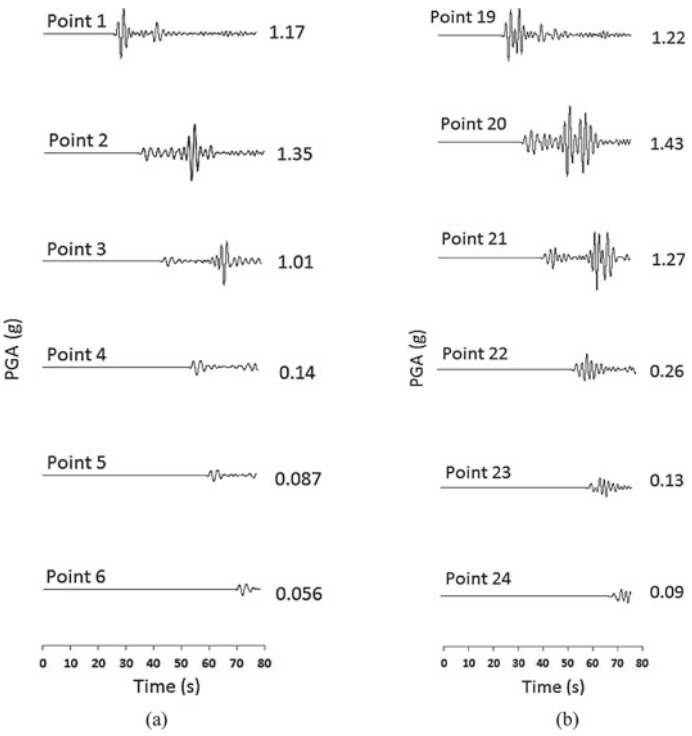

Fig. 2 Acceleration time histories obtained at different points along the longitudinal cross sections **a** AA′ **b** DD′ (modified from Vijaya et al., 2020)

centre. From the figure, the highest amplification at the points of maximum interference of diffracted and scattered surface waves can be certainly apprehended. Thus, the amplification of motion due to 3D basin effect is clearly captured. Discussions on ground motion amplification in the frequency domain can be found in Vijaya et al., (2018, 2020).

5 2D Non-linear Seismic Analysis of Kutch Basin by Finite Difference Method

For 2D analysis, the area lying between longitude range 70.10° E and 70.40° W at a Latitude 23.4° N is selected and modelled using finite difference programme FLAC (Cundall, 2011). This area is selected such that the stations equipped with three-component digital accelerographs with varying sediment thicknesses remain covered in that particular cross section (E-W) of the basin. The site amplification factor estimated at three stations BAN (Bandri), NER (Ner), and MGP (Meghpar) in the Kutch region by Mandal et al. (2008) is used for comparing the 2D numerical

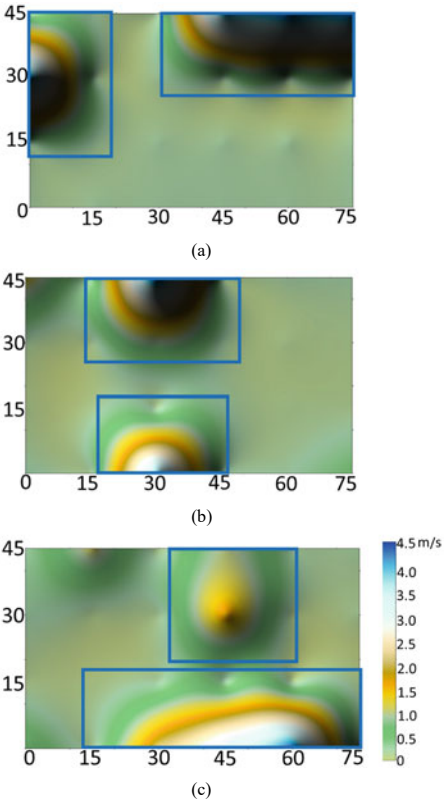

Fig. 3 Snapshots of the velocity field at different time instants **a** T = 30 s, **b** T = 50 s, **c** T = 75 s. X- and Y-axis represents the longitudinal and lateral distance of the basin surface, respectively, in kms (modified from Vijaya et al., 2020)

results at three different locations of the basin, i.e. basin centre, basin edge and region between centre and edge. The Kutch Basin is modelled as a 2D triangular model based on its geological profile (Biswas, 2005) and the sediment thickness of the region (Chopra et al., 2010). As the maximum sediment thickness is 1.5 km and width is 25 km (Longitude 70.10° E to 70.40° W) in the study area, the depth to width (d/b) ratio is around 0.05 which lies in the range of shallow basin, i.e. d/b < 0.25 (Kramer, 1996). Because of the constraints in computational resources, the depth and width of the numerical model is selected as 50 m and 1 km, respectively, so that the d/b ratio (0.05) corresponds to the Kutch Basin. Due to the ambiguity on subsurface basin profile, bedrock slope of 10°, 20° and 30° at the west side of the basin is assumed. Figure 4 shows the schematic layout of the 2D basin model, corresponding to the study region.

The basin is modelled as a heterogeneous medium with 30 m thick medium dense sand 20 m thick dense sand and the region outside the basin is considered as rock. The basin model is discretised into a finite difference mesh composed of quadrilateral elements and the element size is selected based on the material property and the frequency of the input wave. In order to avoid spurious wave reflections free-field

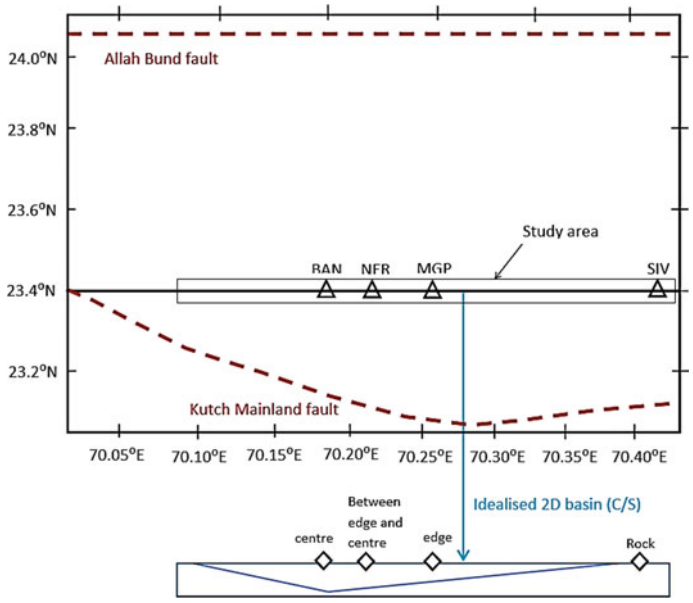

Fig. 4 The study area with the network stations BAN (Bandri), NER (Ner), MGP (Meghpar), SIV (Sivlaka) marked as triangle and the corresponding 2D numerical model with stations marked as diamond

boundaries are coupled to the lateral boundaries. The soil material is modelled using Mohr–Coulomb plasticity and the hysteretic damping is used along with the material model. The modulus degradation and damping curves for sand (average) based on Seed and Idriss (1970) are used. More details on the 2D finite difference modelling can be found in Vijaya et al. (2022, 2017). The measured shear wave velocity of the Kutch region is used. The non-linear seismic site response analysis of the Kutch Basin is then carried out for the recorded motion at Sivlaka station, located at a hillock in Kutch region.

From the 2D ground response analysis, the acceleration time histories are obtained at the surface at 20 locations of regular intervals, as shown in Fig. 5. The basin response is analysed using the normalised distance x/L; where x is the distance from the rock outcrop to the left edge and L is half of the width of basin. Thus, the x/L value of 0 and 2 corresponds to the left and right ends of basin width. It can be noted

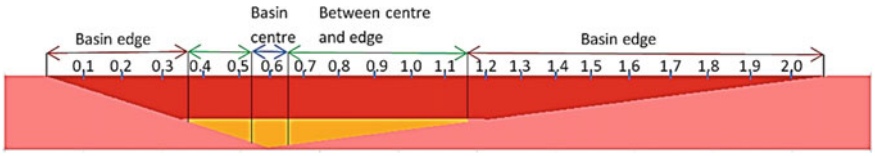

Fig. 5 Schematic representation of location of measurement of acceleration time history

from the figure that, the region of basin surface that is directly above the bedrock slope is defined as basin edge (marked by a red arrow); the region that is completely devoid of bedrock slope is defined as basin centre (marked by a blue arrow) and basin surface between these two is defined as the region between centre and edge (marked by a green arrow). It should be noted that for different bedrock slopes the deepest part of the basin varies with respect to x/L, as the d/b ratio is kept constant.

The horizontal component of acceleration time histories for rock outcrop and three different locations of the basin, i.e. basin edge (x/L = 1.2), region between edge and centre (x/L = 0.8), and basin centre (x/L = 0.6), obtained for three different bedrock slopes are plotted in Fig. 6. It can be seen from Fig. 6a that the PGA of 0.4 g at the rock outcrop is increased to 0.6 g at the basin edge (x/L = 1.2) and 0.8 g both at the basin centre (x/L = 0.6) and at the region between the basin centre and basin edge (x/L = 0.8) for bedrock slope 10°. This could be due to the multiple reflected body waves and surface waves propagating towards the basin centre (Narayan & Kumar, 2014). For bedrock slope 20° (Fig. 6b) it is observed that the PGA is almost the same across the basin surface, whereas for 30° slope (Fig. 6c) PGA is higher at x/L = 0.6 and 1.2 (basin centre and edge region, respectively) than at x/L = 0.8 (region between the centre and edge region). The reason for different trends observed with varying slopes is the difference in thickness of soil layers and the angle of slope between each profile. Due to this the angle of reflection and refraction of the waves vary at the slopes and therefore the location of maximum PGA.

The Fourier amplitude spectra are also computed from the horizontal component of acceleration time histories for rock outcrop and basin surface and the site amplification factor is calculated. The site amplification calculated for three different bedrock slopes is compared with that obtained from recorded ground motion data reported by Mandal et al. (2008). The site amplification estimated at three stations BAN, NER and MGH is used for comparison with results of the numerical study. The locations x/L = 0.6, i.e. basin centre, x/L = 0.8, i.e. region between centre and edge and x/L = 1.2, i.e. basin edge, in the numerical model correspond to the stations BAN, NER and MGH in the site, respectively. It was observed from the comparison of results that the overall site amplification pattern obtained from the numerical model with 10° slope matches well with that of the recorded motions across the basin surface than at other bedrock slopes.

6 Parametric Studies on Factors Influencing Basin Response

A parametric study is carried out using the developed 2D numerical model, to study the influence of basin shape and input motion characteristics on the ground motion parameters. The basin shapes considered are trapezoidal, triangular, rift, rectangular and semi-circular. Aspect ratio of 0.05 and bedrock slope of 10° is assumed for all basin models and the basin is subjected to Sivlaka motion. Amongst the basin shapes

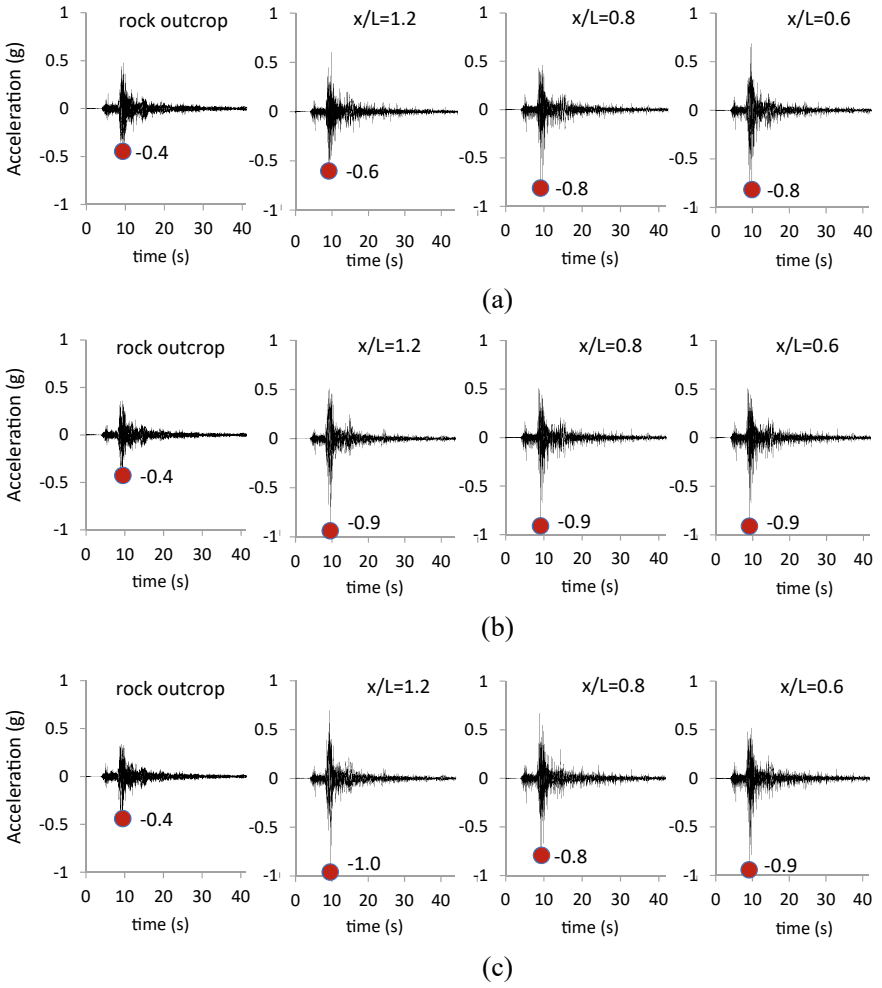

Fig. 6 Acceleration time history obtained at the surface of the triangular basin with bedrock slope **a** 10° **b** 20° and **c** 30° when subjected to Sivlaka input motion (PGA encircled)

considered, trapezoidal, triangular, rift and rectangular basins are 50 m thick and 1 km wide. For semi-circular basin, the basin radius is taken as 50 m. To study the effect of input motion, the basins are subjected to four input motions of different frequency: Sivalaka earthquake, Kobe earthquake, Imperial earthquake and Kocaeli earthquake. The details of the input motion used are presented in Table 1. The surface acceleration is obtained across the basin surface at regular intervals and at rock outcrop. For evaluation of the ground motion modification due to the 2D basin effects, the PGA amplification factor and predominant frequency is calculated. In this study, the "PGA amplification factor" is defined as the ratio of the peak ground acceleration of the basin

Table 1 Details of input motion and element size used in the model

Earthquake	Magnitude M_w	Station	Epicentral distance (km)	PGA (g)	Predominant frequency (Hz)	Significant Duration (s)	Cut-off frequency (Hz)	Element size (m)
2006 Sivlaka	4.8	SIV	32	0.17	7	10.5	20	1.5
1995 Kobe	6.9	KAKOGAWA	24	0.26	0.6	13.3	5	6
1979 Imperial	6.5	USGS STATION 5115	29	0.35	1.3	9.0	8	4
1999 Kocaeli	7.4	YARIMCA	16	0.29	0.3	15.8	4	7

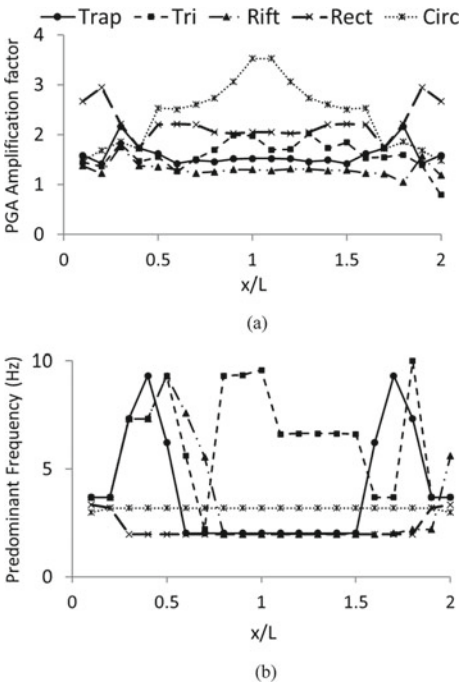

Fig. 7 Effect of basin shape on **a** PGA amplification factor and **b** Predominant frequency (d/b = 0.05; θ = 10°; Sivlaka earthquake)

surface to reference rock outcrop at each point; while the frequency corresponding to the maximum value of Fourier amplitude is defined as the predominant frequency.

The spatial variation of the PGA amplification factor and predominant frequency of the ground motion obtained from basin models of different shapes are presented in Fig. 7.

It is seen from Fig. 7 a that the PGA amplification factor ranges from 1.4 to 2.2, 1.0 to 2.05, 1.05 to 1.75, 1.75 to 3.0, 1.5 to 3.5 for trapezoidal, triangular, rift, rectangular and semi-circular basin shape basins, respectively. The maximum amplification occurs at basin edge region for trapezoidal, rift and rectangular basins; whereas for the triangular and semi-circular basin, it occurs at the region between centre and edge and basin centre. It can be observed that the maximum amplification occurs for the semi-circular basin. It is because of the shape of the circular basin, significant wave focussing and trapping occurs in the entire basin medium. The attenuation of waves will also be less in circular basins since the size of the circular basin is less compared to other basins. It is observed from Fig. 7b that the predominant frequency of surface ground motion varies across the entire basin surface for the triangular basin. Whereas for trapezoidal and rift basins the spatial variation of predominant frequency is limited to the basin edges, i.e. till x/L = 0.7 and for rectangular and circular basins the variation is found only till x/L = 0.2. It can be seen that the surface motion's predominant frequency increases than input motion's predominant frequency at basin edge region for triangular, trapezoidal and rift basin. For all basin shapes, except triangular, the

predominant frequency of surface ground motion decreases than that of input motion at the basin centre and the region between centre and edge. Thus, it can be concluded that the 2D basin effect on the frequency of surface ground motion is constrained to the edges, except for triangular basins.

For studying the effects of input motion characteristics on the seismic response of basin, shallow trapezoidal basin with 10° bedrock slope is subjected to recorded ground motion from various basin sites across the world. Thus, the basin is subjected to four different earthquakes: 2006 Sivlaka Mw 4.8, 1995 Kobe Mw 6.9, 1979 Imperial Mw 6.5 and 1999 Kocaeli Mw 7.4 (Source: PEER strong motion database). The peak ground acceleration (PGA) of the input motions varies from 0.17 g to 0.35 g and predominant frequency varies from 0.3 to 7 Hz. Figure 8 presents the effect of input motion on ground motion amplitude and frequency.

It is seen from Fig. 8a that the PGA amplification factor ranges from 1.4 to 2.2, 1.1 to 1.6, 1.1 to 2.1, 1.0 to 1.7 for Sivlaka, Kobe, Imperial and Kocaeli earthquake respectively. It can also be seen from Fig. 8a that the PGA amplification of more than 2 is obtained when the basin is subjected to high-frequency Sivlaka motion and medium-frequency Imperial motion; while for low-frequency Kobe and Kocaeli earthquakes, the maximum amplification is around 1.7. The maximum PGA amplification factor is found to occur at the basin edge region for all input motions and

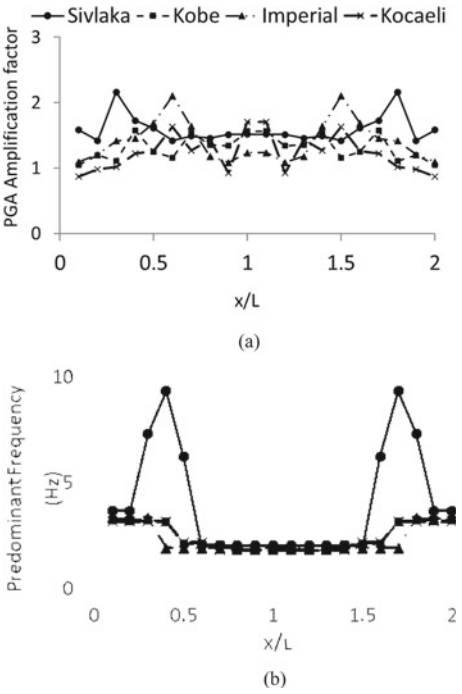

Fig. 8 Effect of input motion on **a** PGA amplification factor and **b** Predominant frequency (shape–trapezoidal; d/b = 0.05; θ = 10°)

the peak is found to drift away from the edge with the increase in amplitude of the input motion. It is observed from Fig. 8b that the predominant frequency of surface ground motion is not influenced substantially by the input motion characteristics. It can be seen that the predominant frequency of surface ground motion is around 3.5 Hz at the edges and 2 Hz at the region between centre and edge and the basin centre for all input motions. However, when the basin is subjected to Sivlaka motion significant increase in the predominant frequency is observed between x/L = 0.3 and 0.5. It is found that the predominant frequency of the surface ground motion obtained from the basin response analysis is the same as that of the fundamental frequency of the site (f_0) obtained from the 1D linear wave propagation analysis (f_0 = Vs/4H) for all input motion. It should be noted that the predominant frequency of the input motion used in the present parametric analysis varies from 0.3 to 7 Hz whereas the predominant frequency of basin surface motion obtained from the analysis lies in the range of 2 Hz to 3.5 Hz. There is no influence of input motion characteristics on predominant frequency, except for Sivlaka motion for which there is a spike in frequency observed at the edge.

7 Summary and Conclusion

The numerical modelling of basin effects is carried out for the Kutch region to analyse the ground motion variation observed during the aftershocks of 2001 Bhuj earthquake. Initially a 3D linear analysis of the Kutch Basin is carried out by spectral element method and the results are interpreted in terms of acceleration time history and peak ground velocity. The study showed that the basin edge effect played a key role in the significant amplification observed at the corners of 3D basin. In addition, the Kutch Basin is modelled as a shallow scalene triangular basin model with bedrock slopes varying from 10° to 30° by finite difference method and 2D non-linear site response analysis is carried out. The overall pattern of site amplification factor computed at three different locations of the basin with 10° bedrock slope matches with the corresponding stations in the site. The study showed that the seismic response of shallow scalene triangular basin model with 10° bedrock slope compares well with the recorded data in the Kutch region. Further, a parametric study is carried out using the developed finite difference-based numerical basin model, to study the effect of basin shape and input motion characteristics on surface ground motion. The triangular and circular basin shapes are found to be more critical than other shapes since the basin edge effect is predominant over the entire basin medium. The predominant frequency of the surface ground motion is altered across the basin surface only for high-frequency input motion, whereas for other input motions the predominant frequency of the surface ground motion is the same as that of the fundamental frequency of the site obtained from 1D linear wave propagation analysis.

Acknowledgements The authors acknowledge the use of the computing resources at HPCE, IIT Madras. The authors wish to thank Dr. Prantik Mandal, Principal Scientist at National Geophysical

Research Institute–CSIR, Hyderabad for providing the strong motion data and geophysical data of the Kutch region used in the present study. Authors also acknowledge the help rendered by Dr. Ilario Mazzieri, Senior Assistant Professor at Politecnico di Milano, Milan, Italy in advanced scientific computing.

References

Bagchi, S., & Raghukanth, S. T. G. (2017). Seismic Response of the Central Part of Indo-Gangetic Plain. *Journal of Earthquake Engineering, 2469*(August), 1–25.

Bajaj, K., & Anbazhagan, P. (2019). Comprehensive amplification estimation of the Indo Gangetic Basin deep soil sites in the seismically active area. *Soil Dynamics and Earthquake Engineering, 127*, 105855.

Bard, P. Y., Campillo, M., Chavez-Garcia, F. J., & Sanchez-Sesma, F. (1988). The Mexico earthquake of September 19, 1985-A theoretical investigation of large- and small-scale amplification effects in the Mexico City valley. *Earthquake Spectra, 4*(3), 609–633.

Biswas, S. (2005). A review of structure and tectonics of Kutch basin, western India, with special reference to Earthquakes. *Current Science, 88*(10), 1592–1600.

Chopra, S., Rao, K. M., & Rastogi, B. K. (2010). Estimation of sedimentary thickness in Kachchh Basin, Gujarat using SP Converted Phase. *Pure and Applied Geophysics, 167*, 1247–1257.

Cundall, P. A. (2011). FLAC 2D manual: A computer program for fast Lagrangian analysis of continua (Version 7.0), Minneapolis, Minnesota, USA.

Davis, P. M., Rubinstein, J. L., Liu, K. H., Gao, S. S., & Knopoff, L. (2000). Northridge earthquake damage caused by geologic focusing of seismic waves. *Science*, *289*, 1746–1750.

Flores-Estrella, H., Yussim, S., & Lomnitz, C. (2007). Seismic response of the Mexico City Basin: A review of twenty years of research. *Natural Hazards, 40*, 357–372.

Frankel, A. (1993). Three-dimensional simulations of ground motions in the San Bernardino valley, California, for hypothetical earthquakes on the San Andreas fault. *Bulletin of the Seismological Society of America, 83*, 1020–1041.

Graves, R. W. (1995). Preliminary analysis of long-period basin response in the Los Angeles region from the 1994 Northridge earthquake. *Geophysical Research Letters, 22*, 101–104.

Hanks, T. C. (1975). Strong ground motion of the San Fernando, California, earthquake: Ground displacements. *Bulletin of the Seismological Society of America, 65*(1), 193–225.

Kawase, H., & Aki, K. (1989). A study on the response of a soft basin for incident s, p, and Rayleigh waves with special reference to the long duration observed in Mexico city. *Bulletin of the Seismological Society of America, 79*, 1361–1382.

Kramer, S. L. (1996). *Geotechnical earthquake engineering*. New Delhi: Prentice Hall.

Malagnini, L., Bodin, P., Mayeda, K., & Akinci, A. (2006) Unbiased moment-rate spectra and absolute site effects in the Kachchh Basin, India, from the analysis of the aftershocks of the 2001 Mw7.6 Bhuj earthquake. *Bulletin of the Seismological Society of America*, *96*(2), 456–466.

Mandal, P., Chadha, R. K., Satyamurty, C., Raju, I. P., & Kumar, N. (2005). Estimation of site response in Kachchh, Gujarat, India, region using H/V spectral ratios of aftershocks of the 2001 Mw7.7 Bhuj earthquake. *Pure and Applied Geophysics, 162*(12), 2479–2504.

Mandal, P., Dutta, U., & Chadha, R. K. (2008). Estimation of site response in the Kachchh seismic zone, Gujarat, India. *Bulletin of the Seismological Society of America, 98*(5), 2559–2566.

Mandal, P. (2006) Sediment thicknesses and Qs vs. Qp relations in the Kachchh Rift basin, Gujarat, India using Sp converted phases. *Pure and Applied Geophysics*, *164*(1), 135–160.

Mazzieri, I., Stupazzini, M., Guidotti, R., & Smerzini, C. (2013). SPEED: SPectral elements in elastodynamics with discontinuous Galerkin: A non-conforming approach for 3D multi-scale problems. *International Journal for Numerical Methods in Engineering, 95*(July), 991–1010.

Narayan, J. P., Kamal. (2015). Quantification of effects of geometry of sediment bedrock interface on ground motion in 3D basin with circular free surface. *Geofizika*, *32*(1), 1–25

Narayan, J. P., & Sharma, M. (2004). Effects of local geology on damage severity during Bhuj, India Earthquake. In *Proceedings of the 13th World Conference on Earthquake Engineering*, Paper No. 2040.

Narayan, J. P., & Kumar, R. (2014). Spatial spectral amplification of basin-transduced Rayleigh waves. *Natural Hazards, 71*, 751–765.

Olsen, K. B. (2000). Site amplification in the Los Angeles basin from three-dimensional modeling of ground motion. *Bulletin of the Seismological Society of America, 90*(6B), S77–S94.

Paolucci, R., Evangelista, L., Mazzieri, I., & Schiappapietra, E. (2016). The 3D numerical simulation of near-source ground motion during the Marsica earthquake, central Italy, 100 years later. *Soil Dynamics and Earthquake Engineering, 91*(June), 39–52.

Pitarka, A., Irikura, K., & Iwata, T. (1997). Modelling of ground motion in the Higashinada (Kobe) area for an aftershock of the 1995 January 17 Hyogo-ken Nanbu, Japan, earthquake. *Geophysical Journal International, 131*, 231–239.

Pitilakis, K., Raptakis, D., Makra, K., Ktenidou, O. J., Pandi, K., Manakou, M., Pitilakis, D., and Diagourtas, D.: Effects of surface and subsurface topography on strong ground motion at the city of Aegion-Greece. In *Proceedings of the 13th World Conference on Earthquake Engineering,* Vancouver, Canada, (2004).

Rajendran, C. P., & Rajendran, K. (2001). Characteristics of deformation and past seismicity associated with 1819 Kutch earthquake, Northwestern India. *Bulletin of the Seismological Society of America, 91*, 407–426.

Sairam, B., Singh, A. P., Vandana, P., Chopra, S., & Ravi Kumar, M. (2019) Vs_{30} mapping and site characterization in the seismically active intraplate region of Western India: implications for risk mitigation. *Near Surface Geophysics*, *17*, 533–546.

Sawada, S., Uehan, F., Hayashi, Y., & Arai, H. (2001). Ground condition estimated from microtremor observations. In: T. Sato, M. Hamada, Y. Hayashi, Y. Hisada, T. Kato, V. Katta, G.S. Lakhina, J.N. Malik, K., Miyashita, J.J. Mori, H. Murakami, T. Nakata, H. Negishi, D.K. Paul, H. Sato, S. Sawada, R.P. Singh, T. Yoshioka (Eds.), *A Comprehensive Survey of the 26 January 2001 Earthquake (Mw 7.7) in the State of Gujarat, India.* Japanese Ministry of Education, Culture, Sports, Science and Technology, pp. 71–74.

Seed, H. B., & Idriss, I. M. (1970) Soil moduli and damping factors for dynamic response analysis. Report EERC 70–10. Univ. of California, Berkeley, California.

SEFINDIA (Structural Engineering Forum of India). Appendix C: properties of soils. Retrieved from https://www.sefindia.org/forum/files/appc_soil_properties_718.pdf. (n.d.).

Semblat, J. F., & Pecker, A. (2009). *Waves and vibrations in soils : Earthquakes, traffic, shocks, construction works.* IUSS Press.

Semblat, J. F., Dangla, P., Kham, M., & Duval, A. M. (2002). Seismic site effects for shallow and deep alluvial basins: In-depth motion and focusing effect. *Soil Dynamics and Earthquake Engineering, 22*(9–12), 849–854.

Smerzini, C., Paolucci, R., & Stupazzini, M. (2011). Comparison of 3D, 2D and 1D numerical approaches to predict long period earthquake ground motion in the Gubbio plain, Central Italy. *Bulletin of Earthquake Engineering, 9*(6), 2007–2029.

Stacey, R. (1988). Improved transparent boundary formulations for the elastic wave equation. *Bulletin of the Seismological Society of America, 78*, 2089–2097.

Vijaya, R., Boominathan, A., & Mandal, P. (2017) Seismic wave amplification studies for shallow basins considering basin edge effect. In *Proceedings of 3rd International Conference on Performance based design in Earthquake Geotechnical Engineering*, Vancouver, Canada

Vijaya, R., Boominathan, A., Mandal, P., & Mazzieri, I. (2018) Seismic wave amplification studies considering 3D basin effect by Spectral Element Method. In *Proceedings of 16th Symposium on Earthquake Engineering*, Roorkee, India, (2018).

Vijaya, R., Boominathan, A., & Mazzieri, I. (2020). 3D Ground response analysis of simplified Kutch basin by spectral element method. *Journal of Earthquake and Tsunami, 14*(1), 2050003.

Vijaya, R., & Boominathan, A. (2022). Modelling the 2D seismic response of the Kutch basin on the Indian Subcontinent. *Soil Dynamics and Earthquake Engineering, 152*, 107014.

Controlled Ground-Borne Vibrations for Design of Sub-structural Systems—Theory and Practice

Deepankar Choudhury, Milind Patil, and Ritwik Nandi

1 Introduction

In urban areas, underground mass rapid transit systems are becoming popular to fulfill the transportation demand of the public. The construction activities of these transportation systems generate heavy vibrations that propagate through the soils to the ground and create disturbance to nearby buildings and residents. In recent years, ground-borne vibration and their mitigation is receiving much attention from researchers and practitioners. Majority of research work has been conducted on train-induced vibrations, very few studies are available related to excavation or tunneling induced ground vibration. Several researchers used semi-analytical approaches to model ground vibrations induced by underground railway (He et al., 2018; Hussein et al., 2014; Kuo et al., 2011; Yuan et al., 2016, 2017). These are the simplified methods that may not be suitable in engineering practice because of their limitation in simulating geometries. Many researchers have used numerical methods to predict vibration generation and transmission (Amado-Mendes et al., 2015; Galvín et al., 2010; Lopes et al., 2014; Yaseri et al., 2018). However, most of the studies neglected the effect of mechanical process during tunneling. Present and future ground-borne vibration levels are highly depending on the construction method of tunnels. Muller et al. (2008) developed three-dimensional numerical model on a coupling of analytical method and finite element method for both circular and rectangular tunnels.

D. Choudhury (✉) · R. Nandi
Department of Civil Engineering, Indian Institute of Technology Bombay, Mumbai 400076, India
e-mail: dc@civil.iitb.ac.in

R. Nandi
e-mail: ritnandi@iitb.ac.in

M. Patil
IITB-Monash Research Academy, Mumbai 400076, India

AFRY India Pvt. Ltd, Noida, India

T. G. Sitharam et al. (eds.), *Advances in Earthquake Geotechnics*, Springer Tracts in Civil Engineering, https://doi.org/10.1007/978-981-19-3330-1_3

Yaseri et al. (2014) used coupled finite element and boundary element methods to predict underground train-induced ground-borne vibration. The scaled boundary finite-element method (SBFEM) was used to model outer media around the tunnel. Patil et al. (2015, 2017, 2018) and Choudhury et al. (2019) investigated the factors affecting the behavior of tunnel under seismically induced vibrations using finite element method. Nandi and Choudhury (2018, 2019, 2021) investigated the effect of earthquake-induced vibration on the behavior of embedded cantilever retaining walls, reinforced soil wall and passive earth pressure. Few researchers used physical modeling approach to study ground-borne vibration problems (Thusyanthan & Madabhushi, 2003; Trochides, 1991; Tsuno et al., 2005). Yang et al. (2013a, b) used centrifuge modeling to study the effects of soil non-homogeneity on propagation of ground-borne vibration. The results show that it is important to consider the soil non-homogeneity of soil in determination of soil dynamic response. Many field measurement studies have also been conducted to investigate the vibration phenomena (Auersch, 2005; Galvín & Domínguez, 2007; Paolucci & Spinelli, 2006).

An attempt has been made through this study to provide an insight into theory and practice of controlling ground-borne vibration in sub-structural systems. The open and infill trench methods of vibration mitigation and their efficiency are discussed first. Then the response of multilayer railway track system under cyclic loading is briefly explained. Additionally, a generalized empirical model is explained, this model determines uses basic soil properties to determine the blast-induced vibration parameters. Finally, an emphasis has been given on evaluating the effect of excavation of underground metro station and other related construction activities such as tunneling, blasting, piling, on adjacent structures. Tunneling-induced vibration impact assessment of heritage structure has been explained through a case study.

2 Mitigation of Ground-Borne Vibration

Bose et al. (2018) investigated the use of trenches as a wave barrier in mitigating ground vibration. A numerical model was developed using PLAXIS to study the factors affecting the vibration isolation efficiency of open and infill trenches. Open trench is characterized by three variables: depth (d), width (w) and screening distance (l). These parameters were optimized through parametric study under harmonic loading to achieve maximum screening efficiency. Results of parametric study are plotted in terms of variation of efficiency (amplitude reduction ratio) with change in trench's geometrical parameters. From Fig. 1, it can be observed that normalized depth is a key parameter that controls the efficiency of the isolation system. Efficiency increases with increase in depth. In all the cases of parametric study, the minimum efficiency noted was 55%, whereas maximum was more than 80%. Barrier location and width of trench appear to be the insensitive parameters. Only in case of shallow trenches, the width has played the significant role in blocking wave energy.

At high wavelength, construction and stability of open vertical cuts become difficult. In such cases, infill trenches are more suitable compared to open trenches. In

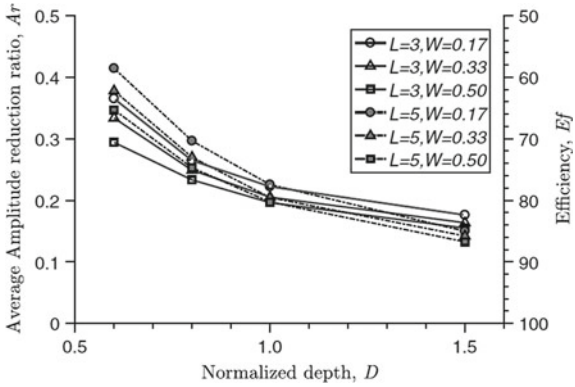

Fig. 1 Variation of average amplitude reduction ratio with depth of an open trench (republished with permission from ASCE, from Bose et al. (2018)

open trench, efficiency is governed by the wave reflection, whereas in infill trenches the combination of reflected and transmitted waves plays the major role. Performance of high-density and low-density materials with varying shear wave velocity is compared through finite element analysis.

Figure 2 shows the variation in the average amplitude ratio with change in shear wave velocity ratio of infill material and in situ material. It can be seen that low-density materials performed well as the wave barriers compared to high-density materials. Moreover, the response of materials depended on the relative shear wave velocity of fill material and in situ soil. Infill trenches showed better efficiency when the shear wave velocity of fill material was less than that of in situ soil. It can be said that the low-density materials possess sufficient energy dissipation capacity. Efficiency of system decreased with an increase in shear wave velocity of fill material. High-density fill materials also performed effectively in mitigating ground vibration. The materials having sufficient stiffness are capable of resisting incoming wave.

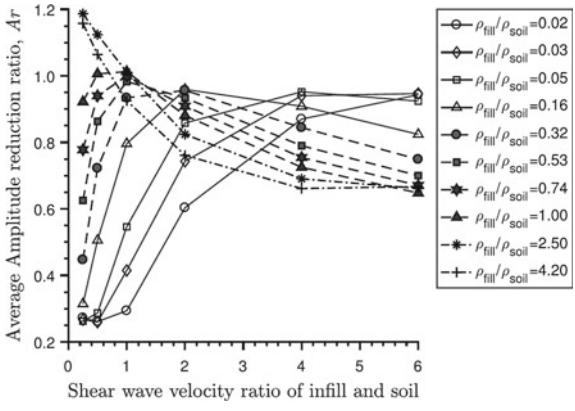

Fig. 2 Variation in average amplitude reduction ratio with the shear-wave velocity ratio of fill material and in situ soil (republished with permission from ASCE, from Bose et al. (2018))

3 Response of Railway Track System Under Cyclic Loading

Ballast and subgrade are the most important components of the railway track system, which distribute the large cyclic wheel loads from the wheel to the underlying soil strata. Typical representation of railway track system is shown in Fig. 3. Choudhury et al. (2008) and Bharti et al. (2006) presented analytical model of a multilayered track using 2 degrees of freedom (2DOF) mass-spring dashpot system, as shown in Fig. 4.

Dynamic behavior of both ballast and subgrade layers was investigated using time zone and frequency domain analyses. The subgrade is considered as an elastic half-space, and the ballast is assumed to be an elastic layer, this makes the 2DOF approach

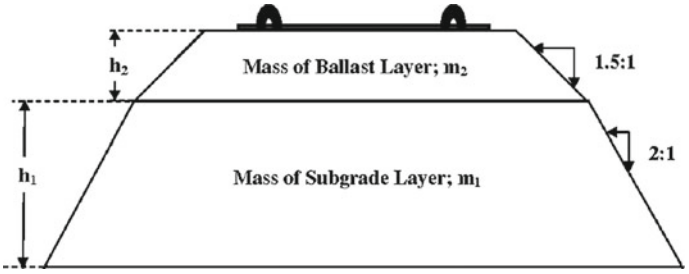

Fig. 3 Typical ballast and subgrade layer below railway track (republished with permission from ASCE, from Choudhury et al. (2008))

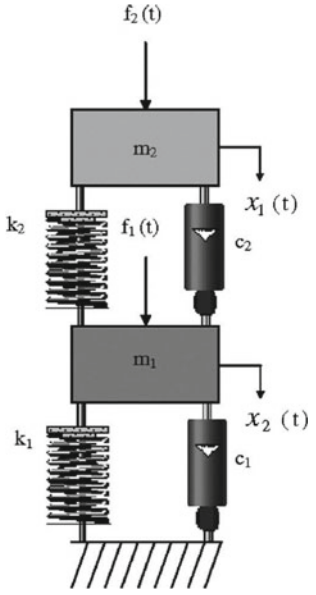

Fig. 4 2-DOF MSD mathematical model (republished with permission from ASCE, from Choudhury et al. (2008))

more realistic compared to normal SDOF model. The differential equations of the system have been derived by considering the dynamic equilibrium and D'Alembert's principle. The system of equations obtained is as follows:

$$\begin{bmatrix} m_1 & 0 \\ 0 & m_2 \end{bmatrix} \begin{Bmatrix} \ddot{x}_1 \\ \ddot{x}_2 \end{Bmatrix} + \begin{bmatrix} c_1 + c_2 & -c_2 \\ -c_2 & c_2 \end{bmatrix} \begin{Bmatrix} \dot{x}_1 \\ \dot{x}_2 \end{Bmatrix} + \begin{bmatrix} k_1 + k_2 & -k_2 \\ -k_2 & k_2 \end{bmatrix} \begin{Bmatrix} x_1 \\ x_2 \end{Bmatrix} = \begin{Bmatrix} f_1(t) \\ f_2(t) \end{Bmatrix} \tag{1}$$

The above system of equations can be solved by using Newmark's method. The solutions give the displacement and acceleration response for both the granular and the subgrade layer. The spring stiffness "k_1" and "k_2" in the model have been calculated by following equation:

$$k = \frac{0.8(1-\mu)G}{(1-2\mu)h} \tag{2}$$

where,

μ = Poisson's ratio.

G = shear modulus, and.

h = depth of the particular layer.

The equivalent damping coefficients of the dashpots "c_1" and "c_2" have been calculated by,

$$c = \sqrt{\frac{2}{1-\mu} G\rho} \tag{3}$$

where,

ρ = mass density of the layer.

Fundamental circular natural frequency of the ballast and the subgrade has been calculated by,

$$\omega = \frac{\pi v_s}{2h} \tag{4}$$

where,

v_s = shear wave velocity for the medium.

4 Determination of Blast-Induced Vibration Parameters

Kumar et al. (2017) developed empirical relations through random number generation technique. These relations are useful in determining strength parameters of rock, such as Young's modulus, Poisson's ratio, cohesion and angle of friction based on uniaxial compressive strength. Kumar et al. (2016) proposed a methodology for the estimation of engineering properties of soils from field SPT using random number generation. Kumar et al. (2015, 2019) investigated the effects of blast on underground soil media with the help of a finite difference program, FLAC3D.

Kumar et al. (2012a, b, 2014a, b, 2016) proposed model for blast vibration prediction in terms of PPV for a soil site and can be written as,

$$v = kD^{-b} \tag{5}$$

$$D = SD = R/Q^{1/3} \tag{6}$$

where,

D = scaled distance (SD) (m/kg$^{1/3}$).

v = peak particle velocity (PPV) in mm/s.

k and b = site constants.

R = distance from the blast point

Q = charge per delay.

Various combinations of three soil properties, namely, Young's modulus, degree of saturation and unit weight were fitted into linear equations. It was observed that ratio of Young's modulus and unit weight closely fit the linear equation. Based on the collected experimental data, the following generalized empirical relation (with $r^2 = 0.907$) is proposed to evaluate PPV for soil sites.

$$v = \left(\frac{E}{\gamma}\right)^{0.229} D^{-(1.6985-0.175S)} \tag{7}$$

where,

E = Young's modulus of soil.

v = peak particle velocity (PPV) in mm/s.

D = scaled distance (SD) (m/kg$^{1/3}$).

S = degree of saturation.

γ = unit weight of soil.

The performance of proposed model has been investigated by comparing experimental and predicted PPV. The predicted PPV found to be in good agreement with experimentally obtained PPV. For blast-related design, this empirical model can be used in practical applications.

5 Impact Assessment Study of Heritage Structures

The alignment of the proposed metro construction for Phase IV in Delhi, India is passing by few heritage sites (see Fig. 5). The list of the heritage site affecting the metro alignment is listed in Table 1. The metro rail project involves large-scale construction works and other activities at site. There are many construction activities like foundation piling, drilling and blasting, driving, compaction, chiseling, excavation, tunneling (using Tunnel Boring Machine) and such others, which may induce ground vibration and transmission. Hence, a careful assessment of soil–structure interaction and ground-borne vibration transmission to the existing heritage monuments is required. The present study evaluates the effect of ground-borne vibrations on the structures located in the close vicinity of the proposed metro rail alignment. In order to evaluate the adequacy of the proposed metro alignment, the impact assessment of construction activities such as excavation, piling, tunneling and drilling/blasting activities has been carried out on these heritage structures.

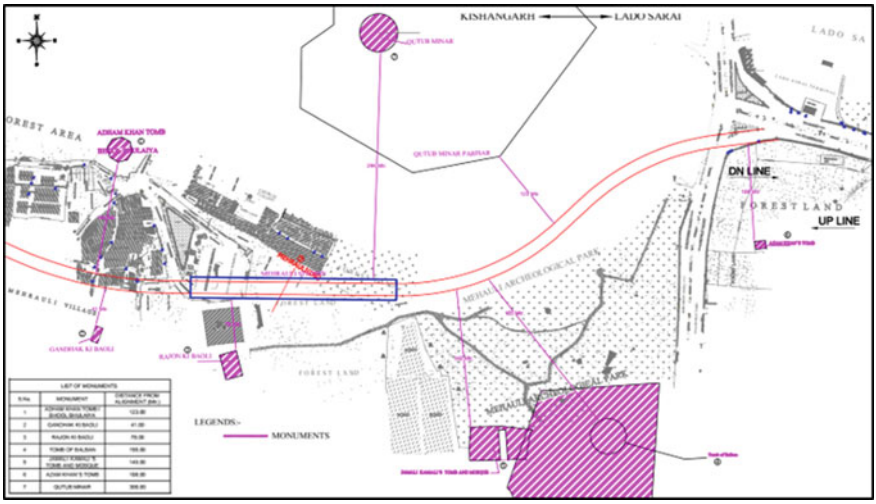

Fig. 5 Layout of the proposed metro line alignment and location of Heritage monuments

Table 1 List of heritage structures in the close vicinity of the proposed metro alignment

Sr. no	Name of heritage monument	Built-in (year)	Distance from the proposed metro alignment (in m)
1	Adham Khan's Tomb/Bhool Bhulaiya	1562	123
2	Gandhak ki Baoli	1211–1236	41
3	Rajon ki Baoili	1506	78
4	Tomb of Balban	1287	455
5	Jamali Kamali Tomb and Mosque	1528–1529	149
6	Azam Khan's Tomb	Seventeenth century	108
7	Qutub Minar	1220	300

5.1 Geotechnical Conditions at Site

The deposits in the proposed site location belong to the "Indo Gangetic Alluvium". Deposits of the Indo-Gangetic Basin are composed of gravels, sands, silts and clays with remains of animal and plants. The geophysical investigation is carried out due to restrictions for drilling of the subsoil in the areas around the heritage site. The layered profile and respective output of seismic refraction test results (in form of compressional wave velocity) are presented in Table 2. In the present analysis, the location of the tunnel section is considered to be at 15 m depth from the ground surface. The investigation results indicate that tunnel is passing through highly weathered rock layer pertaining shear wave velocity (v_s), 400 to 600 m/s.

Table 2 Interpreted stratum based on seismic refraction test

Location	Layer	Depth (m)		Interpreted v_p (m/s)	Interpreted strata
		From	To		
Azam Khan Tomb	1	0	5–12	600–1000	Overburden soil
	2	5–12	30	1500–2500	Rock
ASI Park	1	0	7–8	400–1000	Overburden Soil
	2	7–8	30	1500–3000	Rock
	1	0	8–9	600–1000	Overburden soil
	2	8–9	37	1300–2700	Rock
	1	0	4–8	400–1000	Overburden soil
	2	4–8	25	1300–3500	Rock

5.2 Effect of Ground-Borne Vibration Due to Construction Activity on Heritage Structures

Various sources generate different kinds of ground-borne vibrations that transmit through the soil in different ways, like, transient vibrations, steady-state vibrations and pseudo-steady state vibrations. Vibration can be defined by four parameters: frequency, displacement, velocity, acceleration. Among these variables, the vibration velocity of a particle is directly related to stress generated in the structures, and it is usually measured to evaluate the influence of the vibration on structures. Therefore, the magnitude of vibration is measured in terms of peak particle velocity (PPV). This maximum velocity value, referred to as PPV, is a commonly accepted descriptor for ground vibration amplitude. Given a certain level of vibration, the structural response of a structure to an excitation also depends on its dynamic behavior and in particular of its natural period of frequency. Therefore, predominant frequency is one of the important variables in evaluating the effects of vibration on a structure. The factors that influence the damage to structure subjected to ground-borne vibration are as follows:

- Duration of vibration.
- State of stress to which the structure is subjected.
- Properties of structure, like, foundation type, soil-structure interaction, the quality of materials, the method of construction, and its current state.
- Energy per blow/cycle.
- Distance between source and receiver.

Vibration effects on historic buildings are similar to those for ordinary buildings and structures, although some added complications and uncertainties may be encountered because historic buildings are generally older and may not be structurally as sound as the modern buildings.

5.3 Estimation of Vibration Level Due to Piling Activities

Hiller and Crabb (2000) derived empirical formulae relating resultant PPV with a number of other parameters for vibratory compaction, percussive and vibratory piling, dynamic compaction, the vibration of stone columns and tunnel boring operations from field measurements. These predictions for a variety of scaling factors and parameter ranges are available in BS 5228–2:2009 (British Standard, 2014). Using these formulae, a prediction of resultant peak particle velocities (PPV) can be made conservatively. It suggests that vibration level is practically 0.5 to 1 mm/s for all the cases for the distance more than 30 m.

In the present study, bored piling operation using modern rotary rig is considered and vibration (in the form of PPV) from various distances to the metro rail complex can be calculated from Eq. (8).

$$V_{res} = K_p \left[\frac{\sqrt{W}}{r^{1.3}} \right] \tag{8}$$

where,

W = nominal torque (applied energy in KJ).

K_p = coefficient depends upon soil type (for pile drilling at refusal $K_p = 5$ and for Pile through dense granular soil $K_p = 3$ is considered in the present study).

r = slope distance from the pile toe or tunnel crown, in meters (m).

Though it is recommended to use the slope distance from the point of application of impact/energy to point of interest where resulting vibration V_{res} (in terms of PPV m/s) is to be obtained, in the present study, absolute horizontal plan distance from the metro rail corridor to the Adham Khan tomb is used conservatively. The calculated vibration level is presented in Figs. 6 and 7. Figure 6 represents the situation where piling is carried out at the refusal end, and Fig. 7 represents the situation where piling is carried out through dense gravely/sandy layer. For the drilling through softer layer, the obtained vibration is even lower than these situations due to wave absorption in the softer soils.

Cenek et al. (2012) used correlation (see Eq. (9)) to estimate the magnitude of ground vibrations at any distance from source of construction vibration. This allows estimation of critical separation distances required to ensure that the guideline vibration levels for human comfort and building damage given in BS 5228–2:2009 (British Standard, 2014) and DIN 4150–3:1999 (German Standard, 1999) are not exceeded.

$$V_2 = V_1 \left[\frac{R_1}{R_2} \right] e^{-\alpha(R_2 - R_1)} \tag{9}$$

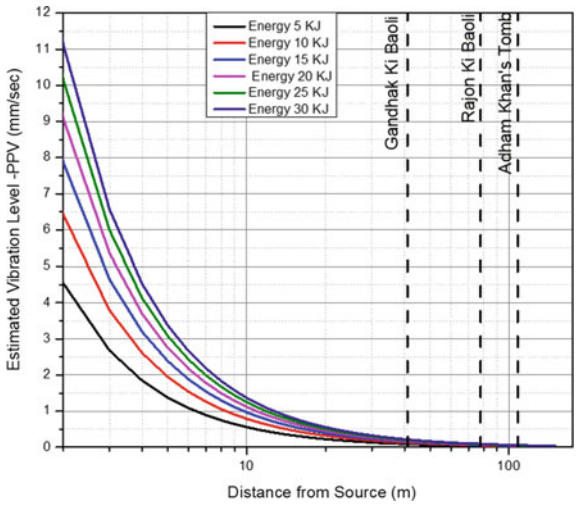

Fig. 6 Calculated vibration at various distances due the percussive piling at various frequencies of impact blow (for piles drilled at refusal)

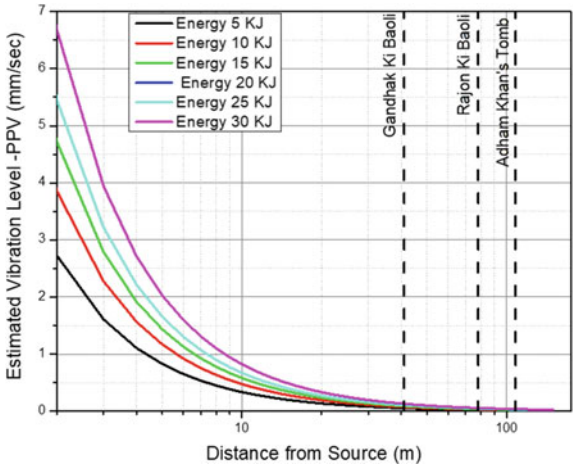

Fig. 7 Calculated vibration at various distances due the percussive piling at various frequencies of impact blow (for piles drilled through dense granular/ sandy stratum or weathered rock)

where,

V_1 = the measured peak particle velocity (mm/s) at distance R_1 (m).

V_2 = the peak particle velocity (mm/s) at distance R_2 (m) from source.

α = soil coefficient for the dominant frequency = $2\pi Df/v_s$.

D = soil damping presently assumed 0.2 on conservative side.

f = frequency of the applied vibration (considered as 10, 20 and 30 Hz).

v_s = shear wave velocity of the soil layers (average along the depth of pile) = 600 m/s conservatively in the weathered rock.

Considering $R_1 = 1$ m and assuming the vibration at the source will be approximately equal to that of a distance of 1 m and considered to be 10 mm/s as given in BS 5228–2:2009 (British Standard, 2014). Eq. (9) is reduced to Eq. (10),

$$V_2 = 10\left[\frac{1}{R_2}\right]e^{-\alpha(R_2-1)} \tag{10}$$

Considering the frequency of applied vibration as 10, 20 and 30 Hz, respectively, due to rotary piling operation, the calculated peak particle velocity (mm/s) at various distances from 2 to 150 m is presented in Fig. 8.

Based on the threshold vibration PPV recommended by various standards, it is considered that for heritage structure like Adham Khan Tomb, maximum allowed PPV is 2 mm/s. Estimated PPVs are based on above widely followed equations indicate that, in no case, the magnitude of estimated PPVs is close to above 0.1 mm/s. The obtained PPVs from the aforementioned analytical formulations are not transmitted beyond 100 m in all the cases analyzed. In fact, all the estimation suggests

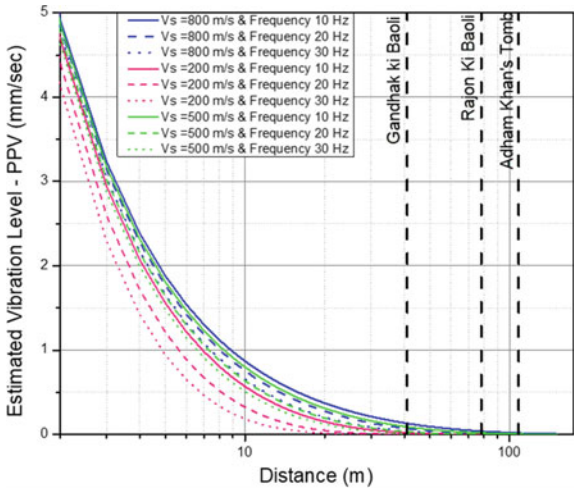

Fig. 8 Calculated vibration at various distances due bored piling (applied vibration PPV 10 mm/s; applied at three different frequencies 10, 20 and 30 Hz, respectively), (v_s = 800 represents weathered rock site, v_s = 500 represents medium dense soil and v_s = 200 represents loose soil profile

that no vibration will be transferred beyond 40 m of the proposed Metro rail corridor. Hence, there is no anticipated vibration at the Adham Khan tomb due to any type of the rotary piling activity at any depth.

In order to investigate the influence of the geotechnical conditions, the variation in the geotechnical profile is considered in the form of variation in the average shear wave velocity of the stratum. Three variations in the shear wave velocity are considered,

- v_s = 800 m/s represents weathered rock site.
- v_s = 500 m/s represents medium dense soil.
- v_s = 200 m/s represents loose soil profile.

From the estimated vibration transmission (PPVs), it is observed that for loose soil profile, the estimated PPVs are lower compared to rock sites. This indicates that considering v_s = 800 represents the conservative scenario, where estimated PPVs are higher, and it can be considered to be representative to bored piling activities for the construction of present metro rail complex. Practically, this is in agreement with the geotechnical profile where sound rock is present at shallow depth, that is, 6 m below natural ground level. Table 3 shows the comparison of estimated vibrations at various distances from the vibration source.

5.4 Estimation of Vibration Due to Tunneling

The estimation of ground-borne vibration due to tunneling is carried out using recommendations of BS 5228–2:2009 (British Standard, 2014). The estimated values are presented in Fig. 9. The estimated PPVs at specified sites are as shown in Table 4.

Table 3 Calculated vibration transmission at various distances from vibration source

Distance (m)	Estimated vibration (PPV) at various distances for $v_s = 800$ m/s		
	10 Hz	20 Hz	30 Hz
10	0.868	0.754	0.654
20	0.371	0.275	0.204
30	0.211	0.134	0.085
40	0.135	0.073	0.040
50	0.093	0.043	0.020
100	0.021	0.004	0.001
120	0.013	0.002	0.000

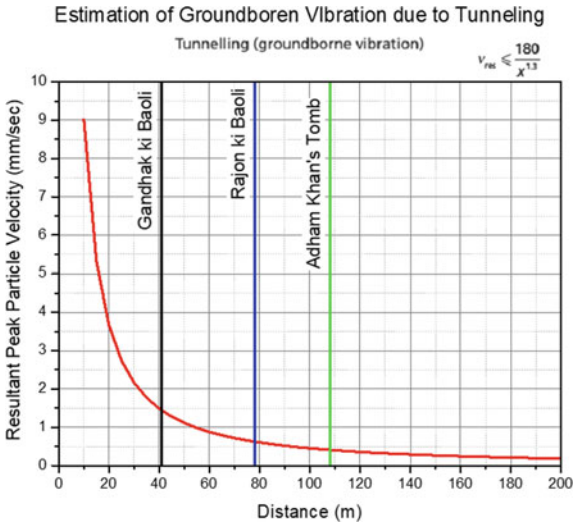

Fig. 9 Obtained ground-borne vibration at various distances due to tunneling

Table 4 Obtained PPVs (peak particle velocity) of vibration originating from tunneling

Sr. no	Name of heritage monument	Distance (m)	PPV (mm/s)	Existing traffic vibration exposure (mm/s)	Total PPV (mm/s)
1	Adham Khan's Tomb/Bhool Bhulaiya	123	0.345	1.230	1.575
2	Gandhak ki Baoli	41	1.441	0.735	2.176
3	Rajon ki Baoili	78	0.625	0.151	0.776
4	Tomb of Balban	155	0.256	0.477	0.733
5	Jamali Kamali Tomb and Mosque	149	0.269	0.357	0.626
6	Azam Khan's Tomb	108	0.409	0.157	0.566
7	Qutub Minar	300	0.108	0.486	0.594

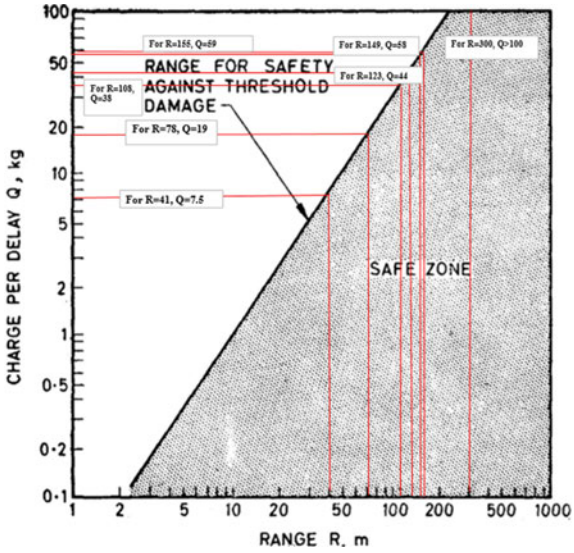

Fig. 10 Charge per delay as a function of range R for safety against damage during underground blasting (Indian Standard, 1973 Adapted from IS 6922)

Table 5 Safe distance for blasting as per IS 6922 (Indian Standard, 1973)

Sr. No	Name of heritage monument	Distance (m)	Blast charge per delay (kg)
1	Adham Khan's Tomb/Bhool Bhulaiya	123	44
2	Gandhak ki Baoli	41	7.5
3	Rajon ki Baoili	78	19
4	Tomb of Balban	155	59
5	Jamali Kamali Tomb and Mosque	149	58
6	Azam Khan's Tomb	108	38
7	Qutub Minar	300	100

5.5 Vibration Due to Blasting

IS 6922 (Indian Standard, 1973) specifies the safe distance for blast vibrations. For charge weight up to 100 kg per delay, the safe distance of the structures from the blast point may be obtained from Fig. 10. Safe distances for the various heritage sites have been determined from Fig. 10 and are presented in Table 5.

5.6 Numerical Analysis

A part/section of the proposed Delhi metro line (Phase IV) passing through Mehrauli has been analyzed using numerical simulations to investigate the effect of excavation

of subway station and tunnel driving operations on heritage structures in surrounding area. The construction of proposed metro station (named Mehrauli Metro Station) requires open excavation up to a depth of 15 m from natural ground level. However, such open excavation may induce surface settlement close to the excavation area around the periphery of the proposed metro station. In order to predict possible surface settlement extent and their magnitude, a 3D finite element (FE) analysis was performed using PLAXIS3D v.2017.1.0 (PLAXIS, 2017), a finite element geotechnical computer program. The proposed station is connected to twin tunnels of diameter 6.35 m in both up and down direction. In numerical analysis, tunneling geometry can be simplified into two-dimensional framework considering the infinite length of tunnel in third direction. In order to optimize the computational effort in numerical simulation, twin tunnel excavation is modeled using PLAXIS2D v.2017.1.0 (PLAXIS, 2017). In addition, response of the tunnel-soil system has been examined under seismic loading. A developed 2D FE model was further extended to perform a nonlinear dynamic analysis by applying the acceleration-time history of 1989 Loma Prieta earthquake. As per the soil investigation report, subsoil stratum was divided into three different layers namely sandy silt (0 to 3 m depth), dense sand (3 to 9 m) and quartzite (9 to 40 m), which are modeled using conventional Mohr–Coulomb (MC) constitutive model. The geotechnical properties of each layer adopted in the analysis are given in Table 6. The top soil layer is modeled under drained condition, whereas second and third soil layers are modeled as undrained considering the presence of water table at the 3 m depth from ground level. The proposed station is to be constructed as a cut-and-cover tunnel (of dimensions 270 m in length $\times$ 27 m in width $\times$ 15 m in depth), using top-down excavation method. Excavation depth of 15 m is divided into five-stage process considering layer of 3 m each at a time. The effect of excavation and tunnel driving on surrounding heritage structures has been observed, and the outcomes are reported here.

3D FE analysis of estimation of excavation induced settlements

The soil model of dimensions 950 m $\times$ 600 m $\times$ 40 m has been adopted in the present numerical analysis by discretizing it into 10-noded tetrahedral elements. The horizontal extent of model dimensions was chosen based on the sensitivity analysis to eliminate boundary effects and covering the locations of nearby heritage structures. Standard fixities are assigned wherein the sides are restricted to move laterally, and the base is restrained in all directions. At the bottom of excavation, 300 mm thick PCC layer was laid. All vertical walls of excavation block were secured against lateral deformation by installing diaphragm wall of thickness 800 mm. M40 grade concrete (assuming 70% strength) is used to construct diaphragm wall up to depth of 20 m (15 m excavated portion + 5 m embedded at bottom). Main beams (waling) are provided in the longitudinal direction in the periphery of excavation block at an interval of 5 m. Internal struts were installed in the shorter direction at a center to center distance of 10 m. Figure 11 illustrates the three-dimensional view of the model with dimensions. Figure 12 highlights the excavation portion along with diaphragm wall, waling and struts. The excavation-induced surface subsidence was recorded at different locations, and an attempt has been made to predict the zone of influence

Table 6 Geotechnical material properties

Layer	Thickness (m)	Υ_{unsat} (kN/m^3)	E (kN/m^2)	μ	c' (kN/m^2)	ϕ' (°)
1—Sandy silt	3	17	123	0.3	20	22
2—Dense sand	6	19	41	0.25	10	34
3—Quartzite	31	20	300	0.2	55	24

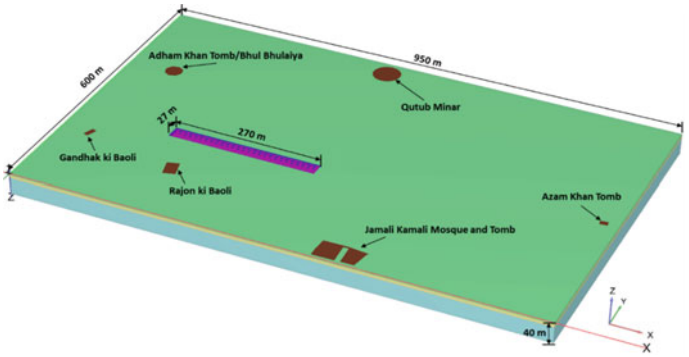

Fig. 11 Three-dimensional view of numerical model used in PLAXIS3D

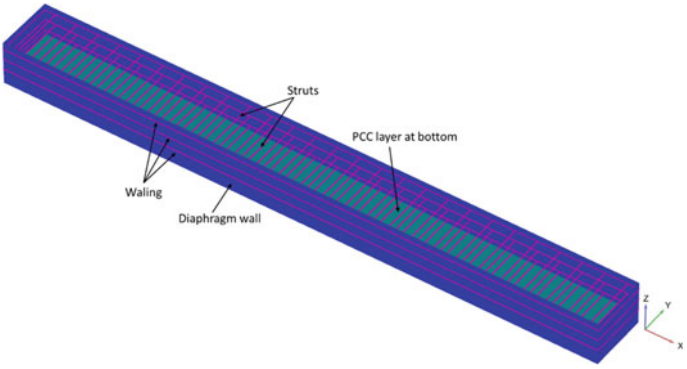

Fig. 12 3D view of excavation portion showing diaphragm walls, waling and struts

around the proposed underground station. Figure 13 demonstrates the surface settlement resulting from the excavation of the proposed station. Displacement contours clearly show that most of the heritage structures are not affected by deep excavation. Only Rajon ki Baoli (indicating displacement of 2.867 mm) may be slightly influenced due to excavation-induced settlements. Controlled excavation operation and proper monitoring can avoid damages to Rajon ki Baoli. The maximum displacement of 13.97 mm was observed in the excavation area, which gets minimized as distance from the excavated pit increases. Figure 14 shows the sectional view of the model cutting across the proposed station and two of the heritage structures, namely, Rajon ki Baoli and Qutub Minar. Displacement contours clearly show that Qutub Minar is located far away from the influence zone of excavation region. However, Rajon ki Baoli may slightly experience the differential settlement that is well within allowable limit. Figure 15 shows the development of plastic zone around excavation pit. However, there are no plastic points/yielding observed in the proximity of any of the heritage structures. The output results in form of displacement are summarized in Table 7.

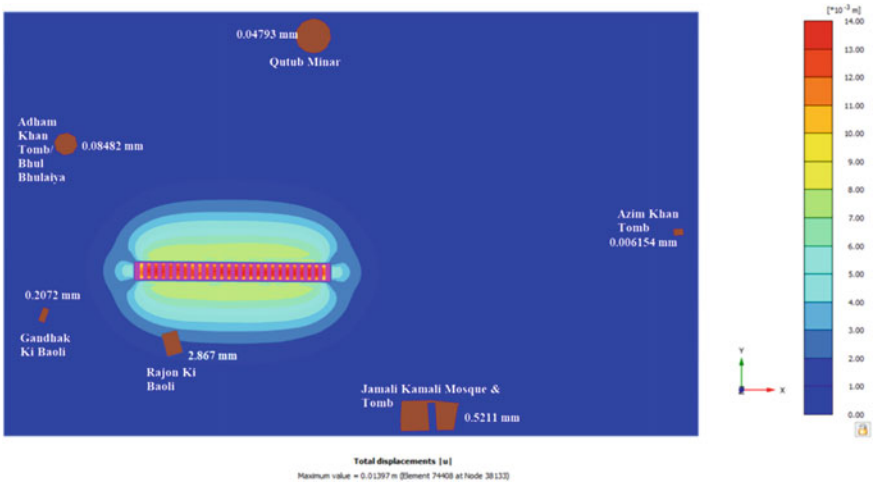

Fig. 13 Final stage displacement contours for the deep excavation for proposed Mehrauli Metro Station

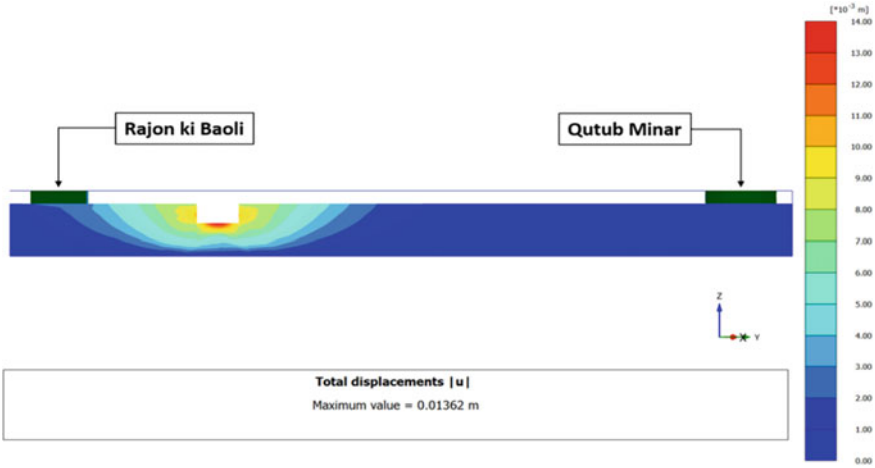

Fig. 14 Section to illustrate the displacement extent around the monuments

2D FE analysis of tunneling operations

The construction of a shield tunnel has been modeled using finite element computer program, PLAXIS2D v2017.1.0. In tunneling process, soil is generally over excavated, which means the cross-sectional area of the final tunnel lining is always less than the excavated soil area. Although measures are taken to fill up this gap, the stress redistributions and deformations in the soil resulting from the tunnel construction process cannot be prevented. To avoid damage to existing buildings and foundations

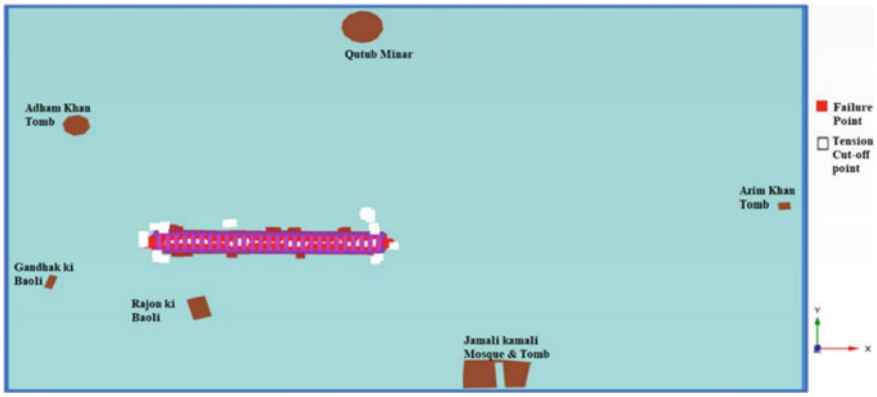

Fig. 15 Accumulation of plastic points around excavation of the proposed Mehrauli Metro Station

Table 7 Obtained phase-wise and total displacements (in mm) for the deep excavation

Monument	Phase displacement (in mm) during each excavation stage of 3 m					Total displacement (mm)
	1st(3 m)	2nd(6 m)	3rd(9 m)	4th(12 m)	5th(15 m)	
Rajon ki Baoili	0.2186	0.5456	0.4760	0.7210	0.7770	2.7382
Gandhak ki Baoli	0.0108	0.0435	0.0379	0.0506	0.0484	0.1912
Adham Khan's Tomb/Bhool Bhulaiya	0.0068	0.0149	0.0143	0.0206	0.0211	0.0778
Qutub Minar	0.0000	0.0000	0.0000	0.0000	0.0479	0.0479
Jamali Kamali Tomb and Mosque	0.0042	0.0083	0.0081	0.0122	0.0124	0.0453
Azam Khan's Tomb	0.0000	0.0000	0.0000	0.0000	0.0062	0.0062

resting on the soil above tunnel, it is necessary to predict these stresses and deformations and to take proper measures. A soil model of dimensions 280 m × 40 m has been adopted in the present plane–strain numerical analysis. The twin tunnel of diameter 6.35 m with center-to-center distance of 16 m is located at an average depth of 15 m. The soil profile and geotechnical properties of material are already explained in above section while explaining 3D FE analysis (refer to Table 6). Also, the constitutive material modeling principles of 3D numerical analysis are applicable in 2D FE analysis as well. Tunnel lining (of M45 grade concrete) of thickness 275 mm is modeled using plate element. For more realistic model, simulation of the construction of the tunnel has been defined in a stage-wise process like excavation, contraction, grouting and final lining.

Figure 16 illustrates the developed 2D model in PLAXIS 2D v2017.1.0. Figure 17 shows the sectional geometry and mesh discretization of the 2D FE tunneling model. Twin tunnel has been constructed one after another assuming there is some lag duration in excavating two tunnels in the field. Figure 18 shows the displacement contours resulting from the construction of left tunnel of the twin tunnel. It can be seen from Fig. 19 that as a result of construction of second (right) tunnel there is some

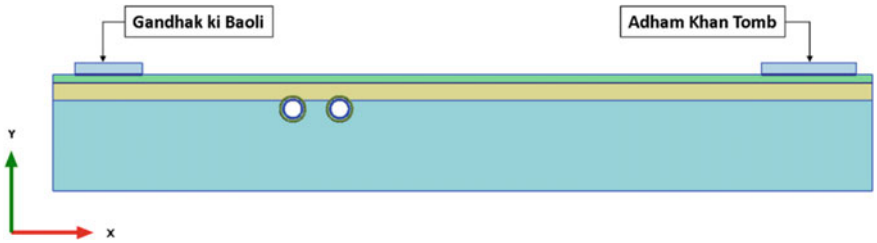

Fig. 16 Two-dimensional view of numerical model used in PLAXIS2D

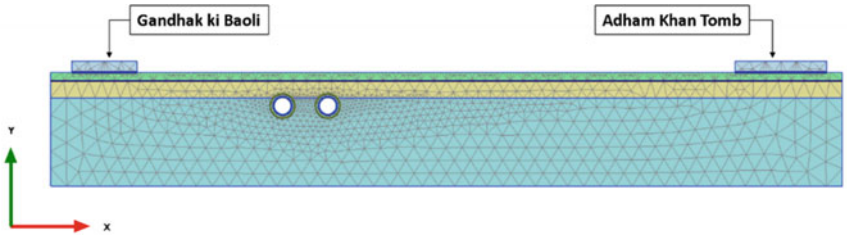

Fig. 17 Sectional geometry and mesh discretization for the 2D FE tunneling model

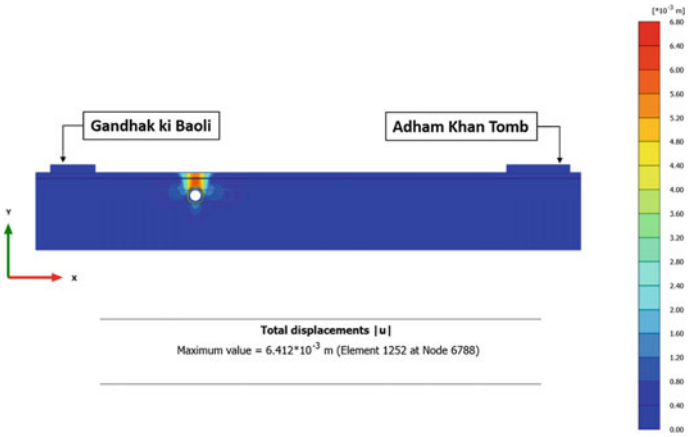

Fig. 18 Displacement contours resulting from the construction of left tunnel of the twin tunnel

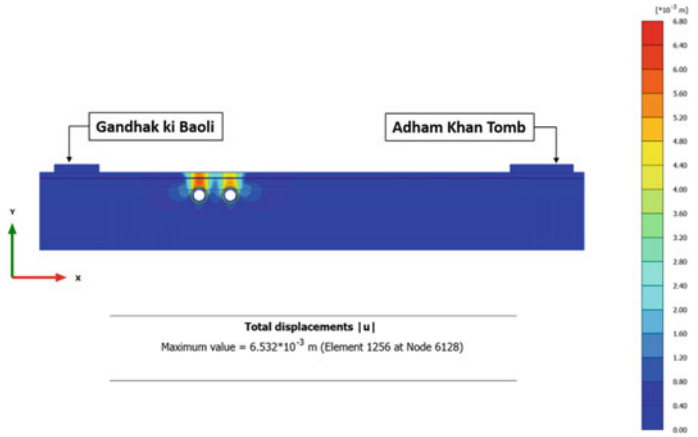

Fig. 19 Displacement contours resulting from the construction of twin tunnel

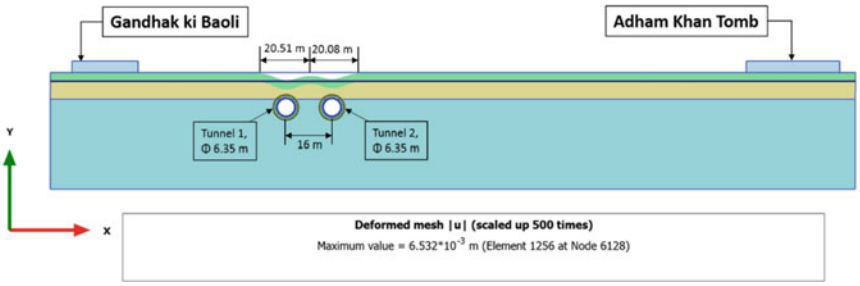

Fig. 20 Tunnel induced surface subsidence due to construction of twin tunnel

settlement of the soil surface. From Fig. 20, the maximum settlement of the tunnel crown is observed to be 6.52 mm and extent of the settlement is limited within the 10 m from the outer periphery of the tunnel. Hence, the tunnel excavation operation or volume contraction due to tunneling will have no significant effect on any of the monument site. Gandhak ki Baoli is the nearest site from the tunnel centerline (i.e. 41 m; refer Fig. 5), and it is observed that settlement due to tunneling is not affecting the closest monument site. The plot of effective stresses (Fig. 21) shows that arching occurs around the tunnel. This arching reduces the stresses acting on the tunnel lining, which in turn lowers the axial force in the final tunnel lining.

5.7 Seismic Analysis of Twin Tunnel

A non-linear dissipative behavior of soil subjected to cyclic loading has been simulated through a plane-strain numerical analysis using PLAXIS2D v2017.1.0. The

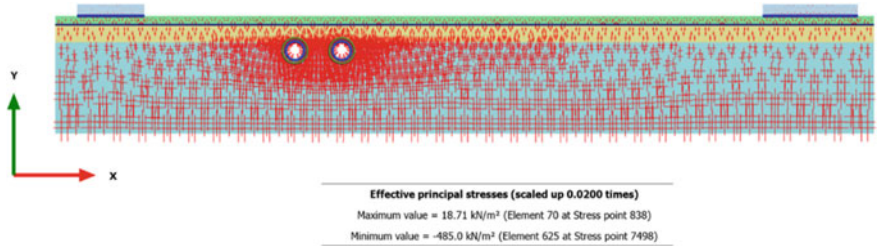

Fig. 21 Effective principal stresses after the construction of the twin tunnel

small size of the numerical model represents the infinite continuous soil medium in reality. An appropriate geometry of the model and boundary conditions were adopted to represent the far-field medium. Already developed 2D FE model of static analysis was further extended to perform non-linear dynamic analysis. Geometric details and geotechnical material properties of the soil as explained in the above section were used in the present seismic analysis. Under earthquake loading conditions, the behavior of the soil is primarily governed by its dynamic properties. Therefore, the shear wave velocity (v_s) was treated as the primary input parameter. The stiffness parameters are calculated from dynamic properties of the soil. During an earthquake, the soil is subjected to cyclic loading and unloading, which generates a hysteresis loop with the dissipation of energy and consequent damping. The Mohr–Coulomb model cannot simulate hysteretic damping in the numerical analysis. To compensate for the modeling limitation in simulating hysteretic damping, the total amount of damping was introduced through the frequency-dependent Rayleigh formulation in terms of viscous damping. The viscous boundary conditions were assigned to vertical boundaries that can absorb the incident waves, and seismic ground motion was assigned to the base of the model. The scaled ground motion data of the Loma Prieta earthquake of 1989 were used as dynamic input motion (see Fig. 22).

Figure 23 shows the location of points where displacements were recorded under the seismic loading. Figure 24 explains the distribution of displacement at various points with respect to dynamic time.

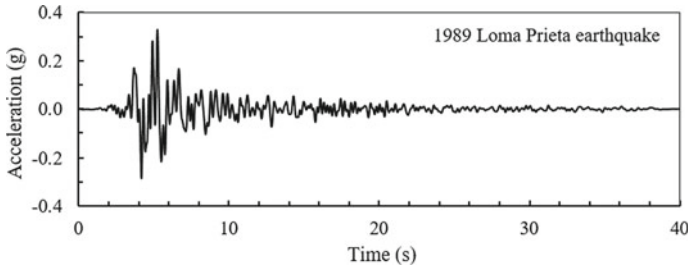

Fig. 22 Acceleration time history of input ground motion (1989 Loma Prieta earthquake)

Fig. 23 2D model of seismic analysis with details of observation points

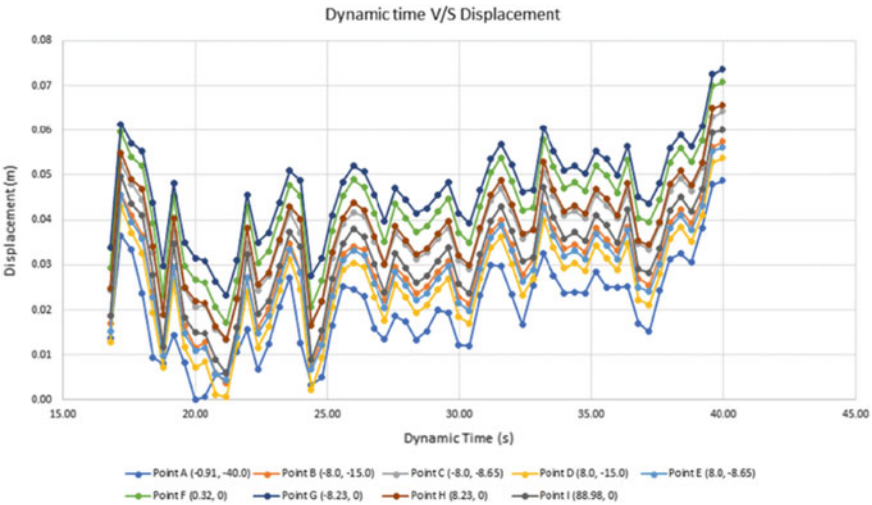

Fig. 24 Plot of displacement versus dynamic time

6 Conclusions

An attempt has been made to provide an insight into theory and practice of evaluation of ground-borne vibration and its control in sub-structural systems. A trenching method of mitigating ground vibration problem discussed and the factors affecting behavior of open and infill trenches have been studied. Optimum values of geometrical and material properties of trenches were determined through parametric study. From results of numerical analysis, it can be concluded that normalized depth is a decisive factor in case of open trenches, whereas width is important in shallow trenches. Performance of the low-density material as an infill material is found out to be exceptionally well but their effectiveness is highly depending on the relative shear-wave velocity between the in situ soil and the infill material. Overall, it is found that the trenches are easy and cost effective solution for controlling ground-borne vibrations. A generalized empirical model has been discussed for estimating blast-induced vibration parameters using extensive experimental data of various sites. This model gives the PPV as a function of scaled distance and three basic soil properties,

namely, unit weight, Young's modulus and degree of saturation. It has been observed that this model predicts reasonably well in case of fully saturated soils irrespective of soil type. Moreover, it predicts higher values for partially saturated soils, in absence of field data, this model can be used to predict vibration parameters by using three basic soil properties.

The behavior of multilayer railway track system subjected to cyclic loading has been explained with the help of analytical approach. The displacement of different layers of railway track systems can be computed using simple 2DOF mass-spring-dashpot system. It can be said that steady-state condition for dense sand achieved much quicker as compared to clay. Dense uniform sand is identified as a most appropriate material for subgrade under cyclic loading because it undergoes least settlement compared to the other soil types.

The vibration transmission due to piling activities (bored piling through rotary boring method) is estimated using widely acceptable empirical equations, and estimated levels are compared with threshold limits recommended by various international standards. Various literatures and standard guidelines were reviewed for identifying the threshold limit of vibration transmission for typical heritage site. The estimated levels of vibration are presented in graphical forma, and the estimated vibration is compared for various distances. It is observed that for heritage structures, for all the scale distance from 40 to 100 m, the estimated values are lower than the threshold limit of vibration transmission, that is, 2 mm/s. As per the results of vibration estimation study carried out considering bored piling, it is observed that estimated PPVs are practically nil, and vibration transmission is calculated to be 0.1 mm/s (<<2 mm/s threshold limit) beyond 50 m distance from proposed location of metro rail complex. Hence, the archaeological structures are at safe distance, and there would be no major vibration impact on these structures due to any type of construction activities. The estimated vertical vibrations are practically zero at the referred distance more than 70 m. However, it is recommended to take precautionary measures during construction for the two sites, namely, Rajon Ki Baoli and Gandhak ki Baoli.

The peak particle velocities due to tunneling were estimated as per recommendations of BS 5228–2:2009. Except Gandhak Ki Baoli, at all the other sites, the estimated PPVs are less than 2 mm/s. Since the threshold limiting value of PPV for heritage structure is considered to be 2 mm/s, the PPV must be restricted within limit during the actual construction process. For rock excavations, blasting charge weights are calculated. It is noted that charge weight should not be exceeded than 7.5 kg at two closest sites, namely, Rajon ki Baoli and Gandhak ki Baoli, to avoid any structural damage due to blasting.

The deep excavation of the proposed Meharauli metro station is modeled numerically using 3D finite element analysis, and influence of the resulting displacements/settlements has been investigated. The estimated maximum settlement is observed to be 2.73 mm at Rajon ki Baoli, which is approximately 78 m away from the proposed excavation footprint. For all other monument sites, the estimated total displacement due to proposed excavation is lower than 1 mm thereby not influencing the structure of the sites. Surface subsidence due to tunneling has been predicted

by 2D numerical analysis. Estimated maximum surface settlement due to tunneling is 6.52 mm above the tunnel centerline, that is, tunnel crown. This surface settlement extent is limited to approximately 12 m from the tunnel centerline towards the monument side, which indicates that monuments are free from any tunneling-induced surface settlement. Additionally, a sample seismic analysis of twin tunnels has been carried out to check the possible displacement caused by seismic shaking.

Acknowledgements Authors want to acknowledge the partial funding received from GeoDynamics vide project number RD/0218-CEGEODS-506 to carry out a portion of the work reported in this paper. Also, a portion of the technical content of this article is reproduced from past literature (Figures) to set the tone of the current study. In accordance, the authors are grateful to American Society of Civil Engineers (ASCE) for granting the permission to reproduce/reuse the appropriate figures in this article.

References

Amado-Mendes, P., Alves, P., Godinho, L., & Lopes, P. (2015). 2.5D MFS–FEM model for the prediction of vibrations due to underground railway traffic. *Engineering Structures, 104*, 141–154.

Auersch, L. (2005). The excitation of ground vibration by rail traffic: Theory of vehicle track-soil interaction and measurements on high-speed lines. *Journal of Sound and Vibration, 284*(1), 103–132.

Bharti, R. K., Choudhury, D., & Chauhan, S.: Behaviour of subgrade under cyclic load below railway track. In *Proceedings of Indian geotechnical conference, IGC-2006, December 14–16, 2006, IIT Madras* (pp. 731–7320). Chennai.

Bose, T., Choudhury, D., Sprengel, J., & Ziegler, M. (2018). Efficiency of open and infill trenches in mitigating ground-borne vibrations. *Journal of Geotechnical and Geoenvironmental Engineering, 144*(8), 04018048.

British Standard, BS 5228.2:2009+A1: Code of practice for noise and vibration control on construction and open sites – Part 2: Vibration (2014).

Cenek, P. D., Sutherland, A. J., & Mclver, I. R. (2012). *Ground vibration from road construction*, 485.

Choudhury, D., Bharti, R. K., Chauhan, S., & Indraratna, B. (2008). Response of multilayer foundation system beneath railway track under cyclic loading. *Journal of Geotechnical and Geoenvironmental Engineering, 134*(10), 1558–1563.

Choudhury, D., Patil, M., Ranjith, P. G., & Zhao, J. (2019). Dynamic tunnel-soil interaction in soft soils considering site-specific seismic ground response. In *Frontiers in geotechnical engineering* (pp. 249–271). Springer.

Galvín, P., & Domínguez, J. (2007). High-speed train-induced ground motion and interaction with structures. *Journal of Sound and Vibration, 307*(3–5), 755–777.

Galvín, P., Francois, S., Schevenels, M., Bongini, E., Degrande, G., & Lombaert, G. (2010). A 2.5D coupled FE-BE model for the prediction of railway induced vibrations. *Soil Dynamics and Earthquake Engineering, 30*(12), 1500–1512.

German Standard, DIN 4150–3: Structural Vibration – Part 3: Effects of vibration on structures (1999).

He, C., Zhou, S., Di, H., Guo, P., & Xiao, J. (2018). Analytical method for calculation of ground vibration from a tunnel embedded in a multi-layered half-space. *Computers and Geotechnics, 99*, 149–164.

Hiller, D. M., & Crabb, G. I. (2000). Groundborne vibration caused by mechanised construction works. TRL Report 429. Wokingham: TRL (2000).

Hussein, M., Francois, S., Schevenels, M., Hunt, H., Talbot, J., & Degrande, G. (2014). The fictitious force method for efficient calculation of vibration from a tunnel embedded in a multi-layered half-space. *Journal of Sound and Vibration, 333*(25), 6996–7018.

Indian Standard, I.S. 6922: Criteria for safety and design of structures subjected to underground blast. Bureau of Indian Standards, New Delhi, India (1973).

Kumar, R., Choudhury, D., & Bhargava, K. (2012). Response of foundations subjected to blast loadings: State of the art review. *Disaster Advances, 5*(1), 54–63.

Kumar, R., Choudhury, D., & Bhargava, K. (2013). Recent development in modeling, analysis and design of foundation systems subjected to blast loading considering uncertainties. In *Proceedings of the international symposium on engineering uncertainty: Safety assessment and management (ISEUSAM – 2012b)* (pp. 927–938). Springer, India (2013).

Kumar, R., Choudhury, D., & Bhargava, K. (2014a). Prediction of blast-induced vibration parameters for soil sites. *International Journal of Geomechanics, 14*(3), 04014007.

Kumar, R., Choudhury, D., & Bhargava, K. (2014b). Response of shallow foundation in rocks subjected to underground blast loading using FLAC3D. *Disaster Advances, 7*(2), 64–71.

Kumar, R., Choudhury, D., & Bhargava, K. (2015). Simulation of rock subjected to underground blast using FLAC3D. *Japanese Geotechnical Society Special Publication, 2*(12), 508–511.

Kumar, R., Bhargava, K., & Choudhury, D. (2016). Estimation of engineering properties of soils from field SPT using random number generation. *INAE Letters, 1*(3–4), 77–84.

Kumar, R., Choudhury, D., & Bhargava, K. (2016). Determination of blast-induced ground vibration equations for rocks using mechanical and geological properties. *Journal of Rock Mechanics and Geotechnical Engineering, 8*(3), 341–349.

Kumar, R., Bhargava, K., & Choudhury, D. (2017). Correlations of uniaxial compressive strength of rock mass with conventional strength properties through random number generation. *International Journal of Geomechanics, 17*(2), 06016021.

Kumar, R., Bhargava, K., & Choudhury, D. (2019). Effect of underground blast on underlying ground media below substructure. In R. Sundaram, J. T. Shahu, & V. Havanagi, (Eds.), *Geotechnics for transportation infrastructure*. Lecture notes in civil engineering (Vol. 28, pp. 363–370). Springer.

Kuo, K., Hunt, H., & Hussein, M. (2011). The effect of a twin tunnel on the propagation of groundborne vibration from an underground railway. *Journal of Sound and Vibration, 330*(25), 6203–6222.

Lopes, P., Alves, P., Ferraz, M., Calçada, R., & Silva, A. (2014). Numerical modeling of vibrations induced by railway traffic in tunnels: From the source to the nearby buildings. *Soil Dynamics and Earthquake Engineering, 61–62*, 269–285.

Müller, K., Grundmann, H., & Lenz, S. (2008). Nonlinear interaction between a moving vehicle and a plate elastically mounted on a tunnel. *Journal of Sound and Vibration, 310*(3), 558–586.

Nandi, R., & Choudhury, D. (2018). Seismic analysis of reinforced soil wall considering oblique pull-out of reinforcements: A review. *Geotechnical Engineering, 49*(1), 90–98.

Nandi, R., & Choudhury, D. (2019). Seismic analysis and design of embedded cantilever retaining wall considering non-linear earth pressure distribution effect. In *Earthquake geotechnical engineering for protection and development of environment and constructions* (pp. 4103–4110). CRC Press.

Nandi, R., & Choudhury, D. (2021). Evaluation of Passive Earth Resistance Using an Improved Limit Equilibrium Method of Slices. *International Journal of Geomechanics, 21*(11), 04021207.

Paolucci, R., & Spinelli, D. (2006). Ground motion induced by train passage. *Journal of Engineering Mechanics, Proceedings of ASCE, 132*(2), 201–210.

Patil, M., Choudhury, D., Ranjith, P. G., & Zhao, J. (2015). Seismic analysis of tunnels in soft soils: a state of-the-art review. In: *Proceeding of the international conference on soft ground engineering (ICSGE 2015), 3–4 Dec 2015* (pp. 625–634). Singapore (2015).

Patil, M., Choudhury, D., Ranjith, P. G., & Zhao, J. (2017). A numerical study on effects of dynamic input motion on response of tunnel-soil system. In *Proceeding of the 16th world conference on earthquake engineering (16th WCEE 2017)*, Paper ID: 3313. Santiago.

Patil, M., Choudhury, D., Ranjith, P. G., & Zhao, J. (2018). Behavior of shallow tunnel in soft soil under seismic conditions. *Tunnelling and Underground Space Technology, 82*, 30–38.

PLAXIS 2D v2017.1.0 [Computer software]. PLAXIS BV, Netherlands.

PLAXIS 3D v2017.1.0 [Computer software]. PLAXIS BV, Netherlands.

Thusyanthan, N. I., & Madabhushi, S. P. G. (2003). Experimental study of vibrations in underground structures. *Proceedings of Institution of Civil Engineers - Geotechnical Engineering, 156*(2), 75–81.

Trochides, A. (1991). Ground-borne vibrations in buildings near subways. *Applied Acoustics, 32*(4), 289–296.

Tsuno, K., Morimoto, W., Itoh, K., Murata, O., & Kusakabe, O. (2005). Centrifugal modeling of subway-induced vibration. *International Journal of Physical Modelling in Geotechics, 5*(4), 15–26.

Yang, W. B., Hussein, M. F. M., & Marshall, A. M. (2013a). Centrifuge and numerical modelling of ground-borne vibration from surface sources. *Soil Dynamics and Earthquake Engineering, 44*(1), 78–89.

Yang, W. B., Hussein, M. F. M., & Marshall, A. M. (2013b). Centrifuge and numerical modelling of ground-borne vibration from an underground tunnel. *Soil Dynamics and Earthquake Engineering, 51*(8), 23–34.

Yaseri, A., Bazyar, M. H., & Hataf, N. (2014). 3D coupled scaled boundary finite-element/finite-element analysis of ground vibrations induced by underground train movement. *Computers and Geotechnics, 60*(1), 1–8.

Yaseri, A., Bazyar, M., & Javady, S. (2018). 2.5D coupled FEM-SBFEM analysis of ground vibrations induced by train movement. *Soil Dynamics and Earthquake Engineering, 104*, 307–318 (2018).

Yuan, Z., Cai, Y., & Cao, Z. (2016). An analytical model for vibration prediction of a tunnel embedded in a saturated full-space to a harmonic point load. *Soil Dynamics and Earthquake Engineering, 86*, 25–40.

Yuan, Z., Bostrom, A., & Cai, Y. (2017). Benchmark solution for vibrations from a moving point source in a tunnel embedded in a half-space. *Journal of Sound and Vibration, 387*, 177–193.

Geotechnical, Geological and Geophysical Investigations for Seismic Microzonation and Site-Specific Earthquake Hazard Analysis in Gujarat

B. K. Rastogi, Kapil Mohan, B. Sairam, A. P. Singh, and Vasu Pancholi

1 Introduction

Rapid development in India having moderate to great earthquakes warrants assessment of seismic hazard at the micro level. Most of Gujarat state in western India is prone to earthquakes of magnitude 5–8. It has experienced great earthquakes in the historical past, the last being the Bhuj earthquake (Mw 7.6, MMI + X) on 26 January 2001 which was the most destructive intraplate earthquake, causing catastrophic damage and killing about 14,000 people and injuring many more. The role of site effect was strongly realized due to this earthquake that caused damage to all types of buildings in the near distance and tall buildings up to 250 km in many cities. Dozens of multi-storeyed buildings collapsed in Ahmedabad at a distance of 225 km.

Several earthquakes like Mexico (1985) have shown that local site conditions have a significant role in the amplification of ground motion, especially on those areas that are located on unconsolidated young sedimentary materials. The softness of surface layer not only tends to amplify ground motion at certain frequencies but also extends the duration, which may cause further damage during earthquakes. The fundamental phenomenon responsible for the amplification of motion over soft sediments is trapping of seismic waves due to the impedance contrast between sedimentary deposits and the underlying bedrock.

It is also a well-known fact that the site amplification/shaking is stronger in low-shear-wave velocity areas. Mapping the seismic hazard at local scales to incorporate the effects of local ground conditions is the essence of seismic microzonation. Shallow shear-wave velocity structure to a depth of 30 m is a key parameter to

B. K. Rastogi (✉)
In. Society of Earthquake Science, 1-2-63/3, Habsiguda 500007, India
e-mail: bkrastogi12@gmail.com

K. Mohan · B. Sairam · A. P. Singh · V. Pancholi
Institute of Seismological Research, Raisan, Gandhinagar 382010, India

T. G. Sitharam et al. (eds.), *Advances in Earthquake Geotechnics*, Springer Tracts in Civil Engineering, https://doi.org/10.1007/978-981-19-3330-1_4

evaluate the near-surface stiffness and for characterizing the given site. The classification of sites based on Vs30 is given by the US-NEHRP (National Earthquake Hazard Reduction Program).

Natural frequency of each soil layer depends on the physical properties of soil and the depth to bedrock. The main aim of the site response study is to evaluate the amplification of ground motion and the determination of natural resonance frequency of the soil. Several Geotechnical, Geological and Geophysical investigations done for seismic microzonation and site-specific earthquake hazard analysis in Gujarat are outlined. Estimating depth of Engineering Bed Layer (EBL) and preparation of seismicity map are described. The required soil properties for site characterization are obtained from either geotechnical tests or geophysical tests. Assigning fault line and its maximum magnitude, estimation of strong motion time history at the EBL, amplification factor and strong ground motion at the surface are explained.

In the microzonation studies in Gujarat by the Institute of Seismological Research (Rastogi et al., 2007), the MASW test and PS-logging surveys have been carried out to estimate the shear-wave velocities. Shear-wave velocity profiles have been used to estimate the depth of EBL. Site amplification has been computed using the earthquake records besides using geotechnical data. We have used Broadband Seismographs (BBS) for recording earthquakes as well as microtremors at a sampling rate of 100 samples/s. Microtremors were recorded for 4 h at each site. ISR has done seismic microzonation and site-specific studies in the following areas of Gujarat.

Microzonation of various cities like Gandhinagar, Gift city (Mohan et al., 2018), Ahmedabad, Gandhidham–Kandla, Bhuj, Bharuch and Surat. Figure 1 shows some of these sites. Microzonation in Areas of Special Development: Ports of

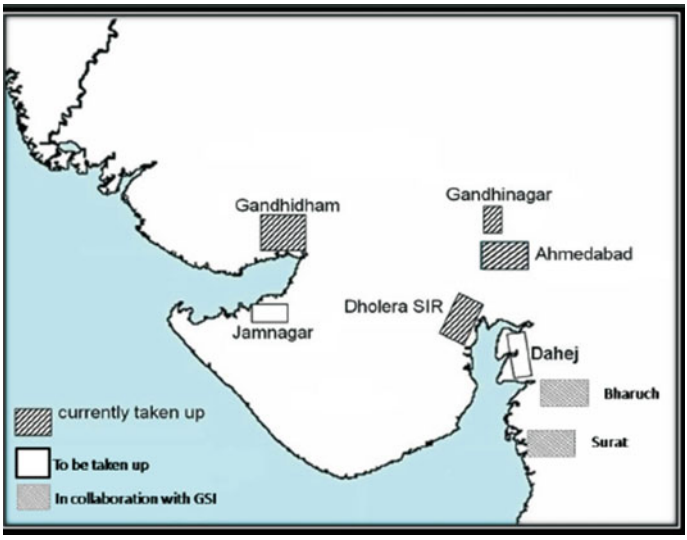

Fig. 1 Major sites of microzonation in Gujarat

Gujarat, Dholera Special Investment Region, Exhibition ground of Gandhinagar, and proposed sites of Devni Mori (Budha Statue in Shamlaji town in Sabarkantha District Nr. Mesow dam) and Sant Nagari (Nr. Dharoi dam).

Seismic Hazard Assessment of Specific Sites: Nuclear Power Plants of Kakrapar and Jaitapur, LNG Terminals of Mundra and Dahej, Statue of Unity, Multistorey VS Hospital, the Capital-Multistorey Commercial Complex, E-City (ISCON Circle, Ahmedabad).

2 Geological Investigations

Local geological conditions are assessed which affect ground motion at a given site. When subjected to the earthquake ground motions the response of different soil types differ. Usually, the younger softer soil amplifies ground motion relative to older, more compact soils or bedrock. Local amplification of the ground is often controlled by the soft surface layer, which leads to the trapping of the seismic energy, due to the impedance contrast between the soft surface soils and the underlying bedrock. Geological investigation involves the following steps to be followed:

- Determining the bedrock geology, including major structural features such as faults, surface geology in terms of soil types on a regional or if possible, local basis.
- Determining the climate conditions, which influence soil development, groundwater fluctuations, erosion, flooding, slope failures, etc.
- Determining associated geological hazards such as ground subsidence and collapse and slope failures.

2.1 Site Characterization Based on Geomorphological Mapping

Geomorphology map is prepared by 3D Digital mapping and ground check. Both site characteristics and geomorphology (e.g. valley, basin, ridge effects, etc.) play an important role in the observed response of surface ground motions. The selection of ground response analysis (e.g. 1D, 2D or 3D ground response analysis), depends upon mainly the topography (geomorphology) of the site.

2.2 Terrain Analysis

It is the most important part of the site investigation. Landforms and other surface characteristics are strong indices of geologic conditions and help to choose an appropriate ground response model. Characteristic terrain features reveal several useful information such as rock type, structural forms (where rock is shallow or deep) and weathering conditions, erosion, or representation of typical soil formations in terms of their origin, mode of deposition and thickness of the deposits. Engineering geology maps can be prepared from the terrain analysis that provides information about the geologic conditions over an entire study area.

3 Geotechnical Investigations

Geotechnical investigations are done for a variety of reasons like whether the soil strength can safely support a structure or which soil/rock layer is strong enough or whether soil is liquefiable or is there any other geologic hazard. Geotechnical investigations are performed by drilling and in situ tests. Small-diameter borings are used to allow retrieval of samples and to perform in-place soil tests. Soil samples are categorized as being either 'disturbed' or 'undisturbed'. A disturbed sample is one in which the structure of the soil has been changed sufficiently that tests of structural properties of the soil will not be representative of in situ conditions, and only properties of the soil grains (e.g. grain size distribution, Atterberg's limits and possibly the water content) can be accurately determined. An undisturbed sample is one where the condition of the soil in the sample is close enough to the conditions of the soil in situ to allow tests of structural properties.

Field investigations include drilling of boreholes, Standard Penetration Tests (SPTs), trial pits and load tests. Lab tests include grain size analysis (sieve and hydrometer), Atterberg's limit, specific gravity, density and water content, triaxial compression test, direct shear test and consolidation test. Geophysical surveys such as seismic surveys, electrical resistivity surveys, Ground Penetrating Radar (GPR) surveys and other geophysical methods for layer thickness and shear-wave velocity. Liquefaction susceptibility test is also done (Dwivedi et al., 2019).

4 The 2D and 3D Soil Modelling: Lithological Set-Up

2D and 3D soil profiles are prepared for all the study areas. Figure 2 shows soil profiles for Ahmedabad area constructed with 16 boreholes to 80 m depth and 208 boreholes to 30 m depth. There is more sand in the northern part, while clay and silt are in other parts.

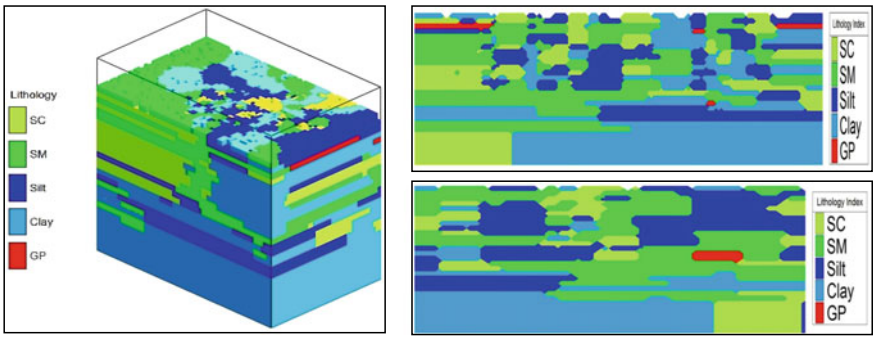

Fig. 2 The 3D (left), 2D N–S (upper right) and 2D E–W (lower right) soil profiles for all the boreholes up to 50 m depth in Ahmedabad. Sand (silty and clayey) shown by green colour is more, while clay and silt in blue colour are in small patches until 30 m depth

5 Estimation of Shear-Wave Velocity and Engineering Bed Layer

The shear-wave velocity, Vs with depth is estimated by various methods like PS-logging, shallow seismic (MASW) and microtremor surveys and contours are drawn for the areas of seismic microzonation. The N-values from standard penetration test are correlated with Vs in order to uniformly distribute the soil properties in grid pattern throughout the area of investigation. EBL is decided on the basis that this layer with Vs > 500 m/s and the same type of soil/rock exists throughout the area at known depths. These methodologies are described in the subsections below.

5.1 PS-Logging

Suspension PS-logging (Fig. 3) is used for the estimation of accurate vertical 1D Vp and Vs profile to a depth of 70 m or so. Suspension PS-logger is 8 m long and contains a weight, source driver, source (trigger), filter tube, lower and upper geophones connected by cables to a logger/recorder. The interval between upper and lower receivers is usually 1 m and distance from PS source to lower receiver is 4 m.

For measurement, the borehole is filled with water and the data is acquired by giving a trigger command in the acquisition software. Three to nine stacks of triggers are used as an energy source. The source generates a pressure wave in the borehole fluid. The pressure wave is converted to P and S waves and received by the geophones, which send the data to the recorder on the surface. Samples of P and S waves at one of the sites are shown in Fig. 3. Data is processed using the Glog-SUS processing software of OYO Inc, Japan. The elapsed time between arrivals of the waves at the

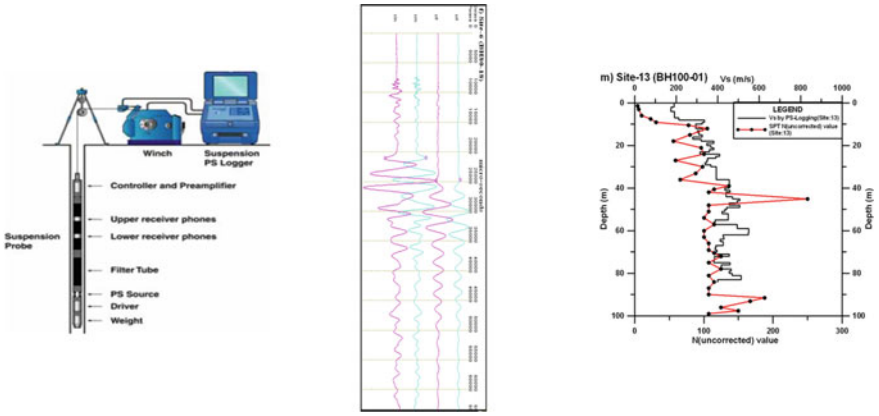

Fig. 3 From left to right, PS-logger set-up, a sample of waveforms as detected by PS-logger and a sample of Vs profile by PS-logging and SPT N-values for comparison

receivers is used to determine the average velocity of a 1-m-high column of soil around the borehole. Processing of the data involves the accurate picking of P-wave and S-wave phases.

5.2 Shallow Seismic Survey and Multichannel Analysis of Surface Waves (MASW)

Multichannel Analysis of Surface Waves (MASW) is a non-invasive method developed to estimate shear-wave velocity profile from surface wave energy. Measurements of phase velocity of Rayleigh waves of different frequencies can be used to determine a velocity–depth profile.

5.3 Shear-Wave Velocity Profiles Throughout Gujarat

We have carried out MASW test (using Engineering Seismograph) and PS-logging surveys to measure shear-wave velocity profiles at over 1000 locations throughout Gujarat covering all geological units (Fig. 4). Thus, we have characterized the whole Gujarat based on Vs30 (average shear-wave velocity to a depth 30 m). This has helped generate site characterizing map and seismic hazard map of Gujarat at surface. S-wave velocity profiles were measured and PS-logging was done in Bhuj, Gandhinagar, Gift city, Anjar, Dholera, Ahmedabad, Mundra, Bharuch, coastal areas, industrial sites and sites of Strong Motion Accelerograph (SMA), BBS, etc. (Sairam et al., 2011, 2018, 2019) (Fig. 5).

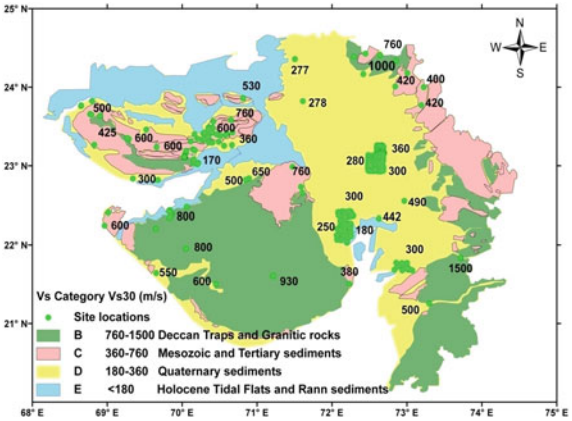

Fig. 4 Vs30 map of Gujarat using Shallow seismic survey at 301 sites by MASW method and PS-logging

5.4 MASW Test to Identify Faults

We have used MASW and Refraction surveys for delineating the fault. We are able to identify shallow (30 m) faults as well as deeper (~100 m) faults. For shallow fault identification, we keep 5 m geophone interval, while 10 m geophone interval for deeper faults. MASW results at the Kodki fault near Bhuj are shown in Fig. 6a. Three MASW N–S Vs profiles of 25–75 m length were taken across the South Wagad Fault (the causative fault for the 2001 earthquake) to decipher the subsurface nature of the fault. The profile closest to the 2001 mainshock epicentre shows presence of fault.

5.5 Determination of Relation Between Vs30 and SPT N Values

We have prepared a relationship between Vs30 and SPT N values for different areas. These are useful in assigning reasonable N-value in case measurement is missed or the value is an outlier.

5.6 MASW Test at Anjar to Detect Possible Site Amplification Effects During Past Earthquakes

MASW tests have been carried out in Anjar area to study the possible side effects causing the damage during the past earthquake events (Rastogi et al., 2011) (Fig. 6b). MASW tests have been carried out at a) undamaged site, b) less-damaged site and c) severely damaged site, which show a remarkable difference in soil structure. The

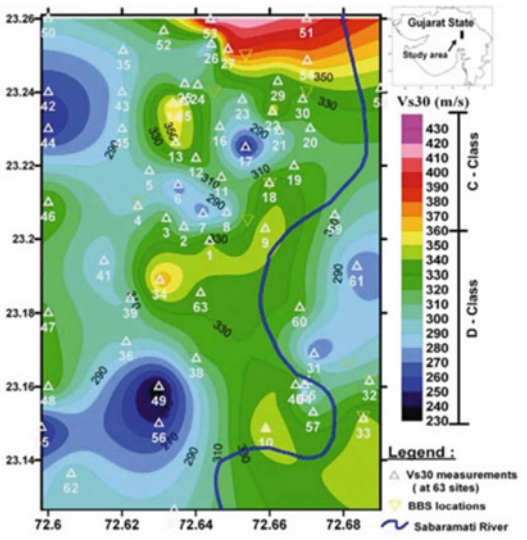

(a)

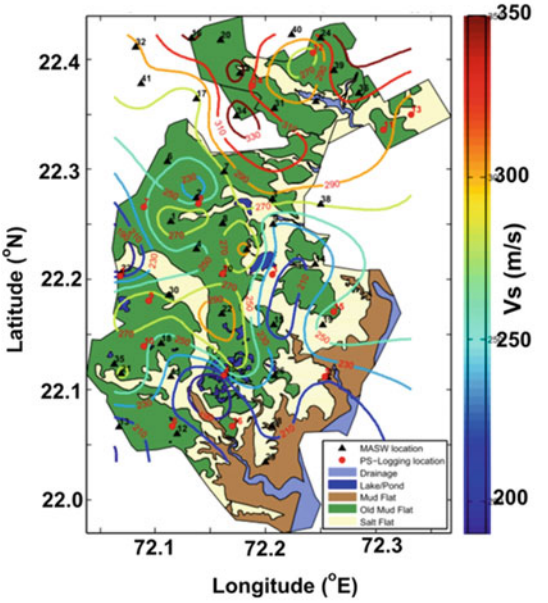

(b)

Fig. 5 **a** Contour map of Vs30 in the Gandhinagar area. **b** Contour map of Vs30 in Dholera area. **c** Contour map of Vs30 in GIFT city area. **d** Sites of MASW tests carried out at SMA, SRR and Industrial locations in Gujarat

Fig. 5 (continued)

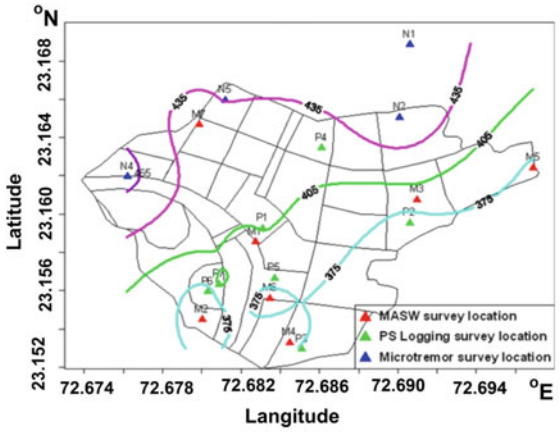

(c)

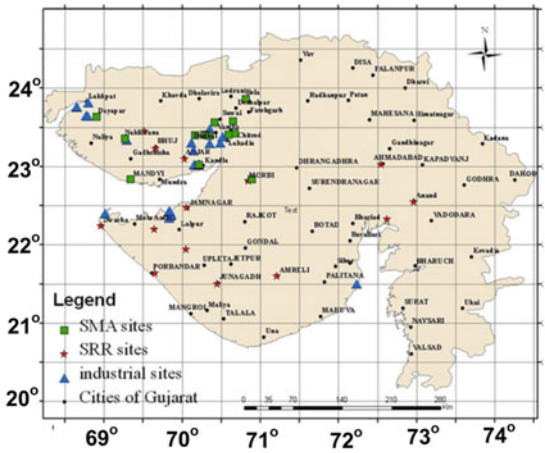

(d)

layers with high Vs > 500 m/s are at 4 m depth at undamaged sites but such high-velocity layers are at 15 m depth at the less-damaged site. Also at the severely damaged sites, the Vs is much lower, only 200–300 m/s to 20 m depth. Thus, the softer soil deposit is confirmed at severely damaged sites from shear-wave velocity profiles. From these results, it is inferred that possibly amplification is caused due to local geology resulting in damage at severely damaged area of Anjar. Traces of a filled-up pond were found in the severely damaged sites by MASW test.

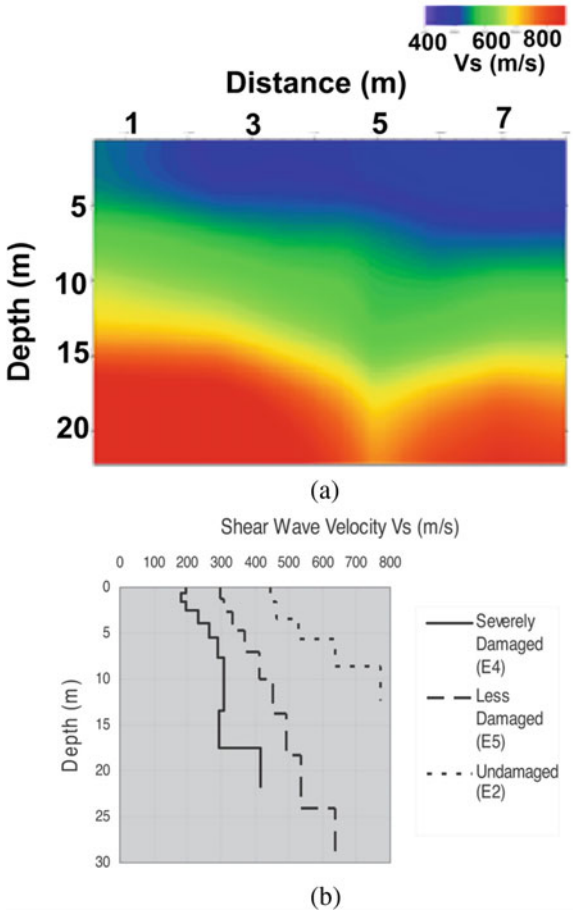

Fig. 6 **a** Delineating fault by MASW test at Kodki village near Bhuj city. **b** Vs versus Depth profiles in Anjar city

5.7 Refraction Survey at Mundra

In addition to MASW surveys, refraction surveys can also be conducted with engineering seismograph to identify the faults. Refraction surveys were conducted at Mundra for a kilometre-long profile (Table 1) with the objective of the study (i) to see whether hypothetical fault is there or not and (ii) to know the velocity and depth of shallow layers for tying up with 2D reflection survey. Results are correlating well with local geology.

Table 1 Velocity model of Mundra area by combined interpretation of Refraction and Reflection data

Depth of the layer, m	Vs, km/s
0–5	0.6
5–12	1.7
12–90	2.3
>90	2.5

6 Application of Microtremor Investigation for Subsurface Modelling

The term microtremor includes all ground vibrations, not due to events of short duration, such as earthquakes or explosions. Microtremor studies were originated in Japan and have gained broad recognition in the study of site effect on earthquake ground motion.

Several researchers have applied the Nakamura method (Nakamura, 1989) of microtremor H/V spectrum for site investigation and measuring the thickness of the topsoil cover over the bedrock in India and abroad (Al & Luzon, 2000; Bour et al., 1989; Hunter et al., 2002; Rodriguez & Midorikawa, 2003). The H/V spectral ratio of microtremor is used to map the thickness of different soil layers and bedrock depth in contrasting layered lithological formations, where frequencies of amplification are converted to the thickness of layers if Vs is known.

The instrument used for survey consists of a set of 7 number seismometers of 5 s natural period, digitizer, master remote control, GPS system and electronic distance measurement system. The data of individual recorders is used for estimating the fundamental frequency and amplification due to entire soil thickness, while, an array gives the 1D velocity section of the underlying strata. The array arrangement is circular with three recording stations on the circumference of inner circle, three on outer circle (radius 100 m) and one in the centre of circle. For each array measurement, two distances R, D were used for better resolution. R is the distance between the central and outer stations and D is the distance between two outer stations. Seven sets of Lennartz LE-3D-5 s seismometers with Lennartz Marslite digital recorders are deployed. The master remote control is used to trigger all seven stations at a time in order to avoid any phase shift. In order to establish geometry of the array, it is necessary to measure the distance as precisely as possible between stations in the field. The electronic Digital Meter (EDM) is used to estimate the distances of the different pairs of stations. The principle of EDM is based on the focusing laser beam to a target plate which gives the distance at cm accuracy. This array method uses low-frequency ambient vibrations generated due to ocean tides and vibration of trees due to winds while avoiding cultural vibrations. The observations are carried out for an hour with the sampling rate of 100 samples/s at each site. For reliable experimental conditions, we follow the guidelines proposed by Koller et al. (2004).

The array microtremor data is used for determining the 1D velocity structure using inversion tools. The dispersion curve is determined and then inversion tool is applied

to infer the ground structure, especially the seismic velocity Vs. The H/V (horizontal to vertical) ratio is calculated using at least 50–70 s time windows, overlapping one another by 5%. A FFT (Fast Fourier transform) is applied to the signal of the three components to obtain the three spectral amplitudes in microtremor analysis. The spectra are then smoothed. H/V is computed by merging the horizontal (North–South and East–West) components with a quadratic mean.

7 Estimating Depths to Different Layers

Resonant frequencies in H/V spectra of earthquakes recorded on BBSs and microtremor records give depths to different soil layers and basement using the relation.

$$f = Vs/4h$$

where f is the amplified frequency, h is the depth of the layer and Vs is the assigned shear-wave velocity based on our knowledge of the area. Kindly note that due to the low energy of microtremors only some period waves may reverberate with certain layers and not all. We have estimated the approximate depths of different layers in several areas of study in Gujarat (Singh & Navaneeth, 2013). Results of broadband earthquake records and microtremor records are compared with those by MASW and drilling for shallow layers. Results from Dholera area are shown in Fig. 7 and Table 2.

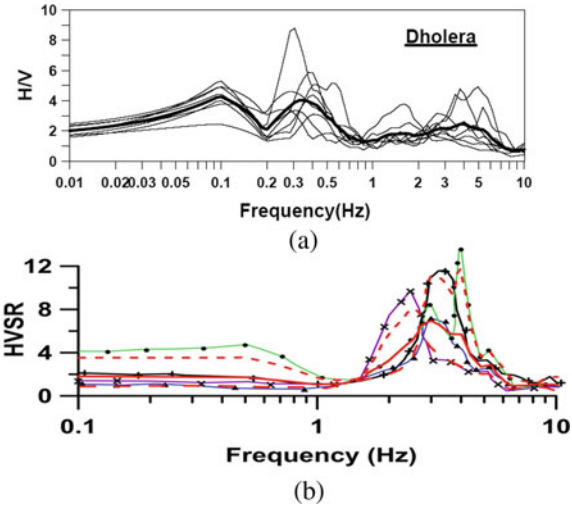

Fig. 7 Dholera area resonant frequencies in H/V spectra of earthquakes recorded on broadband seismographs give depths to different soil layers and basement (f = Vs/4 h). **b** the amplified frequency ~ 3 Hz in H/V spectra of microtremor records on broadband seismographs gives a layer at 20 m depth which is confirmed by MASW

Table 2 Determining depths to different layers from Broadband Seismograms in Dholera area (refer to Fig. 7a)

Layer	f in Hz	H in m	Vs m/s
Basement	0.1	5000	2000
DT/Meso	0.35	350	1500
Q/T	1.5	100	500
Holocene I/II	4	15	250

8 Assessment of Strong Ground Motion

First, the EBL is worked out for the area and its depth at each borehole and at each grid point is estimated and contoured. The EBL in the area is usually decided at a shear-wave velocity of 450 m/s. Input ground motion is estimated at EBL by modelling. A ground model is constructed based on the results of geotechnical and geophysical investigations. The input ground motion is passed through ground model in 'SHAKE91' program to obtain the ground motion at surface.

8.1 Preparation of Ground Model for Response Analysis

To conduct the response analysis, the ground models are prepared for each borehole in the following format:

A. Number of Layers and Depth of each layer (m)
B. Damping Factor (%), Vs (m/s), Density (g/cm^3), Thickness (m), Non-linear Characteristic id (integer) for each layer

A sample ground model for Mundra area is shown in Fig. 8.

8.2 Input Motion at the Engineering Bed Layer

The input ground motion at a site can be generated by various methods like Empirical Green's Function (EGF), Stochastic Finite Fault Source Model (SFFSM) of Motazedian and Atkinson (Motazedian & Atkinson, 2005), Semi-Empirical or Composite Source model. ISR has installed BBSs at selected places on varied geomorphological units to record earthquakes from sources in Kachchh and Saurashtra. These BBS stations recorded earthquakes from these regions in the magnitude range 3.5–5.0. These earthquakes can be used as element earthquakes for EGF analysis. Quite often the signal-to-noise ratio is quite low and the records are noisier and not usable. The best method for generating strong ground motions is found to be the SFFSM and is used in most of our studies. An example is shown in Fig. 8.

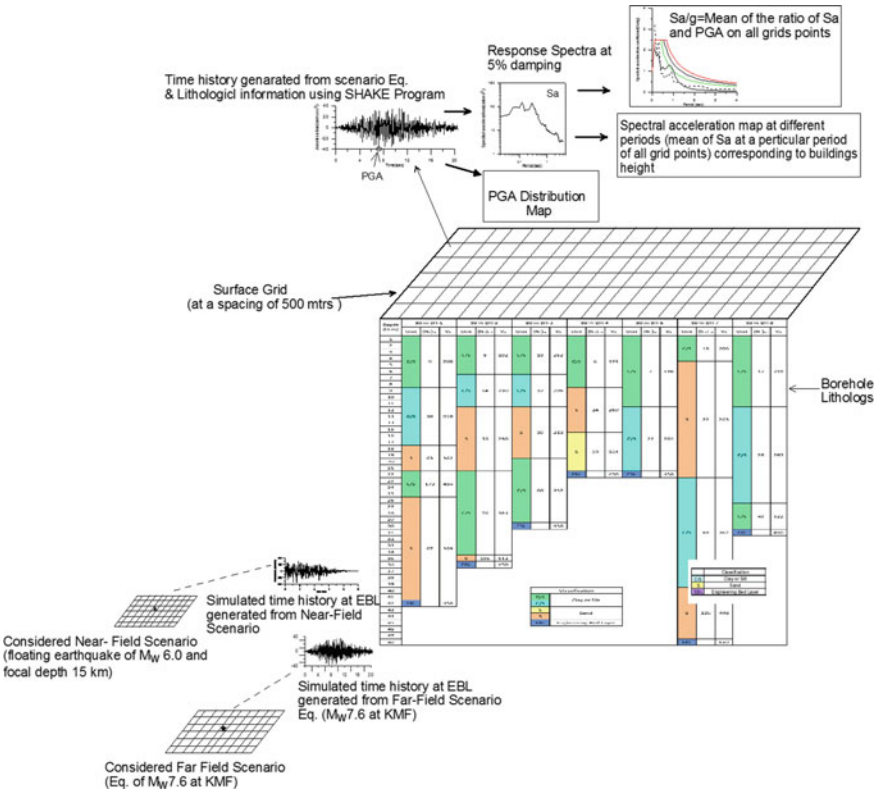

Fig. 8 The process of Response Analysis for Seismic Microzonation of Dholera Special Investment Region (Mohan & Rastogi, 2011)

8.3 Stochastic Finite Fault Source Modelling (SFFSM)

The basis of the stochastic method is that the high-frequency strong ground motion from earthquakes can be approximated by finite duration band-limited white Gaussian noise. The band limitation is defined by spectral corner frequency and the highest frequency passed by the accelerograph or the Earth's attenuation. According to this method, a site-specific shape of the theoretical Fourier amplitude spectrum of the free field acceleration is estimated based on point source model. Next, a band-limited white noise is windowed with a shaping function of prescribed duration. The windowed time series is transformed into frequency domain and scaled to the square root of the mean-squared absolute spectra. The site-specific theoretical Fourier amplitude spectrum generated above is multiplied by the scaled spectrum of windowed time series. The Fourier transformation back into the time domain generates the simulated acceleration time series. This method was extended to large faults by subdividing the large fault into sub-faults each of which is then treated as a point

source. The ground motions at a site can be obtained by summing the contributions over all sub-faults. the concept of 'dynamic corner frequency' is used whereby the corner frequency reduces as the function of time accounting for the effect of an increase in fault length.

8.4 Ground Motion Parameters of Target Earthquakes

The result of the stochastic method depends on how well one knows the source, path and site characteristics of the given region where the ground motion is required. The researchers of ISR have determined the ground motion parameters for Gujarat region from the records of earthquakes in Kachchh, Saurashtra and the Mainland region separately. It is necessary that one should consider two target earthquakes, one far-field and another near-field for the generation of strong ground motions. The effects of local and regional earthquakes are different for different engineering structures. The far-field earthquake will affect the high-rise structures because of the dominance of low-frequency content and near-field will affect low-rise engineering structures. The probability of a large earthquake (Mw > 7) is very low for Saurashtra and the only region from where large earthquakes are expected is Kachchh where many faults are active. One far-field target earthquake will be generated like the 2001 Bhuj earthquake of Mw 7.6. Local active faults are also considered. The ground motion from these two scenario earthquakes will be used in the ground response analysis.

9 Measurement of Soil Amplification

Soil amplification is measured by several methods. In India and abroad, the Nakamura (1989) method of H/V spectral ratio is widely used. However, it has been found to give unreliable results due to weak ambient vibrations or earthquake data considered (Bard, 1998). The resonance frequencies obtained with this method are reliable. We have used the geotechnical data as input in the SHAKE program to get amplification, and compared the results with the following additional methods using:

i. Average frequency-dependent amplification for the strongest few earthquakes recorded in the area.
ii. Empirical amplification given by Boore (2006) method (developed using world-wide data whereby frequency-dependent amplification is given for generic soils with Vs of 760 or 520 or 450 m/s, etc., for EBL and 350 m/s at surface).
iii. The relationship developed by Midorikawa et al. (1994) between shear-wave velocity and amplification factor of PGA, which is as follows.

log ARA = 1.35–0.47 log AVS30.

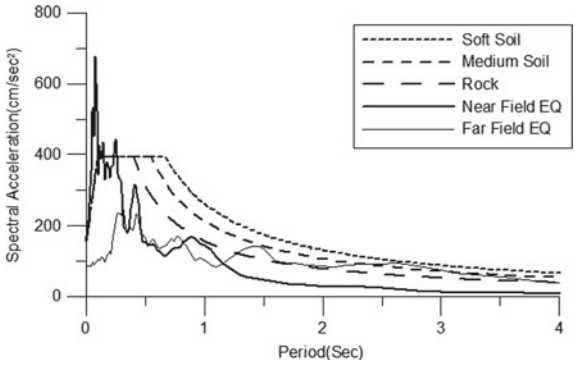

Fig. 9 Spectral Acceleration for near-field and far-field earthquakes compared with BIS curves for Gandhinagar in Seismic Zone III

Here, ARA is the amplification factor of PGA at shear-wave velocity AVs30. From the formula, the amplification factor difference of PGA may be calculated, say between Vs 450 m/s and 520 m/s, i.e. (ARA (450)–ARA (520)).

10 Response Analysis

In the response analysis, a complete accelerogram (acceleration values with respect to time), PGA (maximum amplitude of the accelerogram), response spectra (spectral acceleration of single degree of freedom system vs. time) at 5% damping at the ground surface for hundreds or thousands of grid points distributed uniformly in the entire area with a spacing of 500 m or so are calculated. The spectral acceleration distribution maps are prepared at all grid points for different periods (0.1, 0.2, 0.4, 0.55, 0.67, 0.75, 1 and 1.25 s) from the computed response spectra. The spectral acceleration coefficient (Sa/g) values at all the grid points are also calculated by taking the ratio of the spectral acceleration and PGA at all the grid points. Mean Sa/g is also estimated for an area.

The spectral accelerations estimated for different periods in different areas of study in Gujarat indicate 50–70% more value in the period range 0.2–0.3 s than that is recommended in the BIS code (Fig. 9). The distance of higher damage potential increases to 20 km for faults with expected magnitude 6–7 and 40 km for faults with expected magnitude 8.

11 Liquefaction Potential

Investigations done for estimation of liquefaction potential are water depth (> 50 m may not liquefy), PGA, type of soil (sand, silt and gravel are liquefied), soil properties, N-value (layers at >30 m may not liquefy, tri-axial cyclic test of failure

of soil samples under simulation of repeated seismic waves). The methods given by Japan Road Association Method (Specifications for Highway Bridges & Part V Earthquake Resistant Design., 1980) and Seed and Idriss (Seed & Idriss, 1971) were adopted for liquefaction analysis.

12 Conclusions

The Institute of Seismological Research has conducted microzonation in Gujarat state of western India since 2007. Seismic microzonation has been done at Dholera Special Investment Region (SIR) along the Mumbai–Delhi corridor and Gandhidham–Anjar–Kandla area in collaboration with Oyo International Corporation, Japan. Seismic microzonation has been carried out for the cities of Bhuj, Gandhinagar and Ahmedabad. Microzonation studies in 250–500 m grid including measurements of Vs30, resistivity and geotechnical investigations through numerous boreholes were carried out in these areas. Earthquake hazard assessment was done for Kakrapar and Jaitapur Nuclear Power Plants, Mundra and Dahej LNG Terminals, Gujarat Infrastructure and Finance Tech (GIFT) city which is the first smart city in the country, several high-rise buildings, Dwarka, Deoni Mori and Santnagari religious sites, Gandhinagar Exhibition ground, etc.

The majority of microzonation studies in the country are not standardized as far as procedure, type of surveys and interpretation of data are concerned. ISR has done wide research on the development of methodology of seismic microzonation (geotechnical investigations, strong motion simulation techniques, Shear-wave velocity (Vs) estimation, Vs & SPT-N-value (Vs–N) relationship using data from MASW, Microtremor and PS Logging, establishment of EBL, estimation of liquefaction potential and response analysis. Therefore, now, we have a very well-tested and established technique of seismic microzonation.

Outcomes of these studies are peak ground acceleration, spectral acceleration at different periods (site-specific response spectra) corresponding to different heights of the buildings at a particular site of interest considering tectonic setting, shear-wave velocity structure, and subsurface soil/geotechnical properties. The liquefaction potential assessment is also an important outcome of the microzonation.

References

Al, Y. Z., & Luzon, F. (2000). On the horizontal to vertical spectral ratio in sedimentary basins. *Bulletin of the Seismological Society of America, 90*(4), 1101–1106.

Bard, P. Y. (1998). Microtremor measurements: A tool for site effect estimation? In Irikura, K., Okada & Sasatani (Eds.) *Proceedings of the 2nd international symposium on the effects of surface geology on seismic motion.* (pp. 1251–1279). Balkema.

Boore, M. D. (2006). Determining Subsurface Shear-wave velocities: A review. In *ESG2006 conference*, (p. 103). Grenoble.

Bour, M., Fouissac, D., Dominique, P., & Martin, C. (1989). On the use of microteremor recordings in seismic microzonation. *Soil Dynamics and Earthquake Engineering, 17*(7–8), 465–474.

Dwivedi, V. K., Dubey, R. K, Vasu, P., Mohan, R. M, Pawan, S., Sairam, B., Chopra, S., & Rastogi, B. K. (2019). Multi criteria study for seismic hazard assessment of UNESCO world heritage Ahmedabad City, Gujarat, Western India. *Bulletin of Engineering Geology and the Environment,* 1–13.

Hunter, J. A., Benjumea, B., Harris, J. B., Miller, R. D., Pullan, S. E., Burns, R. A., & Good, R. L. (2002). Surface and down hole shear wave seismic methods for thick soil site investigations. *Soil Dynamics and Earthquake Engineering, 22*(9–12), 931–941.

Japan Road Association (1980, 1992, 2002). Specifications for highway bridges, Part V Earthquake resistant design.

Koller, M. G., Chatelain, J. -L., Guillier, B., Duval, A.-M., Atakan, K., Lacave, C., Bard, P. Y., & The SESAME WP12 Participants (2004) Practical user guidelines and software for the implementation of the *H/V* ratio technique on ambient vibrations: Measuring conditions, processing method, results and interpretation. *Proceedings of the 13th world conference on earthquake engineering, Vancouver, BC, Canada, August 1–6, 2004*, paper no. 3132.

Midorikawa, S., Matsuoka, M., & Sakugawa, K. (1994). Site effects on strong-motion records observed during the 1987 Chhiba-Ken-Toho-Oki, Japan Earthquake. In *Proceedings of the 9th Japan earthquake engineering on symposium* (pp. E-085–E-090).

Mohan, K., & Rastogi, B. K. (2011). Seismic response analysis of Dholera SIR and preparation of spectral acceleration maps at various periods. *ISR Annual Report, 2010–11*, 73–74.

Mohan, K., Rastogi, B. K., Pancholi, V., & Gandhi, D. (2018). Seismic hazard assessment at micro level in Gandhinagar (the capital of Gujarat, India) considering soil effects. *Soil Dynamics and Earthquake Engineering, Science Direct, 109*, 354–370. https://doi.org/10.1016/j.solidyn.2018.03.007.

Motazedian, D., & Atkinson, G. M. (2005). Stochastic finite-fault modelling based on dynamic corner frequency. *Bulletin of the Seismological Society of America, 95*, 995–1010.

Nakamura, Y. (1989). A method for dynamic characteristics estimation of subsurface using microtremor on the ground surface. *Quarterly Report of the Railway Technical Research Institute (Tokyo), 30*(01).

Rastogi, B. K., Gupta, A., Kumar, P., Sairam, B., & Singh, A. P. (2007). Microzonation of in and around Gujarat. In *Proceedings of the workshop on Microzonation* held at Indian Institute of Science @*internet publishing, Bangalore.*

Rastogi, B. K., Singh, A. P., Sairam, B., Jain, S. K., Kaneko, F., Segawa, S., & Matsuo, J. (2011). The possibility of site effects: The Anjar case, following the past earthquakes in Gujarat, India. *Seismological Research Letters 82*(1): 692–701. https://doi.org/10.1785/gssrl.82.1.692.

Rodriguez, H. S., & Midorikawa, S. (2003). Comparison of spectral ratio techniques for estimation of site effects using microtremor data and earthquake motions recorded at the surface and boreholes. *Earthquake Engineering and Structural Dynamics, 32*(11), 1691–1714.

Sairam, B., Rastogi, B. K., Sandeep, A., Mukesh, C., & Uday, B. (2011). Seismic site characterization using Vs30 and site amplification in Gandhinagar region, Guajarat, India. *Current Science, 100*, 754–761.

Sairam, B., Singh, A. P., Patel, V., Pancholi, V., Chopra, S., Dwivedi, V. K., & Ravi Kumar, M. (2018). Influence of local site effects in the Ahmedabad mega City on the damage due to past earthquakes in north-western India. *Bulletin of the Seismological Society of America, 108*(4), 2170–2182.

Sairam, B., Singh, A. P., Patel, V., Chopra, S., & Kumar, M. R. (2019). VS30 mapping and site characterization in the seismically active intraplate region of Western India: Implications for risk mitigation. *Near Surface Geophysics, 17*(5), 533–546.

Seed, H. B., & Idriss, I. M. (1971). Simplified procedure for evaluating soil liquefaction potential. *J SMFD, ASCE, 97*(9), 1249–1273.

Singh, A. P., & Navaneeth, A. (2013). Vs estimation by micro-tremor method. *ISR Annual Report, 2012–13*, 135–139.

Thokchom, S., Rastogi, B. K., Dogra, N. N., Pancholi, V., Sairam, B., Bhattacharya, F., & Patel, V. (2017a). Empirical correlation of SPT blow count vs Shear wave velocity for different soils in Dholera. *NHAZ, 86*(3), 1291–1306. https://doi.org/10.1007/s11069-017-2744-3.

Thokchom, S., Rastogi, B. K., Dogra, N. N., & Vasu, P. (2017b) Geotechnical investigation in southern part of Ahmedabad district, Gujarat. *Journal of Indian Geophysical Union, 21*(2), 105–115.

Thokchom, S., Rastogi, B. K., Dogra, N. N., & Vasu, P. (2018). Liquefaction potential mapping of Dholera region. *Gujarat, Natural Hazards,*. https://doi.org/10.1007/s11069-018-3214-2.

Seismic Analysis of Pile Foundations Using an Integrated Approach

Pradeep Kumar Dammala and A. Murali Krishna

1 Introduction

Pile foundations in soft or incompetent soils have been found to be severely affected in earthquake-hit regions despite being structurally intact (Mylonakis et al., 2006). The complex dynamic Soil–Structure Interactions (SSI) involved in soft soils during earthquakes are considered to be the major attributors of such severe damages (Bhattacharya & Madabhushi, 2008). Several dynamic SSI analysis approaches ranging from simple to advance in nature are in use for dealing with such SSI mechanisms. Traditionally adopted dynamic SSI approaches are simplified pseudo-static approach (Liyanapathirana & Poulos, 2005), dynamic Winkler spring approach (Novak et al., 1978), and advanced continuum approach (Randolph, 1981). Since the advanced continuum approaches involve high computational expertise and budgetary constraints, design engineers often adopt simplified dynamic Winkler spring-based approaches. Researchers, based on extensive experimental and numerical analysis, suggested that the dynamic Winkler approaches provide a satisfactory and reliable response to pile foundations under dynamic loading conditions (Dash et al., 2009; Finn, 2005; Wang et al., 1998). However, it is pointed out by several studies that any such simplified methods must not overlook the inherent nonlinear behavior of soil (Boulanger et al., 1999; Sarkar et al., 2014).

Further, it is to be noted that effective simplified SSI analysis involves various steps as shown in Fig. 1. The objective of the present article is to provide an integrated approach for the seismic analysis of pile foundations in soft soils and demonstrate the same through an example considering the local soil conditions and the nonlinearity of subsoil conditions.

P. K. Dammala
Department of Civil and Infrastructure Engineering, IIT Jodhpur, Karwar 342037, India

A. Murali Krishna (✉)
Department of Civil and Environmental Engineering, IIT Tirupati, Chindepalle 517506, India
e-mail: amk@iittp.ac.in

T. G. Sitharam et al. (eds.), *Advances in Earthquake Geotechnics*, Springer Tracts in Civil Engineering, https://doi.org/10.1007/978-981-19-3330-1_5

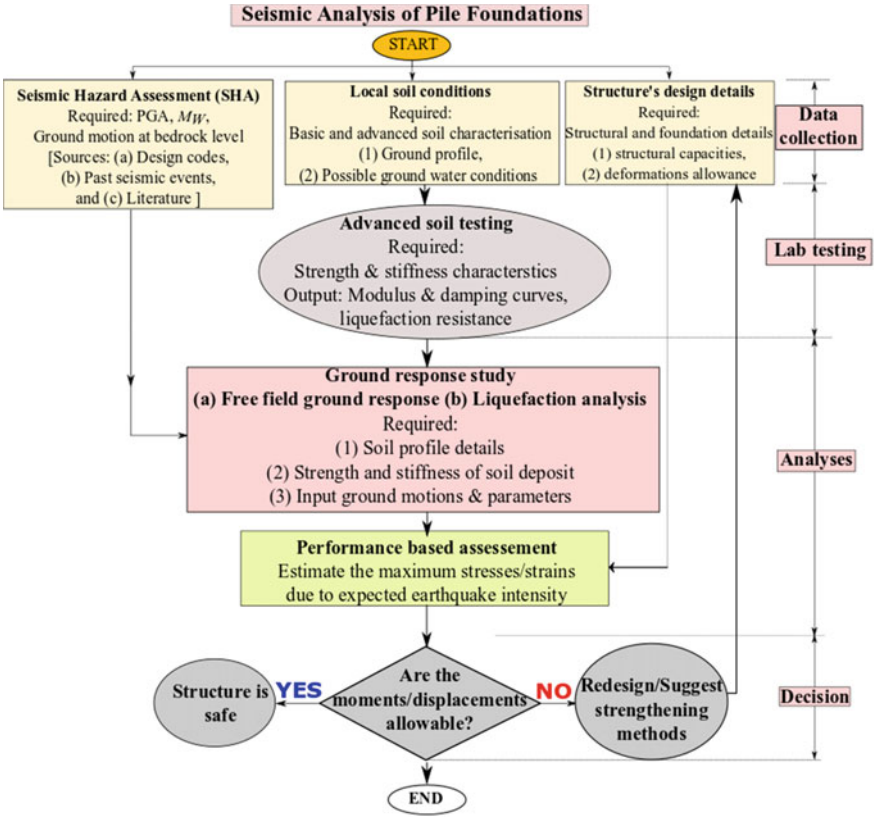

Fig. 1 Integrated seismic analysis strategy for pile foundations (modified after Dammala et al., 2017a)

2 Integrated Approach of Seismic Analysis of Pile Foundations

Krishna et al. (2014) proposed an integrated strategy for seismic requalification of geotechnical structures. Dammala et al. (2017a) adopted a similar approach for the requalification study of a caisson-supported bridge located in a high seismic zone. Figure 1 illustrates the integrated strategy for seismic analysis of pile foundations. The approach essentially consists of various components: (1) Identification of seismic source at the site of interest (traditionally termed as seismic hazard assessment); (2) Characterization of the subsoil, including under dynamic conditions, through field or laboratory tests; (3) Analyzing the seismic response of ground through ground response and liquefaction studies; and (4) Performing dynamic structural analysis with integrated results obtained from earlier steps. Finally, the foundation is assessed based on performance criteria and if the assessed results don't satisfy the requirements

of safety or serviceability, the structure must be redesigned or some strengthening suggestions should be made.

The individual components of the methodology are briefly presented below in a step-wise manner.

2.1 Step 1: Quantification of Seismic Hazard

In this step, it is necessary to obtain design ground motion parameters [for example, Peak Ground Acceleration (PGA), Moment Magnitude (M_w)] and time histories of anticipated ground motion at the site. These are estimated either deterministically (Deterministic Seismic Hazard Assessment-DSHA) or probabilistically (Probabilistic Seismic Hazard Assessment, PSHA) which requires historical earthquake catalogues and the location of active seismic sources nearby the site. In case of scarce seismic recordings, it may be necessary to generate synthetic ground motions using advanced stochastic seismological models based on fault geometry, directivity, and path, see for example, Boore (2003) and Hanks and McGuire (1981), or code-based spectral matching, see for details Mukherjee and Gupta (2002) and Somerville et al. (1997).

2.2 Step 2: Site Characterisation and Site Response Analysis

In this step, information such as the ground type and stratification, sloping of the ground, location of the groundwater level are first obtained either from the available sources or from the engineering correlations. In case of major engineering projects, geophysical (field and or laboratory element) tests may also be conducted to understand the dynamic behavior of underlying soils. This includes the establishment of strain-dependent dynamic soil properties and assessing liquefaction potential. Chattaraj and Sengupta (2016), Dammala et al. (2017a, b, c, 2019a, b), Dammala (2019), Puri et al. (2019), Kumar et al. (2017) and Sitharam et al. (2004) performed rigorous laboratory dynamic characterization tests on soils sampled from active seismic regions of India.

Subsequently, the established dynamic properties will be utilized in ground response and liquefaction analyses for the earthquake scenario predicted in Step 1. Similar ground response studies have been conducted by Dammala et al. (2019a), Kumar et al. (2018a), and Zhang et al. (2005).

2.3 Step 3: Integrated Seismic Analysis

This stage involves seismic analyses of the pile foundation using the results obtained from the earlier stages with the help of simplified Winkler spring approach. Actual built conditions of the structure and different existing loading conditions as well as predictable severe loading conditions are to be adopted from the available details together with proper engineering judgment. With all these details and using the available design guidelines, the response of pile foundation is assessed for its performance typically presented in terms of bending moments and displacements. In case of liquefiable soils, a novel bilinear strain-hardening model has been proposed by Lombardi and his research team (Dash et al. 2017; Lombardi et al. 2016; Rouholamin et al. 2017) to estimate the bending response of pile foundations in fully liquefied soils through Winkler spring approach. Dammala et al. (2017c) and Rouholamin (2016) proposed experimental-based simplified Winkler theories to estimate the transient behavior of pile foundations during partial liquefaction phase.

Case studies of pile foundations under seismic loads have been performed using such Winkler theories, see for example, Showa Bridge analysis by Bhattacharya et al. (2014), Dash et al. (2009) for Kandla Port Tower, Dammala and Krishna (2019) for a single and group pile-supported building.

If the performance of the structure against an anticipated earthquake is within the allowable limits, the structure can be considered safe or requalified and if not, it is treated as seismically unstable and a redesign or a strengthening measure should be suggested.

2.4 Step 4: Redesign or Strengthening Measures

Seismic redesign or strengthening methodologies are to be planned to meet the requirements in order to make the structure seismically safe. Based on the analysis, the strengthening may be suggested to improve the soil shear strength and or the structure's load-carrying capacity. For example, the liquefaction resistance of loose granular soils can be improved by ground improvement techniques such as the inclusion of granular piles (Krishna & Madhav, 2009). In structural terms, a retrofitting strategy can be to reduce foundation settlements or improve flexibility through isolation (Rele et al., 2019), avoiding plastic hinge formation against excessive bending moments Rostami et al. (2017).

In the current article, a pile-supported building is considered as an example application to effectively demonstrate the proposed integrated seismic analysis approach. Each of the components of the approach is presented independently followed by the integration of all the components to finally arrive at a performance-based decision on the pile foundation.

3 Seismic Analysis of Pile Foundation—Example Application

In order to demonstrate the applicability of proposed integrated approach, a pile-supported structure is considered. The chosen structure is located at Tezpur city of Assam (one of the seven northeastern states of India). Various aspects involved in integrated seismic analysis are briefly presented in further subsections.

3.1 Seismic Hazard Analysis

Identifying and establishing the seismic sources leading to possible future scenario earthquake is the primary step involved. It must be noted that the structure is located in the most active seismic zones of the country (Zone V), as established by (IS:1893, 2016). Figure 2a presents the seismic map of the country wherein the location of the chosen site is also highlighted (with a star mark). A deterministic hazard assessment of the chosen site reveals the location of active seismic faults and the historic seismic events in and around the site (≈500 km). Figure 2b depicts the seismotectonic faults of northeastern India. From the DSHA, the 1897 Shillong Plateau event is considered the controlling earthquake (in terms of epicentral distance of 99 km and moment magnitude of 8.7). Once the hazard is established, the required parameters for further analyses are the expected peak ground acceleration (PGA) and anticipated seismic ground motion at the site. Raghukanth et al. (2008) developed artificial ground motions for the 1897 Shillong Plateau earthquake at Guwahati city,

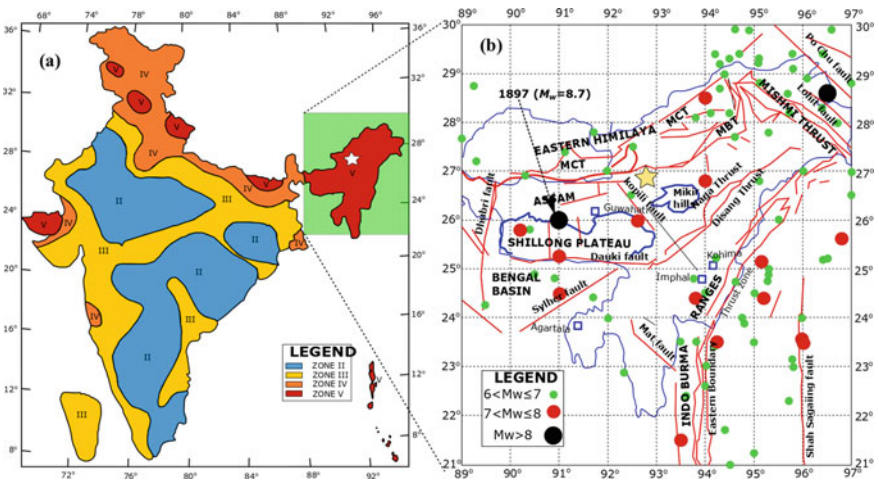

Fig. 2 **a** Seismic zonation map of India (modified after IS 1893–2016) **b** Seismotectonic setting of northeast India (modified after Raghukanth & Dash, 2010)

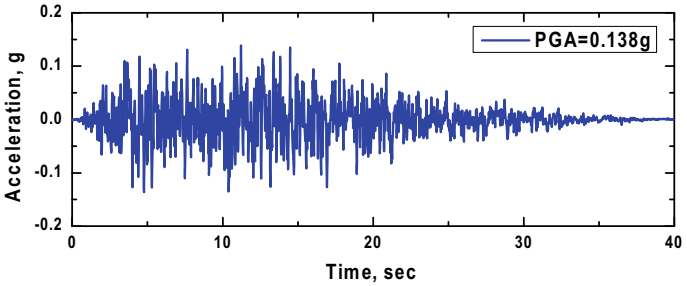

Fig. 3 Input motions chosen for the site based on DSHA

based on stochastic seismological model proposed by Boore (1983). Since Guwahati city is closer to the chosen site in Tezpur, the same ground motion is considered for further analyses. The average PGA for the generated motion is 0.138 g. Figure 3 depicts the chosen ground motion from the study of Raghukanth et al. (2008).

3.2 Local Soil Conditions

The subsoil conditions play a vital role in the seismic stability of foundations and thereby the superstructure. Subsequent subsections detail the subsoil conditions and dynamic characterization of the soils, followed by the utilization of established properties in seismic ground response and liquefaction analyses.

3.2.1 Soil Profile and Dynamic Characterization of Soils

Soil exploration studies at the chosen site revealed the existence of three-layered strata (based on the average of four borehole data provided by the local consultancy firm). Figure 4a, b depicts the subsoil conditions of the chosen site in terms of stratification and average measured SPT-N-values. The shear wave velocity (V_s) has been correlated following the relationship proposed by Imai and Tonouchi (1982), Fig. 4b. Major stratifications of the profile are surficial loose sand of 5 m thickness followed by a stiff red soil of 5 m thick and 15 m thick highly dense sand. Further details of the site and subsoil conditions can be found in Dammala (2019).

In order to assess the dynamic behavior of the soils and evaluate the seismic response, the strain-dependent dynamic soil properties (represented through normalized modulus G/G_{max} and damping ratio (D) variation with shear strain (γ)) along with liquefaction potential parameters must be established. Many recent studies (Chattaraj & Sengupta, 2016; Dammala et al. 2017b, 2019; Kumar et al., 2018b, c) reveal that the utilization of empirical/literature-based dynamic soil properties in seismic design of foundations may not be ideal and may lead

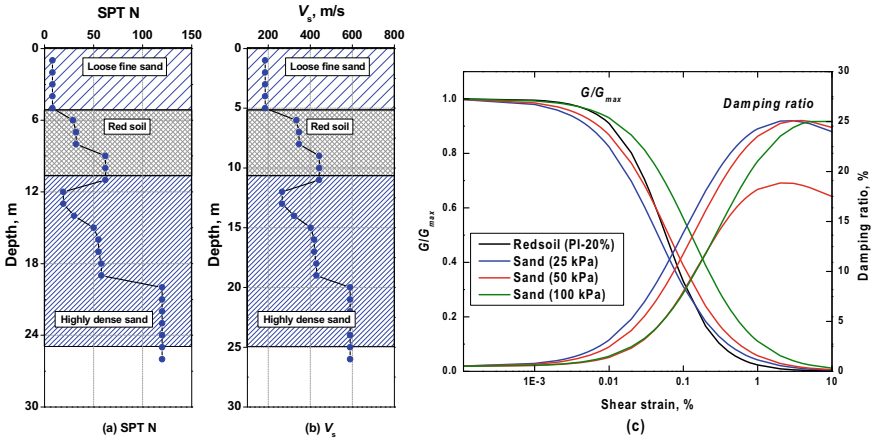

Fig. 4 Soil profile details of the chosen site in terms of **a** SPT-N variation along with the depth **b** Shear wave velocity **c** Dynamic soil properties of the strata (modified after Dammala & Krishna, 2019)

to under/overestimation of the actual seismic demands. This calls to develop site-specific properties for major infrastructural projects. In view of this, soil samples from the site were collected at different depths representing different stratifications. Advanced element testing techniques (bender element, resonant column, dynamic simple shear, and cyclic triaxial tests) were adopted (Dammala & Krishna, 2019) to establish comprehensive dynamic soil properties over a wide range of cyclic shear strains (0.0005–10%). Figure 4b presents the established dynamic soil properties for the sampled soils for the three different layers. It can be observed that three pressure-dependent modulus reduction and damping curves have been developed for sandy stratum (since granular soil behavior is dependent on overburden pressure), while only one curve has been generated for red soil (cohesive in nature). Lanzo et al. (1997) and Vucetic and Dobry (1991) concluded that the major influencing parameter for cohesive soil dynamic response would be the plasticity index and therefore only one curve is utilized for red soil in this study.

To obtain liquefaction resistance parameters of the soil undrained multi-stage (isotropic consolidation + cyclic shearing followed by post-cyclic monotonic axial shearing) cyclic triaxial tests have been conducted on both sand and red soil specimens with varying test conditions. Dammala et al. (2019) presented the results on sandy specimens in the form of a generalized pressure-dependent pore water pressure (PWP) model, while Kumar et al. (2018c) established the liquefaction potential of red soil.

3.2.2 Ground Response Analysis (GRA)

Nonlinear effective stress-based seismic response of the ground is traditionally evaluated through ground response studies in time/frequency domain. Various three-dimensional finite element/boundary element-based numerical programs are available to simulate ground response in a sophisticated manner. However, simplified one-dimensional GRA studies have been evolved based on effective validation of field and experimental tests (Boulanger et al., 1999; Garala & Madabhushi, 2019; Park & Hashash, 2008). For the present study, one-dimensional GRA has been performed utilizing the DEEPSOIL V6.1 (Hashash et al., 2016).

Major ingredients of GRA studies are the subsoil conditions (dynamic soil properties and liquefaction parameters) and input ground motions. The V_s profile along with the dynamic soil properties are shown in Fig. 4b and c, respectively. Liquefaction parameters of the soils have been considered from Kumar et al. (2018c) and Dammala et al. (2019) for cohesive and cohesionless soils, respectively. The input ground motion chosen for the site is shown in Fig. 3. Along with the originally generated ground motion of 0.138 g PGA, two more ground motions have been generated using linear scaling (0.05 and 0.24 g) to understand the effect of different levels of intensity on the ground response.

Figure 5 presents the ground response results in terms of peak accelerations, peak displacements, and pore water pressure ratio generated in the soil column for the three chosen motions. It can be seen that a steady amplification of seismic waves for 0.05 and 0.138 g motions could be realized, while 0.24 g motion showed an attenuation towards reaching the surface. This has been attributed to the high strains induced in the soil at high intensities leading to a higher damping ratio and reduced accelerations at the surface (Dammala et al., 2017b, 2019).

3.2.3 Liquefaction Analysis

Liquefaction potential of the chosen site is evaluated based on both semi-empirical procedure (Boulanger & Idriss, 2006; Idriss & Boulanger, 2006) and GRA study. The semi-empirical procedure yielded a surficial liquefaction of 5 m for the loose sandy stratum for 0.138 and 0.24 g motions. Similarly, from the nonlinear effective stress-based GRA study, both the 0.138 and 0.24 g motions lead to the liquefaction of surficial loose sandy stratum. In order to identify the stresses and strains at the location, the GRA results are presented in Fig. 6a and b. It can be seen that the 0.05 g motion at 5 m depth from surface did not yield any significant strains (<0.001%) in the soil column as well as no observable pore water pressures exist. However, the 0.24 g motion completely liquefied the loose sandy stratum in the very first few cycles (with a PWP ratio of unity) of the motion (Fig. 6b) due to the large strains developed in the soil column.

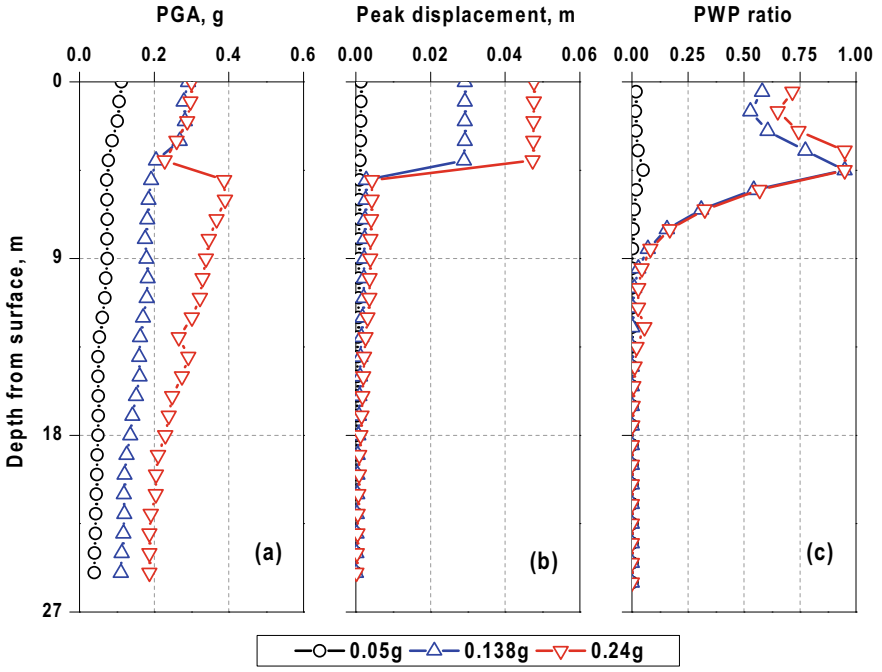

Fig. 5 Free field GRA results in terms of **a** peak ground acceleration **b** peak soil displacement and **c** pore water pressure variation

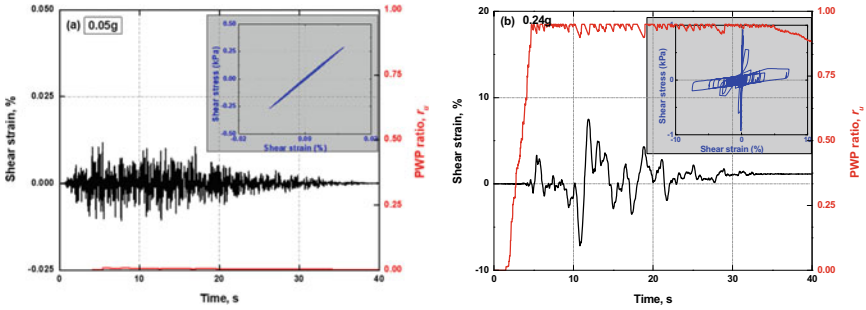

(a) (b)

Fig. 6 Shear strain and pore water pressure history in loose sand (at 5 m depth from surface) for **a** 0.05 g and **b** 0.24 g motions

3.3 Seismic Analysis

The next step in the seismic analysis of pile foundations is the dynamic analysis considering the complete nonlinearity of the soil established from previous steps.

The present study adopts the Beams on Nonlinear Winkler Foundation (BNWF) approach (Nogami et al., 1992), which is a widely used method (also called *p–y* approach) for the seismic analysis of pile foundations. In this approach, seismic soil–pile–structure interaction (SPSI) arising due to the incoming waves is modeled through discrete spring element (*p–y* element, where *p* is the soil resistance offered for a unit pile horizontal displacement, *y*), manifesting the nonlinear behavior of SPSI during dynamic loading. Kinematic and bending response of pile foundations in seismic conditions which arise due to the kinematic and inertial interactions can be reasonably simulated using the nonlinear time history analysis of BNWF approach (Nogami et al., 1992; Wang et al., 1998).

The BNWF approach involves three major steps and is schematically briefed using Fig. 7.

1. *Step 1:* The first step involves the independent ground response analysis whereby the soil displacements (without structure) caused by the seismic waves along the depth are determined using 1D or advanced models (step 1 in Fig. 7).
2. *Step 2:* The SPSI is modeled through closely spaced nonlinear *p–y* elements. A *p–y* element is a combination of both linear and nonlinear behaviors and can also simulate the far-field effects adequately. Various standard empirical forms (based on the shear strength properties of soils) are available to develop the *p–y* element properties, such as (API, 2000; DNV, 2014), etc. (step 2 in Fig. 7).
3. *Step 3:* Final component involves the nonlinear time history analysis of developed soil–pile model by inputting the free field soil displacements (obtained

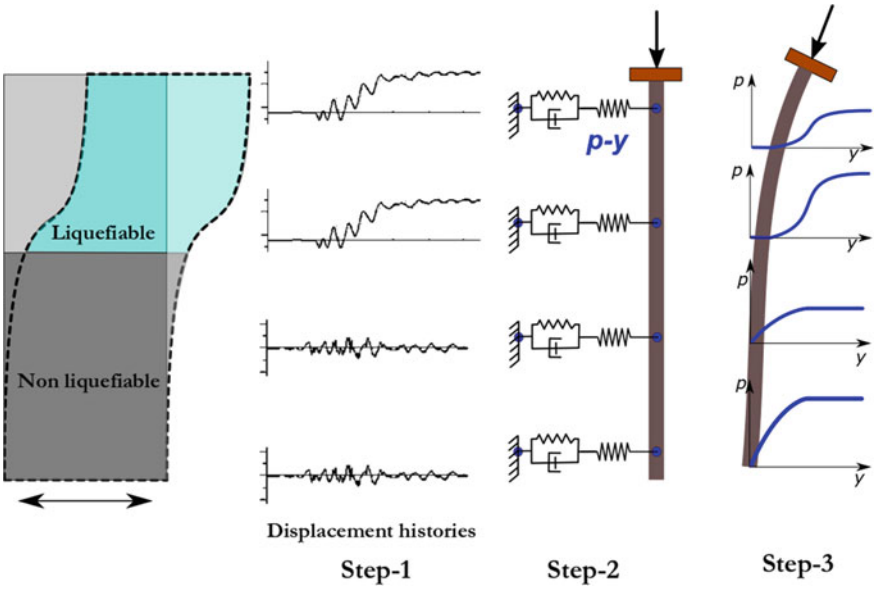

Fig. 7 Steps involved in dynamic BNWF approach of pile foundations (Dammala, 2019)

from free field 1D GRA) at various elevations. This step requires a structural analysis program (SAP2000 or OpenSees) which can apply the free field motions via multi-support excitation along with the depth.

The commercially available numerical program-SAP2000 (CSI Analysis Reference Manual, 2015) has been used for performing the dynamic nonlinear time history analysis (step 3 shown in Fig. 7) of pile foundations.

3.3.1 Validation

The dynamic BNWF approach has been successfully validated against the centrifuge test results of a single pile, as reported by Boulanger et al. (1999). The description of numerical program and validation details are described in detail in Dammala (2019) and Dammala and Krishna (2019).

In the current study, two pile configurations (single pile and 2 × 2 pile group) have been chosen to assess their seismic stability against different intensities of earthquake motions (0.05, 0.138, and 0.24 g). Pile is modeled as a solid frame element with 27 nodes (26 frame elements of each 1 m depth) and M25 concrete properties are assigned to it. The base of the pile is given a hinged condition which restricts the lateral movement with no restraint on rotation and the top of the pile is considered to be a free condition to represent a free-headed pile. In case of 2 × 2 pile group, piles are modeled as frame elements, and a pile cap of 0.9 m thick, modeled as thick shell element representing a rigid body with M25 properties. Piles are taken to the half of the depth of pile cap to represent the full fixity condition. The pile cap is given a rotation fixity and translation possibility representing the typical pile cap support scenario. Soil–pile interaction is modeled using two-joint link elements (representing *p–y* behavior). One end of the *p–y* elements is grounded and fixed against all degrees of freedom, while the other end is connected to the pile node at different depths. Figure 8 a presents the modeled view of chosen pile configurations for the study.

The next step is to develop *p–y* curves for SPSI modeling. It must be noted from the GRA and liquefaction analyses that the surficial loose sandy stratum is prone to liquefaction. The standard API (2000) *p–y* springs cannot capture the response of liquefied soils. Therefore, the recently validated strain-hardening model by Lombardi et al. (2016) has been adopted herein to model the SPSI of liquefied stratum for intense motions. The base layers have been modeled using the standard API (2000) recommendations. Figure 8b presents a comparison of *p–y* curves for a nonliquefied and liquefied strata.

3.3.2 Analysis and Discussion

Analyses have been performed independently for single pile and 2 × 2 pile group configurations for the three chosen ground motions (0.05, 0.138, and 0.24 g). Figure 9a and b presents the displacement histories of single pile for 0.05 and

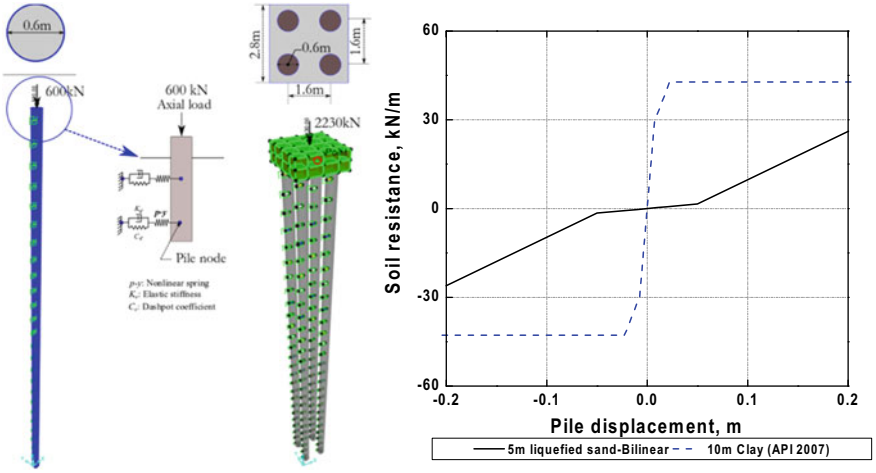

Fig. 8 **a** Present pile configuration and **b** Liquefied and nonliquefied *p–y* springs at a depth of 5 m from surface

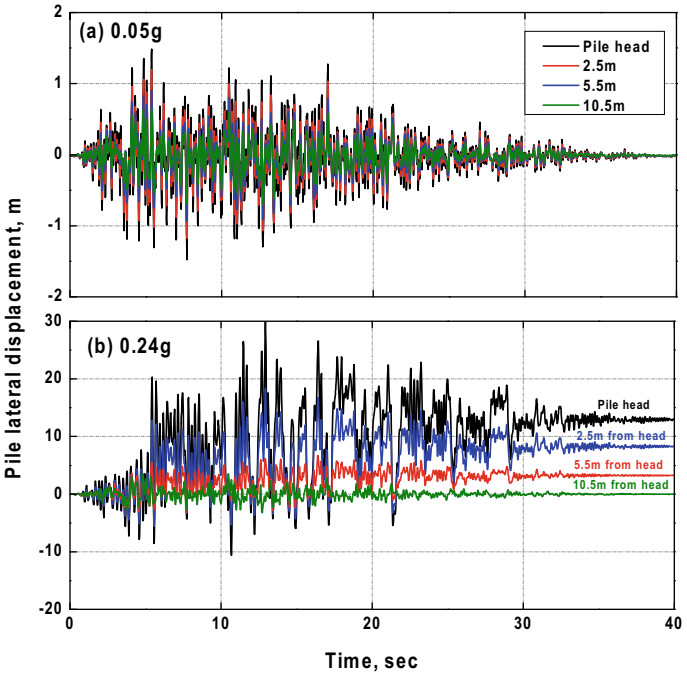

Fig. 9 **a** Displacement histories of single pile for 0.05 g and **b** 0.24 g events

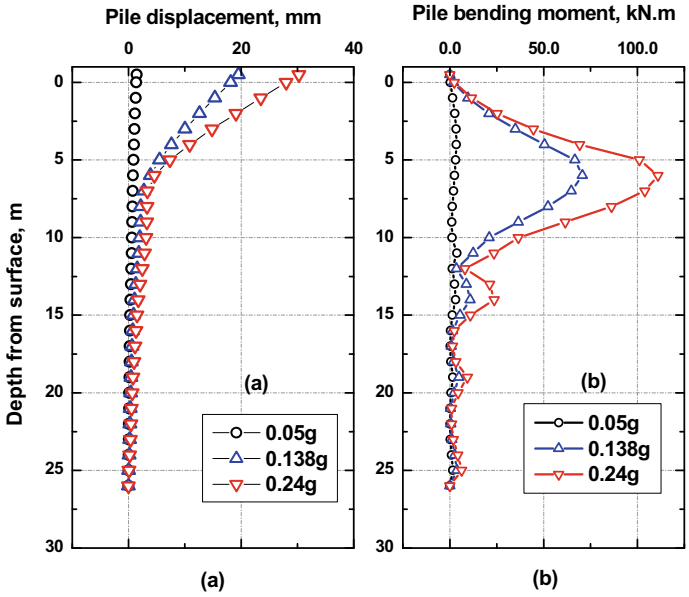

Fig. 10 **a** Variation of peak displacement and **b** peak bending moment

0.24 g motions, respectively. It can be observed that no significant displacements are induced in pile for lower intensity motion (0.05 g), while excessive deformations have been witnessed in the pile for 0.24 g motion. The deformations increase towards the surface of the ground due to the additional stresses of the liquefied ground at the surface. A similar response was also reported for liquefiable soils by Haldar and Babu (2010) and Wilson et al. (2000). The variation of peak pile displacement and peak bending moments along the depth of the single pile are shown in Fig. 10a and b, respectively. It can be visualized that the displacements and bending moments of pile increase with an increase in the intensity of ground motion. Also, an abrupt change in displacement and bending moments seems to happen at the interface of liquefied and nonliquefied strata. Stiffness contrast between the two layers has been the contributor to such abrupt changes in response as reported by Mylonakis (2001) and Nikolaou et al. (2001).

The performance of the pile is compared against the allowable displacements and bending moments. The serviceability limit state (SLS) suggests to limit the displacement of the pile to be less than 5% of the diameter. Also, the plastic hinge formation must be avoided. The induced moments must be less than the plastic moment capacity of piles for plastic hinge formation arrest. Figure 11 a and b present the normalized pile displacement (with respect to pile diameter) and normalized pile bending (with respect to plastic moment capacity, M_p), respectively. The induced pile displacements for two events (0.05 and 0.138 g) fall in the lines of safety according to SLS criteria, however, the 0.24 g motion yielded beyond the serviceability criteria. However, the bending moments generated in the pile are lower than the plastic moment capacity

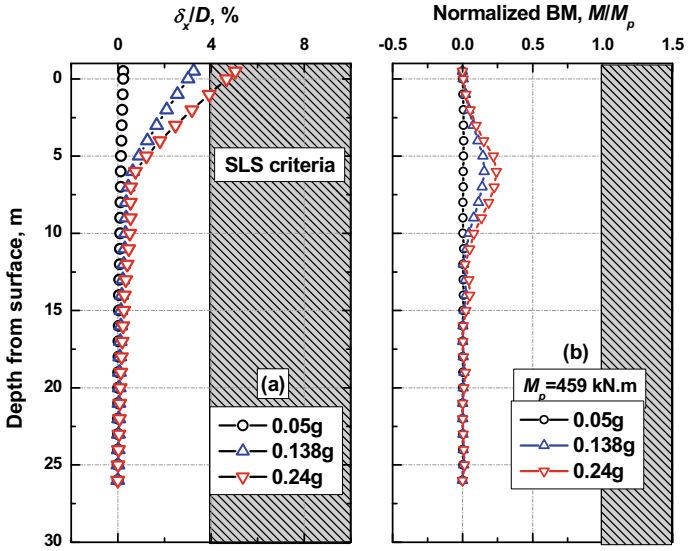

Fig. 11 **a** Variation of normalized peak displacement and **b** Normalized peak bending moment

of the pile, concluding that no excessive bending may not be possible. This ensures the seismic safety of chosen pile configuration for the anticipated seismic hazard at the site.

In order to compare the response of single pile to the 2 × 2 group pile, the displacement and bending moments generated are compared and presented in Figs. 12 and 13, respectively. It can be noted that in case of nonliquefied soils (Figs. 12a and 13a), the displacement and bending moments seem to be higher for the group pile than for the single pile. On the contrary, for liquefied stratum (in case of 0.138 g and 0.24 g motions), single pile seems to exert higher pile displacements and severe bending moments. Such phenomenon of higher response (displacements and BM) of pile group in nonliquefiable soils and lower response in liquefiable soils can be attributed to the shadowing effects in nonliquefiable soils. In case of nonliquefiable soils (or in typical static cases), it is expected that pile group would yield a higher response compared to a single pile of similar loadings due to the interference of strain contours from pile to soil to pile (pile–soil–pile) as reported experimentally by Brown et al. (1988). However, in case of liquefiable events due to the loss of surrounding soil support and resulting absence of shadowing effect, pile group is in beneficial condition and yields relatively lower compared to the single pile of similar loading conditions. Kumar et al. (2016) noted a similar lower response of combined pile raft foundation in liquefiable soils in comparison to a single pile of similar loading.

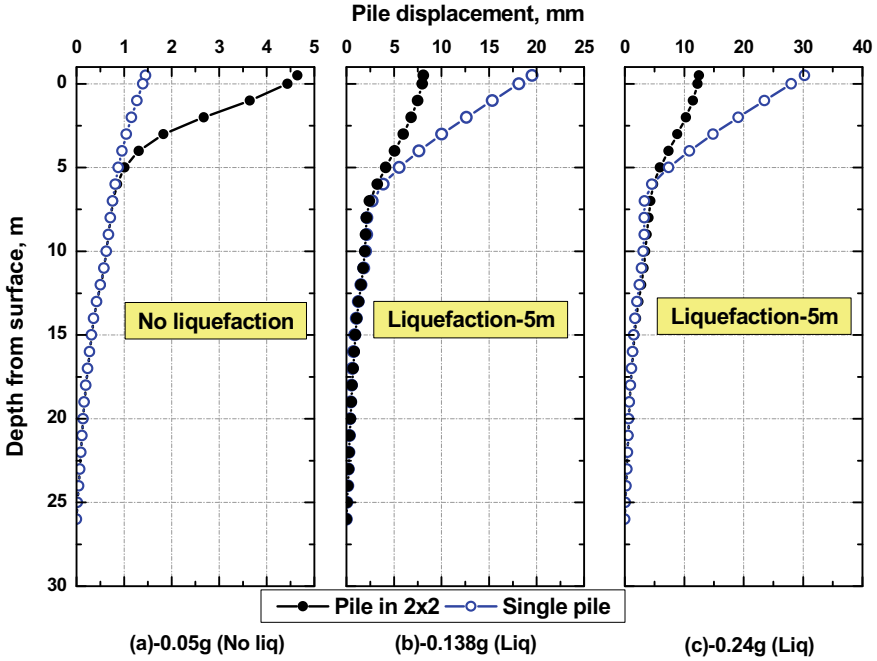

Fig. 12 Comparison of variation of peak displacement for single and 2 × 2 pile group

4 Concluding Remarks

An integrated approach for seismic analysis of pile foundations in liquefiable soils has been presented with a demonstrating example. The approach involves various components like studying the seismicity of the site, determining the local soil conditions and performing seismic ground response analysis for the site followed finally with the integrated seismic analysis of the structure. The complete soil nonlinearity was considered in nonlinear effective stress ground response analysis using experimentally derived dynamic soil properties and liquefaction parameters. Also, the possible liquefied stratum has been modeled using the bilinear strain-hardening model in seismic analysis module. The numerical results indicate that the pile foundation is stable against performance-based criteria in terms of acceptable deformations and bending moments. The pile group showcased better seismic performance in case of liquefiable conditions.

The demonstrated integrated seismic analysis approach simulates the pile foundation response reasonably well. The approach is easy to use with simple 1D programs with soil nonlinearity considerations which can be adopted for designing new structures in seismically active regions as well as requalification studies of existing structures.

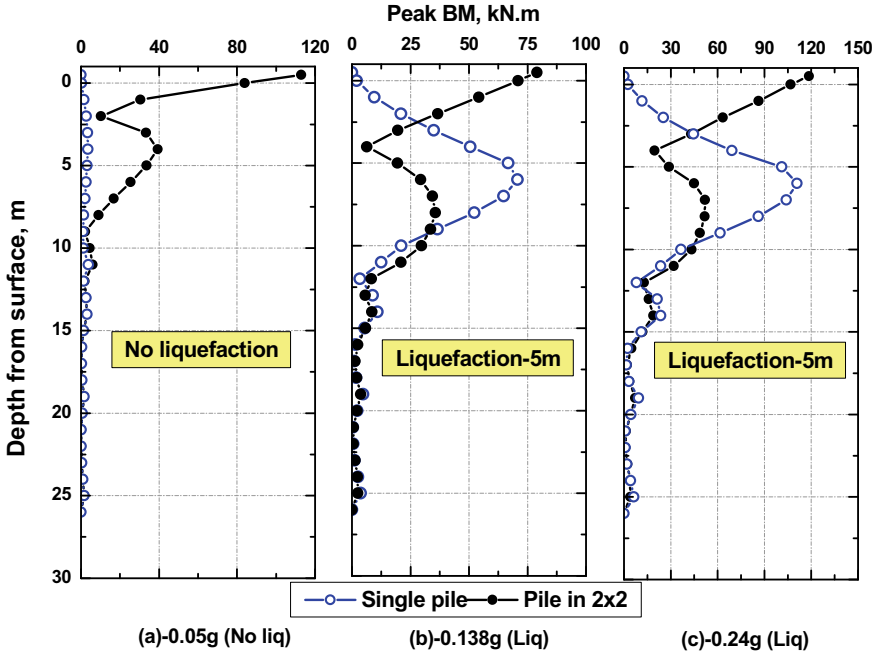

Fig. 13 Comparison of variation of peak bending moment for single and 2 × 2 pile group

References

API 2000 American Petroleum Institute (2014). *API Recommended Practice 2A-WSD. 7056* (November).

Bhattacharya, S., & Madabhushi, S. P. G. (2008). A critical review of methods for pile design in seismically liquefiable soils. *Bulletin of Earthquake Engineering, 6*(3), 407–446. https://doi.org/10.1007/s10518-008-9068-3.

Bhattacharya, S., Tokimatsu, K., Goda, K., Sarkar, R., Shadlou, M., & Rouholamin, M. (2014). Collapse of Showa Bridge during 1964 Niigata earthquake: A quantitative reappraisal on the failure mechanisms. *Soil Dynamics and Earthquake Engineering*, *65*(55), 71. https://doi.org/10.1016/j.soildyn.2014.05.004.

Boore, D. M. (1983). Stochastic simulation of high-frequency ground motions based on seismological models of the radiated spectra. *Bulletin of the Seismological Society of America*, *73*(6), 1865–1894. http://www.bssaonline.org/cgi/content/abstract/73/6A/1865.

Boore, D. M. (2003). Simulation of ground motion using the stochastic method. *Pure and Applied Geophysics, 160*(3), 635–676. https://doi.org/10.1007/PL00012553.

Boulanger, R. W., & Idriss, I. M. (2006). Liquefaction susceptibility criteria for silts and clays. *Journal of Geotechnical and Geoenvironmental Engineering, 132*(11), 1413–1426. https://doi.org/10.1061/(ASCE)1090-0241(2006)132:11(1413).

Boulanger, B. R. W., Curras, C. J., Member, S., Kutter, B. L., Wilson, D. W., Member, A., & Abghari, A. (1999). Seismic soil-pile-structure interaction experiments and analyses. *Journal of Geotechnical & Geoenvironmental Engineering, 125*(9), 750–759. https://doi.org/10.1061/(ASCE)1090-0241(1999)125.

Brown, B. D. A., Morrison, C., & Reese, L. C. (1988). Lateral laod behavior of pile group in sand. *Journal of Geotechnical Engineering, 114*(11), 1261–1276.

Chattaraj, R., & Sengupta, A. (2016). Liquefaction potential and strain dependent dynamic properties of Kasai River sand. *Soil Dynamics and Earthquake Engineering, 90*, 467–475. https://doi.org/10.1016/j.soildyn.2016.07.023.

Computers and Structures Inc. (2015). *CSI Analysis Reference Manual*. *December*, 496.

Dammala, P. K. (2019). *Dynamic characterisation of soils and seismic analysis of deep foundations* (Doctoral dissertation).

Dammala, P. K., & Krishna, A. M. (2019). Kinematic response of pile foundations in liquefiable soils. In F. Silvestri & Moraci (Eds.), *Earthquake Geotechnical Engineering for Protection and Development of Environment and Constructions* (Issue 1999, pp. 1944–1951).

Dammala, P. K., Bhattacharya, S., Krishna, A. M., Kumar, S. S., & Dasgupta, K. (2017a). Scenario based seismic re-qualification of caisson supported major bridges: A case study of Saraighat Bridge. *Soil Dynamics and Earthquake Engineering, 100*, 270–275. https://doi.org/10.1016/j.soildyn.2017.06.005.

Dammala, P. K., Krishna, A. M., Bhattacharya, S., Nikitas, G., & Rouholamin, M. (2017b). Dynamic soil properties for seismic ground response studies in Northeastern India. *Soil Dynamics and Earthquake Engineering, 100*, 357–370. https://doi.org/10.1016/j.soildyn.2017.06.003.

Dammala, P. K., Rouholamin, M., Nikitas, G., Bhattacharya, S., & Murali Krishna, A. (2017c). Bending response of pile foundations during partial liquefaction. *IGC*, 1–10.

Dammala, P. K., Kumar, S. S., Krishna, A. M., & Bhattacharya, S. (2019a). Dynamic soil properties and liquefaction potential of northeast Indian soil for non-linear effective stress analysis. *Bulletin of Earthquake Engineering*, vol. 17, Issue 6. Springer Netherlands. https://doi.org/10.1007/s10518-019-00592-6.

Dammala, P. K., & Murali Krishna, A. (2019b). Dynamic characterization of soils using various methods for seismic site response studies. In *Frontiers in geotechnical engineering* (pp. 273–301). Springer, Singapore.

Dash, S. R., Govindaraju, L., & Bhattacharya, S. (2009). A case study of damages of the Kandla port and customs office tower supported on a mat-pile foundation in liquefied soils under the 2001 Bhuj earthquake. *Soil Dynamics and Earthquake Engineering, 29*, 333–346. https://doi.org/10.1016/j.soildyn.2008.03.004.

Dash, S., Rouholamin, M., Lombardi, D., & Bhattacharya, S. (2017). A practical method for construction of p-y curves for lique fi able soils. *Soil Dynamics and Earthquake Engineering, 97*(March), 478–481. https://doi.org/10.1016/j.soildyn.2017.03.002.

DNV. (2014). *DNV-OS-J101 design of offshore wind turbine structures. May.*

Finn, W. D. L. (2005). *a study of piles during earthquakes : Issues of design and analysis*. 141–234. https://doi.org/10.1007/s10518-005-1241-3.

Garala, T. K., & Madabhushi, G. S. P. (2019). Seismic behaviour of soft clay and its influence on the response of friction pile foundations. *Bulletin of Earthquake Engineering, 17*(4), 1919–1939. https://doi.org/10.1007/s10518-018-0508-4.

Haldar, S., & Babu, G. L. S. (2010). Failure mechanisms of pile foundations in liquefiable soil: Parametric study. *International Journal of Geomechanics, 10*(April), 74–84.

Hanks, T. C., & McGuire, R. K. (1981). The character of high-frequency strong ground motion. *Bulletin of the Seismological Society of America*, *71*(6), 2071–2095. http://www.bssaonline.org/content/71/6/2071.abstract.

Hashash, Y. M. A., Musgrouve, M. I., Harmon, J. A., Groholski, D. R., Phillips, C., & Park, D. (2016). *DEEPSOIL 6.1, User Manual*.

Idriss, I. M., & Boulanger, R. W. (2006). Semi-empirical procedures for evaluating liquefaction potential during earthquakes. *Soil Dynamics and Earthquake Engineering*, *26*(2–4 SPEC. ISS.), 115–130. https://doi.org/10.1016/j.soildyn.2004.11.023.

Imai, T., & Tonouchi, K. (1982). Correlation of N-value with S-wave velocity and shear modulus. *Proceedings of the 2nd European Symposium on Penetration Testing*, 57–72.

IS:1893. (2016). Criteria for earthquake resistant design of structures. *Indian Standard*, 1–44.

Krishna, A. M., & Madhav, M. R. (2009). Engineering of ground for liquefaction mitigation using granular columnar inclusions: Recent developments. *American Journal of Engineering and Applied Sciences, 2*(3), 526–536. https://doi.org/10.3844/ajeassp.2009.526.536.

Krishna, A. M., Bhattacharya, S., Choudhury, D. (2014). Seismic requalification of geotechnical structures. *Indian Geotechnical Journal*, *44*, 113–118. https://doi.org/10.1007/s40098-014-0115-5.

Kumar, A., Choudhury, D., & Katzenbach, R. (2016). *Effect of earthquake on combined pile—raft foundation. 16*(5), 1–16. https://doi.org/10.1061/(ASCE)GM.1943-5622.0000637.

Kumar, S. S., Krishna, A. M., & Dey, A. (2017). Evaluation of dynamic properties of sandy soil at high cyclic strains. *Soil Dynamics and Earthquake Engineering*, *99*(May 2016), 157–167. https://doi.org/10.1016/j.soildyn.2017.05.016.

Kumar, S. S., Adapa, M. K., & Dey, A. (2018a). Importance of site-specific dynamic soil properties for seismic ground response studies. *International Journal of Geotechnical Earthquake Engineering*, *In press.*

Kumar, S. S., Dey, A., & Krishna, A. M. (2018b). Response of saturated cohesionless soil subjected to irregular seismic excitations. *Natural Hazards, 93*(1), 509–529. https://doi.org/10.1007/s11069-018-3312-1.

Kumar, S. S., Krishna, A. M., Dey, A. (2018c). Dynamic properties and liquefaction behaviour of cohesive soil in northeast India under staged cyclic loading. *Journal of Rock Mechanics and Geotechnical Engineering* 1–10 https://doi.org/10.1016/j.jrmge.2018c.04.004.

Lanzo, G., Vucetic, M., & Doroudian, M. (1997). Reduction of shear modulus at small strains in simple shear. *Journal of Geotechnical and Geoenvironmental Engineering, 123*(11), 1035–1042. https://doi.org/10.1061/(ASCE)1090-0241(1997)123:11(1035).

Liyanapathirana, D. S., & Poulos, H. G. (2005). Pseudostatic approach for seismic analysis of piles in liquefying soil. *Journal of Geotechnical and Geoenvironmental Engineering, 131*(12), 1480–1487. https://doi.org/10.1016/j.compgeo.2009.07.001.

Lombardi, D., Dash, S. R., Bhattacharya, S., Ibraim, E., Muir Wood, D., & Taylor, C. A. (2016). Construction of simplified design *p—y* curves for liquefied soils. *Géotechnique, 1*(3), 1–12. https://doi.org/10.1680/jgeot.15.P.116.

Mukherjee, S., & Gupta, V. K. (2002). Wavelet-based generation of spectrum-compatible time-histories. *Soil Dynamics and Earthquake Engineering, 22*(9–12), 799–804. https://doi.org/10.1016/S0267-7261(02)00101-X.

Mylonakis, G. (2001). Simplified model for seismic pile bending at soil layer interfaces. *Soils and FoundationsSoils and Foundations, 41*(4), 47–58.

Mylonakis, G., Syngros, C., Gazetas, G., & Tazoh, T. (2006). The role of soil in the collapse of 18 piers of Hanshin expressway in the Kobe earthquake. *Earthquake Engineering and Structural Dynamics, 35*(5), 547–575. https://doi.org/10.1002/eqe.543.

Nikolaou, S., Mylonakis, G., Gazetas, G., & Tazoh, T. (2001). Kinematic pile bending during earthquakes: Analysis and field measurements. *Geotechnique, 51*(5), 425–440.

Nogami, B. T., Otani, J., Konagai, K., & Chen, H. (1992). Nonlinears oil–pile interaction model for dynamic lateral motion. *118*(1), 89–106.

Novak et al., 1978 Novak, M., Aboul-Ella, F., Nogami, T. (1978). Dynamic soil reactions for plane strain case. *Journal of Engineering Mechanics*, *104*(4), 953–959.

Park, D., & Hashash, Y. M. A. (2008). Rate-dependent soil behavior in seismic site response analysis. *Canadian Geotechnical Journal, 45*(4), 454–469. https://doi.org/10.1139/T07-090.

Puri, N., Nikitas, G., Jain, A., Dammala, P. K., & Bhattacharya, S. (2019). Dynamic soil properties and seismic ground response analysis for North Indian seismic belt subjected to the great Himalayan Earthquakes. *Soil Dynamics and Earthquake Engineering*, *(Under Rev).*

Raghukanth, S. T. G., & Dash, S. K. (2010). Evaluation of seismic soil-liquefaction at Guwahati city. *Environmental Earth Sciences, 61*(2), 355–368. https://doi.org/10.1007/s12665-009-0347-3.

Raghukanth, S. T. G., Sreelatha, S., & Dash, S. K. (2008). Ground motion estimation at Guwahati city for an Mw 8.1 earthquake in the Shillong plateau. *Tectonophysics*, *448*(1–4), 98–114. https://doi.org/10.1016/j.tecto.2007.11.028.

Randolph, M. F. (1981). The response of flexible piles to lateral loading. *Geotechnique, 31*(2), 247–259.

Rele, R., Dammala, P. K., Bhattacharya, S., & Balmukund, R. (2019). Seismic behaviour of rocking bridge pier supported by novel elastomeric pads on pile foundation. *Soil Dynamics and Earthquake Engineering, 124*, 98–120.

Rostami, R., Hytiris, N., Bhattacharya, S., & Giblin, M. (2017). Seismic analysis of pile in liquefiable soil and plastic hinge. *Geotechnical Research, 4*(4), 203–213. https://doi.org/10.1680/jgere.17.00009.

Rouholamin, M. (2016). *An experimental investigation of transient dynamics of pile-supported structures in liquefiable soils. Mehdi Rouholamin A thesis submitted for the degree of Doctor of Philosophy at the University of Surrey* , (Issue April).

Rouholamin, M., Bhattacharya, S., & Orense, R. P. (2017). Effect of initial relative density on the post-liquefaction behaviour of sand. *Soil Dynamics and Earthquake Engineering*, *97*(September 2016), 25–36. https://doi.org/10.1016/j.soildyn.2017.02.007.

Sarkar, R., Bhattacharya, S., Maheshwari, B. K. (2014) Seismic requalification of pile foundations in liquefiable soils. https://doi.org/10.1007/s40098-014-0112-8.

Sitharam T, Govindaraju L, Sridharan, A (2004) Dynamic properties and liqefaction potential of soils. *Current Science*, *87*(10), 1370–1378.

Somerville, P. G., Smith, N. F., Graves, R. W., & Abrahamson, N. A. (1997). Modification of empirical strong ground motion attenuation relations to include the amplitude and duration effects of rupture directivity. *Seismological Research Letters, 68*(1), 199–222. https://doi.org/10.1785/gssrl.68.1.199.

Vucetic, M., & Dobry, R. (1991). Effect of soil plasticity on cyclic response. *Journal of Geotechnical & Geoenvironmental Engineering, 117*(1), 89–107.

Wang, S., Kutter, B. L., Chacko, J., Wilson, D. W., Boulanger, R. W., & Abghari, A. (1998). Nonlinear seismic soil-pile structure interaction. *Earthquake Spectra, 14*(2), 377–396.

Wilson, B. D. W., Member, A., Boulanger, R. W., & Kutter, B. L. (2000). Observed seismic lateral resistance of liquefying sand. *Journal of Geotechnical & Geoenvironmental Engineering, 126*(October), 898–906.

Zhang, J., Andrus, R. D., & Juang, C. H. (2005). Normalized shear modulus and material damping ratio relationships. *Journal of Geotechnical and Geoenvironmental Engineering, 131*(4), 453–464. https://doi.org/10.1061/(ASCE)1090-0241(2005)131:4(453).

Numerical Modeling of Liquefaction

Sunita Kumari and V. A. Sawant

1 Introduction

Prediction of liquefaction is always been a challenge to various interactions between fluid–soil structure. Length of drainage path available for dissipation of excess pore pressure is a crucial governing factor. A large number of studies have been presented to access liquefaction potential for a soil domain. Cyclic Resistance Ratio (CRR) has been related to either sounding resistance or shear wave velocity. Although this approach has been wildly adopted by practitioners to access liquefaction potential, they are unable to link the behavior with change in drainage path or intrusion of reinforcement. In this case, fluid continuity equation must be incorporated to investigate the effect of drainage path. Effect of any foreign element in the form of pile or reinforcement must be considered with their proper interaction with soil. Load sharing mechanism between soil–reinforcement–fluid is of paramount importance.

For very slow events like consolidation with proper drainage, drained static behavior can be assumed for the behavior of the solid and fluid phases. These two phases can be decoupled. Solutions can be found separately for the soil skeleton and pore fluid via usual mechanics and effective stress principles. For a rapid even and undrained condition, the pore pressure can be calculated via the bulk modulus of the fluid. Again a single set of field equations need to be solved. However, under transient consolidation and dynamic conditions, such decoupling does not occur.

First approach considering decoupling between soil and fluid phase is being referred as partially-coupled analysis. Total stress equilibrium equations are solved for unknown displacements. Then plastic components of volumetric strains are obtained from shear strains, which are used to derive the generated excess pore

S. Kumari
National Institute of Technology Patna, Patna, India

V. A. Sawant (✉)
Indian Institute of Technology Roorkee, Roorkee, India
e-mail: vishwas.sawant@ce.iitr.ac.in

T. G. Sitharam et al. (eds.), *Advances in Earthquake Geotechnics*, Springer Tracts in Civil Engineering, https://doi.org/10.1007/978-981-19-3330-1_6

pressure (Finn et al., 1976; Martin et al., 1975). However, predictions from numerical simulation either by partially-coupled or uncoupled solution are not completely in order with the results of VELACS project. This shows that some other numerical tools based on finite element scheme or coupling methodology of porous media can perform better.

In coupled numerical analysis, the interaction between soil and fluid phase is being incorporated considering coupled field equations. Total stress equilibrium equations are solved by considering coupling with fluid continuity equation. A fully-coupled effective stress analysis accounts for the dynamic interaction between the solid and fluid phase. Resulting dynamic equilibrium equation and flow continuity equation are solved simultaneously. Various researchers have studied the effectiveness of different fully coupled finite element codes for predicting the response of saturated soil under dynamic loading. Zienkiewicz et al. (1999), Zienkiewicz and Shiomi (1984) summarized different analyzing methods on numerical simulation of the Biot-type formulation. Later, the numerical solution has been applied to study the undrained, drained and dynamic behavior of saturated porous media. Taiebat et al. (2007) developed a fully coupled dynamic algorithm based on u–P formulation to evaluate the liquefaction potential of saturated sandy deposits. Coupled equations were integrated in time domain using generalized Newmark method. A critical state two-surface plasticity model and a densification model were considered to characterize soil behavior. Taiebat et al. (2010) presented the simulation of pore fluid and soil skeleton responses using fully coupled dynamic field equations with $u-p-U$ formulation. This model also takes into account water accelerations (U) in the analysis. Kumar et al. (2020) investigated behavior of stone column improved ground for mitigation of liquefaction using coupled analysis. The Pastor-Zienkiewicz-Chan model (1990) has been incorporated to describe the inelastic behavior of soils under isotropic monotonic and cyclic loadings. Kumari and Sawant (2021) discussed numerical simulation of liquefaction phenomenon considering infinite domain.

Review of literature suggests that coupled analysis can predict liquefaction behavior rationally due to proper interaction between soil–fluid phase. However, partially coupled approach is also popular due to relatively simple computations.

The present paper discusses a qualitative and quantitative prediction of the phenomena leading to permanent deformation or unacceptably high buildup of pore pressure. There are categorized as partially coupled and coupled approaches. In the uncoupled analysis, the response of saturated soil is modeled without incorporating the interaction between soil and fluid, and then the pore pressure is accounted separately through a pore pressure generation model. In the coupled analysis, a mathematical framework is developed for computation of displacements and pore pressures at each time step. A comparison study has been done to understand modeling perception of both approaches so that, a numerical code should be critically selected after examining its ability to predict the liquefaction behavior for the range of applied conditions.

2 Partially-Coupled Approach

2.1 Finn Model

An effective stress-based simple analysis approach was first introduced by Martin et al. (1975). Martin et al. (1975) presented quantitative data in their milestone paper and showed that the amount of compaction per cycle is proportional to the cyclic shear strain amplitude and accumulated volume compaction and is independent of normal effective stress. They also showed that the pore pressure generated per cycle is dependent on the *plastic volumetric strain*, the *rebound modulus of the soil*, and the *stiffness of the pore fluid*. For drained condition, the increment in volumetric strain can simply be added to the accumulated volumetric strain with number of cycle Finn et al. (1976).

Now in case of undrained condition, the accumulated volumetric strain will lead to rise in pore water pressure, which is generally quantified by imposing volume constraints together with an elastic rebound modulus. Using this approach, pore pressure can be obtained after each cycle or half cycle of strain; and this procedure is referred to as *loose-coupled analysis.* The first effective stress-based dynamic analyses by this procedure were presented by Finn et al. (1976).

In this loose-coupled effective stress analysis, the key factor is the cyclic shear-volume coupling equation. At first Martin et al. (1975) proposed a four-parameter Eq. (1) for estimating volume change at a particular density of sand.

$$\Delta\varepsilon_v = C_1(\gamma - C_2\,\varepsilon_v) + \frac{C_3(\varepsilon_v)^2}{\gamma + C_4\,\varepsilon_v} \tag{1}$$

where, $\Delta\varepsilon_v$ is the incremental volumetric strain per cycle of shear strain (%) and ε_v is the accumulated volumetric strain from previous cycles (%). γ is the amplitude of shear strain (%) for the current cycle of shear strain. C_1, C_2,C_3 and C_4 are the constants for the sand at relative density under consideration. Later based on the detailed study done by Tokimatsu and Seed (1987), Eq. (1) has been modified into a two-parameter-based cyclic shear volume coupling Eq. (2).

$$(\Delta\varepsilon_v/\gamma) = C_1\,\mathrm{EXP}(-C_2\,\varepsilon_v/\gamma) \tag{2}$$

For an irregular strain cycle pattern, the basic equation (Eq. 2) is modified again in order to compute the volumetric strain per $\frac{1}{2}$ cycle (Eq. 3)

$$(\Delta\varepsilon_v/\gamma)_{\frac{1}{2}\,cycle} = 0.5\,C_1\,\mathrm{EXP}\,(-C_2\,\varepsilon_v/\gamma) \tag{3}$$

where, C_1 and C_2 can be expressed in the following equation (Eq. 4).

$$C_1 = 7600\,(D_r)^{-2.5} \quad \text{and} \quad C_2 = 0.4/C_1 \tag{4}$$

Volume Compatibility equation:

$$\Delta\varepsilon_v = \Delta\varepsilon_v^e + \Delta\varepsilon_v^p \tag{5}$$

where, $\Delta\varepsilon_v$, $\Delta\varepsilon_v^e$ and $\Delta\varepsilon_v^p$ are total, elastic and plastic incremental volumetric strain per $\frac{1}{2}$ cycle. From the simple shear condition, the elastic volumetric strain can be represented as

$$\Delta\varepsilon_v^e = \Delta\sigma_m'/K_b \tag{6}$$

$\Delta\sigma_m'$ is change in mean effective stress per $\frac{1}{2}$ cycle. K_b is the bulk modulus of sand. The irrecoverable volumetric strains, also known as plastic strains are evaluated from Eq. (3). In case of saturated undrained condition $\Delta\varepsilon_v = 0$,

$$\Delta\sigma_m' = -K_b\,\Delta\varepsilon_v^p \tag{7}$$

As there is no change in total stress then change in pore pressure is calculated as

$$\Delta u_v = -\Delta\sigma_m' = K_b\,\Delta\varepsilon_v^p \tag{8}$$

Bulk modulus is related with mean stress σ_m' as

$$K_b = \mathrm{K}_m \mathrm{p}_a \left(\sigma_m'/\mathrm{p}_a\right)^m \tag{9}$$

Values of $\mathrm{K_m}$ and m are considered to be 1600 and 0.5, respectively, for better agreement against the values reported by Martin et al. (1975).

2.2 UBC3D-PLM Model

PLAXIS-3D uses the UBC3D-PLM model. This model is extended from UBCSAND model originally introduced by Puebla et al. (1997). Galavi et al. (2013) extended this formulation UBC3D-PLM model for liquefaction study. New features were introduced to obtain higher accuracy under seismic loading. The present analysis is an effective stress analysis in which liquefaction occurs as a result of pore pressure generation. In this analysis, all parameters are effective stress parameters, and total stress is the summation of effective stress and pore pressure. Undrained conditions

are stimulated and volumetric strain and bulk modulus of water in pores are considered. Parameter selection and use of numerical tool play a significant role in this type of analysis.

A Drucker Prager criterion-based modified non-associative plastic potential function has been considered to maintain the coaxiality of stress–strain behavior in deviator plane for a stress path initiated from isotropic line. Soil densification mechanism is also included to obtain higher accuracy in predicted excess pore water pressure (EPWP) during seismic excitation. This mechanism permits for the increase of EPWP with decreasing rates when shearing takes place. This behavior is also found in the experimental studies. Main characteristics of the model are presented as follows:

Two types of yield surfaces have been incorporated, primary yield surface and secondary yield surface. Primary surface is based on isotropic hardening and becomes active when mobilized friction angle is equal to maximum mobilized friction angle that soil has ever reached. Here current stress ratio is the highest stress ratio in the loading history. Simplified kinetic hardening rule is utilized for secondary yield surface. It becomes active when mobilized friction angle is less than maximum mobilized friction angle. Here, current stress ratio is lower than maximum stress ratio in the loading history. This distinction between yield surfaces is made to be able to have densification rule in secondary yield surfaces.

A stress state is considered on the isotropic axis, and both yield surfaces are in the same position. From isotropic stress state, both primary and secondary yield surfaces expand according to the same hardening rule. When soil is unloaded, secondary yield surface shrinks and soil acts in an elastic behavior. Upon reloading secondary yield, surface becomes active and behavior becomes elastoplastic. When mobilized friction angle reaches maximum mobilized friction angle, the primary yield surface becomes active again and behavior becomes softer. Mohr–Coulomb yield formulation is used to define both yield surfaces.

$$f_m = \frac{\sigma'_{\max} - \sigma'_{\min}}{2} - \left(\frac{\sigma'_{\max} + \sigma'_{\min}}{2} + c' \cot \phi'_p \right) \sin \phi'_{mob} \tag{10}$$

In which, $\sigma'_{\max}$ *and* $\sigma'_{\min}$ are the maximum and minimum principal effective stress, respectively. c' and ϕ'_p are defined as cohesion and peak effective friction angle. ϕ'_{mob} is the mobilized friction angle during hardening. It is assumed that intermediate principal stress is not affecting the yield surface in 3D yield space.

Elastic behavior

The secondary yield surface shows the elastic behavior, and it is governed by stress-dependent nonlinear mechanism described by Puebla et al. (1997). Pure elastic behavior has been obtainable by the model in case of unloading phase.

$$K^e = K_B^e P_A \left(p'/P_A\right)^{n_k} \quad ; \quad G^e = K_G^e P_A \left(p'/P_A\right)^{n_g} \tag{11}$$

In which, K^{e} is the elastic bulk modulus. G^{e} is the elastic shear modulus. $K_B^e \; and \; K_G^e$ are bulk and shear moduli at reference stress condition. p' is mean effective stress n_{k} and n_{g} define the rate of stress dependency of stiffness. P_{A} is atmospheric pressure and defined as pressure at reference level.

Plastic potential function

Direction of plastic strain increment is specified by the gradient of plastic potential function. Non-associated flow rule based on Drucker Prager model is expressed as follows

$$g = q - p(6 \sin \psi_{mob})/(3 - \sin \psi_{mob}) \tag{12}$$

In which, g is the plastic potential function. ψ_{mob} is the mobilized dilation angle. p is mean effective stress. q is known as deviatoric stress.

Direction of plastic strain increment is perpendicular to Drucker Prager surface. Mobilized dilatancy angle ψ_{mob} is computed using flow rule as defined in Puebla et al. (1997), which results from stress dilatancy concept, linearized and simplified in accordance with energy considerations. It is defined as $\sin \psi_{mob} = \sin \phi'_{mob} - \sin \phi'_{cv}$.

Hardening rule

Hardening rule is described by Puebla et al. (1997) and given by the following expression:

$$d \sin \phi'_{mob} = 1.5 \; K_G^p \left(\frac{p'}{P_A} \right)^{n_p} \left(\frac{P_A}{p'_m} \right) \left(1 - \frac{\sin \phi'_{mob}}{\sin \phi'_{ult}} \right)^2 d\lambda \tag{13}$$

In which, K_G^p is the plastic shear modulus. n_{p} is a model parameter stands for stress dependency of the plastic shear modulus. p' is the mean effective stress. P_{A} is the effective stress. $d\lambda$ is defined as plastic strain increment multiplier. ϕ'_{ult} is the ultimate mobilized friction angle. It is obtained from the failure ratio ($R_{\mathrm{f}} < 1$) as $R_f = \sin \phi'_p / \sin \phi'_{ult}$.

Densification rule

Soil densification mechanism is considered to obtain higher accuracy in predicted excess pore pressure (Beaty & Bryne, 1998). Secondary yield surface in the model ensures even transition into liquefied stage of soil mass. Plastic strains generated during this stage are lesser than the primary yield surface. Anisotropic hardening rule is employed during primary yield surface, and simplified kinematic hardening rule is considered during secondary yield surface.

$$K_G^P = K^p_{G,\mathrm{Primary}} (4 + n_{ev}/2) k_{dens} f_{dens} \tag{14}$$

In which, n_{ev} is defined as the number of shear stress reversals in loading to unloading or vice versa. f_{dens} is a parameter input by user to calibrate densification rule. k_{dens} is a factor used to correct densification rule for loose and cohesionless soil having values 0.5 to 1.

$K^{p}_{G,Primary}$ is the initial value of K^{p}_{G} entered by user for primary yield surface. As per experimental validation, the rate of generation of pore pressure decreases with the increase of number of cycle.

Post liquefaction and cyclic mobility

Volumetric locking is vital in modeling cyclic liquefaction. Once stress path reaches the yield surface described by peak friction angles, volumetric strain approaches constant value due to formulation of flow rule ($\phi'_{mob} = \phi'_{p}$) and remains constant while ϕ'_{cv} is also constant. So, stiffness degradation of soil caused by postcyclic mobility of dense sands cannot be modeled. To solve this problem, plastic shear modulus K^{P}_{G} is decreased gradually as a function of induced plastic deviatoric strain during dilation of soil element. This will result in stiffness degradation. Deconstruction of soil element occurs during dilative behavior hence soil stiffness decreases during contraction after unloading phase. Stiffness degradation is given as

$$K^{P}_{G} = K^{p}_{G,Primary} e^{E_{dil}} \tag{15}$$

$$E_{dil} = \min(110\varepsilon_{dil}, f_{post}) \tag{16}$$

ε_{dil} is the accumulated plastic deviatoric strain. f_{post} is used to limit the exponential multiplier term.

Undrained behavior

Increment of the pore pressure is computed by

$$dp_w = \frac{K_w}{n} d\varepsilon_v \tag{17}$$

In which, K_w is defined as the bulk modulus of the pore fluid, n signifies porosity and $d\varepsilon_v$ is the volumetric strain increment.

Bulk modulus when soil is fully saturated is derived as (Galavi et al. 2013):

$$\frac{K^{sat}_{w}}{n} = K_u - K' = \frac{2G^e}{3}\left(\frac{1+\mu_u}{1-2\mu_u} - \frac{1+\mu}{1-2\mu}\right) \tag{18}$$

In which, K_u and K' denote the undrained and drained bulk moduli of the soil. μ and μ_u are the Poisson ratio in drained and undrained conditions. μ_u is assumed equal to 0.495. Drained Poisson ratio can be derived from the elastic parameters of the model as

$$\mu = \left(3\,K^e - 2\,G^e\right)/\left(6\,K^e + 2\,G^e\right) \tag{19}$$

Dynamic Boundary Condition

In dynamic analysis, it is required to absorb stresses at artificial boundaries to prevent reflection of waves. Selection of boundary conditions is made based on the problem, accuracy and stability of the boundary condition. Two types of boundary conditions are used in the proposed model.

Viscous boundaries—Neumann type of boundary conditions where stresses at boundaries are updated to nullify the reflected stresses.

Free field boundaries—Free field motion is given to boundaries by the means of free field elements. It can be assumed as one-dimensional element with connected (one way) dashpots. To absorb the waves reflected from internal structures, viscous boundaries are considered at the boundary of main domain.

2.3 Numerical Study

A numerical study depending on effective stress analysis has been presented here to demonstrate the effect of liquefaction phenomena and its remedial measure for a case of an earth embankment subjected to seismic loading. A 6 m-thick horizontal soil layer is modeled with the borehole option in PLAXIS 3D. Embankment, sheet piles, and soil column are all introduced in structure mode. Soil and embankment are modeled using 10-noded tetrahedral elements. Sheet pile is modeled using six-noded elements. Soil column is also modeled in continuation of foundation soil, with different properties. It is assumed that foundation soils are fully submerged in water. The numerical analysis is divided into different phases, and a specific type of analysis is done for each particular phase. Sheet piles are modeled as six-noded plate elements with six degrees of freedom (three translational and three rotational). These elements are directly integrated over their cross-section and numerically integrated using three-point Gaussian integration. The material properties of the sheet pile are taken from Aydingum and Adalier (2003). These standard penetration test (SPT) values are used as the input to find other values using the aforementioned formulae. The relation between the normalized SPT value and relative density is referred from Cubrinovski and Ishihara (1999). Permeability values and sheet-pile properties were taken as suggested by Aydingum and Adalier (2003).

Material properties of various parameters are reported in Table 1. Input model parameters for UBC3D-PLM are reported in Table 2. Response has been predicted for input ground motions of the El Centro earthquake. For comparison, 10 points (A–J) are considered. Points A–D are 7.5 m away from toe. Points E–H are below the toe. Points I–J are along the centerline. Points A and E are on the surface of the liquefiable soil, whereas Points B–F, C–G, and D–H are 2.25, 3.75, and 6.0 m below the surface, respectively. Point J is on the top surface of embankment, whereas Point J is 2.25 m below the surface of the liquefiable soil.

Table 1 Material properties and boundary conditions

Properties of embankment clayey sand	Properties of sheet pile
Modulus of elasticity $E =$ 20 MPa Poisson's ratio $\mu = 0.3$	Modulus of elasticity $E =$ 200 MPa Poisson's ratio $\mu = 0.29$
Shear strength parameters $\phi' = 31°$, $c' = 22$ kPa	Thickness = 0.15 m
Unit weight $\gamma_{dry} = 19$ kN/m^3 $\gamma_{sat} = 21$ kN/m^3 Void ratio $e_{initial} = 0.5$	**Boundary conditions** Vertical boundaries viscous
Permeability $k = 0.6$ m/day	

Table 2 Input model parameters for UBC3D-PLM (Kumari et al. 2018)

Parameters with description	Nevada sand	Stone Column
Dry unit weight (γ_{dry})	16.60 kN/m^3	18.60 kN/m^3
Saturated unit weight (γ_{sat})	19.64 kN/m^3	20.40 kN/m^3
Relative density (R_D)	40%	90%
Initial void ratio ($e_{initial}$)	0.763	0.546
Co-efficient of permeability k	47.52 m/day	1.987 m/day
Peak friction angle (ϕ'_p)	33.65°	40°
Friction angle at constant volume (ϕ'_{cv})	33°	37°
Elastic shear modulus number (k_G^e)	809.4 kPa	890 kPa
Elastic bulk modulus number (k_B^e)	566.6 kPa	623 kPa
Plastic shear modulus number (k_G^p)	202.6 kPa	3755 kPa
Index for elastic bulk modulus (n_k)	0.5	0.5
Index for elastic shear modulus (n_g)	0.5	0.5
Index for plastic shear modulus (n_p)	0.4	0.4
Failure ratio (R_f)	0.83	0.64
Reference stress (p_a)	100 kPa	100 kPa
f_{dens} for densification rule	0.45	0.45
f_{post} for post liquefaction behavior	0.02	0.02
Corrected SPT blow counts $(N_1)_{60}$	6.5	37

The maximum value of EPWP at Point A is 12.38 kPa without any remedial measure, whereas with remedial measures, these values are being reduced to 9.04 (sheet piles) and 3.05 kPa (soil columns). At Point E (embankment-toe), no significant rise in EPWP has been observed in the case of the soil column. Predictions of EPWP at Locations E, F (below toe), and I (below centerline) during seismic excitation in the case of the model with sheet-pile measure are higher than corresponding values in the benchmark model. Although sheet piles are effective in controlling the displacements, they can act as a barrier in the drainage path and can increase time for dissipation of pore pressure. A very small rise in EPWP was observed in the model with soil column due to availability of drainage path for dissipation.

Phenomenon of EPWP buildup and dissipation are well captured in the predictions. The only significant discrepancy with the response is at Point I (below the centerline) for model with soil column. The central portion sandwiched between the two stone columns may act as a column of weaker strength. In the load-sharing mechanism, more load is shared by pore water as compared with the stone column, resulting in an increase in EPWP as compared with the plain model. At other locations, the computed EPWP was satisfactory. Hence, the stone column seems to be a better remedial measure as compared with the sheet pile.

3 Coupled Approach

In coupled numerical simulation, the analysis domain such as a liquefiable soil deposit is expressed by coupled field equations. These equations are solved by considering coupling between solid and fluid phase under dynamic loading (inertial coupling is an added advantage). A fully-coupled effective stress analysis accounts for the dynamic interaction between the solid and fluid phase. Resulting dynamic equilibrium equation in terms of total stresses and flow continuity equation can be coupled together. This results in two sets of governing equations. The primary variables in this form of equations are solid displacement and fluid pressure and known as *u–p* formulation.

For a saturated porous medium subjected to seismic loading, the dynamic equations of motion can be written solid phase and fluid phase as follows (Biot, 1956).

$$\mathbf{M}\ddot{\mathbf{q}} + \mathbf{K}\mathbf{q} - \mathbf{Q}\mathbf{p} = \mathbf{f_q} \tag{20}$$

$$\mathbf{G}\ddot{\mathbf{q}} + \mathbf{Q}^{\mathbf{T}}\mathbf{q} + \mathbf{S}\dot{\mathbf{p}} + \mathbf{H}\mathbf{p} = \mathbf{f_p} \tag{21}$$

In which, **K** and **M** are stiffness and mass matrices. **Q** is coupling matrix. **H** and **S** are permeability and compressibility matrices. **G** is dynamic seepage force matrix; $\mathbf{f_q}$ and $\mathbf{f_p}$ are force vector for the solid and fluid phase, respectively. **q** and **p** are displacement and pore pressure vectors. Dots over **q** and **p** indicate respective derivative

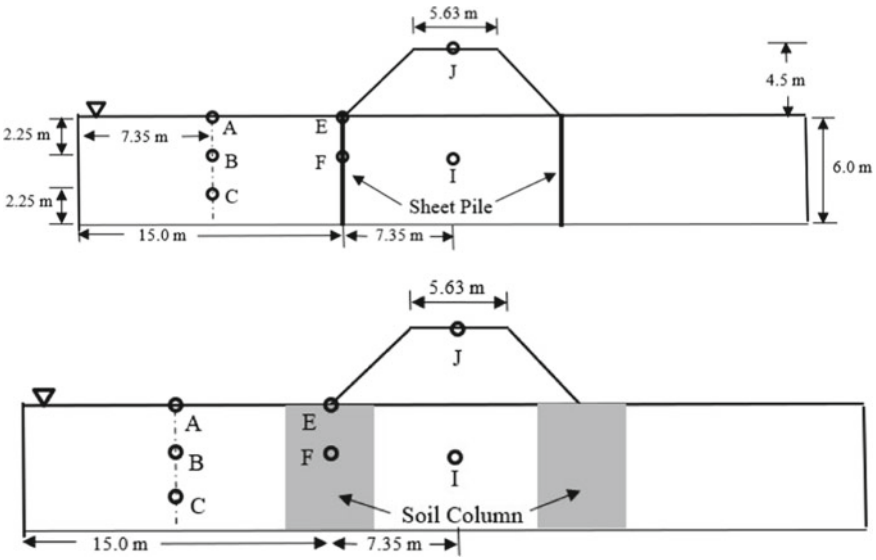

Fig. 1 Computed EPWP with time at different locations of foundation (after Bhatnagar et al. 2015)

with respect to time, which are expanded using implicit Newmark-beta method. The details of the implementation of time marching scheme in the present formulation are described in Kumari and Sawant (2021).

In the present study, the saturated loose sand layer of thickness 10 m, underlain by 4 m depth of gravel had been considered for numerical simulation (Fig. 1). Plane strain condition is assumed to reduce the computational efforts. The unbounded soil domain in *XZ* plane is discretized into 224 elements of uniform finite-infinite element mesh as shown in Fig. 3. The 8–4 Node mixed element having 8 displacement nodes and 4 pore pressure nodes satisfying the Babuska-Brezzi stability condition are used in finite element analysis. As a result, displacements are continuous biquadratic and pore pressures are continuous bilinear in the element. The soil domain was extended infinitesimally in the longitudinal direction and vertical direction. Hence, finite elements could be extended by attaching 5–4 Node mixed infinite elements, having 5 displacement nodes and 4 pore pressure nodes, at the horizontal and vertical boundary, whereas corner element should be extended by attaching 3-noded infinite elements (as shown in Figs. 3 and 4) as to appropriately model the infinite boundary conditions (Kumari & Sawant, 2021). Kelvin elements are attached to transmitting boundary. The purpose of Kelvin elements is to absorb the wave energy and prevent backpropagation of wave into the domain (Fig. 2).

Pastor–Zienkiewicz Mark III Model is working on the concept of effective stress principle. In the elastoplastic analysis, the total strain increment $\Delta\varepsilon$ is further separated into elastic strain $\Delta\varepsilon^{\mathrm{e}}$ and plastic strain components $\Delta\varepsilon^{\mathrm{p}}$ as $\Delta\varepsilon = \Delta\varepsilon^{e} + \Delta\varepsilon^{p}$. The relationships between incremental stress $\Delta\sigma$ and incremental strains $\Delta\varepsilon$ have been derived from the theory of generalized plasticity. This relationship is expressed

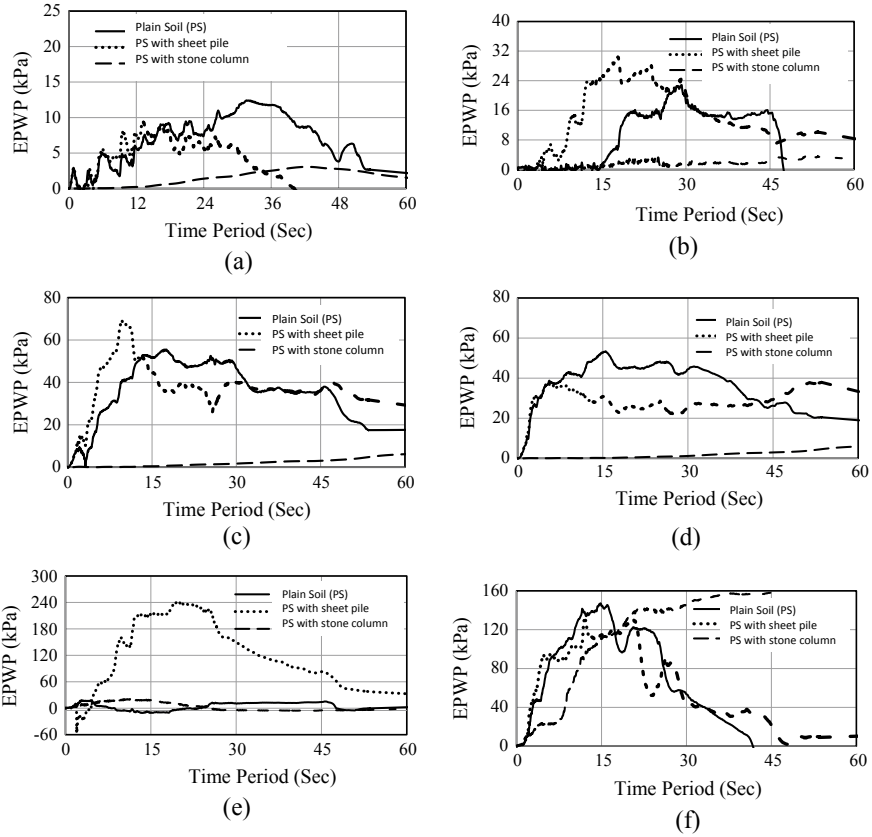

Fig. 2 Predicted EPWP versus time at **a** Point A **b** Point E **c** Point C **d** Point B **e** Point F **f** Point I

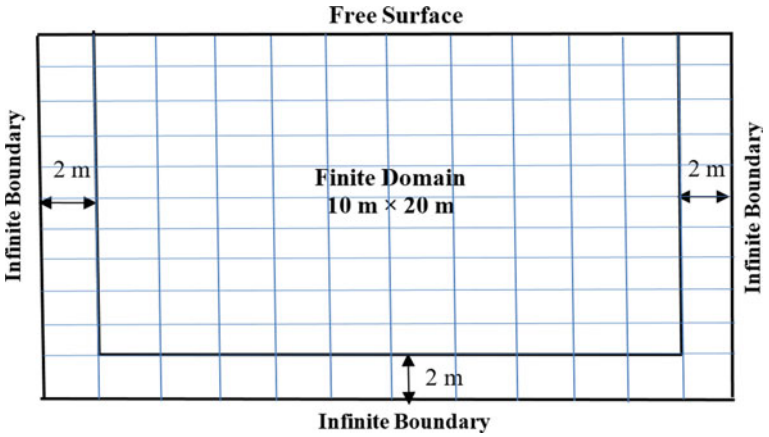

Fig. 3 Finite element mesh of soil domain

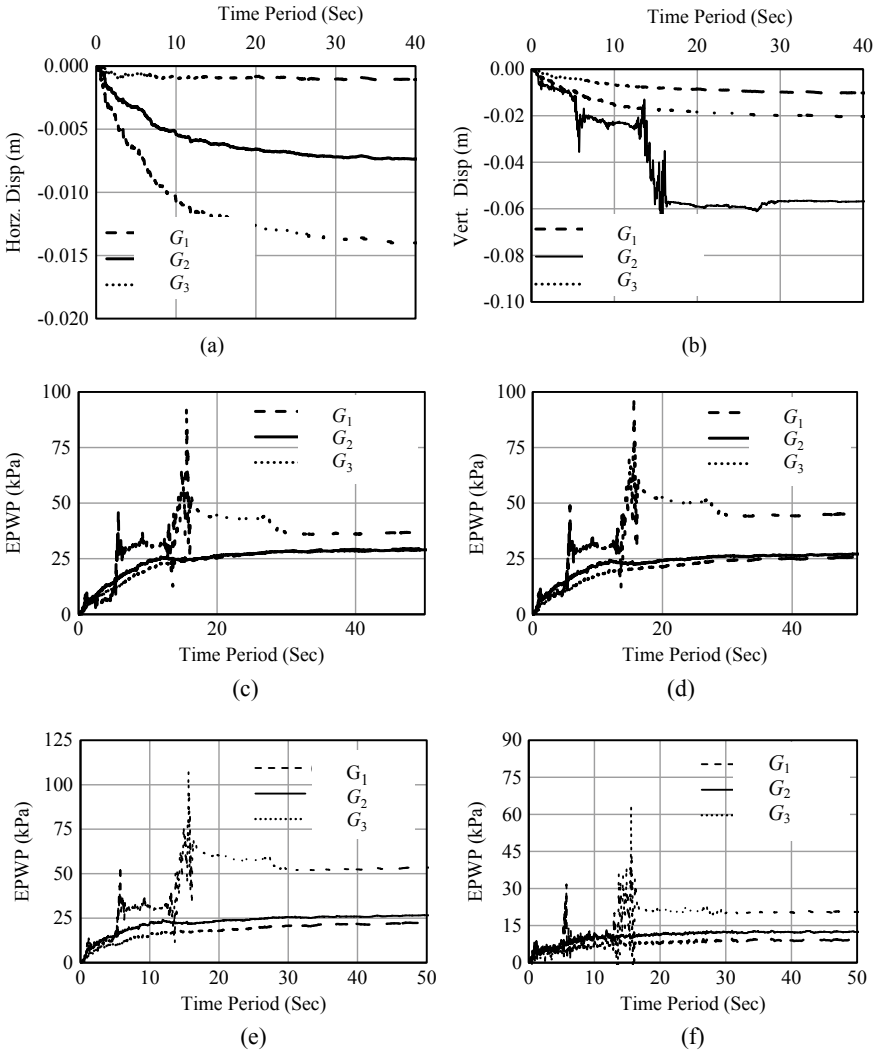

Fig. 4 Predicted displacement at top surfaces versus time **a–b** and EPWP versus time at depth of **c** 2 m **d** 4 m **e** 6 m and **f** 10 m depth for different soil modulus

as: $\Delta\sigma = D^{ep}\ \Delta\varepsilon$. In which, D^{ep} is elastoplastic constitutive matrix, respectively, defined by following relation as given by Zienkiewicz and Mroz (1984).

$$D^{ep} = D^{e} - \frac{D^{e} n_{gL/U} n^{T} D^{e}}{H_{L/U} + n^{T} D^{e} n_{gL/U}} \tag{22}$$

In which, D^e signifies the elastic constitutive matrix, n is vector of normal in loading direction, $n_{gL/U}$ is flow direction vector during loading or unloading condition, and $H_{L/U}$ is defined as loading or unloading plastic modulus. The other details of Pastor–Zienkiewicz Mark III Model have been given Appendix. Also, Pastor et al. (1990) prescribed the detailed description of procedure to evaluate parameters in Pastor–Zienkiewicz Mark III model. The parameter evaluation procedure is dependent of the drained monotonic, undrained monotonic and cyclic triaxial experimental results.

3.1 Numerical Study

A typical sketch of the finite element mesh incorporating various aspects such as transmitting boundary and unbounded domain is presented in Fig. 3. The size of soil domain is taken as 22 × 14 m in the present study. The dissipation of pore pressure was allowed to occur only through the top surface of the sand layer; while the lateral boundaries and the base were considered to be of infinite extent. Material properties of the purposed model are reported in Table 2. The variation of displacement and pore pressure with time at different nodes had been calculated using finite element code written in FORTRAN-90. The variation of both parameters with time was considered for comparing the response. The sand layer was fully saturated with water and excited at the base with El-Centro earthquake ground motion.

To study the effect of shear modulus on liquefaction, shear modulus G has been varied as $G_1 = 6$ MPa, $G_2 = 10$ MPa and $G_3 = 15$ MPa, while keeping other parameters constant. The present study has been carried out at $D_r = 40\%$, permeability of 6.6×10^{-5} m/s. The variations of displacement and excess pore pressure for different value of shear modulus have been shown in Fig. 4. A maximum value of horizontal displacement 1.4 cm has been observed at $G = 6$ MPa whereas a maximum value of 1.07 mm at $G_3 = 15$ MPa indicating 92% reduction. Similarly, a maximum value of vertical displacement 7.43 cm is noticed at $G_2 = 10$ MPa whereas a maximum value of 1.02 cm at $G_3 = 15$ MPa. Vertical displacements at $G_2 = 10$ MPa are higher than those at $G_1 = 6$ MPa. This may be attributed to the fundamental frequency of the domain may be close to operating frequency. At higher value of shear modulus ($G_3 = 15$ MPa), liquefaction does not occur within the soil domain except at a depth of 2 m (Fig. 4). As the shear modulus decreases, liquefaction phenomenon is observed because of generation of higher displacement and pore pressure resulting in reducing the effective stress at shallow depth of soil mass. At higher soil modulus, more loads will be shared by skeleton. This in turn reduces the excess pore pressure at each step.

4 Conclusion

The present developed model is able to predict reasonable changes in excess pore pressure occurring during earthquake loading, which can be useful for analyzing earth structures situated in the regions of moderate to high seismic zone. It allows the distribution of pore pressure and the effects that drainage and internal flow have on the time of liquefaction to be determined quantitatively. The comparison study directs that coupled analysis resembles more closely with the liquefaction phenomena as compared to uncoupled approach. Hence, the usual decoupled and factor of safety approach may not be considered as most appropriate in the analysis of such dynamic behavior.

Appendix

P-Z Mark III model takes into account the linear distribution of the stress ratio for approximating sand dilatancy (Nova & Wood, 1982).

$$d_g = \frac{d\in_v^p}{d\in_s^p} = \left(1 + \alpha_g\right)\left(M_g - \eta\right)$$

where $d\in_v^p$ and $d\in_s^p$ are plastic volumetric and deviatoric strains increments, respectively. M_g is correlated with the angle of friction (∅) as follows:

$$M_g = 6Ssin\varnothing/(3S - sin\varnothing)$$

The plastic potential surface relationship is evaluated as follows:

$$g = \left\{q - M_g p\left(1 + \frac{1}{\alpha}\right)\left[1 - \left(\frac{p}{p_g}\right)^{\alpha}\right]\right\}$$

The bounding or the yield surface is given as follows:

$$f = \left\{q - M_f p\left(1 + \frac{1}{\alpha}\right)\left[1 - \left(\frac{p}{p_c}\right)^{\alpha}\right]\right\}$$

where p and q are the mean effective and deviatoric stress, respectively; α and M_f are constants; M_g is slope of the critical state line and p_g and p_c are size parameters. Fig. shows the plastic potential and yield surface for the loose and dense sand, respectively.

Plastic Flow for Loading and Unloading

The loading plastic flow vector n_{gL} and unloading plastic flow vector n_{gu} are given as follows:

$$\eta_{gL} = \frac{1}{\sqrt{1+d_g}} \begin{Bmatrix} d_g \\ 1 \end{Bmatrix} and\ \eta_{gU} = \frac{1}{\sqrt{1+d_g}} \begin{Bmatrix} -|d_g| \\ 1 \end{Bmatrix}$$

The absolute sign is used in such a way that constant densification occurs during unloading and modeling of the liquefaction is done.

Plastic Modulus for Loading and Unloading

During loading phase, Pastor and Zienkiewicz (1986) have given the relationship for obtaining the plastic modulus as follows:

$$H_L = H_0 p H_f \{H_v + H_s\} H_{DM}$$

where H_0 is the intial plastic modulus for loading and other parameters are defined as follows:

$$H_f = \left(1 - \frac{\eta}{\eta_f}\right)^4 H_v = 1 - \frac{\eta}{M_g}$$

$$H_s = \beta_0 \beta_1 e^{-\beta_0 \xi} \xi = \int d\xi = \int \left| d\epsilon_q^p \right|$$

where $d\epsilon_q^p$ is the plastic shear strain.

Pastor et al. proposed the following relationship for the plastic unloading modulus $\mathrm{H_{U0}}$:

$$H_u = H_{u0} \left(\frac{M_g}{\eta_u}\right)^{\gamma_u} for \left|\frac{M_g}{\eta_u}\right| > 1$$

$$H_u = H_{u0} for \left|\frac{M_g}{\eta_u}\right| < 1$$

where η_{u} is the unloading stress ratio.

References

Aydingum, O., & Adalier, K. (2003). Numerical analysis of seismically induced liquefaction in earth embankment foundations. Part 1. Benchmark model. *Canadian Geotechnical Journal, 40*(4), 753–765.

Beaty, M., & Byrne, P. M. (1998). An effective stress model for predicting liquefaction behaviour of sand. In P. Dakoulas, M. Yegian, & R. Holtz, (Eds.), *Geotechnical earthquake engineering and soil dynamics*, vol. 75 (766–777). Reston, VA: Geotechnical Special Publication, ASCE.

Biot, M. A. (1956). Theory of propagation of elastic waves in a fluid-saturated porous solid. *Jorunal of Acoustical Society of America, 28*(2), 168–178.

Bhatnagar, S., Kumari, S., Sawant, V. A. (2015). Numerical analysis of earth embankment resting on liquefiable soil and remedial measures. *International Journal of Geomechanics*, ASCE, *16*(1), 04015029–1 to 13.

Cubrinovski, M., & Ishihara, K. (1999). Empirical correlation between SPT N-value and relative density for sandy soils. *Soils and Foundations, 39*(5), 61–71.

Finn, W. L.D., Martin, G. R., Byrne, P. M. (1976). Seismic response and liquefaction of sands. *Journal of the Geotechnical Engineering Division, ASCE*, *102*(8), 841–856.

Galavi, V., Petalas, A., & Brinkgreve, R. B. J. (2013). Finite element modelling of seismic liquefaction in soils. *Geotechnical Engineering Journal of the SEAGS & AGSSEA, 44*(3), 55–64.

Kumari, S., & Sawant, V. A. (2021). Numerical simulation of liquefaction phenomenon considering infinite boundary. *Soil Dynamics and Earthquake Engineering*, 142:106–556

Kumar, A., Kumari, S., & Sawant, V. A. (2020). Numerical investigation of stone column improved ground for mitigation of liquefaction. *International Journal of Geomechanics 20*(9):04020144. https://doi.org/10.1061/(ASCE)GM.1943-5622.0001758.

Kumari, S., Sawant, V. A., & Mehndiratta, S. (2018). *Effectiveness of stone column in liquefaction mitigation.* USA: Geotechnical Special Publication of ASCE, pp. 207–216.

Martin, G. R., Finn, W. D. L., & Seed, H. B. (1975). Fundamentals of liquefaction under cyclic loading. *Journal of the Geotechnical Engineering Division, ASCE, 101*(5), 423–438.

Nova, R., & Wood, D. M. (1982). A constitutive model for soil under monotonic and cyclic loading. In G. N. Pande & O. C. Zienkiewicz (Eds.), *Soil Mechanics-Transient and Cyclic loads* (pp. 343–373). New York: John Wiley & Sons Ltd.

Pastor, M., & Zienkiewicz, O. C. (1986). A generalized plasticity hierarchical model for sand under monotonic and cyclic loading. In *Proceedings of the 2nd International Symposium on Numerical Models in Geomechanics* (Vol. 5, No. 1), pp. 141–150.

Pastor, M., Zienkiewicz, O. C., & Chan, A. H. C. (1990). Generalized plasticity and the modeling of soil behavior. *International Journal for Numerical and Analytical Methods in Geomechanics, 14*(3), 151–190.

Puebla, H., Byrne, P. M., & Phillips, P. (1997). Analysis of canlex liquefaction embankments prototype and centrifuge models. *Canadian Geotechnical Journal, 34*(5), 641–657.

Taiebat, M., Shahir, H., & Pak, A. (2007). Study of pore pressure variation during liquefaction using two constitutive models for sand. *Soil Dynamics Earthquake Engineering, 27*, 60–72.

Taiebat, M., Jeremic, B., Dafalias, Y. F., Kaynia, A. M., & Cheng, Z. (2010). Propagation of seismic waves through liquified soils. *Soil Dynamics and Earthquake Engineering, 30*(4), 236–257.

Tokimatsu, K., & Seed, H. B. (1987). Evaluation of settlements in sands due to earthquake shaking. *Journal of Geotechnical Engineering, ASCE*, *113*(8), 861–878.

Zienkiewicz, O. C., Chan, A. H. C., Pastor, M., Schrefler, B. A., & Shiomi, T. (1999). *Computational geomechanic: With special reference to earthquake engineering*. Wiley.

Zienkiewicz, O. C., & Shiomi, T. (1984). Dynamic behaviour of saturated porous media; the generalized Biot formulation and its numerical solution. *International Journal for Numerical Methods in Engineering*, 8, 71–96.

Zienkiewicz, O. C., & Mroz, Z. (1984). Generalized plasticity formulation and applications to geomechanics. In C. S. Desai & R. H. Gallagher (Eds.), *Mechanics of engineering materials* (pp. 655–679). New York: Wiley.

Region Specific Consideration for GMPE Development, Representative Seismic Hazard Estimation and Rock Design Spectrum for Himalayan Region

P. Anbazhagan and Ketan Bajaj

1 Introduction

The current seismic hazard analysis (SHA) of any earthquake-prone area is practically bending towards the development and selection of a regional ground motion prediction equation (GMPE). Additionally, improvement in the seismic networks and geophysical testing resulted in the advancement of the functional form of GMPE by incorporating various site and source parameters. GMPE models describe the distribution of ground motion in terms of median and logarithmic standard deviation (Strasser et al., 2009). The general procedure used in developing any GMPE is the regression analysis of the ground motion recordings either from past events or stochastic simulation. To date, various guidelines and tools are available for selecting a suitable GMPE for any seismic study area. Despite the availability of various methods and criteria for choosing an appropriate GMPE (Cotton et al., 2006; Scherbaum et al., 2009) for many practical applications, there exists an important issue regarding the applicability of a GMPE developed for one region to another region. A vital step in any SHA is the selection of suitable GMPEs based on the region-specific parameters. GMPEs are widely used for predicting the level of ground shaking in terms of Peak Ground Acceleration (PGA), Spectral Acceleration (SA) etc., corresponding to magnitude (moment magnitude, in most of the cases), distance (epicentral or hypocentral), site condition and type of faulting of any site. The essential element of any Probabilistic Seismic Hazard Analysis (PSHA) is an integration of a suitable ground motion model for the determination of ground motion parameters of a given site for each earthquake scenario.

P. Anbazhagan (✉)
Department of Civil Engineering, Indian Institute of Science, Bengaluru, Karnataka, India
e-mail: anbazhagan@iisc.ac.in

K. Bajaj
Swiss Re, Bangalore, Karnataka, India
e-mail: ketan_bajaj@swissre.com

T. G. Sitharam et al. (eds.), *Advances in Earthquake Geotechnics*, Springer Tracts in Civil Engineering, https://doi.org/10.1007/978-981-19-3330-1_7

To date, various GMPEs exist worldwide for the determination of seismic hazards at bedrock or ground surface for various tectonic regions, and these GMPEs are compiled by Douglas (2020). Various authors (Anbazhagan & Kumar, 2013; Bajaj and Anbazhagan 2019b; Das et al., 2006; Gupta, 2010; Iyengar & Ghosh, 2004; Nath et al., 2005, 2009; NDMA, 2017; Ramkrishnan et al., 2020; Sharma & Bungum, 2006; Sharma et al., 2009; Singh et al., 1996) have proposed different GMPEs for the Indian subcontinent. NGA-West 2 project has developed a series of ground motions for the tectonically active region of the shallow crustal earthquakes. These GMPEs are proposed by Abrahamson et al. (2014), Boore et al. (2014), Campbell and Bozorgnia (2014), Chiou and Youngs (2014), and Idriss (2014). Recently, Akkar et al. (2014) and Bindi et al. (2014) have developed new GMPEs for the Pan-European region. Moreover, Zhao et al. (2016a, b, c, d) have developed four new GMPEs for Japan by differentiating the subduction interface earthquakes, subduction slab earthquakes, and shallow crustal and upper mantle earthquakes. Zhao et al. (Zhao et al., 2016) method is being used in different hazard analysis studies around the world, especially for subduction tectonic regimes. The GMPEs developed for the NGA-west, and Japan region is widely used to determine seismic hazard for the various regions of the Indian Subcontinent. The attenuation characteristic of the seismic waves for the Himalayan region is different as compared to the western US and Japan (Bajaj, 2018). Hence, identifying proper GMPEs and arriving shape of the design spectrum for the shallow crustal region of the seismically active Himalayan subduction region is mandatory.

In this study, we collected available recorded earthquake data from the Himalayan region. Then these data are processed and used to identify the best possible GMPEs functional form. Further, applicable GMPEs are reviewed and identified as suitable GMPEs for the Himalayan region with the estimation of ranks and weights by adopting a segmented distance of <100 km, 100–300 km, and >300 km as per Anbazhagan et al. (2015). Available recorded data are further used to arrive a cutoff period for acceleration, velocity, and displacement sensitive regions, thereby developing smoothed and normalized design spectrum shape for the Himalayan region.

2 Seismic Data and Study Area

Instrumented seismic ground motion records are valuable data to understand many seismological, seismotectonic, and engineering aspects of the earthquake in the region. Even though the Himalayan region has a very long history of seismic activity and catastrophic earthquakes, systematic seismic instrumentation in the Himalayan region and data available for researchers are started very recently. The strong motion data is collected from the strong motion instrumentation network of the Indian Institute of Technology, Roorkee (IITR) and also from Virtual Data Center (VDC). A detailed description of these strong motion accelerographs and data processing of the waveforms are given in Kumar et al. (2012) and Bajaj and Anbazhagan (2019b). Out

of the total 520 seismic ground motion recordings, 252 were collected from the IITR, 68 seismic ground motions recorded before 2005 were collected from VDC, and the rest 200 from the Indian seismic and GNSS network. Out of 520 recordings, 241 are rock recordings, and the remaining 279 are soil recordings. Only rock recordings are used in the present study. The processing of strong-motion data involves baseline-correction, instrumental scaling, and frequency filtering. The strong motion database is processed according to the procedure suggested by Boore and Bommer (2005). The earthquake occurred between 1988 and 2015 with a moment magnitude (Mw) of 4.5–7.8, and a hypocentral distance of 10–500 km was complied. Figure 1 shows the location of the seismic station and the earthquake data collected. These stations cover the Indian Himalayan range from Jammu and Kashmir to Meghalaya. Most of the available recorded earthquakes in the Himalayan region were collected, which cover the Western Part, Central Part, and Eastern Part of North India. This region is responsible for an earthquake disaster in India's northern part and the north side of the Indo-Australian plate boundary and subduction zone.

Each earthquake record consists of 3 component records of velocity/acceleration time histories. Anbazhagan et al. (2016b) compiled earthquakes above Mw of 5.0 with an isoseismal map and generated a relationship between Intensity and ground motion and spectral parameters for the Himalayan region. These relations are useful to estimate ground motion and spectral parameters from intensity values, which help to account for old intensity values in seismicity and predict future seismic hazard values. These seismic stations were classified based on the geology of the region,

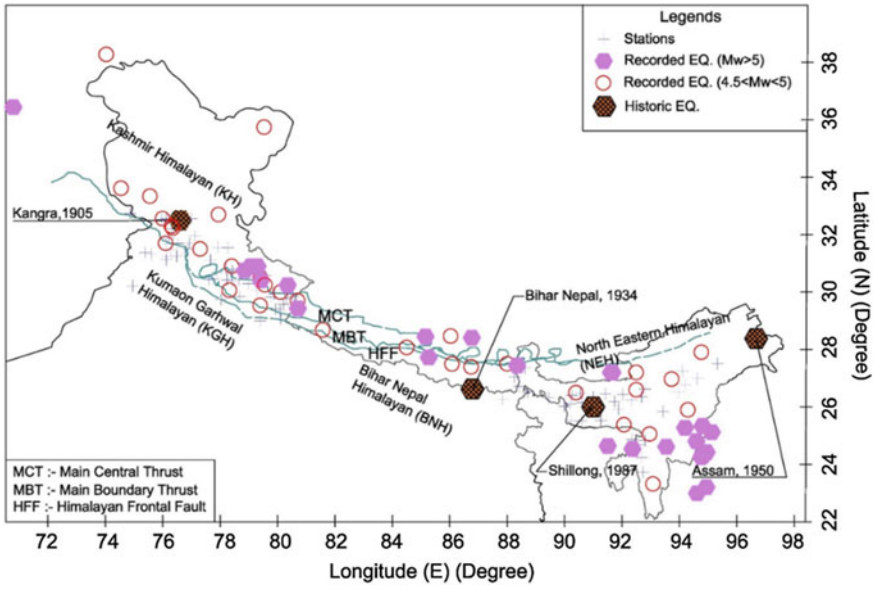

Fig. 1 The recorded database was used in developing the new ground-motion prediction for the Himalayan region (after Bajaj and Anbazhagan 2019b)

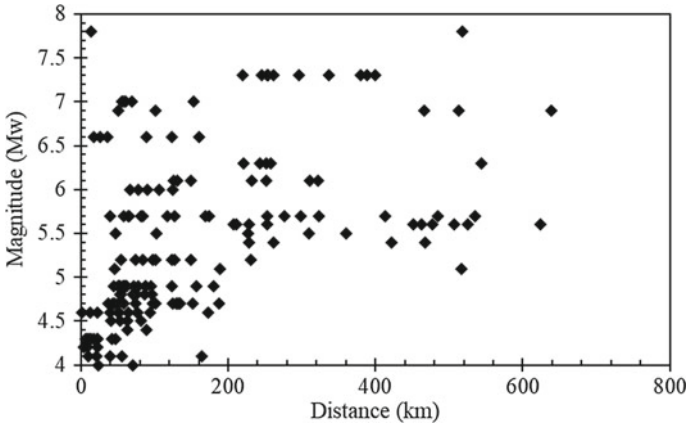

Fig. 2 Rock site recorded ground motions data used in the study

and no site-specific data were used to characterize them as rock and soil stations. So, Anbazhagan et al. (2019) analysed data systematically, processed by applying baseline-correction and band-pass-filter between 0.75 and 0.9 Hz and 25–27 Hz. These data are used to extract time-domain parameters of peak acceleration/velocity and frequency domain parameters of the corner and cutoff frequencies and predominant frequency through H/V ratio. More about data and seismic station classification can be found in Anbazhagan et al. (2019). Figure 2 shows a plot of rock site data used in the study. These data are further used to identify GMPE functional form, select GMPEs for seismic hazard analysis, and drive the design spectrum for the HR.

3 Functional Form and New GMPE

GMPE of the region should reflect the wide range of magnitude, distance, directivity, fault type, etc., to serve various engineering requirements. GMPE model must account for magnitude dependence and saturation, as well as attenuation of stress waves with distance due to spreading and material damping. So GMPE functional form used to regress the recorded data should fulfil the above essential requirement. Many explanatory parameters are necessary for GMPE functional form; that is why NGA-West 2 GMPEs are more complex. Various researchers have used different functional forms for capturing magnitude and distance scaling in GMPEs. To examine the applicability of available functional forms for the Himalayan region where a less recorded strong motion database is available, we reviewed available GMPEs. To date, various GMPEs developed worldwide for the determination of seismic hazards at bedrock or surface for various tectonic regions, and these GMPEs are compiled by Douglas (2020). Douglas started compiling GMPEs from 2000 onwards and group them based on several criteria with highlighted applicability and limitations. He is

updating every year and publishing reports on GMPEs (http://www.gmpe.org.uk/), a recent report is Douglas (2020). Applicable GMPEs for the Himalayan region (HR) were summarized by Bajaj and Anbazhagan (2021a) and they are updated here. Table 1 shows these applicable GMES for HR with the short form.

HR GMPEs can be divided into two major groups i.e., developed for HR, India, and developed elsewhere (NGA-West 2, Pan-European, and Japan GMPEs), applicable to HR. GMPEs applicable for HR can be grouped as magnitude scaling and distance scaling based on functions used in the GMPEs. Recorded rock site data is used to get GMPE coefficients for different functional forms applicable to the HR region. Further, the compatibility of various functional forms for distance and magnitude scaling using the mixed-effect regression of residual calculated from different functional forms. Based on that, uncertainties have been evaluated concerning distance and magnitude ranges within the event and between events. The whole algorithm and different functional form used is explained in detail and presented in Bajaj and Anbazhagan (2018, 2019a). Based on region-specific analysis and data, the representing functional form of HR is given below:

$$lnY = a_1 + a_2(M - 6) + a_3(9 - M)^2 + a_4 \ln R + a_m \ln R(M - 6) + a_7 R + \sigma \quad (1)$$

where, lnY, M, R, and σ are respectively logarithm of ground motion, magnitude, hypocentral distance, and standard deviation and a_1, a_2, a_3, a_4, a_m and a_7 are the corresponding regression coefficients. The coefficient a_m is equal to a_5 when $M_w < 6.0$ and $R < 300$, else is equal to a_6. It can be noted here that many of GMPE developed for HR considering functional form other than Eq. (1) has a considerable bias. PGA is more biased in the case of AN13, NA09, and SH09 as compared to NDMA10 and GU10. In some cases, like ID14, CY14, NDMA10, and AN13, bias is less for long periods. Many recent GMPEs not developed for HR have less bias than GMPEs developed for HR. Hereby we suggest any GMPEs for HR can be developed by considering the functional form given in Eq. (1).

3.1 Regional Seismotectonic Parameters and GMPE

The Himalayan region has a smaller number of GMPEs when compared to similar active seismic areas in the world. Moreover, most GMPEs are developed with lots of assumptions or seismotectonic parameters of another region in the world. This may be due to a smaller number of recorded earthquake data in the region. Anbazhagan et al. (2013) summarized GMPEs developed up to 2013 for HR and widely used GMPEs in HR studies but not developed for the region. The authors concluded that most of the GMPEs developed for the HR area are only applicable for limited range magnitude and distance. GMPEs developed for HR are incapable of predicting hazard values close to highly ranked GMPEs for the entire distance range of interest. Also, many of HR GMPEs were developed using seismological model parameters

Table 1 Available GMPEs considered for seismic hazard analysis of the IGB

S. no	GMPE	Abbreviation	Magnitude range	Distance range
Himalayan GMPE				
1	Singh et al. (1996)	SI_96	5.7–7.2	≤100
2	Iyengar and Gosh (2004)	IYGO_05	5.0–8.0	≤100
3	Nath et al. (2005)	NA_05	3–8.5	≤100
4	Sharma and Bungum (1459)	***SHBU_06***	5.5–7.2	≤300
5	Das et al. (2006)	DA_06	4.6–7.6	≤200
6	Nath et al. (2009)	***NA_09***	4.8–8.1	≤ 100
7	Sharma et al. (2009)	***SH_09***	5.2–6.9	≤100
8	NDMA (2017)	***NDMA_10***	6.3–7.2	150–375
9	Gupta (2010)	GU_10	4–8.5	≤500
10	Anbazhagan et al. (2013)	***AN_13***	5.3–8.7	≤300
11	Bajaj and Anbazhagan (2019b)	***BAN_19***	4.0–9.0	≤750
12	Ramabhadran et al. (2020)	RAM_20	4.2–6.9	<640
Similar region GMPE				
13	Abrahamson and Litehiser (1989)	ABLI_V_89	5–8	≤100
14	Abrahamson and Litehiser (1989)	ABLI_H_89		
15	Youngs et al. (1997)	YO_97	≥ 5	10–500
16	Campbell (1997)	CAM_H_97	4–7.8	3–60
17	Campbell (1997)	CAM_V_97		
18	Spudich et al. (1999)	SP_99	5–7.7	≤200
19	Atkinson and Boore (2003)	ATB_03	≥ 6.5	40–200
20	Takahashi et. al. (1271)	TA_04	5–8.3	≤300
21	Ambraseys et al. (2005)	AMB_05	> 5.0	≤100
22	Kanno et al. (2006)	***KA_06***	≥ 5.5	≤200
23	Zhao et al. (Zhao, Zhang, et al., 2016)	***ZH_06***	5–8.0	≤200
24	Campbell and Bozorgnia (2008)	CABO_08	4.0–8.5	≤200
25	Idriss (2008)	ID_08	4–8.0	≤200
26	Boore and Atkinson (2008)	BOAT_08	5–8	≤200
27	Chiou and Youngs (2008)	CY_08	4.0–8.5	≤200 km
28	Abrahamson and Silva (2008)	ABSI_08	5–8.5	≤200
29	Lin and Lee (2008)	LL_08	5.2–7.9	≥60
30	Cauzzi and Faccioli (2008)	***CAFA_08***	5.0–6.9	
31	Aghabarati and Tehranizadeh (2009)	AGTH_08_09_H	5.3–8.1	15–630

(continued)

Table 1 (continued)

S. no	GMPE	Abbreviation	Magnitude range	Distance range
32	Aghabarati and Tehranizadeh (2009)	AGTH_08_09_V		
33	Akkar and Bommer (2010)	AKBO_10	5–7.6	≤100
34	Akkar et al. (2014)	***AK_14***	4.0–8.0	≤200
35	Bindi et al. (2014)	***BI_14***	4.0–7.6	≤300
36	Abrahamson and Silva (2014)	***ABSI_14***	3.0–8.5	≤300 km
37	Boore et al. (2014)	***BA_14***	3.0–8.5	≤400 km
38	Campbell and Bozorgnia (2014)	***CABO_14***	3.0–8.5	≤500
39	Chiou and Youngs (2014)	***CY_14***	3.0–8.0	≤100 km
40	Akkar and Sandikkaya (2014)	***ID_14***	≥ 5.0	≤100 km
41	Zhao et al. (2016a)	ZH_16_SI	4.5–8.0	≤300 km
42	Zhao et al. (2016b)	ZH_16_SS	4.5–8.0	≤300 km
43	Zhao et al. (2016c)	***ZH_16_CM***	4.5–8.0	≤300 km

developed in other countries. Bajaj and Anbazhagan (2019b) tried for the first time to estimate seismological model parameters using HR region earthquake data discussed earlier. Authors derived geometric spreading and an elastic attenuation using Fourier Amplitude Spectrum (FAS) by dividing HR as Kashmir Himalayan (KH), Kumaon-Garhwal Himalayan (KGH), Bihar-Nepal Himalaya (BNH), and Northeastern part of the Himalayan region (NEH). The stress drop and duration model for HR was established first time using available data. A stress drop was observed with a kink point at 5.5 Mw through the bilinear model. Regional recorded data shows that the duration model broke at 60 km hypocentral distance and helped arrive first time duration model beyond 700 km. Here, the authors also proved that Japan and California's widely used duration model is nowhere close to the regional model. Most of the existing duration models are applicable only up to 300 km. Bajaj and Anbazhagan (2019b) systematically arrived at seismotectonic parameters for most of the historic major earthquakes in HR from literature and calculation.

Even though we have a good amount of data (Fig. 2) to arrive at the seismotectonic parameters of the region still, these are insufficient to cover the entire spectrum of magnitudes and distances required for GMPE development. It can also be noted that many seismologists highlighted the seismic gaps in the study area. Bilham (2015) studied the potential slip in the range of 9–14 m with the expected earthquake as large as 8.9 Mw in the Kashmir Himalayan region. Moderate earthquakes with Mw > 6 that have occurred from 1900 to 2000 in the Kumaon- Garhwal Himalayan region reflect the high seismicity in the area and the possibility of recurrence of large earthquakes in the future (Srivastava et al., 2015). Srivastava et al. (2015) demarked the whole Himalayan region into 10 seismic gaps by studying the micro-seismicity, paleo-seismicity, Global Positioning System, and variation in local tectonics. They

concluded that the Himalayan region is not equally seismogenic to produce a magnitude of 8.5 Mw and above. Here it is very clear that HR has many potential sources that can cause greater earthquakes above Mw of 8 and may results in several seismic geohazards in the Himalayan and Indo-Gangetic Basin (IGB) beyond 300 km. Table 1 and Fig. 2 clearly show that region-specific robust GMPEs are available up to 2019 for the region to arrive at possible future seismic hazards. Bajaj and Anbazhagan (2019b) systematically complied seismotectonic parameters of different past earthquakes and used them to simulate ground motion by adopting Motazedian and Atkinson (2005) procedure by considering new seismological model parameters arrived from regional data. The authors initially simulated time history at recorded seismic stations and validated, then repeated the same 0.1-unit step distance for a distance of 10–750 km by adopting the apparent station concept. The mixed-effect regression analysis was carried out by authors considering the combined set of recorded and region-specific simulated data using the GMPE functional form given in Sect. 2. Figure 3 shows the comparison of new GMPEs with existing GMPEs widely used in hazard analysis of HR for the major Magnitude of 8.7 (maximum reported 1950 Assam–Tibet earthquake) for rock level. This can be observed that the current GMPE is predicting SA values in between crustal GMPEs developed by NGA. NDMA10 (2017) is a widely used GMPE in most of the hazard studies in India and predicts low values for large earthquakes compared to HR GMPEs.

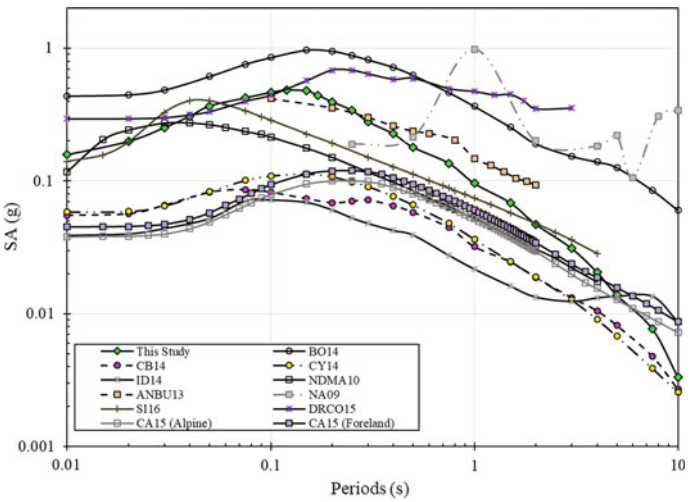

Fig. 3 Comparison of new GMPEs with other active crustal GMPEs for magnitude of 8.7 and hypocentral distance of 150 km

4 Ranks and Weights of GMPEs for HR

Predictive models/equations for peak ground and spectral acceleration are a requirement for seismic hazard analysis. Most representatives of such equations for HR are less when compared to the similar seismically active regions in the world. In this study, in order of rank and weight GMPEs applicable to HR using recorded data, we have updated compiled GMPEs by Anbazhagan et al. (2013) and also recently developed in the region by Bajaj and Anbazhagan (2019b). Even though, as of now, 15 GMPEs were developed for the study area, only 4 GMPEs marked can be used for both deterministic and probabilistic Seismic Hazard Analysis (SHA) within the specified applicable range. Among these 43 GMPEs, only marked in italic bold in Table 1 can be used to arrive uniform hazard spectrum as other GMPEs don't have coefficients for spectral acceleration at a different period. Table 2 shows GMPEs applicable to the study with spectral acceleration coefficient for the zero period. In order to model uncertainty through a logic tree approach, we need a larger number of GMPEs, so it is necessary to include applicable GMPEs developed for similar seismotectonic regions.

Narrowing down the most appropriate GMPEs to the region is essential for reliable SHA and representative PGA and SA estimation. Various authors have given quantitative (Delavaud et al., 2009; Scherbaum et al., 2009) and qualitative (Bommer et al., 2010; Cotton et al., 2006) approaches for selecting the GMPE. In this study, both approaches are used. In total, 43 GMPEs are considered suitable for the HR for the analysis using the criteria proposed by Bommer et al. (2010). Scherbaum et al. (2009) and Delavaudet al. (2009) defined an information-theoretic approach that makes use of average sample log-likelihood (LLH) for ranking the available GMPE of a study area. LLH is defined as

$$LLH(g, x) = -\frac{1}{n}\sum_{i=1}^{n} log_2(g(x_i)) \tag{3}$$

where, $x = \{x_i\}, i = 1, \ldots, \mathrm{N}$ are the empirical data and $g(x_i)$ is the likelihood that model g has produced the observation x_i. Here g is the probability density function given by GMPE to predict the observation produced by an earthquake with a magnitude M_w and distance R for the source (Delavaud et al., 2012). LLH values are used to rank the GMPEs and the low LLH value indicates a better ranking. Further, to determine the weight of each GMPE, Delavaudet al. (2012) defined the weight factor and data support index (DSI). The weight and DSI are defined as

$$w_i = \frac{2^{-LLH(g_i,x)}}{\sum_{k=1}^{n} 2^{-LLH(g_i,x)}} \tag{4}$$

$$DSI_i = 100\frac{w_i - w_{unif}}{w_{unif}} \tag{5}$$

Table 2 List of GMPEs used in the study for LLH calculations

Sl no.	Abbreviation of the equation	Standard form of equation	Coefficients value for zero periods
1	SHBU-06	$\ln(A) = c_2 M - \text{bln}\left[X + exp^{(c_3 M)}\right]$, Where, A is spectral acceleration in g	$c_2 = 0.8295$, $b = 1.2$, $c_3 = 0.5666$
2	NATH-09	$\ln(PSA) = c_1 + c_2 M + c_3 (10 - M)^3 + c_4 \ln\left(r_{rup} + c_5 exp^{c_6 M}\right)$, Where, PSA is peak spectral acceleration in g	$c_1 = 9.143$, $c_2 = 0.247$, $c_3 = -0.014$, $c_4 = -2.697$, $c_5 = 32.9458$, $c_6 = 0.0663$
3	SH-09	$\log(A) = b_1 + b_2 M + b_3 \log\left(\sqrt{R_{JB}^2 + b_4^2} + b_5 S + b_6 H\right)$, Where, A is spectral acceleration in m/s^2	$b_1 = 1.0170$, $b_2 = 0.1046$, $b_3 = -1.0070$, $b_4 = 15$ km, $b_5 = -0.0735$, $b_6 = -0.3068$ S = 1 for rock site and 0 for other case, H = 1 for strike slip mechanism and 0 for other cases
4	NDMA-10	$\ln(PSA) = c_1 + c_2 M + c_3 M^2 + c_4 R + c_5 ln\left[R + c_6 exp^{(c_7 M)}\right] + c_8 \ln(R) f_o$ Where, PSA is peak spectral acceleration in g, $f_o = \max(\ln\left(\frac{R}{100}\right), 0)$	$c_1 = -3.7438$, $c_2 = 1.0892$, $c_3 = 0.0098$, $c_4 = -0.0046$, $c_5 = -1.4817$, $c_6 = 0.0124$, $c_7 = 0.9950$, $c_8 = 0.1249$

(continued)

Table 2 (continued)

Sl no.	Abbreviation of the equation	Standard form of equation	Coefficients value for zero periods
5	ANBU-13	$\log(y) = c_1 + c_2 M - b log\left(X + e^{c3M}\right) + \sigma$ Where y is SA in g, X is the hypocentral distance in km	$c_1 = -1.283$, $c_2 = 0.544$, $c_3 = 0.381$, $b = 1.792$
6	ZH_06	$\ln(y) = aM + bX - \ln(r) + e(h - h_c)\delta_h + F_R$ $r = X + cexp^{(dM)}$ Where, y is peak spectral acceleration in cm/s^2	$a = 1.101$ $b = -0.00564$ $c = 0.0055$ $d = 1.080$ $e = 0.01412$
7	KA_06	If d < = 30 km $\log(\text{Pre}) = \text{a}_1\text{M} + \text{b}_1\text{X} - \log\left(\text{X} + \text{d}_1.10^{\left(\text{e}^1\text{M}_\text{W}\right)}\right) + c_1$ If d > 30 km $\log(\text{Pre}) = \text{a}_2\text{M} + \text{b}_2\text{X} - \log(\text{X}) + c_2$ Where Pre is peak spectral acceleration in cm/s^2	$a_1 = 0.56$ $b_1 = -0.0031$ $c_1 = 0.26$ $d_1 = 0.0055$ $e_1 = 0.37$ $c_2 = 1.56$ $a_1 = 0.41$ $b_1 = -0.0039$
8	CAFA_08	$\log_{10} y = a_1 + a_2 M_w + a_3 \log_{10} R + a_B S_B + a_C S_C + a_D S_D$ Where, y is in m/s^2 A – Rock like $V_{s30} > 800$\;m/s, $S_B = S_C = S_D = 0$ B – Stiff ground $360 \leq V_{s30} < 800$\;m/s, $S_B = 1$, $S_C = S_D = 0$ C – $180 \leq V_{s30} < 360$\;m/s $S_B = 0$, $S_C = 1$,$S_D = 0$ D – Very soft ground $V_{s30} < 180$\;m/s, $S_B = 0$, $S_C = 0$,$S_D = 1$	$a_1 = -1.296$ $a_2 = 0.556$ $a_3 = -1.582$ $a_B = 0.22$ $a_C = 0.304$ $a_D = 0.332$

(continued)

Table 2 (continued)

Sl no.	Abbreviation of the equation	Standard form of equation	Coefficients value for zero periods
9	AK_14	$\ln Y = \ln Y_{Ref} + \ln S + \varepsilon\,\sigma$ $\ln Y_{REF} = \begin{cases} a_1 + a_2(M-6.75) + a_3(8.5-M)^2 + [a_4 + a_5(M-6.75)] \\ \quad \ln\sqrt{R^2 + a_6^2} + a_8 F_N + a_9 F_R + SM_w \le 6.75 \\ a_1 + a_7(M-6.75) + a_3(8.5-M)^2 + [a_4 + a_5(M-6.75)] \\ \quad \ln\sqrt{R^2 + a_6^2} + a_8 F_N + a_9 F_R + SM_w > 6.75 \end{cases}$ $\ln S = \begin{cases} b_1 \ln(V_{s30}/V_{REF}) + b_2 \ln\left[\frac{PGA_{REF} + c(V_{s30}/V_{REF})^n}{(PGA_{REF}+c)(V_{s30}/V_{REF})^n}\right] \quad for \quad V_{s30} \le V_{REF} \\ b_1 \ln\left[\frac{min(V_{s30}, V_{CON})}{V_{REF}}\right] \quad for \quad V_{s30} > V_{REF} \end{cases}$ Where, Y is in g $\ln S$ = is the non-linear site amplification factor R may be R_{JB}, R_{epi} or R_{hyp} and according the coefficient varies For strike-slip fault, $F_N = F_R = 0$ For Normal fault, $F_N = 1$, $F_R = 0$ For reverse fault, $F_N = 0$, $F_R = 1$ Φ, τ and σ are intra-event, inter-event and total standard deviation respectively $PGA_{REF} = \begin{cases} 0.273722398 \text{ for } R_{JB} \\ 0.418813071 \text{ for } R_{epi} \\ 0.579508611 \text{ for } R_{hyp} \end{cases}$	$a_1 = 3.26685$ $a_2 = 0.0029$ $a_3 = -0.04846$ $a_4 = -1.47905$ $a_5 = 0.2529$ $a_6 = 7.5$ $a_7 = -0.5096$ $a_8 = -0.1091$ $a_9 = 0.0937$ $b_1 = -0.41997$ $b_2 = -0.28846$ $\Phi = 0.6475$ $\tau = 0.3472$ $\sigma = 0.7347$ $V_{REF} = 1000$ $V_{CON} = 750$ $c = 2.5$ $n = 3.2$

(continued)

Table 2 (continued)

Sl no.	Abbreviation of the equation	Standard form of equation	Coefficients value for zero periods
10	BI_14	$\ln Y = e_1 + F_D + F_M + F_s + F_{sof}$ $F_D = [c_1 + c_2(M - 5.5)]\log\left(\sqrt{R^2 + h^2}/R_{REF}\right) - c_3\left(\sqrt{R^2 + h^2} - R_{REF}\right)$ $F_M = \begin{cases} b_1(M - 6.75) + b_2(M - 6.75)^2 \text{ for } M_W \leq 6.75 \\ b_3(M - 6.75) \text{ for } M_W \leq 6.75 \end{cases}$ $F_{sof} = f_j E_j$ Where, j = 1,2,3 and 4 for normal, reverse, strike-slip and unspecified faults $F_S = \gamma\log(V_{S30}/800)$ if V_{S30} is used $F_S = s_j C_j$ if used site class is used Where, C_j is the dummy variable J = 1, 2, & 4 for site class A,B,C&D $C_j = 0$ R = R_{JB}, i.e., Joyner-Boore distance $R_{REF} = 1$ km	$e_1 = 3.45078$ $c_1 = -1.36061$ $c_2 = 0.215873$ $c_3 = 0.000733$ $h = 6.14717$ $b_1 = -0.02087$ $b_2 = -0.07224$ $b_3 = 0$ $f_1 = -0.03228$ $f_2 = 0.073678$ $f_3 = -0.01943$ $f_4 = 0$ $\tau = 0.180904$ $\phi = 0.276335$ $\sigma = 0.330284$ $s_1 = 0$ $s_2 = 0.137715$ $s_3 = 0.233048$ $s_4 = 0.214227$

(continued)

Table 2 (continued)

Sl no.	Abbreviation of the equation	Standard form of equation	Coefficients value for zero periods
11	ABSI_14	$\ln Sa = f_1 + F_{RV} f_7 + F_N f_{11} + f_5 + F_{HW} f_4 + f_6 + f_{10} + Regional$ $f_1 = \begin{cases} a_1 + a_5(M - M_1) + a_8(8.5 - M)^2 + [a_2 + a_3(M - M_1)]\ln R + a_{17} r_{rup} \\ M \geq M_1 \\ a_1 + a_4(M - M_1) + a_8(8.5 - M)^2 + [a_2 + a_3(M - M_1)]\ln R + a_{17} r_{rup} \\ M_2 \leq M < M_1 \\ a_1 + a_4(M_2 - M_1) + a_8(8.5 - M)^2 + a_6(M - M_2) + a_7(M - M_2)^2 + \\ [a_2 + a_3(M - M_1)]\ln R + a_{17} r_{rup} \\ \\ M < M_2 \end{cases}$ $R = \sqrt{r_{rup}^2 + c_{4M}^2}$ $c_{4M} = \begin{cases} c_4 M > 5 \\ c_4 - (c_4 - 1)(5 - M) 4 < M \leq 5 \\ 1 M < 4 \end{cases}$ $f_7 = \begin{cases} a_{11} M > 5 \\ a_{11}(M - 4) 4 < M \leq 5 \\ 0 M < 4 \end{cases}$ $f_8 = \begin{cases} a_{12} M > 5 \\ a_{12}(M - 4) 4 < M \leq 5 \\ 0 M < 4 \end{cases}$	$c_4 = 4.5$ $M_1 = 6.75$ $M_2 = 5$ $a_1 = 0.587$ $a_2 = -0.790$ $a_3 = 0.275$ $a_4 = -0.1$ $a_5 = -0.41$ $a_6 = 2.154$ $a_8 = -0.015$ $a_{10} = 1.735$ $a_{11} = 0$ $12 = -0.1$ $a_{13} = 0.6$ $a_{14} = -0.3$ $a_{15} = 1.1$ $a_{17} = -0.0072$ $a_{43} = 0.1$ $a_{44} = 0.05$ $a_{45} = 0$ $a_{46} = -0.05$ $a_{25} = -0.015$ $a_{28} = 0.0025$ $a_{29} = -0.0034$ $a_{31} = -0.1503$ $a_{36} = 0.265$ $a_{37} = 0.337$ $a_{38} = 0.188$ $a_{39} = 0$ $a_{40} = 0.088$ $a_{41} = -0.196$ $a_{42} = 0.044$

(continued)

Table 2 (continued)

Sl no.	Abbreviation of the equation	Standard form of equation	Coefficients value for zero periods
		$f_5 = \begin{cases} (a_{10} + b_n)\left(\frac{V_s30^*}{V_{Lin}}\right) V_s30 \geq V_{Lin} \\ a_{10}\ln\left(\frac{V_s30^*}{V_{Lin}}\right) - b\ln\left(\widehat{Sa} + c\right) + b\ln\left[\widehat{Sa} + c\left(\frac{V_s30^*}{V_{Lin}}\right)^n\right] V_s30 < V_{Lin} \end{cases}$ $V_s30^* = \begin{cases} V_s30\, V_s30 < V_1 \\ V_1\, V_s30 \geq V_1 \end{cases}$ $V_1 = \begin{cases} 1500T \leq 0.5s \\ exp\left[-0.35\ln\left(\frac{T}{0.5}\right) + \ln 1500\right] 0.5s < T < 3s \\ 800T \geq 3\,\mathrm{s} \end{cases}$ $f_4 = a_{13} T_1 T_2 T_3 T_4 T_5$ $T_1 = \begin{cases} (90 - dip)/45\ dip > 30^\circ \\ \frac{60}{45}\ dip < 30^\circ \end{cases}$ $T_2 = \begin{cases} 1 + a_{2HW}(M - 6.5) M \geq 6.5 \\ 1 + a_{2HW}(M - 6.5) - (1 - a_{2HW})(M - 6.5)^2 5.5 < M < 6.5 \\ 0M \leq 6.5 \end{cases}$ $T_3 = \begin{cases} h_1 + h_2\left(R_x/R_1\right) + h_3\left(R_x/R_1\right)^2 R_x < R_1 \\ 1 - \left(\frac{R_x - R_1}{R_2 - R_1}\right) R_1 \leq R_x < R_2 \\ 0R_x > R_2 \end{cases}$ $T_4 = \begin{cases} 1 - \frac{Z_{TOR}^2}{100} Z_{TOR} \leq 10\ \mathrm{km} \\ 0Z_{TOR} > 10\,\mathrm{km} \end{cases}$	$V_{Lin} = 660$ $b = -1.47$ $n = 1.5$ $c = 2.4$

(continued)

Table 2 (continued)

Sl no.	Abbreviation of the equation	Standard form of equation	Coefficients value for zero periods
		$T_5 = \begin{cases} 1 & R_{y0} - R_{y1} \le 0 \\ 1 - \frac{R_{y0} - R_{y1}}{5} & 0 < R_{y0} - R_{y1} < 5 \\ 0 & R_{y0} - R_{y1} < 5 \end{cases}$ $R_1 = W\cos(dip)$ $R_2 = 3R_1$ $R_{y1} = R_x \tan(20)$ $h_1 = 0.25$ $h_2 = 1.5$ $h_3 = -0.75$ If R_{y0} is not available $T_5 = \begin{cases} 1 & r_{jb} = 0 \\ 1 - \frac{r_{jb}}{30} & r_{jb} < 30 \\ 0 & r_{jb} \ge 30 \end{cases}$ $f_6 = \begin{cases} a_{15}\frac{Z_{TOR}}{20} & Z_{TOR} < 20\,\text{km} \\ a_{15} & Z_{TOR} \ge 20\,\text{km} \end{cases}$ $f_{10} = \begin{cases} a_{43}\ln\left(\frac{Z_1+0.01}{Z_{1,ref}+0.01}\right) & V_s30 \le \frac{200\,\text{m}}{s} \\ a_{44}\ln\left(\frac{Z_1+0.01}{Z_{1,ref}+0.01}\right) & 200 < V_s30 \le \frac{300\,\text{m}}{s} \\ a_{45}\ln\left(\frac{Z_1+0.01}{Z_{1,ref}+0.01}\right) & 300 < V_s30 \le \frac{500\,\text{m}}{s} \\ a_{46}\ln\left(\frac{Z_1+0.01}{Z_{1,ref}+0.01}\right) & V_s30 > \frac{500\,\text{m}}{s} \end{cases}$ $Z_{1,ref} = \begin{cases} \frac{1}{1000}exp\left[-\frac{7.15}{4}\ln\left(\frac{V_{s,30}^4+570.94^4}{1360^4+570.94^4}\right)\right] & \text{for California} \\ \frac{1}{1000}exp\left[-\frac{5.23}{2}\ln\left(\frac{V_{s,30}^4+412.39^4}{1360^4+412.39^4}\right)\right] & \text{for Japan} \end{cases}$	

(continued)

Table 2 (continued)

Sl no.	Abbreviation of the equation	Standard form of equation	Coefficients value for zero periods
		$f_{11} = \begin{cases} a_{14} C R_{jb} \le 5\,\text{km} \\ a_{14}\left[1 - \frac{CR_{jb}-5}{10}\right] 5 < CR_{jb} \le 15\,\text{km} \\ 0 CR_{jb} \ge 15\,\text{km} \end{cases}$ $Regional = F_{TW}(f_{12} + a_{25} r_{rup}) + F_{CN} a_{28} r_{rup} + F_{JP}(f_{13} + a_{29} r_{rup})$ $f_{12} = \ln\left(\frac{V^*_{s30}}{V_{Lin}}\right)$ $f_{13} = \begin{cases} a_{36} V_{s30} < \frac{200\,\text{m}}{s} \\ a_{37} 200 \le V_{s30} < \frac{300\,\text{m}}{s} \\ a_{38} 300 \le V_{s30} < \frac{400\,\text{m}}{s} \\ a_{39} 400 \le V_{s30} < \frac{500\,\text{m}}{s} \\ a_{40} 500 \le V_{s30} < \frac{700\,\text{m}}{s} \\ a_{41} 700 \le V_{s30} < 1000\,\text{m/s} \\ a_{42} V_{s30} \ge 1000\,\text{m/s} \end{cases}$ Where, Sa is in g $\widehat{Sa}$ is median spectral acceleration in g for reference W is the down-dip rupture width	

(continued)

Table 2 (continued)

Sl no.	Abbreviation of the equation	Standard form of equation	Coefficients value for zero periods
12	BA_14	$\ln Y = F_E + F_P + F_S$ $F_E = \begin{cases} e_0 U + e_1 SS + e_2 NS + e_3 RS + e_4 (M_w - M_h) + e_5 (M_w - M_h)^2 M \le M_h \\ e_0 U + e_1 SS + e_2 NS + e_3 RS + e_6 (M_w - M_h) M > M_h \end{cases}$ $F_P = \left[c_1 + c_2 \left(M_w - M_{ref}\right)\right] \ln\left(R/R_{ref}\right) + (c_3 + \Delta c_3)\left(R - R_{ref}\right)$ $R = \sqrt{r_{jb}^2 + h^2}$ $F_S = \ln(F_{Lin}) + \ln(F_{nl}) + F_{\delta z_1}(\delta z_1)$ $\ln(F_{Lin}) = \begin{cases} c \ln\left(\frac{V_s 30}{V_{ref}}\right) V_s 30 \le V_c \\ c \ln\left(\frac{V_c}{V_{ref}}\right) V_s 30 > V_c \end{cases}$ $\ln(F_{nl}) = f_1 + f_2 \ln\left(\frac{PGA_r + f_3}{f_3}\right)$ $f_2 = f_4\left[exp\left\{f_5(\min(V_s 30, 760) - 360)\right\} - \exp f_5 (760 - 360)\right]$ $F_{\delta z_1} = \begin{cases} 0 T < 0.65 \\ f_6 \delta z_1 T \ge 0.65 \text{ and } \delta z_1 \le f_7/f_6 \\ f_7 T \le 0.65 \text{ and } \delta z_1 > f_7/f_6 \end{cases}$ $\delta z_1 = z_1 - \mu_{z1}$ $\ln \mu_{z1} = \begin{cases} -\frac{7.15}{4} \ln\left(\frac{V_{s,30}^4 + 570.94^4}{1360^4 + 570.94^4}\right) \text{ for California} \\ -\frac{5.23}{2} \ln\left(\frac{V_{s,30}^4 + 412.39^4}{1360^4 + 412.39^4}\right) \text{ for Japan} \end{cases}$ Where, Y is in g PGA_r is median PGA for reference rock (i.e., $V_s 30 = V_{ref}$) If strike slip faulting mechanism, then SS = 1 If Normal faulting mechanism, then NS = 1 If Reverse faulting mechanism, then RS = 1 If unspecified faulting mechanism, then U = 1	$M_{ref} = 4.5$ $R_{ref} = 1\,\text{km}$ $V_{ref} = 760\,\text{m/s}$ $e_0 = 0.4473$ $e_1 = 0.4856$ $e_2 = 0.2459$ $e_3 = 0.4539$ $e_4 = 1.4310$ $e_5 = 0.05053$ $e_6 = -0.1662$ $M_h = 5.5$ $c_1 = -1.134$ $c_2 = 0.1917$ $c_3 = -0.008088$ $\Delta c_{3,\text{China, Turkey}} = 0.0028576$ $\Delta c_{3,\text{Italy, Japan}} = -0.00255$ $h = 4.5$ $c = -0.6$ $V_c = 1500\,\text{m/s}$ $f_1 = 0$ $f_3 = 0.1$ $f_4 = -0.15$ $f_5 = -0.00701$ $f_6 = -9.9$ $f_7 = -9.9$

where, $w_{unif} = 1/M$, M is the number of models used for the calculation of LLH. Positive DSI indicates the GMPE supports the observed model, whereas negative DSI rejects the GMPE model. This LLH, weight, and DSI are further used to select and weight the GMPEs for the hazard estimation of the Himalayan region. In the present study, an efficacy test has been carried out by considering the macroseismic intensity maps of 1897 Shillong (8.0 M_w), 1934 Bihar–Nepal (8.0 M_w), 1991 Uttarkashi (6.8 M_w), 2005 Kashmir (7.6 M_w), and 2015 Nepal (7.8 M_w) earthquakes. The intensity map is converted to a PGA map using the PGA-Intensity equations proposed by Anbazhagan et al. (2016b). Using these derived PGA values, LLH values (Eq. (3)) and corresponding weights (Eq. (4)) have been calculated. Observing the applicability and trends in GMPEs, the hypocentral distance is divided into three distance bins 0–100 km, 100–300 km, and more than 300 km. As five different intensity maps are used for ranking of GMPEs and each one of them has a different ranking, commoning these derived PGA values, GMPdEs are selected for different distance bins, and average weights are assigned to the GMPEs. The selected GMPEs, along with the weight for different distance bins, are given in Table 3. The weight factor corresponding to particular GMPE for different distance bins is further used to evaluate the seismic hazard values in terms of PGA and SA.

Table 3 Weights and Ranking of GMPE for different distance bins used in hazard analysis of the IGB

GMPE	Weight	Ranking
Distance $\leq$ *100* km		
BAN_19	0.28	1
ID_14	0.22	2
ZH_06	0.16	3
AN_13	0.14	4
NA_09	0.10	5
CABO_14	0.10	6
100 km < *Distance* $\leq$ *300* km		
BAN_19	0.28	1
ID_14	0.20	2
BA_14	0.17	3
ZH_16_CM	0.15	4
KA_06	0.10	5
CABO_14	0.10	6
Distance > *300* km		
BAN_19	0.65	1
NDMA_10	0.35	2

5 The Shape of Design Spectrum for HR

SHA analysis gives hazard values in PGA and SA at different periods, but these cannot be used directly in the design, as the design spectrum is a normalized and smoothed spectrum. The normalized and smoothed design spectrum reflects the median value of several response spectra with acceleration, velocity, and displacement sensitive zone based on regional recorded earthquake data. In the sixth revision of Indian seismic code BIS:1893 (BIS. IS, 2016), two design spectra were given for equivalent static and response spectra for constructing the acceleration response spectra. The typical design spectra given in BIS:1893 (BIS. IS, 2016) are considered in the present study for comparison. Normalized and smoothed design spectra were introduced in the Indian code 2002 version. In older versions of Indian code, BIS 1893 up to revision 3, 1970, design acceleration is given as average acceleration in cm/sec^2 and 5% damping maximum average acceleration of 190 cm/s^2 (0.28 g) at 0.3 s of the natural period of the structure. In 1984, this was converted as an average acceleration coefficient (Sa/g), and the shape of the design spectrum started here. BIS1893 (BIS. IS, 2016) version Sa/g linear slope up to 0.12 s, the maximum value of 0.28 from 0.12 to 0.33 s constant value and beyond 0.33 s reduced up to 3.0 s of the natural period of vibration of 5% damping. The first normalized and smoothed design spectrum was introduced in the BIS1893 (BIS IS 2002) version with three major types of ground (rock/hard soil/ medium soil and soft soil). The average acceleration coefficient is replaced by the spectral acceleration coefficient (Sa/g), and the natural period of vibration is replaced with a period (natural period of structure). Minimum Sa/g at 0 s, linearly increases Sa/g up to 0.1 s and reaches Sa/g of 2.5 and remains constant Sa/g of 2.5 from 0.1 to 0.4 s then Sa/g decreases non-linearly 0.4–4.0 s of the period. One more normalized and smoothed design spectrum is added in the BIS1893 (BIS. IS, 2016) version with the initial part Sa/g being 2.5 from 0 to 0.4 s for the equivalent static design method. As per the author's knowledge, very limited regional seismic data and analysis went into the shape of the present design spectrum in IS 1893 (BIS. IS, 2016). It may be an appropriate time to arrive at a normalized and smoothed design spectrum considering rock earthquake records available.

5.1 Design Spectrum for Code

In most seismic designs, the estimation of the seismic force of a typical structure is based on the 5% damped design response spectrum. Generally, a given site's design spectrum is obtained by modifying the normalized and smoothed spectrum by considering site factors corresponding to a seismic site class. Conventionally, the design force is specified using response spectrum amplitude. However, with the increased complexity of the modern structure and understanding, the structure's seismic performance is in high demand in seismic prone areas. So, it is necessary to specify the amplitude and shape of the design spectra considering regional parameters.

Initially, Biot (1941) introduced a response spectra concept and proposed the standard spectral shape for earthquake resistant design of a building. Housner () averaged and smoothed the response spectra considering the four strong-motion records and proposed using average spectrum shape in earthquake engineering design. Newmark and Hall (1969, 1982) recommended a smooth response spectrum concentrating on three regions viz. acceleration (short period), velocity (medium period), and displacement (long period). These three spectral regions can be constructed by applying the amplification to the design value of PGA, peak ground velocity (PGV), and peak ground displacement (PGD). The spectral acceleration for periods <0.33 s, between 0.33 and 3.33 s and above 3.33 s, is sensitive to PGA, PGV, and PGD, respectively (Newmark & Hall, 1982). In most engineering practices, Housner and Newmark spectra's fixed shape, normalized to unit peak acceleration, is widely used by scaling it based on the design peak acceleration. Various researchers (Hall et al., 1975; Mohraz, 1976) contributed to the development of the Newmark–Hall spectrum. The response spectra can also be presented using the tripartite plot or four-way logarithmic plot for which all the spectra quantities can be read. This tripartite plot is the compact representation of three response spectra. So, in this study, we arrive at the shape and three regions, viz. acceleration, velocity, and displacement of HR, using data discussed in Sect. 2.

5.2 Spectrum Control Period and Factor

Malhotra (2001) finds that the response of the structure derived using acceleration time history does not correspond to the velocity and displacement time histories. The response of the flexible structures (long period) can be contradictory if computed only using processed acceleration time history (Malhotra 2001). Based on that, Malhotra (2001) proposed a methodology to compute elastic response spectra for incompatible acceleration, velocity, and displacement time histories. Using the acceleration, velocity, and displacement time histories, Malhotra (2006) determined the amplification factors for the spectrum's acceleration, velocity, and displacement sensitive region for various damping values. We followed the procedure recommended by Malhotra (2001, 2009) for deriving the normalized response spectra by adopting an in-house MATLAB code developed by the Authors.

Various authors (Malhotra, 2006; Mohraz et al., 1972; Newmark & Hall, 1982) defined the different cutoff period of the design spectrum that is sensitive to PGA, PGV, and PGD. Newmark and Hall (1982) and Mohraz et al. (1972) assumed that SAs for periods 0.33 s, 0.33 and 3.33 s, and more than 3.33 s are sensitive to PGA, PGV, and PGD. SAs for the periods up to 0.62, 0.62–2.6 s, and the rest correlated well with PGA, PGV, and PGD (Malhotra, 2006). Malhotra (2006) concluded that cutoff periods could change for different sets of seismic ground motions, and also, it was concluded that vertical response spectra do not have the same shape as the horizontal spectra. The recorded bedrock seismic ground motion data in the HR has been used to determine the cutoff periods for PGA, PGV, and PGD sensitive regions. The PGA,

PGV, and PGD sensitive region for HR has been defined by correlating SA at various periods with PGA, PGV, and PGD in a plot (Fig. 4). From Fig. 4, it can be noted that in the region, SA for the period up to 0.38 s is correlating well with PGA, the period between 0.38 and 2.33 s, and SA is correlating well with PGV, and the rest correlate best with PGD for the rock sites. Bureau of Indian Standard (BIS. IS, 2016) defined the cutoff period for rock sites as 0.1 and 0.4 s, which is significantly different from the present study. Similarly, it is noted here that the cutoff period calculated in this study is considerably different from Hall et al. (1982).

All recorded earthquake acceleration time history of engineering interest (PGA > 0.01 g) is further plotted in a tripartite plot and shown in Fig. 5. The spectral velocity (SV) is converted from the spectral displacement. Also, the average of the seismic ground motions has been normalized using Eqs. (6)–(8). Firstly, the central period (T_{cg}) of the seismic ground motion is calculated as

$$T_{cg} = 2\pi\sqrt{\frac{PGD}{PGA}} \tag{6}$$

This T_{cg} caused the horizontal shift in the response spectra, PGA and PGD change to $PGA \times T_{cg}/2\pi$ and $PGD \times 2\pi / T_{cg}$ respectively; however, PGV remains constant. Further, PGV and SV are normalized with respect to $\sqrt{PGA \cdots PGD}$, this makes PGA and PGD unity, and PGV and SV to take the following non-dimensional form

$$\overline{PGV} = \frac{PGV}{\sqrt{PGA \cdots PGD}} \tag{7}$$

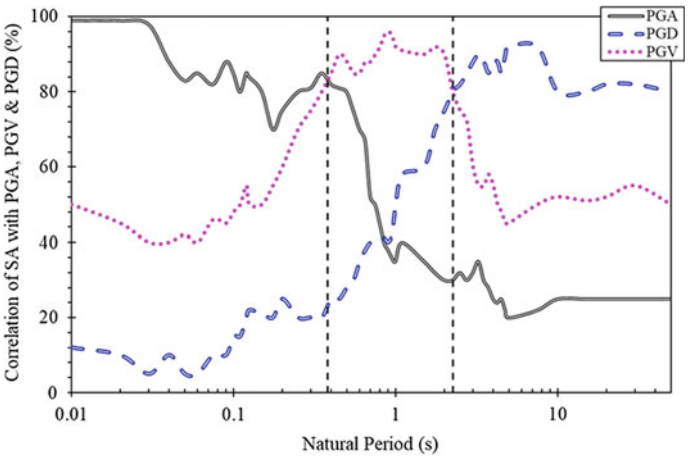

Fig. 4 Correlation of SA at various periods with PGA, PGV, and PGD for the Himalayan Regionat bedrock condition

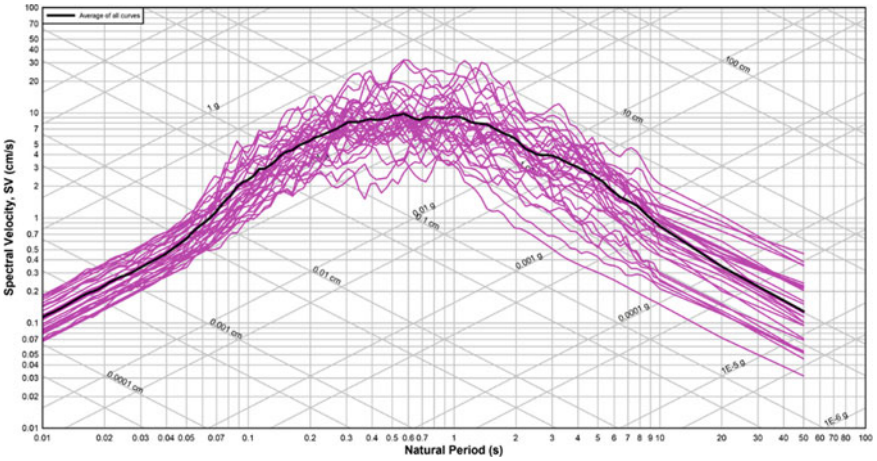

Fig. 5 A tripartite plot of horizontal seismic ground motions recorded at bedrock in the Himalayan region

$$\overline{SV} = \frac{SV}{\sqrt{PGA \cdots PGD}} \tag{8}$$

Further, the normalized spectrum has been smoothened, considering the least-squares fitting of straight-line segments through the median curve. The median normalized spectrum is further obtained by averaging the log $\overline{SA}$ at each normalized period. The median normalized spectrum versus the normalized spectral period is given in Figure 6a for the Himalayan region. The shaded area in Fig. 6a corresponds to ± 1 standard deviation about the median. The smooth response spectrum has been obtained afterwards by using the least-squares fitting of straight-line segments through the median curve as shown in Fig. 6b. Figure 6b shows the smooth medium spectrum of HR. The Himalayan region multiplication factors for PGA, PGV, and PGD are 2.29, 1.97, and 2.05 respectively and denoted as α_A, α_V, and α_D. In Fig. 6b, we can also note the control periods for constant acceleration is 0.15 s, velocity is 0.38 s, and displacement is 2.33 s, respectively, for the region. These values are also comparable with Fig. 4.

5.3 Bedrock Horizontal Design Spectrum for Himalayan Region

The shape of the design spectrum at bedrock in the region depends on smoothed and normalized response spectra for acceleration, velocity and displacement-control period. In the previous section, we find that the control periods of HR based on the

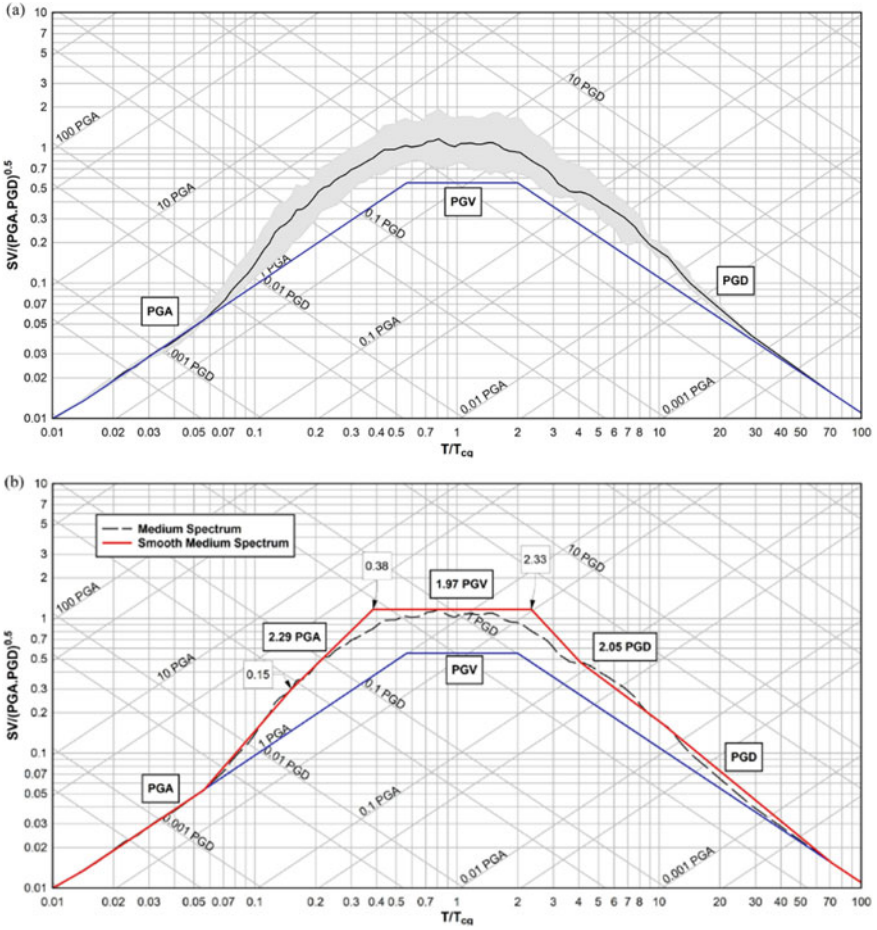

Fig. 6 Himalayan region **a** Normalized 5% damping median spectrum of horizontal seismic ground motions recorded data at bedrock and **b** smooth medium spectrum

recorded data for acceleration is 0.15 s (T_B), velocity is 0.38 s (T_C), and displacement is 2.33 s (T_D). Similarly, modification factors of α_A, α_V, and α_D as 2.29, 1.97, and 2.05. These factors control the shape of the Horizontal Design Spectrum (HDS) in the region. The spectral shape is a composite of the very low period branch from PGA to the constant acceleration i.e., up to 0.15 s (T_B), constant acceleration branch in between 0.15 and 0.38 s, velocity branch from 0.38 to 2.33 s, and displacement branch beyond 2.33 s. The peak of the spectral amplitude is defined as 2.5 ηS, where η is the damping ratio i.e., 5% (CEN 2005). The general form of equations for the elastic response spectra for 5% damping is as

$$0 \le T \le T_B: \frac{S_a(T)}{PGA_{rock}} = s \cdot \left[1 + \frac{T}{T_B}.(\beta - 1)\right] \tag{9}$$

$$T_B \le T \le T_C: \frac{S_a(T)}{PGA_{rock}} = s \cdot \beta \tag{10}$$

$$T_C \le T \le T_D: \frac{S_a(T)}{PGA_{rock}} = s \cdot \beta \frac{T_C}{T} \tag{11}$$

$$T_D \le T: \frac{S_a(T)}{PGA_{rock}} = s \cdot \beta \cdot T_C \frac{T_D}{T^2} \tag{12}$$

Here, PGA_{rock} is the design ground acceleration at rock site conditions, S and β are the soil amplification here it is unity as all sites are rock stations and spectral amplification factors. T_B and T_C are the limits of constant acceleration branch and T_D is the beginning of the constant displacement range of the spectrum. The parameters S, β, T_B, T_C, and T_D depend on on-site class and seismicity. In the present study, these parameters are derived based on recorded seismic data from India's Himalayan region, as discussed in the previous sections. Figure 7 shows the normalized and smoothed spectrum developed for the study area. The shape of the design spectrum from the study is different from IS 1893 (BIS. IS, 2016). The design spectrum for the typical PGA value of 0.24 g and 0.36 g has been generated for the shape obtained in this study and shown in Fig. 8. It can be noted that the design spectrum developed in this is sensitive to the size of an earthquake, similar to modern seismic codes. But BIS

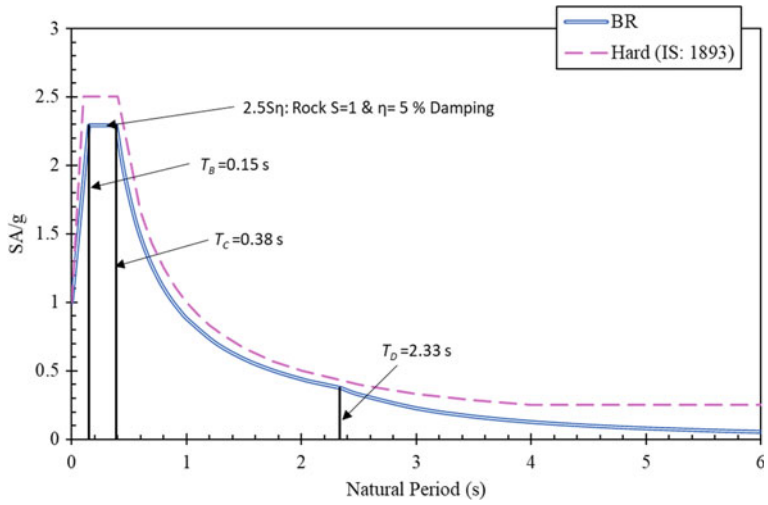

Fig. 7 Normalized and smoothed horizontal design spectrum for Himalayan region

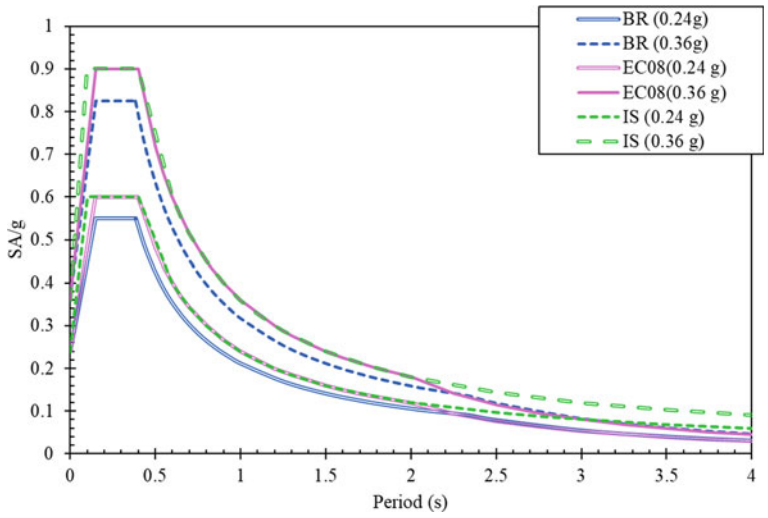

Fig. 8 Typical design spectrum for the region considering PGA value of 0.24 g and 0.36 g

code spectrum does not change with PGA values, and the design spectrum is the function of the period i.e., T rather than PGA, S, β, and variation of T. Proposed spectrum for HDR for 5% damping and other damping values region-specific damping values given by Anbazhagan et al. (2016a) can be used. Similar way, we are also working on a vertical design spectrum based on available data and trying to understand how is the ratio of horizontal to vertical spectrum in the region.

From Fig. 8, we note that IS code design spectrum closely matched with Euro code rather Indian data derived design spectrum. As everyone knows, that design spectrum given in IS 1893 initial version of code was taken from the design spectrum arrived based on western recorded earthquake data. The design spectrum was repeatedly reused in all revisions of IS 1893 without developing a new spectrum based on Indian recorded data. The new design spectrum derived in this study using Indian data has a considerable difference from the Euro/India code, which may be due to changes in seismicity and seismotectonic of both regions. Presently we used all available data from the Himalayan region as one group, but it can also be highlighted that HR can be grouped into three major seismic areas (Western, Central and Eastern Part) based on seismicity and seismotectonic. This spectrum may be updated when more record earthquake data are available from each region. Further, soil layers and their thickness variation in each site can amplify bedrock ground motions. Such kind of amplified ground motions cause catastrophic damage during past earthquakes in HR. The understating and estimating design spectrum for different soil classes are also required.

6 Soil Amplification and Spectrum

Many highly populated cities are located in IGB, which is very close to the Himalayan region. IGB experienced catastrophic damages due to geo-seismic hazards of site amplification and liquefaction during past earthquakes. Limited study has been carried out to understand site amplification considering site-specific soil and seismicity data and dynamic models of shear modulus reduction and damping ratio curves. We made an extensive study to understand the subsurface dynamic properties of IGB. Bajaj and Anbazhagan (2019) carried out the combined active and passive MASW (Multichannel Analysis of Surface Wave) survey at 275 locations, and the shear wave velocity is measured up to a depth of 500 m. The entire IGB was classified based on the average shear wave velocity map at shallow as well as deeper depths. The average shear wave velocity till top 5, 10, 15, 20, 30, 50, 100, 150, 200, 250, and 300 m depths was estimated and mapped. The shear wave velocity near the upper Ganga plain is 215 ± 20 m/s till 10 m depth and increases to 750 ± 50 m/s till 150 m depth, which is due to the thick deposits of Varanasi older alluvium. Further, we mapped the depth of the non/less-amplifying layer in IGB, i.e., depth of layer having Vs ≥ 1500 m/s. Further, the spatial variation of depth at which shear wave velocity is equal/more than 1500 m/s is also studied. Figure 9 shows thickness from surface layer up to layer with Vs ≥ 1500 m/s from our study. It can be noted that for the whole IGB, V_s more than 1500 m/s is observed at different depths, and this may be due to the variation in a deposition in different geological eras. Varying soil stiffness (V_s values) in the vertical and horizontal direction of the IGB may be

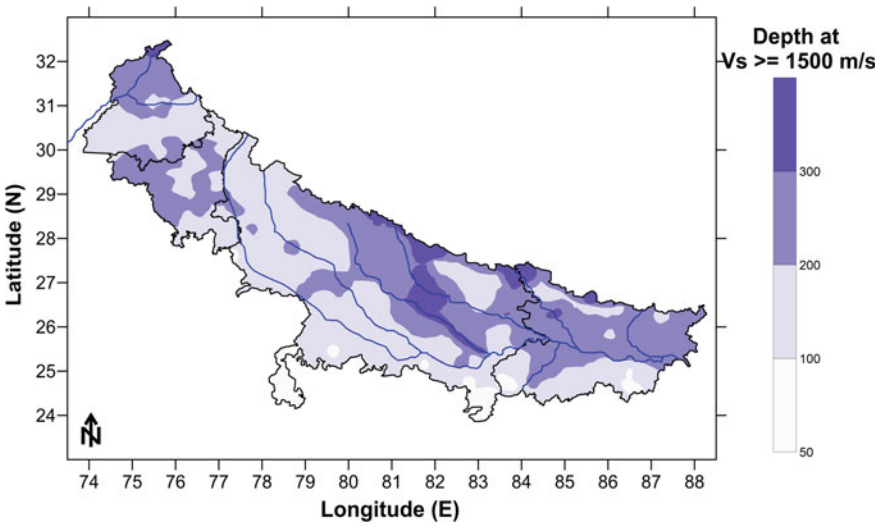

Fig. 9 Depth of amplifiable soil layers in IGB

one of the reasons for past heavy damages due to earthquake geohazards in the IGB (2020). So, the authors highlighted the importance of understating site effects, and liquefaction may be of prime importance to reduce seismic-related losses.

Most amplification studies do not fully account for regional soil and seismic parameters to spell out representative amplification in IGB. Bajaj and Anbazhagan (2019a) used the above study results and generated time average shear wave velocity at 30 m depth (V_{S30}), which is an essential parameter for site characterization and site amplification estimation by an empirical approach. But empirical formulas developed for the different regions should be used with caution. Bajaj and Anbazhagan (2020) produced representative amplification by carrying out a non-linear site response analysis at 275 locations by assigning suitable input motion based on a seismic hazard map for a 10% probability of exceedance in 50 years. The study found the amplification factor in Punjab-Haryana as 2.8–3.9, Uttar Pradesh as 1.5–3.4, and Bihar region as 1.8–6.3. Reliable soil and seismic input parameters were used in the study, but dynamic soil models were assigned from the parametric study by Bajaj and Anbazhagan (2020) for Japan Kiki net soil and earthquake data. IGB is more prone to local site effects due to varying predominant frequency and thickness of soil column (Anbazhagan et al., 2019). So reliable amplification factor estimation and development of HDS for different site classifications in IGB and HR are required to reduce seismic-related damages in north India.

7 Summary and Conclusion

First time compressive regional available earthquake recorded data at rock sites from the Himalayan region was presented here. These data are used to identify GMPE functional form and suggest a list of suitable GMPEs for seismic hazard analysis. The study found that many of the GMPEs developed in the region do not follow the proper attenuation functional form suitable for the Himalayan region. Detailed LLH analysis was carried out considering applicable GMPEs using regional ground motion data. The most suitable GMPEs for SHA has ranked with weight calculation for the logic tree probabilistic calculation. The most ranked Indian GMPEs in all distance segments are proposed by Bajaj and Anbazhagan (2019b). We also arrived design spectrum shape for the rock site first time for HR using recorded data. We found that controlled periods and the highest Sa/g are different from the current BIS 1893 code. This needs to be taken into account while designing structures in the region. There is no systematic amplification estimation found in the area, even though many soil and seismic ground motion data are available. This needs to be addressed in future studies, and some of them are in progress in our research team.

Acknowledgements The authors are thankful for funding and support by the Science and Engineering Research Board (SERB), Department of Science and Technology [SERB/F/162/2015-2016]. Author thanks M/s. SECON Private Limited, Bangalore for funding project "Effect of Shear Wave Velocity Calibration on Amplification of Shallow and Deep Soil Sites."

References

Abrahamson, N. A., & Litehiser, J. J. (1989). Attenuation of vertical peak accelerations. *Bulletin of the Seismological Society of America, 79*, 549–580.

Abrahamson, N., & Silva, W. (2008). Summary of the Abrahamson & Silva NGA ground-motion relations. *Earthquake Spectra, 24*, 67–97.

Abrahamson, N. A., Silva, W. J., & Kamai, R. (2014). Summary of the ASK14 ground-motion relation for active crustal regions. *Earthquake Spectra.* https://doi.org/10.1193/070913EQS198M.

Aghabarati, H., & Tehranizadeh, M. (2009). Near-source ground motion attenuation relationship for PGA and PSA of vertical and horizontal components. *Bulletin of Earthquake Engineering, 7*, 609–635.

Akkar, S., & Bommer, J. J. (2010). Empirical equations for the prediction of PGA, PGV and spectral acceleration in Europe, the Mediterranean region and the Middle East. *Seismological Research Letters, 81*,195–206.

Akkar, S., Sandikkaya, M. A., & Bommer, J. J. (2014) Empirical ground motion models for point and extended-source crustal earthquake scenarios in Europe and the Middle East. *Seismological Research Letters, 12*, 359–387.

Ambraseys, N., Douglas, J. S., Sarma, K., & Smit, P. M. (2005). Equation for the estimation of strong ground motions from shallow crustal earthquakes using data from Europe and the Middle East: Horizontal peak ground acceleration and the spectral acceleration. *Bulletin of Earthquake Engineering, 3*, 1–53.

Anbazhagan, P., Kumar, A., & Sitharam, T. G. (2013) Ground motion prediction equation considering combined dataset of recorded and simulated ground motions. *Soil Dynamics and Earthquake Engineering, 53*, 92–108.

Anbazhagan, P., Bajaj, K., & Patel, S. (2015). Seismic hazard maps and spectrum for Patna considering region-specific seismotectonic parameters. *Natural Hazards, 78*(2), 1163–1195.

Anbazhagan, P., Uday, A., Moustafa, S. S. R., & Al-Arifi, N. S. N. (2016a). Pseudo-spectral damping reduction factors for the himalayan region considering recorded ground-motion data. *Plos One, 11*(9), e0161137.

Anbazhagan, P., Bajaj, K., Moustafa, S. S. R., & Al-Arifi, N. S.N. (2016b). Relationship between intensity and recorded ground motion and spectral parameters for the Himalayan region. *Bulletin of the Seismological Society of America, 106*(4), pp. 1672–1689.

Anbazhagan, P., Janarthan, B., & Shaivan, H. S. (2019a). Empirical correlation between sediment thickness and resonant frequency using HVSR for the Indo-Gangetic Plain. *Current Science, 117*(9), 1182–1491.

Anbazhagan, P., Srilakshmi, K. N., Bajaj, K., Moustafa, S. S. R., & Al-Arifi, N. S. N. (2019b). Determination of Seismic site classification of seismic recording stations in the Himalayan region using HVSR method. *Soil Dynamics and Earthquake Engineering, 116*, 304–316.

Anbazhagan, P., Bajaj, K., Matharu, K., Moustafa, S. S. R., & Al-Arifi, N. S. N. (2019c). Probabilistic seismic hazard analysis using the logic tree approach—Patna district (India). *Natural Hazards and Earth System Sciences, 19*(10), 2097–2115. https://doi.org/10.5194/nhess-19-2097-2019.

Atkinson, G. M., & Boore, D. M. (2003). Empirical ground-motion relations for subduction-zone earthquakes and their applications to Cascadian and other regions. *Bulletin of the Seismological Society of America, 93*, 1703–1717.

Bajaj, K., & Anbazhagan, P. (2018). A comparison of different functional form and modification of NGA-West 2 Ground-Motion Prediction Equation for the Himalayan region. *Journal of Seismology, 22*(1), 161–185.

Bajaj, K., & Anbazhagan, P. (2019a). Seismic site classification and correlation between Vs and SPT-N for deep soil sites in Indo-Gangetic Basin. *Journal of Applied Geophysics, 163*, 55–72.

Bajaj, K., & Anbazhagan, P. (2019b). Regional seismological model parameter estimation and development of GMPE model for the active region of Himalaya. *Soil Dynamics and Earthquake Engineering, 126*, 105825.

Bajaj, K., & Anbazhagan, P. (2020). Comprehensive amplification estimation of the Indo Gangetic Basin deep soil sites in the seismically active area. *Soil Dynamics and Earthquake Engineering, 127*, 105855.

Bajaj, K., & Anbazhagan, P. (2021a). Detailed seismic hazard, disaggregation and sensitivity analysis for Indo Gangetic basin. *Pure and Applied Geophysics,178*, 1977–1999.

Bajaj, K., & Anbazhagan, P. (2021b) Identification of shear modulus reduction and damping curve for deep and shallow sites: Kik-Net data. *Journal of Earthquake Engineering*. Published Online: https://doi.org/10.1080/13632469.2019.1643807.

Bilham, R. (2015). Raising Kathmandu. *Nature Geoscience, 8*, 582–584.

Bindi, D., Massa, M., Luzi, L., Ameri, G., Pacor, F., Puglia, R., & Augliera, P. (2014). Pan-European ground motion prediction equations for the average horizontal component of PGA, PGV, and 5%-damped PSA at spectral periods up to 3.0 S using the RESOURCE dataset. *Bulletin of Earthquake Engineering, 12*, 391–430.

Biot, M. A. (1941). A mechanical analyzer for the prediction of earthquake stresses. *Bulletin of the Seismological Society of America, 31*, 151–71.

BIS IS 1893–2002 (Part 1): Indian standard criteria for earthquake resistant design of structures. Part 1—General provisions and buildings. Bureau of Indian Standards, New Delhi.

BIS. (2016). IS 1893–2016 (Part 1): Indian standard criteria for earthquake resistant design of structures. Part 1—General provisions and buildings. Bureau of Indian Standards, New Delhi.

Bommer, J. J., Douglas, J., Scherbaum, F., Cotton, F., & Bungum, H., & Fäh, D. (2010). On the selection of ground-motion prediction equations for seismic hazard analysis. *Seismological Research Letters, 81*(5), 783–793.

Boore, D. M., & Bommer, J. (2005). Processing of strong motion accelerograms: Needs, options and consequences. *Soil Dynamics and Earthquake Engineering, 25*, 93–115.

Boore, D. M., & Atkinson, G. M. (2008). Ground-motion prediction equations for the average horizontal component of PGA, PGV and 5% damped PSA at spectral periods between 0.01 and 10.0 s. *Earthq Spectra, 24*(1), 99–138.

Boore, D. M., Stewart, J. P., Seyhan, E., & Atkinson, G. M. (2014). NGAWest 2 equations for predicting PGA, PGV, and 5%-damped PSA for shallow crustal earthquakes. *Earthquake Spectra, 30*(3), 1057–1085.

Campbell, K. W. (1997). Empirical near-source attenuation relationships for horizontal and vertical components of peak ground acceleration, peak ground velocity and pseudo-absolute acceleration response spectra. *Seismological Research Letters, 68*(1), 154–179.

Campbell, K. W., & Bozorgnia, Y. (2008). NGA ground motion model for the geometric mean horizontal component of PGA, PGV, PGD and 5 % damped linear elastic response spectra for period ranging from 0.01 to 10 s. *Earthquake Spectra, 24*, 139–171.

Campbell, K. W., & Bozorgnia, Y. (2014). NGA-West 2 ground motion model for the average horizontal components of PGA, PGV, and 5%-damped linear acceleration response spectra. *Earthquake Spectra, 30*(3), 1087–1115.

Cauzzi, C., & Faccioli, E. (2008). Broadband (0.05 to 20s) prediction of displacement response spectra based on worldwide digital records. *Journal of Seismology, 12*(4), 453–475.

CEN (2005) EN 1998-3 Eurocode 8: design of structures for earthquake resistance, part 3: assessment and retrofitting of buildings. European Committee for Standardization.

Chiou, B. S. J., & Youngs, R. R. (2008). An NGA model for the average horizontal component of peak ground motion and response spectra. *Earthquake Spectra, 24*(1), 173–215.

Chiou, B. S. J., & Youngs, R. R. (2014). Update of the Chiou and Youngs NGA model for the average horizontal component of peak ground motion and response spectra. *Earthquake Spectra, 30*, 1117–1153.

Cotton, F., Scherbaum, F., Bommer, J. J., & Bungum, H. (2006). Criteria for selecting and adjusting ground-motion models for specific target regions: Application to central Europe and rock sites. *Journal of Seismology, 10*(2), 137–156.

Das, S., Gupta, I. D., & Gupta, V. K. (2006). A probabilistic seismic hazard analysis of Northeast India. *Earthquake Spectra, 22*, 1–27.

Delavaud, E., Scherbaum, F., Kuehn, N., & Allen, T. (2012). Testing the global applicability of ground-motion prediction equations for active shallow crustal regions. *Bulletin of the Seismological Society of America, 102*(2), 702–721.

Delavaud, E., Scherbaum, F., Kuehn, N., & Riggelsen, C. (2009). Information-theoretic selection of ground-motion prediction equations for seismic hazard analysis: An applicability study using Californian data. *Bulletin of the Seismological Society of America, 99*, 3248–3263.

Douglus, J (2020). *Ground motion prediction equations 1964–2020*. http://www.gmpe.org.uk/gmpereport2014.html.

Gupta, I. D. (2010). Response spectral attenuation relations for inslab earthquakes in Indo-Burmese subduction zone. *Soil Dynamics and Earthquake Engineering, 30*, 368–377.

Hall, W. J., Mohraz, B., & Newmark, N. M. (1975). Statistical studies of vertical and horizontal earthquake spectra. Nathan M. Newmark Consulting Engineering Services, Urbana, Illinois.

Housner, G. W. (1959). Behavior of structures during earthquakes. *Journal of Engineering Mechanics Division, ASCE, 85*(EM 4), 109–29.

Housner, G. W. (1970). *Design spectrum, Chapter 5 in earthquake engineering*. New Jersey: R.L Wiegel: Prentice-Hall.

Idriss, I. M. (2008). An NGA empirical model for estimating the horizontal spectral values generated by shallow crustal earthquakes. *Earthquake Spectra, 16*, 363–372.

Idriss, I. M. (2014). An NGA-West 2 empirical model for estimating the horizontal spectral values generated by shallow crustal earthquakes. *Earthquake Spectra.* https://doi.org/10.1193/070613EQS195M

Iyengar, R. N., & Ghosh, S. (2004). Microzonation of earthquake hazard in Greater Delhi area. *Current Science, 87*(9), 1193–1202.

Kanno, T., Narita, A., Morikawa, N., Fujiwara, H., & Fukushima, Y. (2006). A new attenuation relation for strong ground motion in Japan based on recorded data. *Bulletin of the Seismological Society of America, 96*, 879–897.

Kumar, A., Mittal, H., Sachdeva, R., & Kumar, A. (2012). Indian strong motion instrumentation network. *Seismological Research Letters, 83*, 59–66.

Lin, P. S., & Lee, C. H. (2008). Ground-motion attenuation relationship for subduction-zone earthquakes in Northeastern Taiwan. *Bulletin of the Seismological Society of America, 98*(1), 220–240.

Malhotra, P. K. (2001) Response spectrum of incompatible acceleration, velocity and displacement histories. *Earthquake Engineering and Structural Dynamics, 30*(2), 279–286.

Malhotra, P. K. (2006). Smooth spectra of horizontal and vertical ground motions. *Bulletin of the Seismological Society of America, 96*(2), 506–518.

Mohraz, B. (1976). A study of earthquake response spectra for different geological conditions. *Bulletin of the Seismological Society of America, 66*(3), 915–935.

Mohraz, B., Hall, W. J., & Newmark,. N. M. (1972) A study of vertical and horizontal earthquake spectra, AEC Report WASH-1255, Nathan M. Newmark Consulting Engineering Services, Urbana, Illinois.

Motazedian, D., & Atkinson, G. M. (2005). Stochastic finite-fault modeling based on a dynamic corner frequency. *Bulletin of the Seismological Society of America, 95*, 995–1010.

Nath, S. K., Vyas, M., Pal, I., & Sengupta, P. (2005). A hazard scenario in the Sikkim Himalaya from seismotectonics spectral amplification source parameterization and spectral attenuation laws using strong motion seismometry. *Journal of Geophysical Research, 110*, 1–24.

Nath, S. K., Raj, A., Thingbaijam, K. K. S., Kumar, A. (2009). Ground motion synthesis and seismic scenario in Guwahati city; A stochastic approach *Seismological Research Letters, 80*(2), 233–42.

NDMA. (2011). *Development of probabilistic hazard map of India*. Retrieved July 2017, from http://ndma.gov.in/ndma/disaster/earthquake/PSHATechReportMarch%202011.pdf. Report.

Newmark, N. M., & Hall, W. J. (1969). Seismic design criteria for nuclear reactor facilities. In *Proceedings of World Conference on Earthquake Engineering*, 4th Santiago, Chile, B-4 (pp. 37–50).

Newmark, N. M., & Hall, W. J. (1982). *Earthquake spectra and design*. Earthquake Engineering Research Institute, Oakland, California.

Ramkrishnan, R., Sreevalsa, K., & Sitharam, T. G. (2020) Strong motion data based regional ground motion prediction equations for North East India based on non-linear regression models. *Journal of Earthquake Engineering*. https://doi.org/10.1080/13632469.2020.1778586.

Scherbaum, F., Delavaud, E., & Riggelsen, C. (2009). Model selection in seismic hazard analysis: an information theoretic perspective. *Bulletin of the Seismological Society of America, 99*, 3234–3247.

Sharma, M. L., & Bungum, H. (2006). New strong ground motion spectral acceleration relation for the Himalayan region. In *First European Conference on Earthquake Engineering and Seismology* (p. 1459).

Sharma, M. L., Douglas, J., Bungum, H., & Kotadia, J. (2009). Ground-motion prediction equations based on data from Himalayan and Zagros regions. *Journal of Earthquake Engineering, 13*, 1191–1210.

Singh, R. P., Aman, A., & Prasad, Y. J. J. (1996). Attenuation relations for strong ground motion in the Himalayan region. *Pure and Applied Geophysics, 147*, 161–180.

Spudich, P., Joyner, W. B., Lindh, A. G., Boore, D. M., Margaris, B. M., & Fletcher, J. B. (1999). SEA99: a revised ground motion prediction relation for use in Extensional tectonic regions. *Bulletin Seismological Society of America, 89*(5), 1156–1170.

Srivastava, H. N., Verma, M., Bansal, B. K., & Sutar, A. K. (2015). Discriminatory characteristics of seismic gaps in Himalaya. https://doi.org/10.1080/19475705.2013.839483.

Strasser, F. O., Abrahamson, N. A., & Bommer, J. J. (2009). Sigma: Issues, insights, and challenges. *Seismological Research Letters, 80*, 41–56.

Takahashi, T., Saiki, T., Okada, H., Irikura, K., Zhao, J. X., Zhang, J., Thoi, H. K., Somerville, P. G., Fukushima, Y., & Fukushima, Y. (2004). Attenuation models for response spectra derived from Japanese strong-motion records accounting for tectonic source types. In *13th World Conference of Earthquake Engineering*, Vancouver, BC, Canada, paper 1271.

Youngs, R. R., Chiou, S. J., Silva, W. J., & Humphrey, J. R. (1997). Strong ground motion relationship for subduction earthquakes. *Seismological Research Letters, 68*, 58–73.

Zhao, J. X., Jiang, F., Shi, P., Xing, H., Huang, H., Hou, R., Zhang, Y., Yu, P., Lan, X., Rhoades, D. A., Somerville, P. G., Irikura, K., & Fukushima, Y. (2016a). Ground-motion prediction equations for subduction slab earthquakes in Japan using site class and simple geometric attenuation functions. *Bulletin of the Seismological Society of America, 106*, 1535–1551.

Zhao, J. X., Liang, X., Jiang, F., Xing, H., Zhu, M., Hou, R., Zhang, Y., Lan, X., Rhoades, D. A., Irikura, K., Fukushima, Y., & Somerville, P. G. (2016b). Ground-motion prediction equations for subduction interface earthquakes in japan using site class and simple geometric attenuation functions. *Bulletin of the Seismological Society of America, 106*, 1518–1534.

Zhao, J. X., Zhou, S., Zhou, J., Zhou, C., Zhang, H., Zhang, Y., Gao, P., Lan, X., Rhoades, D. A., Fukushima, Y., Somerville, P. G., & Irikura, K. (2016c). Ground-motion prediction equations for shallow crustal and upper-mantle earthquakes in Japan using site class and simple geometric attenuation functions. *Bulletin of the Seismological Society of America, 106*, 1552–1569.

Zhao, J. X., Zhang, J., Asano, A., Ohno, Y., Oouchi, T., Takahashi, T., Ogawa, H., Irikura, K., Thio, H. K., Somerville, P. G., Fukushima, Y., & Fukushima, Y. (2016d). Attenuation relations of strong ground motion in Japan using site classification based on predominant period. *Bulletin of the Seismological Society of America, 96*, 898–913.

Seismic Response of Shallow Foundations on Reinforced Sand Bed

Monu Lal Burnwal and Prishati Raychowdhury

1 Introduction

Soil–structure interaction (SSI) influences the response of a structure subjected to dynamic loading in various ways, namely, through period elongation, damping enhancement due to capacity mobilization at the soil–foundation interface, geometric and material nonlinearity, transient and permanent deformations at the foundation level and many more. Past studies, both in experimental and analytical capacities, have demonstrated the aforementioned influences of SSI on various characteristics of a structure. Furthermore, it is well known that the influence of SSI on a structure may seem beneficial, in terms of reduction of force demands and enhanced damping, as well as have detrimental effect in terms of excessive settlement and tilting. The aim of the present study is to explore the possibility of retaining the beneficial effect of SSI by allowing foundation rocking, while trying to control and minimize the settlement by placing geogrid reinforcement below the foundations.

Some of the past studies [such as: Veletsos & Meek, 1974; Bhattacharya & Dutta, 2004; Khalil et al., 2007; Gazetas et al., 2013] had mainly concentrated on elastic demand parameters of a soil–foundation system, such as impedance functions and Eigen properties using different analytical and numerical methods. There had been numerous efforts to model the soil–foundation interface using simplified Winkler springs [Boulanger et al., 1999; Raychowdhury & Hutchinson, 2009; Raychowdhury, 2011; Emami & Halabian, 2018]. Significant effort had also been put in experimental investigation on seismic SSI on shallow foundations using mass shakers, vibrators, shake table and centrifuge facilities. For example, Drosos et al. (2012), Anastasopoulos et al. (2014), Varghese and Latha (2014) conducted shake table tests

M. L. Burnwal · P. Raychowdhury (✉)
Department of Civil Engineering, IIT Kanpur, Kanpur 208016, India
e-mail: prishati@iitk.ac.in

M. L. Burnwal
e-mail: monulal@iitk.ac.in

T. G. Sitharam et al. (eds.), *Advances in Earthquake Geotechnics*, Springer Tracts in Civil Engineering, https://doi.org/10.1007/978-981-19-3330-1_8

using the rigid container. Gibson (1996), Turan et al. (2009), Vivek and Raychowdury (2019) conducted experiments using laminar containers in order to minimize the wave reflection and boundary effects. Gajan et al. (2005), and Liu et al. (2015) carried out conducted a series of centrifuge experiments on shallow foundation-supported structures. Kokkali et al. (2014), Star et al. (2015, 2019), Vivek and Raychowdhury (2020) conducted slow cyclic forced vibration tests on different soil-foundation-structure systems. The following studies focused on geosynthetic reinforced soil behaviour: Alawaji (2001), Bahadori et al. (2020), Latha and Varman (2014), Wang et al. (2015), Xu and Fatahi (2019), Yetimoglu et al. (1994), Xu and Fatehi (2019). Most of the above studies focused on static soil behaviour of reinforced soil through element level and/or model testing; however, seismic SSI studies on reinforced soil utilizing shake table experiments with laminar box facilities are particularly sparse. In the above light of inadequacy of the present state-of-the-art in understanding the efficiency and detailed mechanism of interaction between the foundation-structure system with the reinforced soil underneath it, the present study is focused on investigating the suitability and efficiency of geogrid reinforcement to improve the performance of rocking shallow foundations as well as low-to-medium rise buildings supported on them. A series of shake table experiments were conducted on the geogrid-reinforced soil–foundation structure systems for this purpose. A three-storey model structure was placed in the laminar box filled with loose Ganga sand subjected to a series of harmonic base excitations, as well a seismic excitation from 1991 Uttarkashi Earthquake.

2 Test Details

The details of test setup, soil properties, geogrid characteristics, structural design details, instrumentation and input motion details are discussed in this section.

2.1 Soil Bed Preparation

In this study, locally available Ganga sand was used. The characterization of the sand was done at the geotechnical engineering laboratory of IIT Kanpur. The specific gravity was evaluated using pycnometer method (IS 2386-3), gradation index using sieve analysis (IS 2386-1); minimum and maximum void ratio with relative density test at 50 Hz frequency (IS 2720: 1983); shear strength parameters and shear modulus of the soil were obtained from triaxial and direct shear tests conducted at low confining pressure. The geotechnical properties of the sand are summarized in Table 1. The lamina details of the laminar shear box are provided in Table 2. The widely used rainfall pouring method is used to fill the laminar box. The method employed

Table 1 Properties of Ganga sand

Soil properties	Symbol	Value
Specific gravity	Gs	2.67
Gradation	%Sand	98.19
	%Fines	1.81
	D_{10}	0.15 mm
Effective particle size	D_{30}	0.195 mm
	D_{60}	0.25 mm
Maximum void ratio	e_{max}	0.99
Minimum void ratio	e_{min}	0.70
Unit weight	g	14.07 kN/m^3
Friction angle	f	32.5°
Shear modulus	G_{soil}	8.18 MPa
Poisson's ratio	μ	0.2

Table 2 Details of the laminar shear box used in the shake table test

Materials	Dimensions (mm)	Quantity
Hollow steel box	96 × 49 × 3	15
Hollow steel box	50 × 50 × 2.6	2
Steel plate	40 × 2035 × 5	32
Hollow steel box	35 × 35 × 2.6	8
Thin plastic	0.2 thick	–
Steel	φ50	90
Wooden	1600 × 1100 × 16	1

a hand hooper, and the optimum height of fall was estimated as 15 cm to achieve a relative density of 40%.

2.2 Geogrid

The geogrid reinforcement used for the test had an aperture size of 16 mm × 20 mm, and the average tensile strength was obtained as 60 kN/m using wide strip tensile test (ASTM D6637/D6637M–15) in both the machine and cross-machine direction. The geogrid PET was scaled to an aperture size of 8 mm × 10 mm (a scale factor of 2) to simulate in the shake table. The top layer's depth to footing width (u/B) was kept as 0.2, and the second layer to width ratio was kept as 0.3. The geogrid length to width ratio was chosen as 3. The above-mentioned specifications were selected based on previous studies and various published literature. The plastic membrane is marked at a different height for the placement of geogrid during the filling of sand.

2.3 Structure

A three-story steel moment-resisting frame (SMRF) office building structure was taken for the analysis. The building was designed for seismic zone III conforming to the specifications detailed in IS 800:1998 and IS1893:2000. The prototype frame building had a bay of size 6 m × 6 m with a story height of 3 m. The beam had an ISMB 500 section, and Column has an ISMB 600 section. The typical floor load of 35kN and top floor load of 20 kN is assigned. The earthquake load is provided as per IS:1893. Four square footings were of size 1 m × 1 m, with an estimated bearing capacity of about 235 kPa (for the chosen soil). The experimental model structure is also an SMRF structure of reduced scale as per Iai (1989) using scaling and similitude laws for 1 g shake table analysis. The scaled model had the following geometric properties: bay size: 0.6 m × 0.6 m, height column: 0.3 m, beam section: 10 mm × 10 mm, column section: 12 mm × 12 mm, footing size: 10 cm × 10 cm. More details of the prototype and model structure are listed in Table 3. The scaling factors are summarized in Table 4. Figure 1a shows the structure prototype's schematic, whereas, Fig. 1b shows the experimental setup on laminar box along with schematic of instrumentation details. Figure 2 provides the layout of geogrid layers in the sand bed.

Table 3 Details of the prototype and model structure–foundation system

Parameters	Prototype	Model
Building materials	SMRF	SMRF
Bay	6 m × 6 m	0.6 m × 0.6 m
Column height	3 m	0.3 m
Number of stories	3	3
Beams section	ISMB 500	10 mm × 10 mm
Columns section	ISMB 600	12 mm × 12 mm
Fixed base time period	0.57 s	0.19 s
Damping	0.02	0.02
Typical floor load/mass	35 kN	19.71 kg
Top floor load/mass	20 kN	16.63 kg
Earthquake load (as Per)	IS 1893	
Footing size	1 m × 1m	10 cm × 10 cm
Bearing capacity	235.38 kPa	23.5 kPa
Factor of safety	2.7	1.87

Table 4 Similitude and scaling factors chosen in this study

Symbol	Parameters	Scaling factor	Factors
L	Length (INPUT)	Λ	10
ρ	Density of soil	$\lambda\rho$	1
ε	Strain	$\lambda\varepsilon$	1
$\ddot{\upsilon}$	Acceleration of soil or structure	$\lambda\ddot{\upsilon}$	1
u	Shear wave velocity	$\sqrt{\lambda}$	3.16
ω	Frequency	$1/\sqrt{\lambda}$	0.32
I	Mass moment of inertia	λ^3	1000
F	Shear (per unit breadth)	λ^3	1000
M	Moment (per unit breadth)	λ^4	10,000
K	Stiffness	λ^2	100
C	Damping	λ^2	100

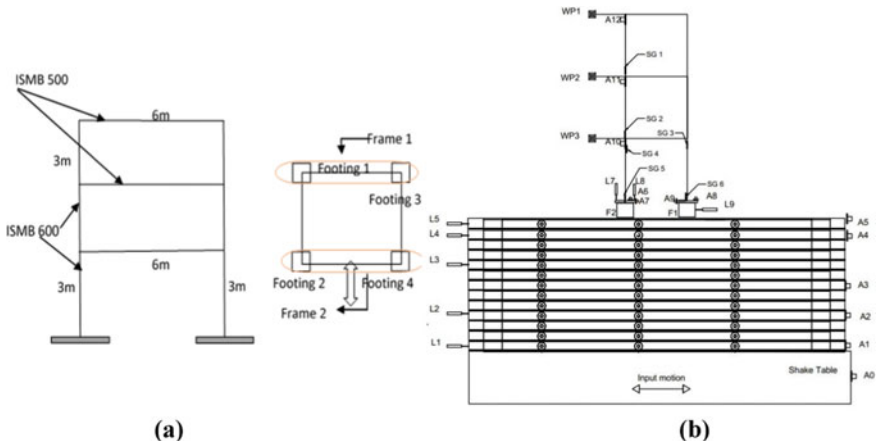

Fig. 1 **a** Details of prototype building and **b** Schematic of test setup with instrumentation details (*Note* A1, A2 etc.: accelerometers, L1, L2 etc.: LVDTs, WP1, WP2 etc.: wire pots, SG1, SG2 etc.: Strain gauges)

2.4 Testing Procedure

The structure was instrumented with several strain gauges, LVDTs, wire potentiometers and accelerometers. The laminar box was instrumented with accelerometers (A1–A5) and LVDT's at 1st, 4th, 7th, 12th, and 13th (surface) laminas. Accelerometers and wire potentiometers are used to measure the displacement and acceleration of the different stories of the structure. The footings F2 and F3 were instrumented with LVDT at different edges, through a thin plate glued using adhesives, to measure

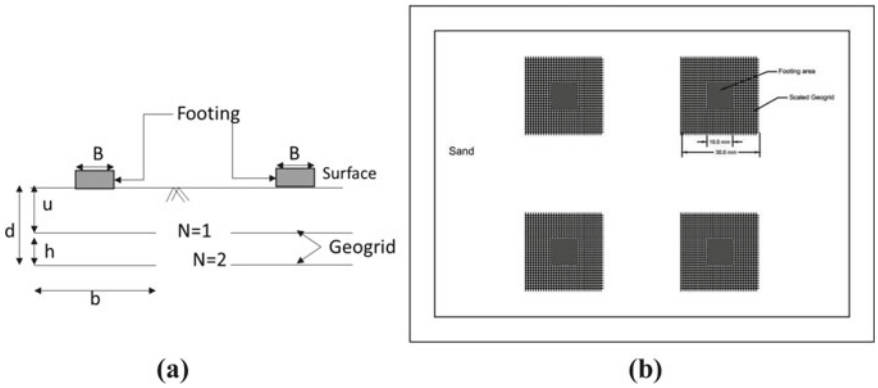

Fig. 2 Geogrid placement details in the sand bed: **a** vertical cross-section and **b** horizontal cross-section

differential settlement and rocking. The footing F1 and F4 were instrumented with horizontal LVDT's to measure the lateral displacement of footings. The F3 was instrumented with a wire potentiometer to measure lateral displacement. All the LVDT's and wire potentiometers were instrumented such that no part of the sensor loads can be influenced by the soil or structure responses. The wires of all the sensors were loosened and tied tightly to supporting beams or to avoid influencing any type of responses. Figure 3 shows a photograph of the set-up during the experiments.

The sensors were connected to a data acquisition system (DAQ) to record and analyze the data. With the help of a crane, the structure was mounted on the compacted and already prepared sand bed. The LVDT's and wire potentiometers mounted on the supporting frames were tied or connected with the structure in such a way that

Fig. 3 Photograph of the instrumented structure–foundation system on laminar soil box

Table 5 Test details with description of input excitations used

Test number	Base condition	Type of loading	Frequency of excitation (Hz)	Target peak spectral displacement (mm)	Peak base acceleration (g)	Duration of shaking (s)
1	Unreinforced soil bed	Harmonic	2.0	1.0	0.016	10.0
2	Unreinforced soil bed	Harmonic	5.0	1.0	0.036	10.0
3	Unreinforced soil bed	Uttarkashi	7.39	1.0	0.027	10.0
4	Single layer geogrid (N = 1)	Harmonic	2.0	1.0	0.016	10.0
5	Single layer geogrid (N = 1)	Harmonic	5.0	1.0	0.036	10.0
6	Single layer geogrid (N = 1)	Uttarkashi	7.39	1.0	0.027	10.0
7	Double layer geogrid (N = 2)	Harmonic	2.0	1.0	0.016	10.0
8	Double layer geogrid (N = 2)	Harmonic	5.0	1.0	0.036	10.0
9	Double layer geogrid (N = 2)	Uttarkashi	7.39	1.0	0.027	10.0

it does not disturb the sand. For the geogrid cases of singly and doubly reinforced sand, the marking of first and subsequent layers was made in the plastic membrane. At each footing, threads are passed from the edges for centring, and the geogrids were placed at these points. The responses of various sensors at different locations were recorded and were analyzed with the data analysis tool in MATLAB. Table 5 provides the details of the tests conducted and the input excitation details used in the study. The unscaled and scaled acceleration time histories and Fourier amplitude spectra of the 1991 Uttarkashi ground motion are shown in Fig. 4.

3 Results and Discussion

The experimental results have been used to understand possible effect of geogrid layers on different parameters of the soil–foundation behaviour, such as: settlement and rocking at footing level and column bending moment of the superstructure. In

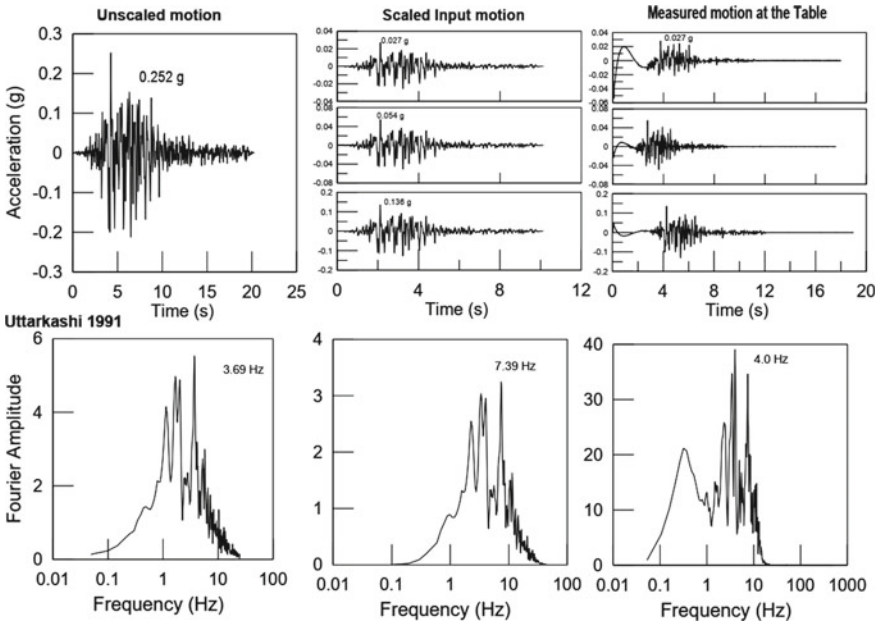

Fig. 4 Original and scaled acceleration time histories and Fourier spectra of 1991 Uttarkashi motion used in this study

addition, the shear stress–strain response of the soil bed has also been analyzed. The following subsections describe about each of the above-mentioned response parameters.

3.1 Footing Settlement

The recorded data from LVDTs placed on the footings of the structure are used to estimate the footing settlement. Figure 5 shows the trend how peak settlement is influenced by the placing of geogrid layers beneath the footing. The geogrid layers are effective to reduce the seismic settlement as much as 18% for the 2 Hz harmonic motion and more than 50% for both Uttarkashi and 5 Hz harmonic motion (when two layers of geogrids are used).

3.2 Footing Rotation

Foundation rotation or tilting is an important parameter in the evaluation of seismic performance of a structure resting on soft to medium dense soils. In this study, the

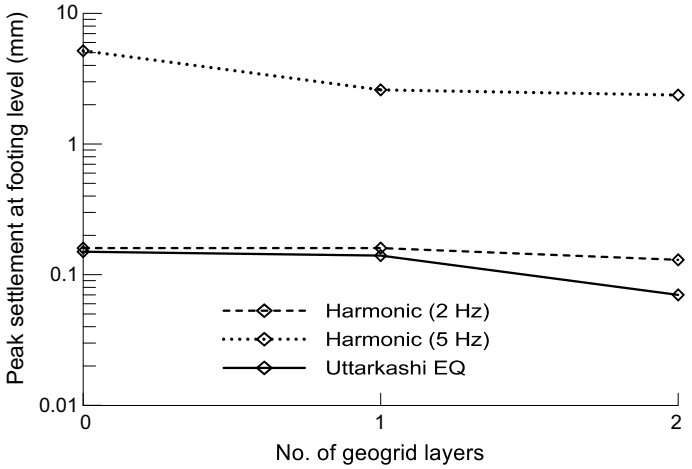

Fig. 5 Influence of geogrid layers on seismic settlement

rotation has been measured from differential vertical displacements of two LVDTs placed on a footing (for example, $L7$ and $L8$ on footing $F2$ as shown in Fig. 1b). Figure 6 presents the peak rotations for different input excitations for three different base conditions: unreinforced, single-layered geogrid case and double-layer geogrid case. It can be observed that the peak rotations are not influenced significantly by placing the geogrid layers.

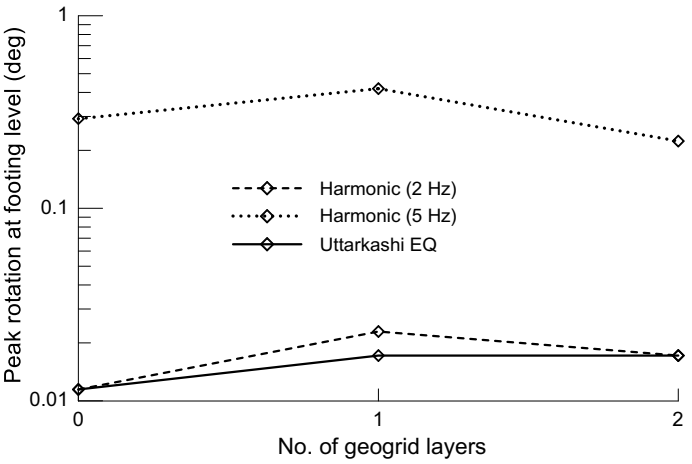

Fig. 6 Influence of geogrid layers on seismic rotation

3.3 Column Moment

Column bending moment has been evaluated from strain gauge data installed at the column at each floor level. The column moment profiles of the structure for various input motions and base conditions are provided in Fig. 7. It can be observed that geogrid-reinforced cases, especially the double-layer case reduce the column moment, particularly at the ground floor level. Since the base moment is one of the most important parameters for damage of a column as well as overall structural failure, the effect of geogrids on the base moments is examined in Fig. 8. It can be noticed that the doubly reinforced layer reduces the base moment in a range of 20–30% for the chosen input motions. The influence is higher for higher intensity motions, which may be due to larger deformations and associated energy dissipation during high intensity shakings.

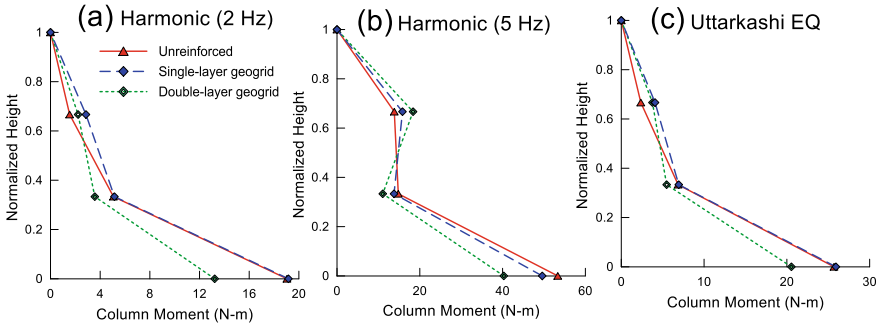

Fig. 7 Column moment profile along height of the structure for different input motions

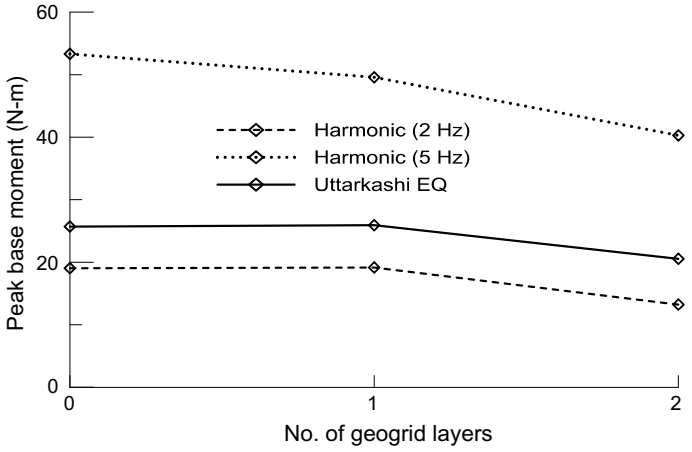

Fig. 8 Influence of geogrid layers on peak base moment

3.4 Shear Stress–Strain Behaviour

Since the response of soil–foundation interface and the superstructure depends largely on the dynamic characteristics and seismic demands of the soil beneath it, it is important to properly characterise the soil deposit. One of the most important aspects of a soil response is its shear stress–strain behaviour, which gives us other crucial dynamic characteristics such as shear modulus, damping ratio and strength estimates. In this study, the shear stress of the soil layer is estimated using the accelerometer record at each lamina using the following relation. At a depth d, shear stress has been estimated from the average of the two accelerometers data as:

$$\tau(d,t) = \tau_{j-1}(d,t) + \rho \frac{\ddot{u}_{j-1} + \ddot{u}_j}{2} \Delta d_{j-1} \tag{1}$$

where, Δd_{j-1} is the spacing between the accelerometer and $\ddot{u}_j$ is the acceleration from the jth accelerometer. The lamina displacement measured from the LVDT directly measures the displacement from the location. Average shear strain γ_j in the jth layer can be evaluated from the recorded data at displacement transducers as:

$$\gamma_j = \frac{1}{\Delta d_{j+1} + \Delta d_j} \left((u_{j+1} - u_j) \frac{\Delta d_{j-1}}{\Delta d_j} + (u_j - u_{j-1}) \frac{\Delta d_j}{\Delta d_{j-1}} \right) \tag{2}$$

Figure 9 shows the shear stress–strain behaviour of the soil at the centre of the deposit (i.e., at the 7th lamina) for harmonic excitation of 5 Hz frequency. All base conditions show a certain amount of energy dissipation and associated strength and stiffness degradations. It is also noticeable that soil with geogrid layers show slightly larger amount of energy dissipation.

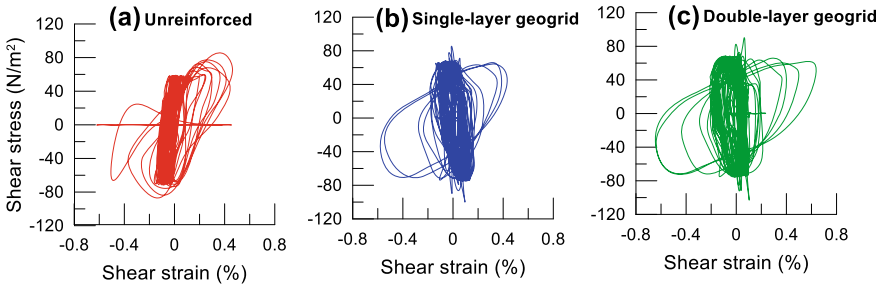

Fig. 9 Shear stress–strain behaviour of soil (at mid depth, for 5 Hz harmonic motion)

4 Conclusions

The present study aims to explore the efficiency of geogrid reinforcement to reduce foundation settlement and excessive tilting during a seismic event. A series of shake table tests on dry medium-dense sand has been performed for this purpose. A three-storey model structure was placed in the laminar box filled with loose Ganga sand subjected to a series of harmonic base excitations, as well a seismic excitation from 1991 Uttarkashi Earthquake. A few critical response parameters have been chosen for the study, namely, column bending moment, foundation settlement and rotation. It has been observed that foundation settlement and column moment at the foundation level significantly decrease when geogrid layers are placed under the footing. The effect is most significant for a doubly reinforced sand bed configuration. The base moment reduces in a range of 20–30% for the chosen input motions, whereas the settlement reduces about 18% for the 2 Hz harmonic motion and more than 50% for both Uttarkashi and 5 Hz harmonic motion (when two layers of geogrids are used). The influence of reinforcement is more significant when high intensity excitations are used compared to the low-intensity motions. It may be concluded that while rocking shallow foundation add benefit to the structural demands such as reduction in base shear and base moment, use of one or two layers of geogrids beneath the foundations may optimally reduce the adverse consequence such as excessive seismic settlement.

References

Alawaji, H. A. (2001). Settlement and bearing capacity of geogrid-reinforced sand over collapsible soil. *Geotextiles and Geomembranes, 19*(2), 75–88. https://doi.org/10.1016/S0266-1144(01)00002-4.

Anastasopoulos, I., Drosos, V., & Antonaki, N. (2014). Shaking table testing of retrofitted 3-storey building. In *Physical Modelling in Geotechnics—Proceedings of the 8th International Conference on Physical Modelling in Geotechnics 2014, ICPMG 2014* (Vol. 2, pp. 1031–1037). https://doi.org/10.1201/b16200-146.

Bahadori, H., Motamedi, H., Hasheminezhad, A., & Motamed, R. (2020). Shaking table tests on shallow foundations over geocomposite and geogrid-reinforced liquefiable soils. *Soil Dynamics and Earthquake Engineering*, *128*(November 2018), 105896. https://doi.org/10.1016/j.soildyn.2019.105896.

Bhattacharya, K., & Dutta, S. C. (2004). Assessing lateral period of building frames incorporating soil-flexibility. *Journal of Sound and Vibration, 269*, 795–821.

Boulanger, R. W., Curras, C. J., Kutter, B. L., Wilson, D. W., & Abghari, A. (1999). Seismic soil-pile-structure interaction experiments and analyses. *ASCE Journal of Geotechnical and Geoenvironmental Engineering, 125*(9), 750–759.

Bureau of Indian Standards (Part 14). (1983). Methods of test for soils: Determination of density index (relative density) of cohesionless soils, IS 2720.

Drosos, V., Georgarakos, T., Loli, M., Anastasopoulos, I., Zarzouras, O., & Gazetas, G. (2012). Soil-foundation-structure interaction with mobilization of bearing capacity: Experimental study on sand. *Journal of Geotechnical and Geoenvironmental Engineering, 138*(11), 1369–1386. https://doi.org/10.1061/(ASCE)GT.1943-5606.0000705.

Emami, A. R., & Halabian, A. M. (2018). Damage index distributions in RC dual lateral load-resistant multi-story buildings considering SSI effects under bidirectional earthquakes. *Journal of Earthquake and Tsunami, 12*(1), 1–46. https://doi.org/10.1142/S1793431118500045.

Gajan, S., Kutter, B. L., Phalen, J. D., Hutchinson, T. C., & Martin, G. R. (2005). Centrifuge modeling of load-deformation behavior of rocking shallow foundations. *Soil Dynamics and Earthquake Engineering, 25*(7–10), 773–783. https://doi.org/10.1016/j.soildyn.2004.11.019.

Gazetas, G., Anastasopoulos, I., Adamidis, O., & Kontoroupi, T. (2013). Nonlinear rocking stiffness of foundations. *Soil Dynamics and Earthquake Engineering, 47*, 83–91. https://doi.org/10.1016/j.soildyn.2012.12.011.

Gibson, A. D. (1996). *Physical scale modeling of geotechnical structures at one-G*. Retrieved from http://resolver.caltech.edu/CaltechEERL:1996.SML-97-01.

Iai, S. (1989). Similitude for shaking table tests on soil-structure-fluid model in 1 g gravitational field. *Soils and Foundations, 29*(1), 105–118.

IS 2386-Part III. (1963). *Method of Test for aggregate for concrete. Part III—Specific gravity, density, voids, absorption and bulking*. Bureau of Indian Standards, New Delhi (Reaffirmed 2002).

Khalil, L., Sadek, M., & Shahrour, I. (2007). Influence of the soil-structure interaction on the fundamental period of buildings. *Earthquake Engineering and Structural Dynamics, 36*(15), 2445–2453. https://doi.org/10.1002/eqe.738.

Kokkali, P., Anastasopoulos, I., Abdoun, T., & Gazetas, G. (2014). Static and cyclic rocking on sand: Centrifuge versus reduced-scale 1g experiments. *Gotechnique, 64*(11), 865–880. https://doi.org/10.1680/geot.14.P.064.

Liu, W., Hutchinson, T. C., Gavras, A. G., Kutter, B. L., & Hakhamaneshi, M. (2015). Seismic behavior of frame-wall-rocking foundation systems I: Test program and slow cyclic results. *Journal of Structural Engineering, 141*(12).

Madhavi Latha, G., & Nandhi Varman, A. M. (2014). Shaking table studies on geosynthetic reinforced soil slopes. *International Journal of Geotechnical Engineering, 8*(3), 299–306. https://doi.org/10.1179/1939787914Y.0000000043.

Raychowdhury, P. (2011). Seismic response of low-rise steel moment-resisting frame SMRF buildings incorporating nonlinear soil-structure interaction (SSI). *Engineering Structures, 33*, 958–967. https://doi.org/10.1016/j.engstruct.2010.12.017.

Raychowdhury, P., & Hutchinson, T. C. (2009). Performance evaluation of a nonlinear winkler based shallow foundation model using centrifuge test results. *Earthquake Engineering and Structural Dynamics, 38*, 679–698. https://doi.org/10.1002/eqe.902.

Star, L. M., Givens, M. J., Nigbor, R. L., & Stewart, J. P. (2015). Field-testing of structure on shallow foundation to evaluate soil-structure interaction effects. *Earthquake Spectra, 31*(4), 2511–2534. https://doi.org/10.1193/052414EQS072.

Star, L. M., Tileylioglu, S., Givens, M. J., Mylonakis, G., & Stewart, J. P. (2019). Evaluation of soil-structure interaction effects from system identification of structures subject to forced vibration tests. *Soil Dynamics and Earthquake Engineering, 116*, 747–760. https://doi.org/10.1016/j.soildyn.2018.09.038.

Turan, A., Hinchberger, S. D., & El Naggar, H. (2009). Design and commissioning of a laminar soil container for use on small shaking tables. *Soil Dynamics and Earthquake Engineering, 29*(2), 404–414. https://doi.org/10.1016/j.soildyn.2008.04.003.

Varghese, R. M., & Madhavi Latha, G. (2014). Shaking table tests to investigate the influence of various factors on the liquefaction resistance of sands. *Natural Hazards, 73*(3), 1337–1351. https://doi.org/10.1007/s11069-014-1142-3.

Veletsos, A. S., & Meek, J. W. (1974). Dynamic behavior of building-foundation systems. *Earthquake Engineering and Structural Dynamics, 3*(2), 121–138. https://doi.org/10.1002/eqe.4290030203.

Vivek, B., & Raychowdhury, P. (2019). Design and calibration of a laminar soil box suitable for a low-capacity shake table using free-field tests on Ganga sand. *Soils and Foundations, 59*(5), 1602–1612. https://doi.org/10.1016/j.sandf.2019.03.010.

Vivek, B., & Raychowdhury, P. (2020). Soil-structure interaction study on 3D SMRFs of Indo-Gangetic plain using resonant vibration tests. *Journal of Earthquake Engineering*. https://doi.org/10.1080/13632469.2020.1822226.

Wang, L., Chen, G., & Chen, S. (2015). Experimental study on seismic response of geogrid reinforced rigid retaining walls with saturated backfill sand. *Geotextiles and Geomembranes, 43*(1), 35–45. https://doi.org/10.1016/j.geotexmem.2014.11.006.

Xu, R., & Fatahi, B. (2019). Novel application of geosynthetics to reduce residual drifts of mid-rise buildings after earthquakes. *Soil Dynamics and Earthquake Engineering, 116*, 331–344. https://doi.org/10.1016/j.soildyn.2018.10.022.

Yetimoglu, T., Wu, J. T. H., & Saglamer, A. (1994). Bearing capacity of rectangular footing on geogrid-reinforced sand. *Journal of Geotechnical Engineering*, *120*, 2083–2099.

Seismic Performance Evaluation of Concrete Gravity Dam on Rock Foundation System with Shear Zone

Bappaditya Manna, Arnab Sur, Amalendu Gope, and Debtanu Seth

1 Introduction

A dam is a massive structure and it stores a huge amount of water. Thus, a thorough analysis is crucial to prevent the failure of dam under different load combinations. In the current paper, a case study is performed on a dam which is constructed with the view of production of hydroelectric energy. The dam is partially resting on a fresh rock and partially on a weathered rock with shear zone. Combined pile–raft foundation is provided particularly for the shear zone to avoid excessive stress and settlement. Moreover, the dam is situated in a seismically very high-risk zone, i.e., in Zone-V. Thus, seismic analysis is very important for the considered dam structure along with the static analysis. There are various numerical models to analyze the effect of static and seismic loading on a concrete dam (Chakraborty & Choudhury, 2013; Wang et al., 2019; Roy et al., 2020) and pile–raft foundation system (Halder & Manna, 2020). However, in the current paper, two types of analysis were performed, such as pseudo-static analysis using the response spectra method as per IS: 1893 (2002) and site-specific time–acceleration dynamic analysis. In addition to earthquake loading, a combination of different other loadings was also applied to the dam structure. The additional loads are—self-weight of dam, water pressure due to full reservoir level and normal dry tailwater, uplift, and hydrodynamic force. Both pseudo-static and dynamic analyses were performed using a finite element (FE) package called Plaxis 2D (Plaxis, 2002).

The main goal of the analysis was to study the compressive stress within the dam body and the ground; the shear force and bending moment distribution within the raft and pile; the total and differential settlement of the raft and the pile; and, the

B. Manna (✉) · A. Sur · D. Seth
Indian Institute of Technology Delhi, Hauz Khas, New Delhi 110016, India
e-mail: bmanna@civil.iitd.ac.in

A. Gope
Ayesa India Private Limited, Noida, Uttar Pradesh 201301, India

T. G. Sitharam et al. (eds.), *Advances in Earthquake Geotechnics*, Springer Tracts in Civil Engineering, https://doi.org/10.1007/978-981-19-3330-1_9

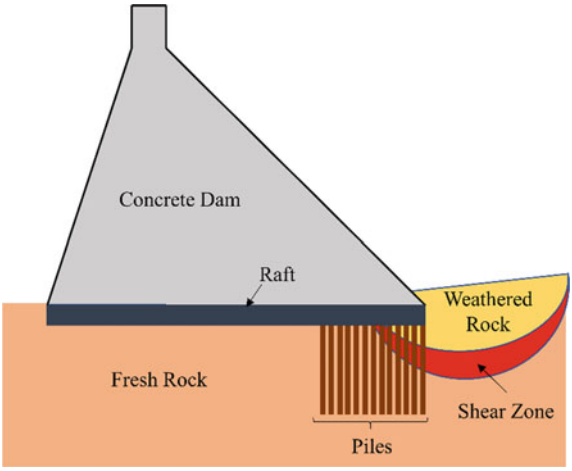

Fig. 1 The typical structure of the considered dam

axial force within the pile. Moreover, the above parameters obtained from the two different methods were also compared. A typical diagram of the concrete gravity dam and foundation system is given in Fig. 1.

2 Methodology

2.1 Material Properties

The dam was made of mass concrete of M15 grade, which is underlain by a raft made of M25 grade concrete. Furthermore, the raft is partially resting on a fresh rock mass and partially on the piles. The properties used in the finite element analysis to model the dam body and the underlying rock layer are given in Table 1.

Table 1 Properties of dam body and underlying rock layer

Parameter	Material Model	Material Behaviour	Wet unit weight, γ (kN/m^3)	Young's Modulus, E (kN/m^2)	Poisson ratio	Cohesion, c (kN/m^2)	Friction angle, ϕ (^{o})
Dam body (M15 mass concrete)	Linear elastic	Non-porous	24	19.4×10^6	0.20	–	–
Fresh Rock	Mohr–Coulomb	Non-porous	27	4.1×10^6	0.25	800	36

The piled raft below the dam was designed for transferring the load from the dam to the underlying rock. The raft was made of M25 grade concrete and had a thickness of 3 m. However, the piles were circular in shape and made of M40-grade concrete. The diameter and length of the piles were 2 m and 25 m, respectively. The piles were installed at a center-to-center distance of 4 m. The material and geometric properties are given in Table 2.

2.2 Modeling

FE analysis is carried out to investigate the performance of gravity dam on rock foundation under seismic condition using PLAXIS 2D (Plaxis, 2002) software. A plain strain model is used for analysis. The dam body, soil, rock mass, and shear zone materials are modeled as 15 nodded triangular plate elements. The pile cap and piles are modeled as beam elements. Interface elements are provided between soil/rock with pile/pile cap elements. The vertical and horizontal boundaries are considered at sufficient distances to avoid the influence of boundary on results. All soil and rock materials are modeled as Mohr–Coulomb material. The fresh rock is considered impermeable. All concrete elements are considered a linear elastic material. The initial ground stress is generated as K_o-method by considering $K_o = 1.0$ for all types of rock mass and $K_o = 0.5$ for soil. The boundaries for static analysis are considered (i) side vertical boundaries as horizontal displacement (u_x) = fixed, vertical displacement (u_y) = free, (ii) for bottom horizontal boundary as u_x = fixed, u_y = fixed. For response spectra method using pseudo-static loading, the dam body is considered a rigid body. For analysis, seismic Zone-V is considered and pseudo-static loads are calculated based on given earthquake coefficients ($\alpha_{hor} = 0.4$ and $\alpha_{ver} = 0.2$) as per Zone-V. Moreover, for dynamic analysis, dynamic load is applied as the time history of acceleration in vertical and horizontal directions. The absorbent boundary is defined by viscous boundary and considering normal and tangential relax coefficients C_1 and C_2 as 1.0. The material damping for soil, rock, and concrete is considered as 5%. The material damping is provided in FE model as Rayleigh damping.

Table 2 Properties of raft and pile

Element	Elasticity modulus, E (MPa)	Moment of inertia, I (m^4)	Axial Stiffness, EA (kN/m)	Flexural Rigidity EI (kN m^2/m)
Raft	2.50×10^4	2.250	7.50×10^7	5.63×10^7
Pile	3.16×10^4	0.785	9.92×10^7	2.48×10^7

3 Results and Discussions

The effect of earthquake force on the dam is observed using two methods. Firstly, the earthquake force on the dam section is considered a pseudo-static load and response spectra method is used for the analysis as per IS: 1893 (2002). Secondly, the dam and the grounds are modeled for dynamic analysis using time history method. A 2D FEM package Plaxis 2D (Plaxis, 2002) is used for analysis in both the cases. The analyses were performed for full reservoir condition.

3.1 Pseudo-Static Analysis

In pseudo-static analysis, the earthquake is represented as pseudo-static loading. The behavior of the dam and the surrounding grounds are studied by dividing the whole structure into three parts (a) Dam body, (b) Raft, and (c) Pile group.

Dam body. The total displacements and compressive stress contours at the different parts of the dam structure under the pseudo-static earthquake loading are shown in Figs. 2 and 3, respectively. It can be seen from Fig. 2, that the total displacement is below 94 mm within the dam body. Similarly, from Fig. 3, the maximum compressive stresses were found at dam heel and toe location. The stresses at the rest of the ground area were within the permissible limit. No tensile force was induced within the dam body or surrounding rock mass. The highest magnitude of the compressive stress within the dam body was found to be 16.41 MPa, which is higher than the allowable compressive stress of the dam made of M15 concrete (Allowable compressive stress = 3.75 MPa).

Raft. The raft below the dam transfers vertical loads from the structure to the bottom rock layer and the pile group. The shear force and bending moment distribution within

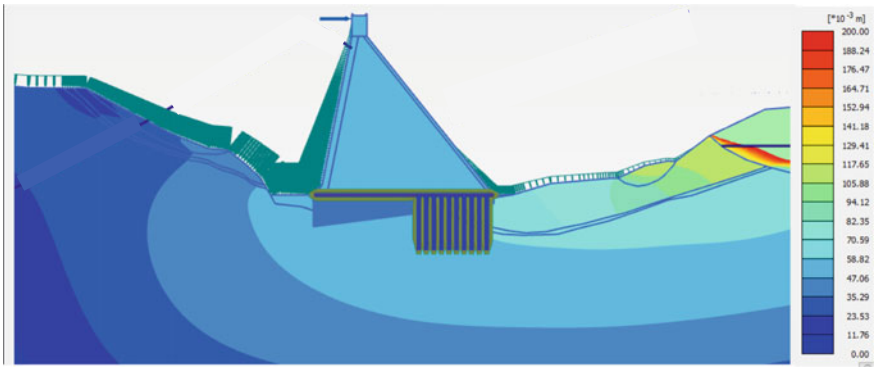

Fig. 2 The displacement contour for the pile-supported dam under pseudo-static earthquake force

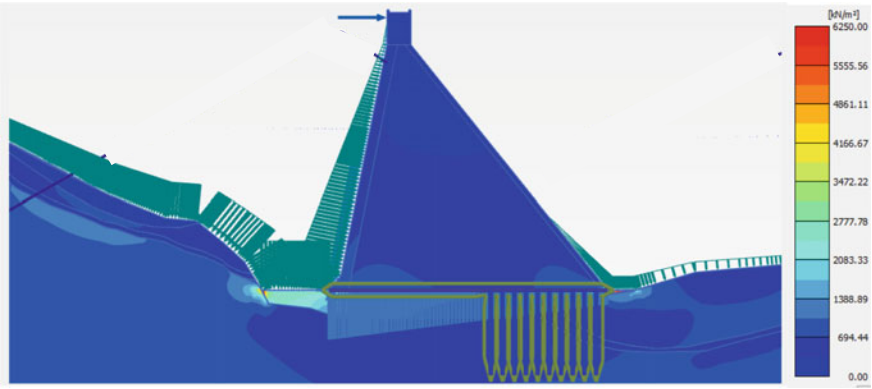

Fig. 3 The compressive stress contour for the pile-supported dam under pseudo-static earthquake force

the raft are shown in Fig. 4a and b, respectively. The shear force and the bending moment within the raft are observed to be positive at the pile heads. Moreover, the bending moment is negative at the rest of the unpiled portion of the raft and positive at the heel of the dam. The peak positive shear force is observed to be at the nearest pile head to the dam toe. The vertical settlement of the raft under the pseudo-static earthquake loading is also studied and the settlement is observed to be slightly higher near the dam heel than the dam toe for the pseudo-static loading. The maximum raft settlement under pseudo-static loading is 42 mm. Moreover, the maximum differential settlement is 1/16500 (in slope) under pseudo-static earthquake loading.

Pile. The load–settlement behavior of the pile was also studied. The shear force and bending moment diagrams for the piles are given in Fig. 5a and b, respectively. Both positive and negative bending moments are induced at the piles near the dam toe. While the positive bending moment is predominant for the distant piles from the dam toe. Moreover, the induced shear force within the pile is predominantly negative.

From the FE analysis, it is observed that negative axial force or axially compressive force is induced within the piles. The maximum axial compressive stress-induced

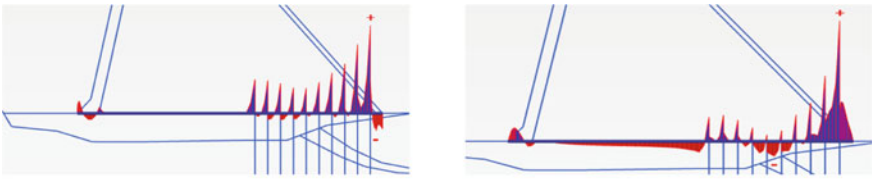

Fig. 4 **a** Shear force and **b** bending moment distribution within the raft under pseudo-static earthquake loading

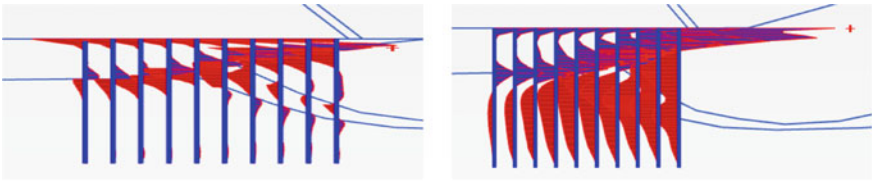

Fig. 5 **a** Shear force and **b** bending moment distribution within the piles under dynamic loading

within a single pile is observed to be 1060 t, which is lesser than the allowable vertical pile capacity of 4082 t. Moreover, the maximum settlement of pile group is obtained as 41 mm at the dynamic earthquake loading.

3.2 Dynamic Analysis

The dynamic analysis was performed using the same model of dam as used for pseudo-static analysis. However, the earthquake loading is induced within dam and ground using design basis earthquake (DBE) with time–acceleration history of earthquakes. For the ease of discussion, the whole structure can be divided into three parts: (a) Dam body, (b) Raft, and (c) Pile group.

Dam body. The magnitude of displacements and compressive stresses within the dam body under the earthquake loading were shown using colored contours in Figs. 6 and 7, respectively. It can be seen from Fig. 6, that the total displacement at the upper portion of the dam is comparatively higher compared to the rest of the dam

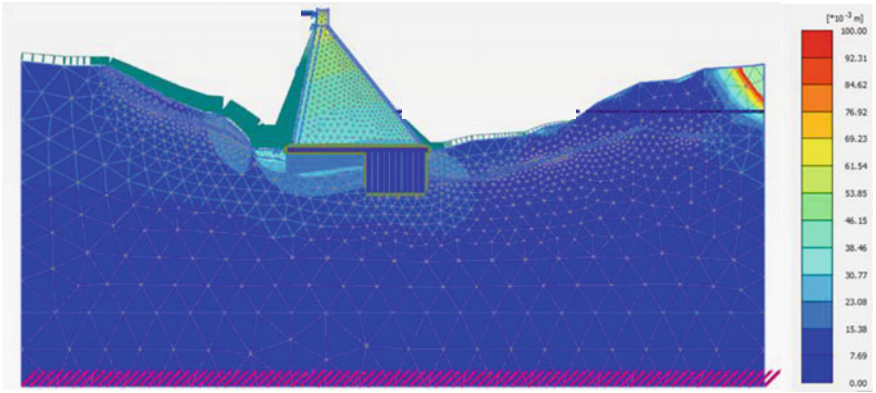

Fig. 6 The displacement contour for the pile-supported dam under earthquake forces obtained using dynamic analysis method

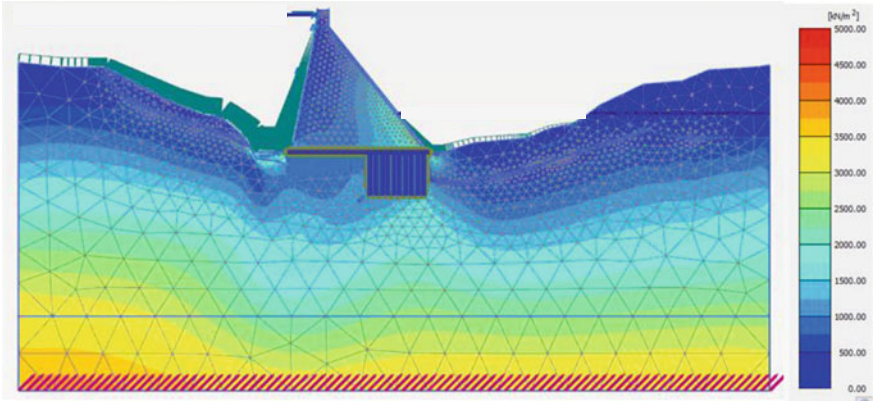

Fig. 7 The compressive stress contour for the pile-supported dam under earthquake forces obtained using dynamic analysis method

body. Similarly, the maximum compressive stresses were found at dam heel and toe locations, as can be seen in Fig. 7. The stresses were exceeding up to 2.0 m zone from the heel and toe. However, at the rest of the dam area and rock mass the stresses were within permissible limits. The maximum tensile stress in dam is found to be zero. The highest magnitude of the compressive stress within the dam body was observed to be 7 MPa, which is higher than the allowable compressive stress of the dam made of M15 concrete (Allowable compressive stress = 3.75 MPa).

Raft. The shear force and bending moment distribution within the raft are shown in Fig. 8a and b, respectively. From Fig. 8a, it is observed that the peak positive shear force occurs at the nearest pile head to the dam toe under dynamic loading condition. Again from Fig. 8b, it is observed that the bending moment within the raft is positive at the pile heads and negative at the rest of the unpiled portion of the raft. The highest positive bending moment is observed at the pile head nearest to the toe of the dam. The bending moment is also positive at the heel of the dam. Moreover, both the shear force and bending moment distribution within the raft are almost similar before and after the application of the dynamic earthquake loading.

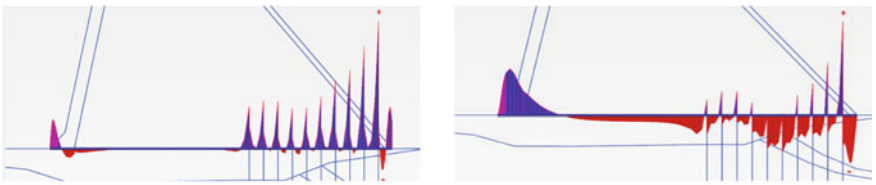

Fig. 8 **a** Shear force and **b** bending moment distribution within the raft under dynamic loading

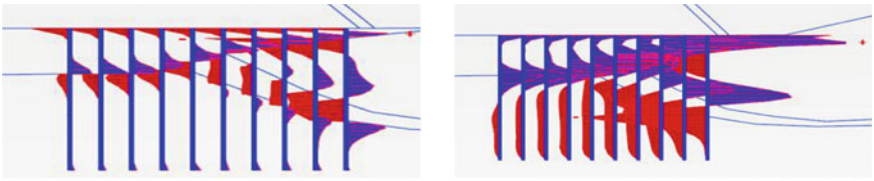

Fig. 9 **a** Shear force and **b** bending moment distribution within the piles under dynamic loading

The vertical settlement is observed to be positive or vertically upward at the dam heel side; while the raft at the dam toe side is subjected to a negative or vertically downward settlement. Moreover, the maximum raft settlement under dynamic earthquake loading is obtained as 44.6 mm, while the slope of maximum differential settlement is observed to be 1/3500.

Pile. The bending shear force and moment diagrams of the piles are shown in Fig. 9a and b, respectively. In both the cases, the peak bending moment and the peak shear force occurred in the pile nearest to the dam toe. Moreover, the induced shear force and bending moment in the pile are decreased with the increasing distance from the dam toe.

From the FE analysis, it is observed that only axially compressive force is induced within the piles. The maximum axial compressive stress-induced within a single pile is reported to be 2348 Ton. Moreover, the maximum settlement of pile group is obtained as 43.7 mm under the dynamic earthquake loading.

3.3 Comparative Study of Pseudo-Static Method and Dynamic Analyses

The results obtained from pseudo-static and dynamic analyses were compared. It is observed that the total displacement and compressive stress within the dam body are in the same range for both pseudo-static and dynamic analyses. The shear force and bending moment distribution within the raft and pile are also observed to be similar for both the analysis methods. However, the raft settlement is negative in pseudo-static analysis, while both negative and positive raft settlement is observed for dynamic analysis.

Table 3 shows the comparison of results obtained from conventional pseudo-static analysis and dynamic time history analysis. It can be seen that all the results are in comparable range except for pile load, for which dynamic analysis predicts a much higher value.

Table 3 Comparison between the observations obtained from pseudo-static analysis and dynamic analysis

Analysis description	Pseudo-static analysis	Dynamic analysis
Maximum compressive stress (MPa) on dam body (M15)	16.41	7.0
Maximum compressive stress (MPa) On dam founding layer (PCC M25)	10.90	9.5
Maximum axial force on single pile (tonne)	1060	2348
Maximum settlement of pile group (mm)	41	43.7
Maximum settlement of raft (mm)	48	44.6
Maximum differential settlement of raft (in slope)	1/16500	1/3500
Maximum stress on rock mass at interface below dam (MPa)	1.7	1.4

4 Conclusions

Finite element analyses have been carried out using Plaxis 2D (Plaxis, 2002) for gravity dam resting on the rock foundation with shear zone. The dam foundation structural system consists of 2 m diameter piles rigidly connected with piled raft below the dam foundation near shear zone. Two types of analyses are performed for seismic performance evaluation of gravity dam: (a) pseudo-static analysis using response spectra method and (b) dynamic analysis using design basis earthquake (DBE). The following observations can be made from the results of finite element analyses:

- The maximum compressive stresses of dam body and dam founding layer exceed the allowable compressive stresses within a significant zone near the dam toe and heel locations.
- The shear force and bending moment distribution within the raft and pile are observed to be similar for both methods of analysis.
- The settlement of piles rigidly connected with raft is found more than the permissible values.
- As the foundation is resting on a strong rock, the major part of the vertical load is transferred through contact between rock and raft foundation.

References

Chakraborty, D., & Choudhury, D.: Pseudo-static and pseudo-dynamic stability analysis of tailings dam under seismic conditions. In *Proceedings of the national academy of sciences, india section a: Physical sciences* (Vol. 83(1), pp. 63–71). Springer, India (2013).

Halder, P., & Manna, B.: Performance evaluation of piled rafts in sand based on load-sharing mechanism using finite element model. *International Journal of Geotechnical Engineering*, 1–18 (2020).

IS: 1893 (Part 1). Criteria for earthquake resistant design of structures. Bureau of Indian Standards (2002).

PLAXIS (2002) PLAXIS 2D: Reference manual, version 8.0. Plaxis BV, Delft.

Roy, J., Kumar, A., & Choudhury, D. (2020). Pseudostatic approach to analyze combined pile-raft foundation. *International Journal of Geomechanics, 20*(10), 06020028.

Wang, P., Zhao, M., Du, X., & Cheng, X. (2019). A finite element solution of earthquake-induced hydrodynamic forces and wave forces on multiple circular cylinders. *Ocean Engineering, 189*, 106336.

Visualization of Liquefaction in Soils with PWP Measurements by Tapping

Chandan Ghosh and Supratim Bhowmik

1 Introduction

Following large earthquakes, liquefaction-induced failure in many geo-structures remains major interests for geotechnical discipline, and various post-failure case studies are available in the literature. With the advent of computer simulation, dynamic shake table-mounted centrifuge tests, laboratory physical scale model tests, and in situ tests, attempts are made to the development of constitutive and numerical modeling tools to characterize the liquefaction-prone soils (Perlea & Beaty, 2010). The computational work reported in Boulanger and Ziotopoulou (2015), Manzari et al. (2018) has revealed that practicing engineers need simple yet elegant field tools to ascertain the liquefaction initiation and subsequent onset of lateral spreading leading to mass-scale failure of geo-structures. The lessons learned from Liquefaction Experiment and Analysis Projects (LEAP) on Ottawa sand (F-65) were that (1) only a few of the available numerical techniques are reliable for liquefaction prediction and (2) there is a wide variability in many of the centrifuge tests (Perlea & Beaty, 2010). It noted that rounded soil particles of uniform size are usually susceptible to liquefaction. While well-graded granular soils, due to their stable configuration, are relatively less prone to liquefaction, the natural silty sands which are deposited in a loose state, are more prone to shear contraction. Clayey soils are resistant to the relative movement of particles during cyclic shear loading and hence are not prone to liquefaction. Non-plastic silts do not create adhesion and hence do not provide appreciable resistance to particle rearrangement and liquefaction. Sandy soils with appreciable fines content may be inherently collapsible, perhaps because of the greater compressibility of the fines between the sand grains.

C. Ghosh (✉)
National Institute of Disaster Management, Ministry of Home Affairs, New Delhi, India
e-mail: chandan.nidm@nidm.gov.in

S. Bhowmik
Ministry of Road and Surface Transport, NHIDCL, New Delhi, India

T. G. Sitharam et al. (eds.), *Advances in Earthquake Geotechnics*, Springer Tracts in Civil Engineering, https://doi.org/10.1007/978-981-19-3330-1_10

The occurrence of earthquakes is inevitable in the Himalayas and almost after eight decades Nepal has been shaken by M7.9 earthquake on 25 April 2015 followed by a series of large aftershocks that rocked the entire northern and northeastern India. The M6.4 Sonitpur (29 April 2021) earthquake in the state of Assam, India, affected several buildings in the Guwahati, which is more than 100 km away and caused several trails of liquefaction in the riverside areas of the Brahmaputra. Likewise, the country has experienced several devastating inter-plate as well as intra-plate earthquakes during the last 125 years, with heavy liquefaction-induced destruction in the hilly terrains. The liquefaction effects were widely observed following the 1934 Bihar–Nepal in India, the 1948 Fukui Earthquake in Japan, the 1964 earthquakes in Niigata, Japan, and Alaska, and more so due to Bhuj (2001), Kashmir (2005) earthquakes. Earthquake causes soft sediments that tend to amplify and prolong shaking duration. Hence, continued interests in the small-scale physical modeling as well as recreating in situ of stress and strain during the onset of liquefaction have been underway since the 1964 Nigata earthquake.

During an earthquake, seismic energy passes from the focus to the sub-structure through which it is transmitted to the superstructure. Excess pore pressure generation in the saturated fine-grained soil deposits has been used to characterize the liquefaction potential. Liquefaction phenomena are the consequence of earthquake-induced excess pore water pressure in the soil. This phenomenon is uncertain and varies with the change in drainage, soil consistency, grain size distribution, earthquake duration, amplitude and frequency of shaking, distance from the epicenter, location of water table, and permeability of soil layer (Chang et al., 2007; Perlea & Beaty, 2010; Rathje et al., 2005). A procedure based on field penetration resistance and cyclic stress resistance has been developed using PGA which assesses the initial liquefaction of soil, now being used widely all over the world (Seed & Idriss, 1971; Seed et al., 1983). A number of case histories of liquefaction-induced ground deformation and their effects on constructed facilities are well recorded in the state-of-the-art reports (Dobry, 1995; Dobry & Abdown, 1998; O'Rourke et al., 1989). The initial excess pore water pressure plays a role in the nonlinear, dynamic response of granular soils. The pore-pressure generation characteristics from field reconstituted specimens are presented. The pore pressure patterns at various strain levels, the observed stages, and pore pressure generation curves are obtained (Jiaer et al., 2580). The semi-empirical liquefaction procedures can be evaluated effectively by providing the in situ pore pressure generation and dissipation behavior of liquefying soils. The liquefaction potential for Delhi and Northeastern India has been evaluated based on the field SPT test data and shear wave velocity survey using different models (Chang et al., 2007; Rathje et al., 2005).

2 Seismic History of Delhi

The National Capital of India, Delhi, has a long history of being vulnerable to earthquake hits (Iyengar & Ghosh, 2004; Agarwal and Chawla, 2006). The first known earthquake jolted the city around 893AD (Oldham, 1883), and the first earthquake

was recorded on 6 July 1505. The first documented earthquake of 6.5 magnitude hit the city on 15 July 1720) (Iyengar, 2000). Besides a number of earthquakes near and far from the city had also caused great damage. These earthquakes are Mathura (1803 and 1842), Kangra (1905, M8.1), Khurja (1956, M6.7), Moradabad (1966), Uttarkashi (1991), Chamoli (1999), Bhuj (2001), and Kashmir (2005). More records on large Himalayan earthquakes, which caused great damage to the capital city are found in Iyengar (2004), Perlea and Beaty (2010), Rajendran and Rajendran (2005), Iyengar (2000). Qutub Minar, a famous landmark in Delhi also faced severe damages from time-to-time earthquakes. Mathura Earthquake on 25 August 1803 had caused great damage to Qutub Minar, documented by Nazir Akbarabadi, 1740–1803, in his Urdu poem Bhucal-nama (Iyengar & Ghosh, 2004). As per Indian Seismic Code, India, has four macro zones (IS 1893: 2002). As this zonation is primarily based on the historical occurrences of the earthquake in the last 600 years, there is significant variation in the intensity of ground motion, which depends largely on the geological properties, as well as the magnitude of earthquake. Microzonation of a few Indian cities, including Delhi, Guwahati, Kolkata, etc., has been completed and similar studies of the most seismically vulnerable cities are in progress.

Delhi being situated on the right bank of the Yamuna River and bounded by Indo-Gangetic alluvial plains in the north- and east-faced severe threats of liquefaction. The soil types consist of low plastic silt, sandy silt, fine sand, clay with low and medium plasticity, and alluvium. The earthquakes being amplified by alluvial soil, the Yamuna River bed section is more vulnerable to liquefaction even under small and moderate earthquakes. The Trans-Yamuna area of Delhi is prone to liquefaction damages based on M7.2 earthquakes. More than 80% of the soil have potential to liquefy. The aim of this paper is to examine the chances of liquefaction of Yamuna River sandy silt by experimenting with two bottles and creating thereby dynamic excitation into the loose specimen by manual tapping vis-à-vis measuring the changes in the excess PWP as compared to eight more soil specimens under similar test conditions. Experimental visualization of the rise in corresponding water level with respect to three sizes of drain pipes has been carried out in a large container.

3 Experimental Investigations

Considering the significance of various laboratory and field studies done since the 1964 Niigata Earthquake, it has no doubt that pre–during–post liquefaction aspect requires more precise yet field-sensitive characterization. To this extent, several physical model test has been performed using shaking table (Perlea & Beaty, 2010; Prasad et al., 2004; Youd & Holzer, 1994; Kramer, 1996). In this study, the following aspects have been incorporated: Use of sandy silty soil in water container that will be able to recreate soil layer in the loosest possible state, which is one of the prerequisite for creating liquefaction; Checking the embedment depth of physical model subjected to excitation by finger-tapping; Effect of continuous vibration versus Initial (loosest) condition; Physical objects are placed inside the soil in such a manner that even little

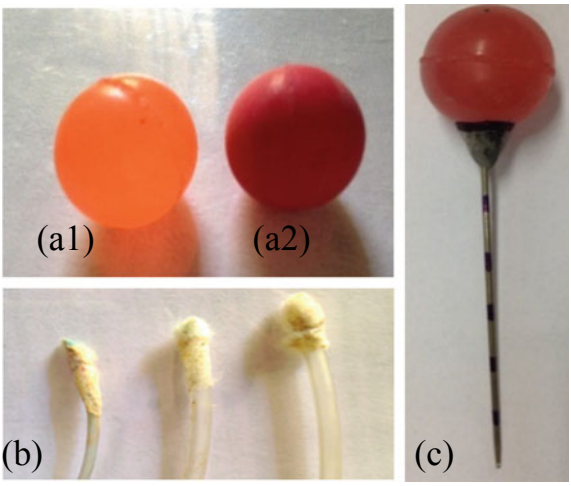

Fig. 1 **a1** Rubber ball lighter than water: **a2** Ball heavier than water being used as underground model utilities **b** Three different plastic tubes with their ends masked with cotton piezometer. **c** Lighter ball pierced with a needle being used as overground model structure

tapping or vibration will be enough to create changes in the density of loose specimen; Measuring relative variation of PWP inside the soil specimen during liquefaction, which is otherwise not possible by existing methodologies, where PWP transducers are placed usually at the specimen boundaries; Use of particular size of stand pipe which will not disturb the grain structure much for the exact capturing of excess PWP; Visualization of liquefaction effect on model objects, e.g., floating of submerged ones and large settlement of building (Fig. 1); Effect of manual tapping (low energy impact) on a small container model on nine different types of soil, including fly ash, clay, stone dust, where liquefaction usually don't occur; The nine different sample (Fig. 2) collected from North and Northeast India are investigated to find the vulnerability of liquefaction and comparing it with fine sand of the Yamuna River, Delhi (Fig. 3). Experiment on a large container signifies relative measure of excess PWP with respect to height.

4 Creating Liquefaction Effect by Tapping

The main aim of this preliminary stage of experiment is the visualization of vibration effect on loose saturated sand in terms of a relative measure of PWP increase; in synchronization with the liquefaction effect on underground objects such as sewerage pipeline, tunnel, manhole cover, earthfill dam, tilting of buildings as well as capturing excess PWP through an open standpipe placed inside soil specimen. Simplified experimental devices explaining the reason for liquefaction by tapping and measuring excess PWP, which is otherwise being done PWP transducer in laboratory. Measuring the relative increase in the density of loose sand as an input energy is applied vis-a-vis impact on the settlement of overground object. Easy process for reconstituting of test specimen ensuring minimum variation in the initial condition before applying tapping energy.

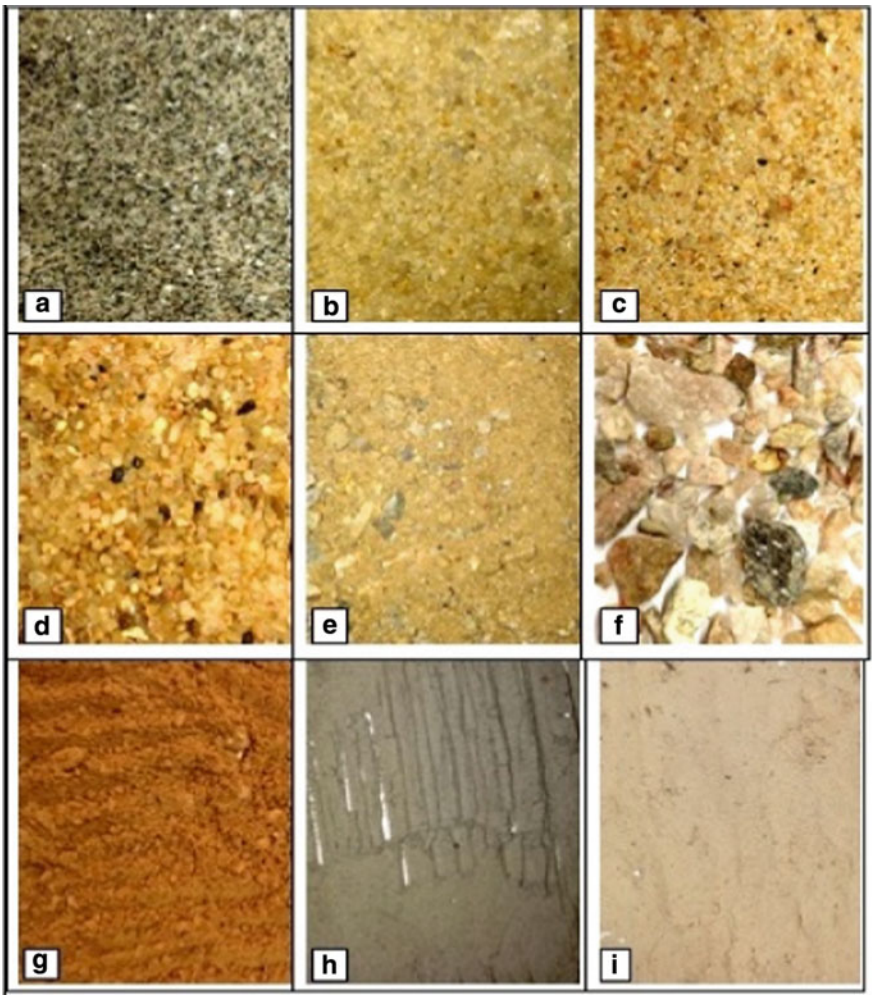

Fig. 2 A close view of the nine soil specimens, **a** The Yamuna River sand, Delhi **b** The Gomoti River sand, Tripura **c** Kolkata medium sand, **d** Khowai coarse sand, Tripura **e** Badarpur well-graded sand, Delhi, **f** Pebbles, **g** Clay, **h** Fly ash, **i** Stone dust

4.1 The Present Investigation

Visualizing liquefaction effect by manual finger tapping, respectively, on 500 ml bottle without PWP measurement, 2000 ml bottle with PWP measurement (keeping bottle cap closed and open), and on 5 L container with three different pipe diameters. Excess PWP being measured in terms of an increase in the water column on the standpipe, which is placed inside the soil specimen. Effect of number of tapping on the gradual increase in the settlement of loose soil at varying initial height. Measurement

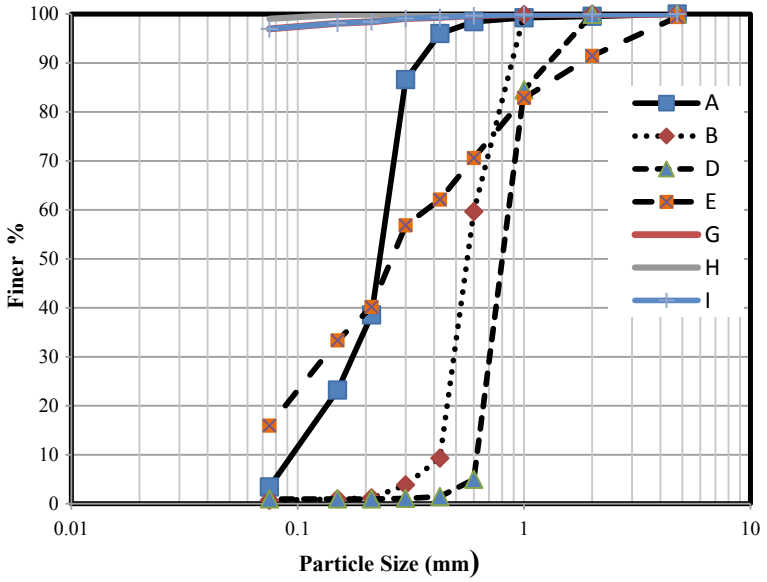

Fig. 3 Grain size distribution curve for the seven different soil specimens

of the liquefaction effect on the embedded and overground objects (Fig. 1), for which amount of settlement is being recorded. Deciding the pipe diameter to be used for the next series of experiments, in which water level fluctuation due to the finger Tapping as input source of dynamic excitation by earthquake are being noted. As the aim of the current experimentation is to visualize the phenomena of liquefaction-induced failure (Fig. 4), the exact amount of energy input by index finger-tapping was not accounted for. As long as the liquefaction event as shown in Fig. 1, is recreated in the series of model experiments by using the same set of small and large bottles and characteristic differences of the same are noted in the nine different types of soils, the exact measurement of input energy to the equivalent earthquake energy is not of prime concern.

5 Discussions

The main inspiration for the laboratory simulation is to recreate the situation shown in Fig. 4. The underground sewerage pipelines got uplifted due to the buoyancy effect. The soils of various consistencies are shown in Fig. 5 and as the size of the bottle is small, spherical rubber balls are used as representative underground utilities.

Height variation (densification) of loose sandy soil (initial height indicated in each case) due to Tapping by Index finger, showing liquefaction in Yamuna and Gomoti sand and lesser in Kolkata sand but no liquefaction is observed in Khowai, Badarpur sand, Badarpur pebbles, clay, fly ash, and stone dust, thus signifying the difference

Fig. 4 Upliftment of Manhole due earthquake-induced liquefaction

Fig. 5 Nine Soil specimens in 500 ml bottle subjected to finger tapping as external excitation

between fine, medium, and coarse sands, while subjected to dynamic force. No PWP measuring device was installed in the small 500 ml container but tapping did not show visually the buoyant effect of 20 mm dia object placed inside in each case. Equivalent thickness of the sand due to 20 mm dia ball is than 1.5 mm. Specimen height showed an insignificant variation compared to the Yamuna fine sand.

Relative changes of excess PWP, which are expressed in terms of water column above static height of water in a 2 L container, are captured by Open Stand Pipe and it is plotted against the No. of tapping. The variation in the water ht. versus No. of tapping curve is the indicative of liquefaction occurrence checked in the Yamuna sand ht of 90 mm, 120 mm, 150 mm, and the Gomoti sand of 130 mm ht., respectively. During liquefaction, the embedded round object (Fig. 1a) moved up and floating

object (Fig. 1c) moved down. This is the case observed in Fig. 4 due to earthquake-induced liquefaction. As the sand specimen was made at the loosest possible state, the experiment showed a significant reduction in height as number of tapping increased. Specimen height and water column in the 1 mm diameter standpipe were taken at every stage of tapping.

Test condition is same as Fig. 7 but with bottle cap open (Fig. 8) as in the 500 ml bottle experiment (Fig. 6). Out of nine soils, only two of them showed liquefaction, subsequent tests on the 2 L bottle were done for the Yamuna sand and Khowai sand only. Excess PWP showed orderly reduction as number of tapping increased.

In Fig. 9a, the test setup is shown. (I): Test on the Yamuna Sand in 5 L container with pipe dia 1 mm(II), 2 mm(III), 2.5 mm(IV). Variation water ht. was recorded using colored ink. Here tapping was done through a hammer. As evident water column variation is relatively more at the initial number of tapping. There is also residual confining pressure marked in the standpipe. Out of three different sizes of the standpipes, distinct measurements in 1 mm dia pipe were seen. Therefore, all other series of experiments were done with 1 mm pipe.

Experiments on large containers gave a more realistic nature of the liquefaction phenomena. Out of nine soil specimens, the Yamuna River fine sand, Delhi, is highly liquefiable. Based on a series of tests on bottles filled up with different types of soils, both visualization of the liquefaction phenomena and measurement of excess PWP have been explained in this paper. The visualization of the liquefaction process, which is mainly due to external forces causing the saturated sandy silty soil to loose shear strength, has been captured by a Piezometer of 1 mm internal diameter standpipe

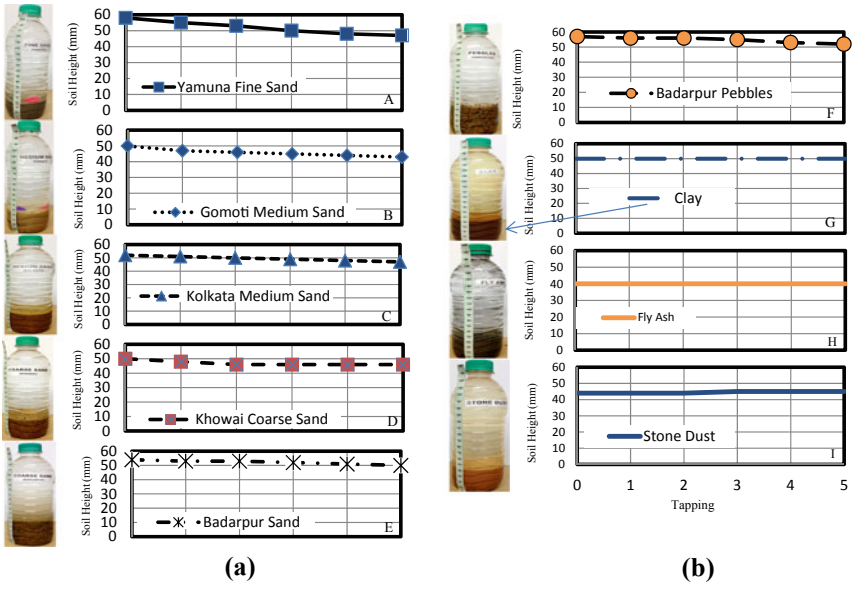

Fig. 6 **a** Soil height versus Tapping energy count No. in 500 ml bottle. **b** Soil height versus Tapping energy count No. in 500 ml bottle

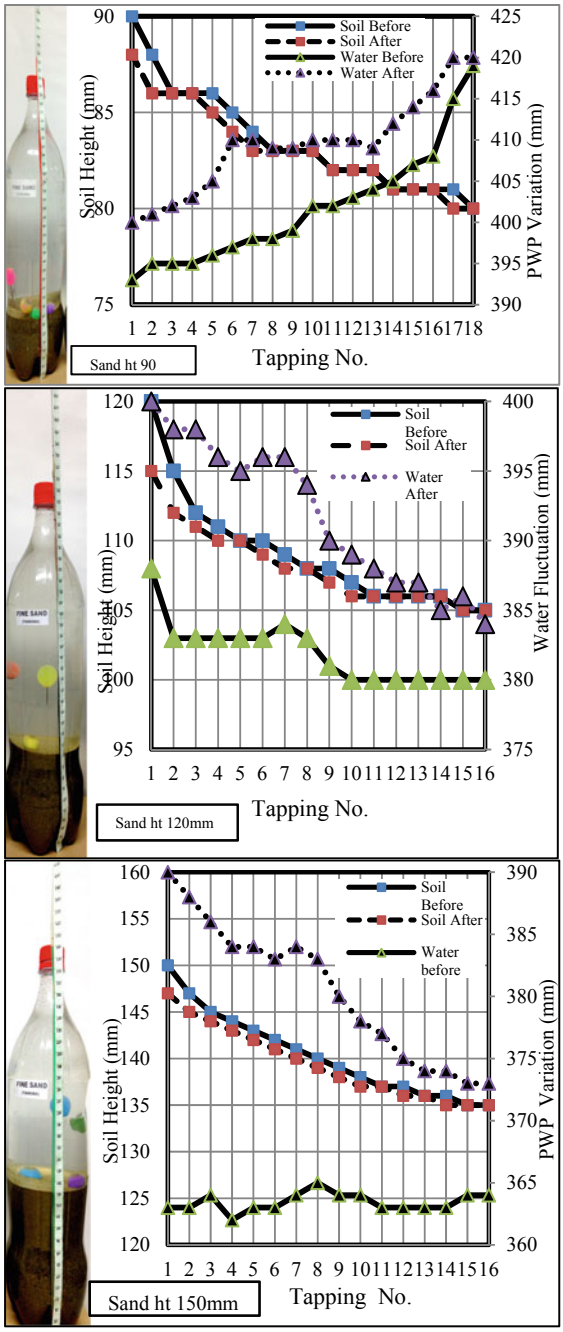

Fig. 7 Soil Height and PWP Variation versus no. of tapping (closed cap condition)

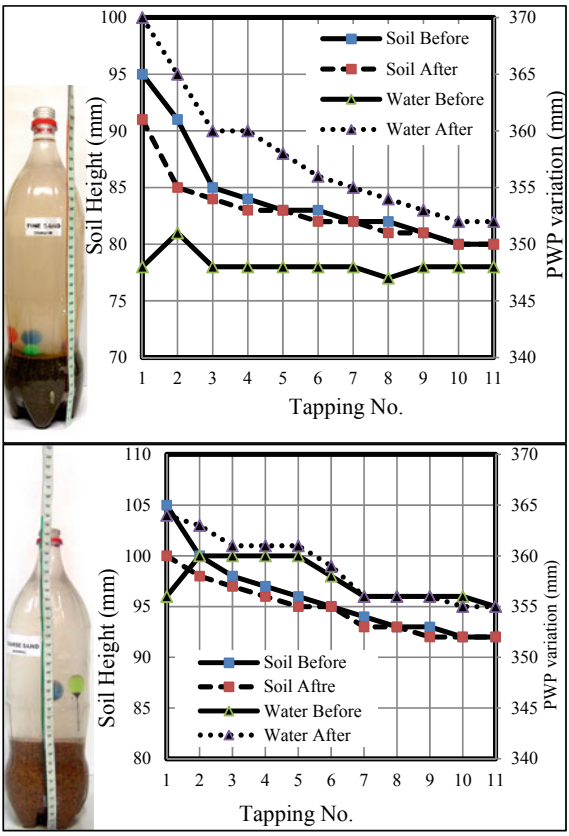

Fig. 8 Soil Height & Water Fluctuation versus no. of tapping (Open Cap Condition)

with its tip filled with cotton foam. The experiments were quick and repetitive, thus eliminate errors in sample preparation. Simulation of underground utilities and overground buildings in a liquefiable soil has been done by 20 mm diameter rubber ball affixed with a needle. Capturing the upward movement of the balls and downward movement of the needle fixed ball vis-à-vis instant jumping of water level in the standpipe is some of the unique experimental findings. The results show that out of nine types specimens tested, the Yamuna River sand in Delhi and the Khowai River sand in the state of Tripura, India, are highly liquefiable and PWP variation during dynamic excitation has been measured and simulated during experiment.

6 Conclusions

Visualization of the liquefaction process, which is mainly due to external forces causing the saturated sandy silty soil to loose shear strength, has been measured by simple experiments. The simplicity of the experiments in bottles and buckets vis-à-vis the liquefaction phenomena being evaluated in sophisticated laboratory tests are

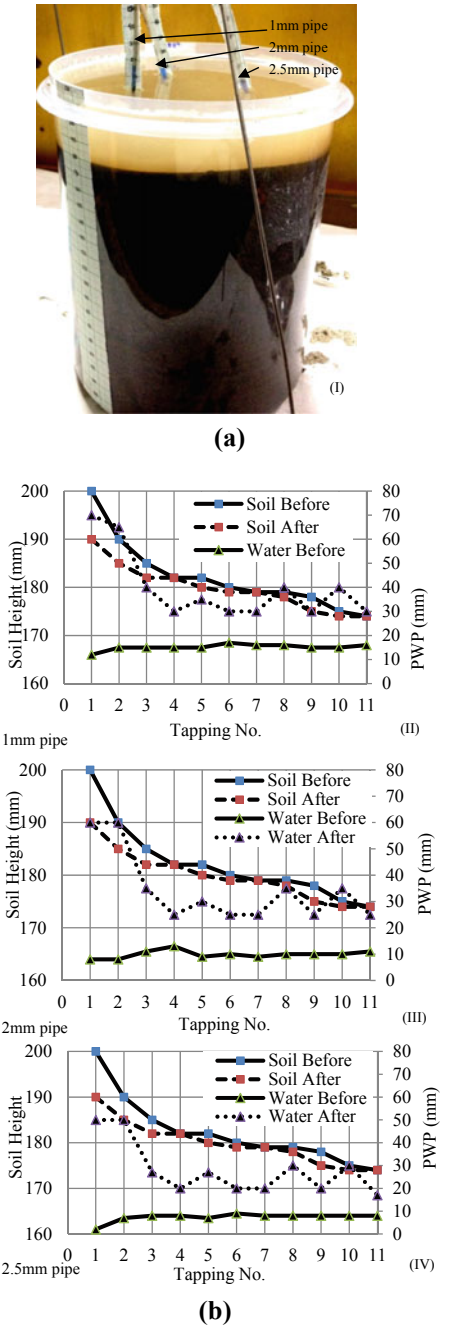

Fig. 9 **a** Soil height and Water Fluctuation versus no. of tapping. **b** Soil height and Water Fluctuation versus no. of tapping

explained. the use of 1 mm diameter open pipe as an equivalent Cassagrande-type piezometer has been very elegant to capture PWP changes during liquefaction. While doing tests in 500 ml and 2 L bottle, its easier to prepare and recreate specimens in the loosest state. Therefore, experiments were quick and repetitive. Several sets of tests were done in order that there is little or no variation in the tapping energy input. Installation of the standpipe at the bottom of 2 L bottle is a simple technique that ensured capturing PWP changes within the specimen, which is otherwise not feasible in routine liquefaction devices. Simulation of underground utilities and overground buildings in a liquefiable soil has been done by 20 mm diameter rubber ball affixed with a needle. Capturing the upward movement of the embedded spheres and downward movement of the needle fixed sphere vis-à-vis instant jumping of water level in the standpipe is the unique experimental findings as reported in this paper. Measurement of excess PWP was possible by these simple experiments and the same is evaluated for nine soil specimens under similar test conditions.

References

Agrawal, S. K., & Chawla. J. (2006). Seismic hazard assessment for Delhi region. *Current Science, 91*, 1717–1724 (2006).

Boulanger, R. W., & Ziotopoulou, K. (2015). PM4Sand (Version 3): A sand plasticity model for earthquake engineering applications. Report No. UCD/CGM-15/01. Davis (CA): Center for Geotechnical Modeling, University of California; 2015, p. 112.

Chang, W.-J., Rathje, E. M., Stokoe, K. H. II, & Hazirbaba, K. (2007). In Situ pore-pressure generation behavior of liquefiable sand. *Journal of Geotechnical and Geoenvironmental Engineering, 133*(8), 921–931.

Dobry, R. (1995). Liquefaction and deformation of soils and foundations under seismic conditions, State-of-the-Art Paper. In S. Prakash (ed.), *Proceedings, Third Intl. Conf. on Recent Advances in Geotechnical Earthquake Engineering and Soil Dynamics.* St. Louis, MO, April 2–7, 3, 1465–1490.

Dobry, R., & Abdown, T. (1988). Post-triggering response of liquefied sand in the free field and near foundations. *Proceedings of the Conf. on Geotechnical Earthquake Engineering and Soil Dynamcs III*, Seattle, WA, ASCE Geotechnical Special Publication No. 75, Vol. I, pp. 270–300.

Iyengar, R. N. (2000). Seismic status of Delhi megacity. *Current Science, 78*, 568–574.

Iyengar, R. N., & Ghosh, S. (2004). Microzonation of earthquake hazard in greater Delhi area. *Current Science, 87*, 1193–1202.

Jiaer, W. U., Kammerer, A. M., Riemer, M. F., Seed, R. B., & Pestana, J. M. (2004). Laboratory study of liquefaction triggering criteria. *13th World Conference on Earthquake Engineering*, Vancouver, B.C., Canada, Paper No. 2580.

Kramer, S. L. (1996). Geotechnical Earthquake Engineering, published by Dorling Kindersley [India] Pvt. Ltd. licensees of Pearson Education in South Asia.

Manzari, M. T., El Ghoraiby, M., Kutter, B. L., Zeghal, M., ... & Ziotopoulou, K. (2018). Liquefaction experiment and analysis projects (LEAP): Summary of observations from the planning phase, *113*(10), 714–743(2018). https://doi.org/10.1016/j.soildyn.2017.05.015.

O'Rourke, T. D., Gowdy, T. E., Stewart, H. E., & Pease, J. W. (1991). Lifeline performance and ground deformation in the Marina During 1989 Loma Prieta Earthquake. *Proceedings of the 3rd Japan-U.S. Workshop on Earthquake Resistant Design of Lifeline Facilities and Countermeasures for Soil Liquefaction*, San Francisco, California, NCEER Technical Report NCEER-91–0001, December 17–19.

Oldham, T. A. (1883). Catalogue of Indian earthquakes from the earliest times to the end of AD 1869. *Memoirs Geological Society India, 19*, 163–215.

Perlea, V. G., & Beaty, M. H. (2010). Corps of Engineers' practice in the evaluation of seismic deformation of embankment dams. In *Proceedings of the Fifth International Conference on Recent Advances in Geotechnical Earthquake Engineering and Soil Dynamics*. San Diego: Special Lecture SPL-6; May 24–29, 2010, pp. 1–30.

Prasad, S. K., Towhata, I., Chandradhara, G. P., & Nanjundaswamy, P. (2004). Shaking table tests in earthquake geotechnical engineering. *Special Section: Geotechnics and Earthquake Hazards, Current Science, 87*(10), 1398–1404.

Rajendran, C. P., & Rajendran, K. (2005). The status of central seismic gap: A perspective based on the spatial and temporal aspects of the large Himalayan earthquakes. *Tectonophysics, 395*, 19–39.

Rathje, E. M., Chang, W. J., & Stokoe, K. H., II. (2005). Development of an in situ dynamic liquefaction. *Geotechnical Testing Journal, 28*(1), 65–76.

Seed, H. B., & Idriss, I. M. (1971). Simplified procedure for evaluating soil liquefaction potential. *Journal of the Soil Mechanics and Foundations Division, ASCE, 97*(SM9), 1249–1273.

Seed, H. B., Idriss, I. M., & Arango, I. (1983). Evaluation of liquefaction potential using field performance data. *Journal of the Geotechnical Engineering Division, ASCE, 109*(3).

Youd, T. L., & Holzer, T. L. (1994). Piezometer performance at Wild- life liquefaction site, California. *Journal Geotechnical Engineering, 120*(6), 975–995.

An Experimental Study on Soil Spring Stiffness of Vibrating Bases on Polypropylene Fibre-Reinforced Fine Sand

C. N. V. Satyanarayana Reddy and M. Nagalakshmi

1 Introduction

The industrial establishments are generally planned in suburban areas and generally encounter low-lying areas which are to be backfilled with conventional materials such as sand or moorum. Due to the scarcity and high cost of these materials, the sites particularly in coastal areas are being backfilled with locally available fine sand. But due to its poor gradation and high susceptibility to liquefaction in a saturated state under dynamic loads, fine sand is an inferior material for filling up the site and to support the vibrating bases. Hence, fine sand is required to be stabilized to render it a suitable fill material in low-lying industrial sites. Research studies indicated that fine sand stabilized with fibres improved its strength and permeability characteristics and can be used as potential fill material (Lindh and Eriksson, 1990; Al-Refeai, 1991; Gao et al., 2013; Satyanarayana Reddy et al., 2014; Hesham et al., 2016; Koutenaei et al., 2019; Patel and Singh, 2019). The synthetic fibres of lengths 6–50 mm have been used and optimum synthetic fibre contents for stabilization are reported in the range of 1–2% by weight of sand.

2 Literature Review

Soil spring stiffness is an important parameter required for the design of machine foundations in industrial establishments. The equivalent soil spring stiffness (k) is used in the determination of the natural frequency and amplitude of vibration of machine foundation. Soil spring stiffness is obtained by multiplying the coefficient

C. N. V. Satyanarayana Reddy (✉) · M. Nagalakshmi
Department of Civil Engineering, A. U. College of Engineering, Andhra University, Visakhapatnam, India
e-mail: prof.cnvsreddy@andhrauniversity.edu.in

T. G. Sitharam et al. (eds.), *Advances in Earthquake Geotechnics*, Springer Tracts in Civil Engineering, https://doi.org/10.1007/978-981-19-3330-1_11

of elastic uniform compression (*Cu*) with an area of vibrating base. *Cu* is determined generally from a cyclic plate load test conducted with a square test plate or block vibration test (IS 5249-1992). Barkan's Eq. (1) was used for obtaining the coefficient of elastic uniform compression of actual footing (*Cuf*), for base areas up to 10 m^2.

$$Cuf = Cu\sqrt{\frac{A}{A_f}} \tag{1}$$

where A is base area of test plate

A_f is the base area of actual footing

For base areas larger than 10 m^2, *Cu* corresponding to 10 m^2 shall be adopted.

The value of *Cu* is influenced by the shape of footing, contact area of foundation block, modulus of elasticity, Poisson's ratio, type of soil and moisture content of soil (Barkan, 1962; IS 5249, 1992; Moghaddas Tafreshi et al., 2008; Prakash & Basavanna, 1969). Kirar et al. (2016) studied the behaviour of poorly graded sand under dynamic conditions and reported that the amplitude of vibration increased with an increase in the angle of eccentricity. The value of *Cu* is reported to increase with an increase in the density of sand (Basavaraj et al., 2016; Tafreshi et al., 2008). The damping in the fine to medium sand is reported in the range of 0.063 to 0.164 (Boominathan et al., 2000).

The settlements of foundation soils are reported to be reduced by improving the stiffness of the soil with the inclusion of geogrids and geocell (Leshchinsky et al., 2013; Sireesh et al., 2013; Hegde & Sitharam, 2016). The coefficient of elastic uniform compression of the foundation bed increased with the inclusion of geocell and the corresponding amplitude of vibration was reduced significantly. The maximum increase in the value of *Cu* was noticed when a combination of geocell and geogrid reinforcement was used (Hegde & Sitharam, 2016; Venkateswarlu & Hegde, 2020).

The studies on dynamic behaviour, in particular, the evaluation of *Cu* of fibre-reinforced fine sand are very few, and not much emphasis is given to highlight the effect of the shape of the footing on *Cu* of fibre-reinforced sand. Hence, in the present study, the dynamic behaviour of fine sand reinforced with polypropylene fibres of 6 mm and 12 mm length at optimum fibre content (fixed based on strength) is evaluated through small-scale cyclic load tests in the laboratory for vibrating bases of square and circular shapes. Also, the effect of the optimum amount of fibre addition in fine sand is evaluated in terms of reduction in amplitude of vibration.

3 Material Properties

Fine sand for the study is collected from Tenneti Park located in the Visakhapatnam beach area and the engineering properties determined from the laboratory tests conducted as per IS 2720 are presented in Table 1. Based on gradation charac-

Table 1 Engineering properties of fine sand

Property	Value
Specific gravity	2.67
Grain size distribution (a) Gravel (%) (b) Coarse sand (%) (c) Medium sand (%) (d) Fine sand (%) (e) Fines (%) (f) Coefficient of uniformity (g) Coefficient of Curvature	0 0 31 68 1 1.8 1.2
Plasticity characteristics (a) Liquid limit (%) (b) Plastic limit (%)	NP NP
IS Classification Symbol	SP
Compaction characteristics (a) Optimum moisture content (b) Maximum dry density (kN/m^3)	12 17.4
Shear Strength Parameters at OMC-MDD condition (i) Cohesion (kN/m^2) (ii) Angle of internal friction	0 30
Coefficient of permeability (m/s)	2.26×10^{-5}

teristics, fine sand is classified as Poorly graded Sand (SP) as per Indian Standard Soil Classification System (IS 1498-1970).

Polypropylene fibres used in the study are procured from Reliance Industries Limited, Mumbai, India. The properties of fibre reported by the manufacturer are presented in Table 2.

Table 2 Properties of Polypropylene Fibres (as provided by M/s Reliance Industries Limited, Mumbai)

Property	Value
Cross-section	Triangular
Fibre length (mm)	6 and 12
Fibre diameter (micron)	35–40
Colour	White
Moisture flat (%)	<1
Tensile strength (MPa)	400–600
Young's modulus (MPa)	16,000–19,000
Softening point (°C)	240–260
Specific gravity	1.36
Elongation (%)	>100

Table 3 Compaction and strength characteristics of fibre-reinforced fine sand

Fibre length	Fibre content by weight (%)	Optimum moisture content (%)	Max. dry unit weight (kN/m^3)	Cohesion (kN/m^2)	Angle of shearing resistance
6 mm	0.5	13.2	17.3	0	32°
	1.0	15.4	16.0	0	38°
	1.5	16.2	15.6	0	36°
12 mm	0.5	15.6	17.5	0	40°
	1.0	17.5	16.3	0	41°
	1.5	18.2	15.8	0	36°

Compaction and strength characteristics of fine sand reinforced with randomly oriented 6 mm and 12 mm length polypropylene fibres in proportions of 0–1.5% are determined from IS heavy compaction tests (IS 2720 part 8-1983) and direct shear tests (IS 2720 part 39 section 1–1979) presented in Table 3. It can be seen from the results that the optimum moisture content values increased and the corresponding maximum dry densities decreased with an increase in fibre content. 12 mm fibre resulted in relatively higher dry densities over 6 mm fibre. The angle of shearing resistance of fibre-reinforced fine sand is observed to be maximum at 1% fibre content for both 6 mm and 12 mm fibres. The higher angle of shear resistance with 12 mm fibres is attributed to better restraining action compared to 6 mm fibre due to the higher aspect ratio. Hence, the optimum fibre content for stabilization of fine sand is 1% for the fine sand under the study.

4 Small-Scale Cyclic Load Tests for Determination of *Cu* of Unreinforced and Fibre Reinforced Fine Sand

Coefficient of elastic uniform compression (*Cu*) values of fine sand and fibre-reinforced sand with optimum fibre content (1%) are determined from small-scale cyclic plate load tests. Small scale load tests are conducted on the specimens prepared in the CBR mould at respective OMC and MDD after soaking for 96 h by loading through a standard CBR test plunger (circular) and a fabricated square plunger of size 50 mm. The load is applied through a manually operated self-straining load frame of 50 kN capacity as it facilitates maintenance of the applied loads and allows for unloading after each stage of loading. A surcharge weight of 5 kg is applied to the sample by placing an annular surcharge plate of 150 mm diameter and 5 kg weight with a central hole and slot width of 5.3 cm. Further, a seating load of 4 kg is applied through the plunger, and the proving ring and penetration dial gauges are set to zero. Loading is done in stages with increments of 1/5th of the anticipated safe bearing capacity (200 kPa) and continued up to 2.5 times the safe bearing capacity. Each stage of loading is maintained till settlement reached equilibrium. The load applied

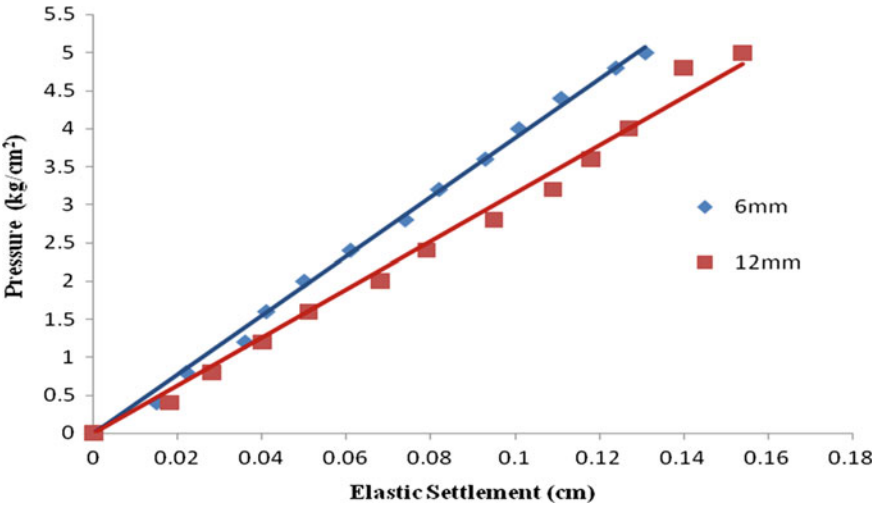

Fig. 1 Pressure-Elastic settlement of fine sand reinforced with 1% fibre for square plunger

at each stage is released and the plate is allowed to rebound. The deformation dial gauge readings under each stage of loading and unloading are recorded after the dial gauge needle movement stopped. The difference in deformation dial gauge readings in loading and unloading stages is recorded as the elastic Rebound/Elastic settlement. The coefficient of elastic uniform compression is determined as the slope of the linear portion of the load-settlement plot drawn from the test results.

Pressure-Elastic settlement plots of fine sand and fibre-reinforced fine sand mixed with 1% polypropylene fibres generated from the results of small-scale cyclic load tests with circular and square plungers are presented in Figs. 1 and 2. The values of *Cu* for square and circular plungers for the specimens under study obtained from laboratory small scale cyclic load tests and estimated values of *Cu* for square and circular footings of 10 m^2 areas from Barkan's equation (Eq. 1) are presented in Table 4.

5 Effect of Fibre Addition on Amplitude of Vibration of Machine Foundations

The amplitude of vibration of the vibrating base under forced damped vibrations is determined by idealizing the vibrating base–foundation system as a single degree freedom system using the following expression:

$$Z = \frac{(F_0/K)}{\sqrt{(1-r^2)^2 + (2Dr)^2}} \tag{2}$$

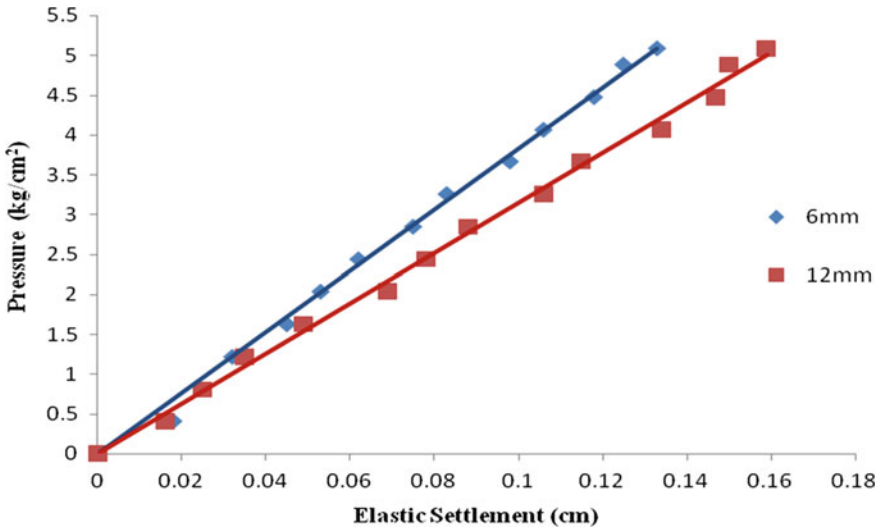

Fig. 2 Pressure-Elastic settlement of fine sand reinforced with 1% fibre for circular plunger

Table 4 Coefficient of elastic uniform compression of fine sand reinforced with 1% polypropylene fibres

Length of fibre (mm)	Fibre content (%)	Coefficient of elastic uniform compression of plate (Cu) (kN/m^3)		Coefficient of elastic uniform compression (Cuf) of footing of 10 m^2 area (kN/m^3)	
		Square plunger	Circular plunger	Square footing	Circular footing
6	0 1.0	6.87×10^5 3.80×10^5	5.89×10^5 3.74×10^5	9618 5320	8246 5236
12	0 1.0	6.87×10^5 3.08×10^5	5.89×10^5 3.09×10^5	9618 4312	8246 4326

where Z = amplitude of vibration

F_0= Exciting force

K = Stiffness of soil = *Cu* A

r = frequency ratio = ω/ω_n

ω = operating frequency

ω_n = natural frequency of foundation soil system

$\omega_n = \sqrt{\frac{K}{m}}$

m = mass of machine + foundation + co-vibrating soil

D = damping ratio

For a given exciting force, the change in amplitudes of vibrations due to a decrease in the value of *Cu* for fine sand reinforced with the addition of optimum fibre content

Table 5 Amplitude of vibration of machine foundations in fine sand reinforced with 1% polypropylene fibre for frequency ratio of 2 (corresponds to r = 1.5 of fine sand)

Length of fibre (mm)	Shape of plunger	Percentage decrease in Amplitude for different values of Damping Ratio (D)			
		0	0.05	0.1	0.15
6	Square	25	24.3	23.2	21.4
	Circular	22.3	22	21	20.2
12	Square	30.6	30.2	29	27
	Circular	27.5	27	26	24.2

of 6 mm and 12 mm fibres are evaluated for frequency ratios of 1.5 corresponding to unreinforced sand for various damping ratios of 0, 0.05, 0.1 and 0.15 and the values are presented in Table 5.

For unreinforced fine sand with r = 1.5 and D = 0;

$$Z = \frac{\mathrm{F_0/(Cu.A)}}{\sqrt{(1-r^2)^2}} = \frac{0.80F_0}{\mathrm{Cu}.A} \tag{3}$$

For fine sand reinforced with 1% fibre of 6 mm length, the frequency ratio increases due to reduced natural frequency (resulting from reduced *Cu*) to 2.0 corresponding to a frequency ratio of 1.5 for unreinforced sand.

For fibre-reinforced sand with r = 2 and D = 0

$$z' = \frac{0.60F_0}{Cu.A} \tag{4}$$

where Cu is the coefficient of elastic uniform compression of fine sand.

The decrease in amplitude of vibration is determined in Eqs. 3 and 4 as 25%. The reduction in amplitude of vibration of fine sand with a randomly distributed optimum fibre content of 1% for 6 mm and 12 mm fibres is determined for different damping ratios.

6 Discussion

From the results presented in Table 4, the values of *Cu* of polypropylene fibre- reinforced fine sand are nearly the same for square and circular Plungers of the same size. Hence, there is no shape effect on *Cu* of vibrating bases on fibre-reinforced fine sand. This is in contrast to the reported result that *Cu* of circular footings is 0.85 times *Cu* of square footings in case of unreinforced Fine sand (Satyanarayana Reddy & Usha Rani, 2020a, b). The observed nearly same values of Cu for circular and square plungers in fibre reinforced are attributed to the isotropic behaviour induced by

fibres in sand. Fine sand reinforced with 6 mm fibres has relatively higher values of *Cu* compared to 12 mm fibre due to lesser elastic rebound arising from better dispersion in fine sand during mixing due to their relatively shorter length. Relatively higher elastic rebound is observed in 12 mm fiber-reinforced soil due to better restrainment/interaction of fibre with fine sand particles due to higher aspect ratio.

From Table 5, it can be seen that the percentage decrease in amplitude of vibration is relatively higher for 12 mm fibre over 6 mm fibre at a given damping for loading plungers of circular and square shapes. Further, square plunger has indicated a higher reduction (27–30%) amplitude of vibration over the circular plunger (24–27.5%) for 12 mm fibre-reinforced fine sand.

7 Conclusions

Based on the experimental and analytical work done on unreinforced fine sand and polypropylene fibre-reinforced fine sand, the following conclusions are drawn:

1. The optimum polypropylene fibre content for the stabilization of fine sand under study based on shear strength improvement is 1% by weight of sand for both 6 mm and 12 mm fibre. 12 mm fibres mobilized a relatively higher angle of shear resistance compared to 6 mm fibres.
2. Coefficient of elastic uniform compression (*Cu*) of fibre-reinforced fine sand is independent of the shape of footing, whereas the value of Cu for the circular vibrating base is 0.85 times the Cu of the square vibrating base on unreinforced fine sand.
3. The amplitude of vibration of the vibrating base decreases due to the addition of polypropylene fibres in fine sand. The amplitude of vibration of bases in fine sand decreased by about 20 and 25% by adding 1% of polypropylene fibres of 6 and 12 mm length, respectively due to an increased frequency ratio of 2 corresponding to a frequency ratio of 1.5 in unreinforced fine sand.
4. 12 mm length fibres are relatively more effective in reducing the amplitude of vibration due to their better restraining effect.

References

Al-Refeai, T. O. (1991). Behaviour of granular soils reinforced with discrete randomly oriented inclusions. *Geotextiles and Geomembranes, 10*(4), 319–333.

Bablu, K., Murali Krishana, A., & Rangwala, H. M. (2016). Dynamic properties of soils for the design of machine foundations. *Proceedings of Indian Geotechnical Conference*, IIT Madras, Chennai, India.

Barkan, D. D. (1962). *Dynamics of bases and foundations.* Mc.Graw Hill Co.

Basavaraj, H., Rakaraddi, P. G., & Sudharani, K. (2016). Behavior of square footing resting on reinforced sand subjected to incremental loading and unloading. *International Journal of Research in Engineering and Technology, 3*(6).

Boominathan, A., Koteswara Rao, P. C., Sivathanu Pillai, C., & Hari, S. (2000). Measurement of dynamic properties and evaluation of liquefaction potential of a 500mw prototype fast breeder reactor site located in south of India. *Proceedings of 12th World Conference on Earthquake Engineering*, Auckland, New Zealand.

Gao, Z., & Zhao, J. (2013). Evaluation on failure of fiber-reinforced sand. *Journal of Geotechnical and Geoenvironmental Engineering, ASCE, 139*(1), 95–106.

Hegde, A., & Sitharam, T. G. (2016). Behaviour of geocell reinforced soft clay bed subjected to incremental cyclic loading. *Geomechanics and Engineering, 10*(4), 405–422.

Hesham, M. E., Mohamed, M. M., & Mohamed, F. M. (2016). Fibre reinforced sand strength and dilatation characteristics. *Ain Shams Engineering Journal, 7*, 517–526.

IS 1498-1970: Classification and identification of soils for general engineering purposes, Bureau of Indian Standards, New Delhi.

IS 5249-1992: Methods of test for determination of dynamic properties of soils, Bureau of Indian Standards, New Delhi.

IS 2720 Part 39 section 1-1977: Direct shear test for soils, Bureau of Indian Standards, New Delhi.

IS 2720 Part 8-1983: Method of test for soils–Determination of water content-dry density relation using heavy compaction, Bureau of Indian Standards, New Delhi.

Koutenaei, R. Y., Choobbasti, A. J., & Kutanaei, S. (2019). Triaxial Behaviour of cemented sand reinforced with Kenaf Fibres. *European Journal of Environmental and Civil Engineering, 1*, 1–19.

Leshchinsky, B., & Ling, H. (2013). Effects of geocell confinement on strength and deformation behavior of gravel. *Journal Geotechnical Geoenvironment Engineering, 139*(2), 340–352.

Lindh and Eriksson. (1990). Sand Reinforced with plastic fibres a field experiment. *International Reinforced Soil* Conference, University of Strathclyde, Glasgow, United Kingdom, pp. 471–473.

Moghaddas Tafreshi, S. N., Zareiand, S. E., & Soltanpour, Y. (2008). Cyclic loading on foundation to evaluate the coefficient of elastic uniform compression of sand. *14 th World Conference on Earthquake Engineering*, Beijing, China.

Patel, S. K., & Singh, B. (2019). Shear strength response of glass fibre-reinforced sand with varying compacted relative density. *International Journal of Geotechnical Engineering, 13*(4).

Prakash, S., & Basavanna, B. M. (1969). Effect of size and shape of foundation on elastic coefficients in a layered soil mass. *Proceedings of IV World Conference on Earthquake Technology*, Chile.

Satyanarayana Reddy, C. N. V., & Sireesha, G. (2014). Effect of randomly distributed synthetic fibre in fine sand and fly ash. *Indian Journal of Geosynthetics and Ground Improvement, 3*(1).

Satyanarayana Reddy, C. N. V., & Usha Rani, G. V. (2020a). Effect of shape of footing on coefficient of elastic uniform compression of polypropylene fibre reinforced fine sand. *SEAGS-AGSSEA Journals, 51*(4).

Satyanarayana Reddy, C. N. V., & Usha Rani, G. V. (2020b). Influence of shape of footing on coefficient of elastic uniform compression of foundation soils. *Indian Geotechnical Journal, 50*(4).

Sireesh, S., Sailesh, P., Sitharam, T. G., & Puppala, A. J. (2013). Numerical analysis of geocell reinforced ballast overlying soft clay subgrades. *Geomechanics and Engineering, 5*(3), 263–281.

Venkasteswarlu, T., & Hegde, A. (2020). Performance evaluation of geocell reinforced machine foundation beds (pp. 199–223). Geocells 2020, Springer Transactions in Civil and Environmental Engineering.

Guidelines for Minimization of Uncertainties and Estimation of a Reliable Shear Wave Velocity Profile Using MASW Testing: A State-of-the-Art Review

Ravi S. Jakka, Aniket Desai, and Sebastiano Foti

1 Introduction

Earthquakes are catastrophic phenomena that cause extremely heavy destruction to society. Hence, preparedness against earthquakes is a very crucial task in geotechnical earthquake engineering. To reduce the effects of earthquakes, an essentially important exercise is the seismic hazard analysis of the study area. For carrying out seismic hazard analysis, the shear wave velocity (V_s) profile of the soil serves as a basic input parameter. For the estimation of the V_s profile of the soil, the most preferred technique currently is the multichannel analysis of surface waves (MASW). It is a geophysical method, based on the dispersion phenomenon in seismic surface waves. The MASW method offers several advantages over other conventionally used methods such as cone penetration test (CPT), seismic cross-hole test, and standard penetration test (SPT). It is a non-invasive method and simpler to carry out. It requires less labor, time, and expense compared to the other methods. Also, it can be used for almost all types of soil, unlike many other methods. These characteristics make the MASW test the most common choice to estimate the V_s profile of the soil. The importance of the V_s profile of soil can be understood from the fact that it is a critical input in seismic site characterization (Long & Donohue, 2007; Anbazhagan & Sitharam, 2008; Foti et al., 2011b; Odum et al., 2013; Asten et al., 2014; Taipodia et al., 2014; Rahman et al., 2016; Rehman et al., 2016; Pandey et al., 2016b; Leyton et al., 2018; Noorlandt et al., 2018; Maklad et al., 2020; Yamanaka et al., 2020; Hobiger et al., 2021; Salas-Romero et al., 2021), surface seismic exploration (Socco et al., 2017; Xia et al., 2018), V_{s30} mapping and site classification (Sandikkaya et al., 2010; Yordkayhun

R. S. Jakka (✉) · A. Desai
Department of Earthquake Engineering, IIT Roorkee, Roorkee 247667, Uttarakhand, India
e-mail: ravi.jakka@eq.iitr.ac.in

S. Foti
Department of Structural, Geotechnical and Building Engineering (DISEG), Politecnico di Torino, Turin, Italy

T. G. Sitharam et al. (eds.), *Advances in Earthquake Geotechnics*, Springer Tracts in Civil Engineering, https://doi.org/10.1007/978-981-19-3330-1_12

et al., 2015), studies on local site effects (Rastogi et al., 2011; Panzera et al., 2013; Michel et al., 2014; Pandey et al., 2016a; Stanko et al., 2017; Mugesh et al., 2022), seismic hazard assessment (Ebrahimian et al., 2019; Dwivedi et al., 2020), seismic microzonation (Martínez-Pagán et al., 2014; Khan & Khan, 2018; Caielli et al., 2020), ground motion modeling (Bozorgnia et al., 2014), liquefaction studies (Andrus & Stokoe, 2000; Lin et al., 2004; Kayen et al., 2013; Yokota et al., 2017; Mase et al., 2020), pavement evaluation and road failure investigation (Nazarian et al., 1983; Ayolabi & Adegbola, 2014), earthquake reconnaissance (Cubrinovski et al., 2010), studies on landfills (Suto, 2013; Zekkos et al., 2014), and many others (Watabe & Sassa, 2008; Kim et al., 2010; Omar et al., 2011; Madun et al., 2012; Connolly et al., 2014; Bergamo et al., 2016; Joh et al., 2019; Rahnema et al., 2021).

The procedure of estimating the V_s profile of soil using seismic surface waves started with the steady-state Rayleigh method (Jones, 1958). It comprised a vertical-vibrating sinusoidal vibrator and two receivers. However, it was too time-consuming and was not utilized much. By now, it has become obsolete. Then, the spectral analysis of surface waves (SASW) method was proposed (Heisey et al., 1982; Stokoe & Nazarian, 1983; Stokoe et al., 1988). It consisted of using an impulse source and two receivers to record the traveling waves. The phase difference and time delay of wave arrival between the two receivers were used to estimate the Rayleigh wave phase velocity as a function of frequency. It has been used widely and has also undergone developments (Stokoe et al., 1994; Tokimatsu, 1995). However, it has shortcomings, such as flaws in the identification of higher modes of vibration and separation of noise from the signal and high consumption of time and labor. So, later, a modified method titled MASW (Park et al., 1999; Xia et al., 1999) was developed which uses a higher number of receivers and overcomes the limitations of SASW. Crice (2005), in his editorial *Journal of Environmental and Engineering Geophysics* in 2005, stated that surface wave surveys would bring a paradigm shift in Geophysics because of their higher productivity, large areal coverage at a modest cost, and other advantages. Over the past two decades, the MASW method has emerged as the most popular method for estimation of near-surface soil stiffness and seismic site characterization due to its viability.

Although the MASW is the most preferred surface wave method at present, there are some issues with the method. The presence of body waves in the generated wavefield, the noise present at the site, and the non-uniqueness of the inversion process induce uncertainties in the MASW results. They have been explained in detail in Sect. 2. All these uncertainties pose some questions about the reliability of MASW. Therefore, it has become necessary to employ some techniques to reduce or account for these uncertainties. A lot of research has been carried out on the uncertainties in surface wave methods and their effects on subsequent analyses (Lai et al., 2005; Roy et al., 2013; Jakka et al., 2014; Griffiths et al., 2016; Saifuddin et al., 2018; Roy & Jakka, 2018). A thorough description of the basics of surface wave testing, its associated uncertainties, and the new developments that occurred on the topic is available in the literature (Park & Ryden, 2007; Socco et al., 2010; Nazarian, 2012). The general recommendations for carrying out different types of

surface wave tests are provided by Foti et al. (2018), while the basic theory on the topic is reported by Foti et al. (2014).

This paper aims at putting forward practical guidelines, with regards to carrying out MASW and producing reliable results with minimum uncertainties. A huge amount of literature on the topic has been covered in the references and from the inferences from them, and the recommendations to implement have been presented. While carrying out the three steps in MASW, certain criteria are to be followed which are compulsory to get legitimate results. This paper puts focus on all these criteria. From the beginning to the end, all these steps and their peculiarities have immense significance in the MASW test. This paper explores all these steps and puts forth a standardized way to execute all these steps. The guidelines provided in this paper are useful to all the people in academia/industry who would use the MASW test for any study or project or anywhere else.

1.1 Basic Principles of MASW Testing

The MASW method utilizes the dispersive nature of Rayleigh-type surface waves. That is, Rayleigh waves of different frequencies travel at different velocities and penetrate to different depths in a layered medium. Higher frequency (shorter wavelength) Rayleigh waves remain confined to shallow depths and give information about their mechanical properties, whereas lower frequency (longer wavelength) components penetrate up to deeper layers (Fig. 1). This property can be used to infer near-surface soil properties, mainly the shear wave velocity profile and the shear modulus of the soil. These properties can be estimated up to the depths of engineering interest. Earlier, many studies on the MASW method and Rayleigh wave dispersion have been carried out (Zhang et al., 2004; Foti et al., 2011a; Lin & Lin, 2012; Diaz-Segura, 2015; Roy & Jakka, 2017; Roy et al., 2020).

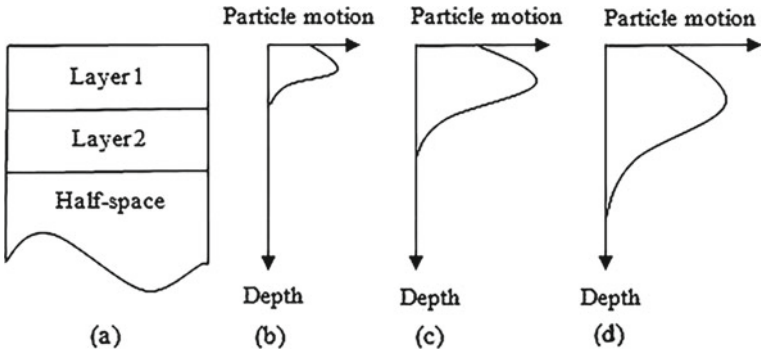

Fig. 1 Rayleigh wave dispersion in a layered media: **a** soil profile, **b** high-frequency wave, **c** intermediate-frequency wave, and **d** low-frequency wave

1.2 MASW Methodology

The MASW test consists of 3 steps: (1) Data acquisition, (2) Data processing and dispersion curve generation, and (3) Inversion (Fig. 2).

Data acquisition involves the deployment of a geophone array, generating waves using a source and its recording (active test), or recording ambient vibrations (passive test). Certain criteria should be followed in this procedure which are elaborated in Sect. 3.

Data processing involves the transformation of the recorded waveform data into a dispersion curve. The dispersion curve is a plot between Rayleigh wave phase velocity and frequency. Some people express it in other terms such as wavelength and slowness. Many methods are available to generate a dispersion curve, which have their own merits or demerits. Detailed information about them is provided in Sect. 4.

Inversion is the procedure of producing the V_s profile of the site from the dispersion curve. For this also, various algorithms are available. A thorough description of the inversion procedure, the considerations in the procedure, and different inversion algorithms have been presented in Sect. 5.

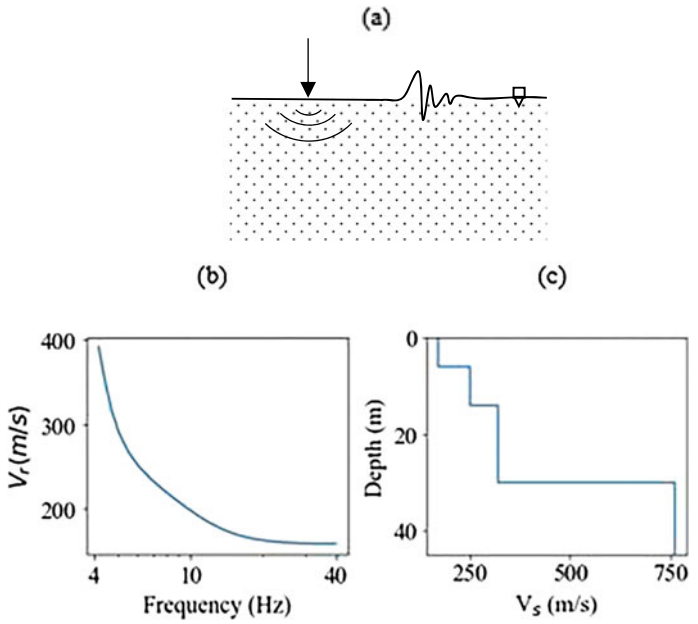

Fig. 2 The three steps of surface wave analysis: **a** Data Acquisition, **b** Processing and dispersion curve generation, and **c** Inversion and retrieval of V_s profile

2 Uncertainties in the MASW Method

The MASW method suffers from several uncertainties during data acquisition and processing. Roy (2015) has provided a thorough description of the types of uncertainties in surface wave analyses. Firstly, while carrying out surface wave analysis, it is assumed that the waves generated by the MASW source are plane Rayleigh waves. However, in reality, the generated wavefield also contains body waves which lead to the underestimation of Rayleigh wave phase velocity. Also, during the MASW testing, the ambient noise and anthropogenic activities such as the passing of vehicles or others interrupt the waves generated by the MASW source during the testing. This noise would be different when the test is conducted at different times at the same location. In addition, the process of retrieving the final V_s profile of soil involves an inversion process that provides a non-unique solution. That means that a single dispersion curve (plot between Rayleigh wave phase velocity and frequency) produced from an MASW test generates numerous V_s profiles equivalent to it. This phenomenon gives rise to ambiguities regarding the actual V_s profile of the soil. The uncertainties associated with surface wave testing can be broadly classified into three main categories and various other categories as shown in Fig. 3.

2.1 Model-Based Uncertainty

Model-based uncertainty is primarily associated with the phenomena known as the near-field effects. The MASW processing assumes the plane Rayleigh wave propagation, i.e., only Rayleigh waves are present and recorded on the receivers. However, in the real scenario, other waves such as P and S waves are also generated from the impact of the MASW source. These waves contaminate the Rayleigh waves and therefore, the Rayleigh wave phase velocity (V_r) is underestimated at lower frequencies, and the underestimation increases as the frequency decreases. Earlier, it has been found that near-field effects lead to the underestimation of phase velocity at wavelengths greater than half the length of the linear geophone array (Bodet et al., 2009) or wavelengths greater than the mean source to geophone distance (Yoon & Rix, 2009). Various factors can influence the near-field effects such as the source type, its height of fall, its contact mechanism with the ground, source to first receiver distance, array length, dispersion (data processing) method, subsurface soil profile, etc.

Many studies have been carried out on the near-field effects and the ways to mitigate them (Zywicki & Rix, 2005; Xu et al., 2006; Li & Rosenblad, 2011; Roy & Jakka, 2017). One way to reduce the near-field effects is to keep the distance between the MASW source and the first receiver as much as possible. However, it should be ensured that the generated wave-train is properly captured at all the receivers, especially the high-frequency components because they attenuate more with distance. Also, the use of the cylindrical beamformer method to generate the dispersion curve

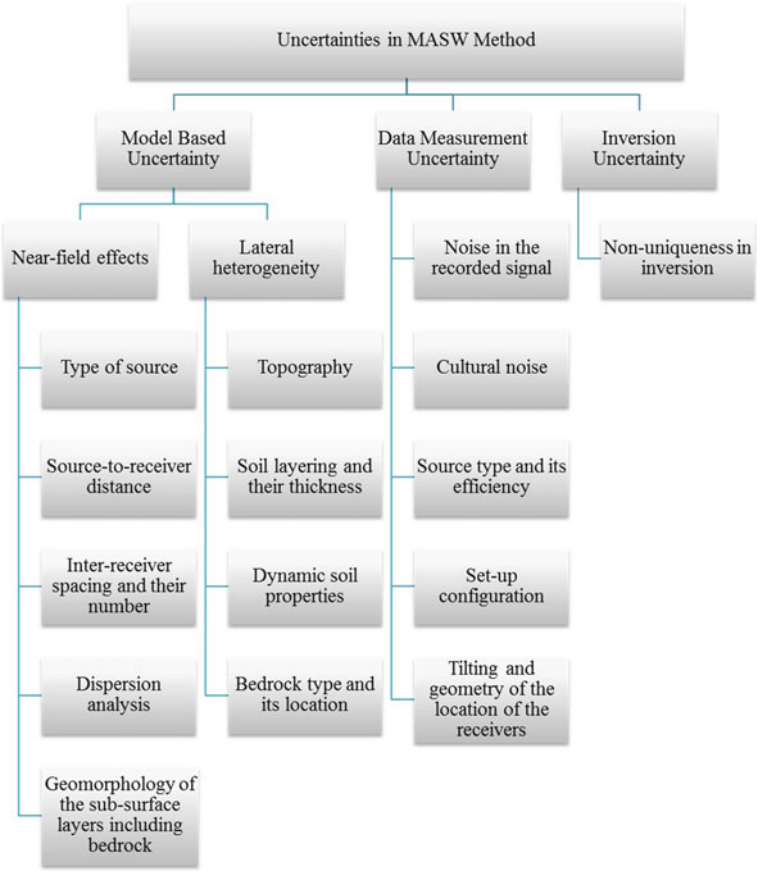

Fig. 3 Types of the uncertainties in the MASW method (Roy, 2015)

from the MASW data was found to be reducing the near-field effects (Tran & Hiltunen, 2011). However, some studies found that this method does not completely serve the purpose (Li, 2008; Jiang et al., 2015).

Another way to tackle the near-field effects is the use of combined active and passive MASW tests. The 2D passive array can be circular, triangular, L-shaped, etc. The passive test uses the wavefield coming from far distances. So, because the body waves attenuate faster with distance than surface waves, at far distances, surface waves become dominant. Hence, the passive MASW test acquisition can be approximated as the plane Rayleigh wave condition which would demonstrate negligible near-field effects. So, the underestimation of V_r at lower frequencies due to near-field effects can be avoided. On the other hand, the active MASW test can provide better resolution at higher frequencies. Hence, the active and passive MASW data complement each other to generate good quality, broadband dispersion curves. By comparing the individual dispersion curves from the active and passive tests, the

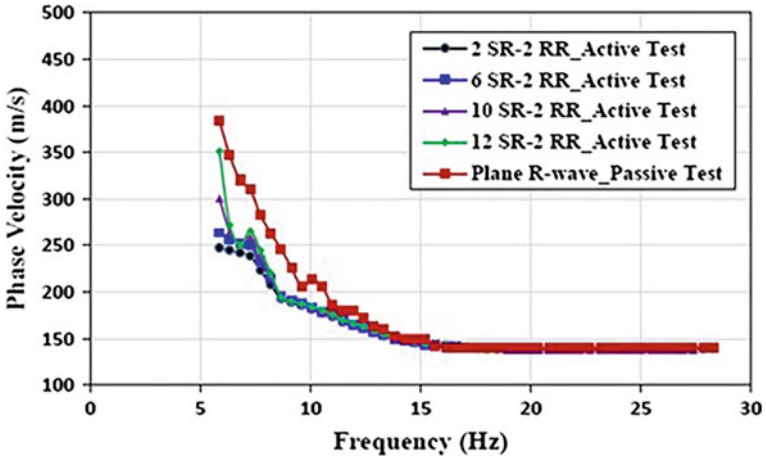

Fig. 4 Comparison of dispersion curves using different source offsets in active MASW test and a passive MASW test (SR: Source to first receiver distance; RR: Receiver to receiver distance) (Roy, 2015)

frequencies at which near-field effects are prominent can be identified and should be removed. For example, Fig. 4 shows the underestimation of V_r at lower frequencies in active test results. Such a portion should be removed from that particular dispersion curve and the remaining portion should be used to prepare a combined dispersion curve to be used for further analyses. Also, for passive MASW acquisition, it is strongly suggested to use the 2D arrays and avoid the linear arrays by many researchers because of a lot of discrepancies in the latter case.

Another source of the model-based uncertainty is the lateral heterogeneity present in the soil. The MASW test is carried out assuming that the soil is laterally homogeneous, i.e., the soil properties do not change in the horizontal direction at the site. However, some locations may exhibit changes, i.e., there may be material boundaries that are not perfectly horizontal. This would affect the test results and the results would have errors. Lateral heterogeneity may depend on the topography of the site, soil layering and their thicknesses, dynamic soil properties, bedrock type, its location, etc.

2.2 Data Measurement Uncertainty

The waveforms recorded in the MASW test invariably contain the ambient noise present at the site. It may be due to the passing of people, vehicles, earth's vibrations, wind, sea waves, instrumental self-noise, etc. This can produce scatter in the dispersion curve. Also, such a type of noise would be different during different acquisitions carried out at the same site. This produces ambiguity about the actual

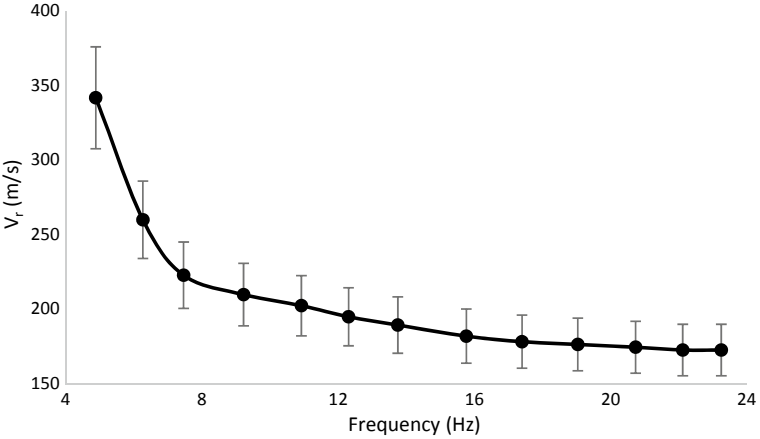

Fig. 5 Representation of dispersion curve with data measurement uncertainty: Curve displaying the Rayleigh wave phase velocity mean value and its standard deviation using several dispersion curves at the same location

dispersion curve at the site. This is termed the data measurement uncertainty. It can get affected by the source type and its efficiency, MASW setup, the alignment, and tilting of the receivers. Many researchers have worked on the data measurement uncertainty and its impact on further analyses (Marosi & Hiltunen, 2004a, b; Lai et al., 2005; Jakka et al., 2014). The data measurement uncertainty increases when the signal-to-noise ratio (SNR) decreases. It is generally suggested to be very careful in using data that has SNR < 10 dB. When the low SNR produces bad quality data or when the COVs of the measured dispersion curves using different source offsets are significantly high, that data should not be used for the analysis (Wood & Cox, 2012). To prevent the data from getting affected by the noise, the test should be carried out when the traffic due to vehicles can be avoided.

One way to deal with this uncertainty is to take multiple shots of the MASW at the same location and generate multiple dispersion curves. Then, using all these curves, the final dispersion curve can be presented as a mean curve and its standard deviation (Fig. 5). This would provide the dispersion curve along with its data measurement uncertainty. Also, taking multiple shots and stacking them together improves the SNR which is very much needed to get good quality data.

2.3 Inversion Uncertainty

The process of inversion involves the generation of the final V_s model of the site using the experimental dispersion curve. However, the inversion process is non-unique, i.e., for a single dispersion curve, several V_s profiles are generated whose theoretical dispersion curves have remarkably similar misfit values. Misfit is the measure of the

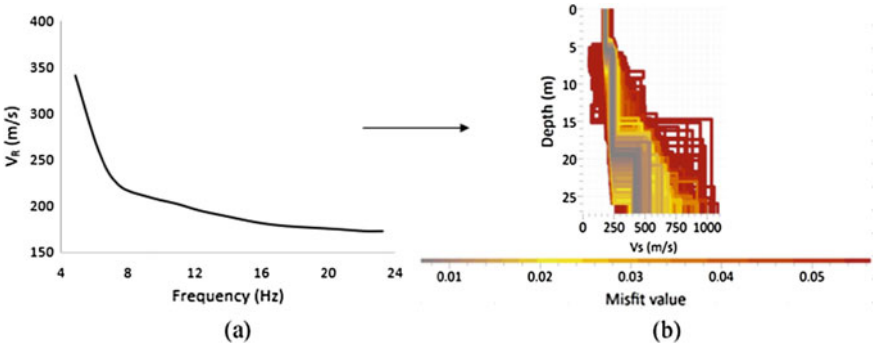

Fig. 6 Concept of inversion uncertainty: A single dispersion curve giving numerous V_s profiles with similar misfit values: **a** Dispersion curve and **b** V_s profiles

difference between the experimental dispersion curve of the site and the theoretical dispersion curve of the generated V_s profiles from inversion (Wathelet, 2008). This creates uncertainty about the actual V_s profile of the site. The inversion procedure is such that a single, true V_s profile of soil cannot be ascertained. This is called inversion uncertainty. The inversion uncertainty or inversion non-uniqueness has been a topic of research for many authors (Foti et al., 2009; Boaga et al., 2011; Roy et al., 2013; Teague & Cox, 2016; Lei et al., 2018; Roy & Jakka, 2020). Figure 6 shows the concept of inversion uncertainty. The inversion process was carried out using the DINVER framework of Geopsy software based on an improved neighborhood algorithm (Wathelet, 2008).

3 Data Acquisition

Data acquisition is the first step in an MASW test. An MASW test can be carried out in the field in two ways: (1) Active test or (2) Passive test. The active test involves the use of a source to generate Rayleigh waves. In the passive test, the waves from the ambient vibrations are recorded.

3.1 Active Test

A typical field MASW setup is shown in Fig. 7. It includes a source to generate waves, a receiver array (geophones), and equipment for data processing. The seismic waves in an MASW test are usually generated using either a hammer, electro-mechanical vibrator, or blasting, etc. Vertical component geophones are used for recording the particle motion at the surface. It is assumed that the maximum energy in the recorded

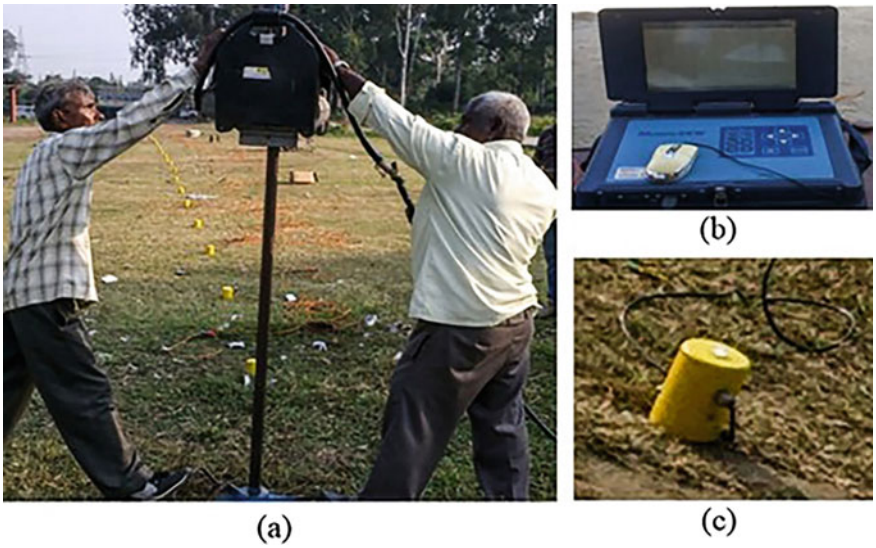

Fig. 7 MASW test setup: **a** Drop weight arrangement and receiver array, **b** A sample recording device: McSeis-SXW 24 channel seismograph, and **c** A sample vertical component geophone (Roy & Jakka, 2018)

motion is from the Rayleigh waves. The recorded signals are then processed to get the dispersion curve and the V_s profile.

Selection of test parameters and their effects on the uncertainties

In the MASW testing, the choice of the data acquisition parameters plays a huge role in the final results. The parameters can influence the uncertainties during all three steps of the test. Consequently, it can affect the resolution, quality, and correct identification of the dispersion curve and also the depth of investigation. A description of different test parameters and their role in MASW testing has been provided below.

Source type

The type of source influences the frequencies that are generated in the wavefield. There are two common active source types: Impact sources such as a sledgehammer/drop weight or a harmonic source such as an electro-mechanical or a servo-hydraulic (Vibroseis) shaker. These different sources have their own merits and demerits and would generate different surface wave energy of different frequencies. Wood and Cox (2012) compared the impact and harmonic sources in which the harmonic source was found to produce better quality data, particularly at lower frequencies.

A major benefit of active source testing is that the generation and measurement of Rayleigh waves can be carried out in a controlled way. It allows a band of frequencies to be measured altogether. The sledgehammer is by far the cheapest and most common impact source. Usually, the hammer used as the seismic source should be of

a minimum of 5 kg (Foti et al., 2018). It can generate frequencies as low as 10–15 Hz. These frequencies may enable the user to obtain a V_s profile up to 30 m depth if the site is stiff, but the uncertainties in generating the dispersion curve would remarkably increase and need to be accounted for in the inversion analyses (Cox & Wood, 2011). Usually, when the sledgehammer is used as the MASW source, the depth of V_s profile obtained is less than 30 m (Park & Carnevale, 2010; Tran & Hiltunen, 2011). In soft soils, it can be substantially less than 30 m. Therefore, a challenge is faced by those who want to estimate V_{s30} (time-averaged V_s of top 30 m soil) at a site. Therefore, to generate low-frequency data to obtain V_s profile at higher depths, heavy sources such as large weight drop systems, Vibroseis, and bulldozers can be used. Efforts have been made to use specific sources to generate low-frequency data and generate V_s profile up to higher depths (Rosenblad et al., 2008; Rosenblad & Li, 2009b). They facilitate the analysis to be focused on a narrow band of frequencies, thereby decreasing the disturbance due to noise (Hebeler & Rix, 2001). Harmonic sources (i.e., Vibroseis) have been used for deep V_s profiling using SASW (Kayen et al., 2005; Wong et al., 2011). Stokoe et al. (2004) developed a low-frequency shaker that can actively generate surface wave energy even at frequencies less than 1 Hz. A description of the large-scale mobile shakers for generating such low-frequency data can be found in Stokoe et al. (2020). However, for MASW, they have been used quite less, because of the cost, difficulty in mobilization, and time-consuming data acquisition and analysis (Rix et al., 2002; Rosenblad & Li, 2009a; Cox & Wood, 2010). Overall, the type of source to be used should be decided based on the desired depth of investigation, portability, available space for the testing, availability of the equipment, and financial considerations.

Array length

The length of the receiver array (L) is associated with the wavenumber (k) resolution (and therefore the investigation depth) and the separation of modes. If the frequency–wavenumber (f–k) method is used for the processing of MASW data, a longer array would yield better wavenumber resolution, i.e., a lower value of minimum wavenumber k_{min}. Therefore, higher λ_{max} and higher depth of V_s profile can be achieved. Usually, as a thumb rule, if the V_s profile is desired up to a depth of D, it is recommended to keep the array length at least equal to 2D; and to be more conservative, it should be 3D. However, it also depends on the stiffness of the soil. If the processing method used is other than f–k, this condition may not be followed exactly. Still, a higher array length would enable to get a higher value of $\lambda_{max.}$ However, to make the array length larger, the inter-receiver spacing should not be kept too high, which would adversely affect the V_s resolution at shallow depths.

The second feature is mode separation. If the array length is less, a lower resolution in the wavenumber domain hampers the identification of higher modes. The operation of zero padding can help up to some extent, but it cannot compensate for the loss of data due to the lower array length (Socco & Strobbia, 2004). Therefore, a longer array is suggested especially for soils having high impedance contrast or inversely dispersive V_s profile in which higher modes may become dominant. However, in the case of a longer array, the waves may get affected by the attenuation of high-frequency

components, lateral variations, and noise at the site. Therefore, an optimum value of array length should be selected, which can provide good quality data, by visual inspection of the acquired data after using different array lengths. Also, the chances of occurrence of lateral heterogeneity are more in longer arrays. So, if long arrays are to be used, it should be ensured before the test that lateral heterogeneities are not present (e.g., considering local geology).

Inter-receiver spacing

The spacing between adjacent geophones (denoted as Δx) should be such that waves of short wavelengths are sufficiently sampled, which is required for a good resolution at shallow depths. As per the Shannon–Nyquist sampling theorem, aliasing will occur for the waves having a wavelength less than $2*\Delta x$. Aliasing might obscure the correct identification of the high-frequency portion in the dispersion curves, especially when higher modes are excited. Therefore, the spacing should be chosen based on the minimum expected wavelength in the signal, which primarily is a function of the MASW source and the stiffness of the site. The choice of inter-receiver spacing can also depend on the desired investigation depth. If the required data is only up to shallow depths, then receiver spacing can be kept smaller. Considering a given number of receivers, a small receiver spacing would help in getting good resolution at shallow depths. The requirement of a higher investigation depth automatically prompts the user to choose large receiver spacing to get a longer array length. The suggested values of inter-receiver spacing for near-surface characterization range from 0.5 to 4 m. Some researchers demonstrated that non-uniform spacing of the receivers can help in producing good experimental dispersion curves (Zywicki, 1999; Hebeler & Rix, 2001; Yoon, 2005). However, the practice of using a non-uniform spacing of receivers has not been adopted widely by now.

Source to first receiver distance (Source offset)

The source offset should be selected keeping in mind the minimization of the near-field effects, which require large offsets, and the adequate capture of high-frequency waves, which undergo high attenuation with distance (far-field effects). The near-field effects contaminate the Rayleigh waves and lead to the underestimation of Rayleigh wave phase velocity. On the other hand, the far-field effects cause a considerable reduction in SNR at traces recorded far from the source. Earlier, a lot of research has been carried out on the near-field effects but still, there is no single rule to entirely eliminate them. Bodet et al. (2009) reported that for linear arrays, the underestimation of phase velocity occurs at wavelengths greater than half of the receiver array length. Yoon and Rix (2009) suggested that the maximum resolvable wavelength to make the near-field effects less than 10–15% is equal to the array center distance (distance from the source to the mid-point of the array). However, Wood and Cox (2012) found that this criterion is not always valid, and it can be site-specific. A study using multiple values of source offsets should be done at the site to understand and minimize the near-field effects. Generally, the source offset can be as taken three to five times the geophone spacing, provided that the signal-to-noise ratio is adequate even at the farthest geophone (Foti et al., 2018). Usually, the range in which the source offset

value should be chosen is suggested as 5–20 m. However, it may depend on the site conditions. Stiff soils require a large source offset value compared to soft soils as presented later in Table 2. Overall, the source offset should be selected as an optimum value such that both the near-field effects and the far-field effects (attenuation of waves at far receivers) are minimized.

Number of receivers

The number of receivers in an MASW test can influence the quality of the dispersion image because a higher number of receivers can reduce the uncertainties in the results (Socco & Strobbia, 2004). It also impacts the depth of investigation because it is connected to the array length. Ideally, based on the required depth of investigation and the resolution at shallow depths, the array length and receiver spacing should be decided and that would fix the number of receivers required. Generally, it is suggested to use 24 or 48 receivers. A large value such as 48 would allow getting V_s profile up to large depths and by allowing for less receiver spacing, and provide higher resolution at shallow depths. However, many times in the field, the number of available receivers is less, or the space is limited. In such cases, multiple shots with different source offsets and receiver spacing should be taken to improve confidence in the results and get more reliable data.

Alignment of the receiver array

The receivers must be in a straight line. Also, they must be placed perfectly vertical and not tilted at all. The slope along the geophone array also affects the MASW results. In an ideal condition, the MASW test must be carried out on the flat ground. The maximum allowed difference in the elevations of the receivers is 0.1*array length, beyond which the MASW results would get significantly altered. Zeng et al. (2012) presented that when the slope along the receiver array is less than 10°, the error in the estimated dispersion characteristics would be within 4%.

Receiver specifications

In MASW, mostly, vertical component geophones are used as the receivers. The natural frequency of the geophones determines the lowest frequency of surface waves that can be recorded and consequently, the maximum depth of V_s profile that can be obtained. A low value of the natural frequency of geophones enables to get deep V_s profiles (Park et al., 2002). If it is required to resolve an extremely thin layer at the top of the soil, high-frequency geophones may be useful. However, as it is obvious, the investigation depth would be comparatively less in the case of high-frequency geophones. Usually, 4.5 Hz geophones are used which can generate V_s profiles up to a maximum of approximately 30 m. If the geophones of about 10–14 Hz frequency are used, the maximum V_s profile can be obtained up to a maximum of 10–15 m approximately (Foti et al., 2018).

Coupling between the source and the base plate

The use of a base plate for taking the shots in MASW can affect the energy transferred to the soil. Using a base plate rather than a direct impact on soil can enhance the

transformation of impact energy into seismic wave energy (Mereu et al., 1963). Kumar and Rakaraddi (2013) found that the use of a base plate increases the maximum wavelength (λ_{max}) that can be extracted, consequently providing higher investigation depth. It was also found that (1) If the height of fall of the MASW source is increased, a higher value of λ_{max} can be obtained. (2) Stiffer soils provide higher λ_{max} compared to softer soils.

Regarding the base plate material, many studies have produced several results. Plates of steel and aluminum generated waves of similar amplitude and frequency content (Keiswetter & Steeples, 1994). A different result by Kim and Lee (2011) stated that polyethylene and steel plates transferred higher energy to the ground compared to the aluminum plate. The use of embedded plates improved the amplitude, but the frequency content was found to be the same (Keiswetter & Steeples, 1995). Larger base plates enabled to get higher seismic energy but an increase in mass without any change in the base plate area did not enhance the spectral content (Keiswetter & Steeples, 1994, 1995). Jeong and Kim (2012) found that compared to a circular plate, a rectangular plate having an aspect ratio of 1–2 increased energy by 10–20%. Also, when the longer side of the rectangular plate is put perpendicular to the array, the frequency bandwidth and power would be maximum. Mahvelati (2019) found that compared to the aluminum plate, Al/EPDM (aluminum/ethylene propylene diene monomer) and polyethylene (PE) plates generated 15–20% larger signal amplitudes, transmitted more energy into the soil, provided more low-frequency energy, and enhanced the SNR. However, although they seem a better option, these plastic/rubber plates undergo more tear. Many times, the benefit compared to metallic plates are not significant and in soft soils; they may have some negative effects. Therefore, the choice of the base plate material should be made very carefully considering the durability and portability of the material and the expected noise at the site (Mahvelati et al., 2020).

Duration of the load

Numerical modeling has been carried out by researchers to study the effect of the duration of load on MASW results. Mahvelati (2019) compared the impact duration of Al and PE base plates. It was found that the PE base plate, which is comparatively softer, ended up transferring the stresses to the soil for a longer time. Because of this, the soil below the PE plate underwent overall higher stresses compared to that below the Al plate, even though the stresses inside the Al plate were larger than the PE plate. It is obvious that when higher stresses (energy) are transferred to the soil, higher λ_{max} can be obtained. In another work, Desai et al. (2019) found that as the duration of load increases, the uncertainty due to the near-field effects decreases.

Sampling frequency

As per the Nyquist criterion, the sampling frequency should have a minimum value of twice the maximum frequency of the propagating signal. However, for the surface wave analyses, usually, sampling frequencies of 500–2000 Hz are considered reasonable. If refraction/reflection analysis is desired to be carried out, higher values of

sampling frequencies should be used. The refraction/reflection analyses are sometimes carried out additionally to be used as a priori information during the inversion procedure. The choice of the sampling frequency can influence the frequency bandwidth that can be extracted.

Recording time

The time to record the waves due to a hammer blow in MASW should be selected such that each receiver captures the full-wave-train passing through it. A check should be made by visually observing in the raw recorded waveform that no wave-train is cut at any receiver. Usually, a recording time of 2 s is sufficient. However, it also depends on the V_s structure of the site (softer soils require higher recording time compared to stiffer soils). Also, a longer receiver array requires a longer recording time. Also, a pre-trigger time of 0.1–0.2 s should be kept so that leakage of waves is avoided and the operations during the signal processing in the frequency domain are not affected.

Filtering and muting of the field data

The field data acquired in an MASW test might be containing the wavefield due to higher modes. However, the surface wave analysis is often based on only the fundamental mode surface waves. The presence of unwanted noise in the data may limit the frequency band of the required dispersion curve or may lead to erroneous results. Therefore, filtering and muting can be applied to the time-offset data before generating the dispersion image. Also, in the recorded data, the portion other than the signal can be muted to avoid the noise in the signal.

Various researchers have implemented different ways of filtering and muting and got good results. Park et al. (2002) presented two methods for the removal of the higher mode data. They are the bow-slice method implemented in the f–k domain and the frequency variant linear move out (FV-LMO) correction. The use of a conventionally used method known as the pie-slice f–k filtering was discouraged because it can also remove parts of the main signal. Ivanov et al. (2005) demonstrated the way of the muting of the portions of the higher modes from the raw waveform, which can improve the bandwidth and resolution of the fundamental mode dispersion curve. However, it generates artificially high velocities at low frequencies. So, the unmuted data should be used at low frequencies while employing this method. Morton et al. (2015) suggested a modified f–k filter, implementing multiple passes of the filter to get better information about the fundamental mode energy. Overall, if implemented properly, the operations of filtering and muting on the MASW field data can enhance the generation of the dispersion image. However, it must be taken care that these operations are applied only to unnecessary noise without hindering the main signal to be used for dispersion image generation. Also, care must be taken because insufficient spatial resolution may cause insufficient mode separation. In this case, an effective/apparent velocity is obtained and filtering cannot be applied.

Forward and backward shots

The shots in the MASW test are suggested to be taken on both sides of the receiver array (forward and reverse shots). If the dispersion curves are the same in both cases,

it ensures that the medium is laterally homogeneous which is the basic assumption in surface wave analysis. If any lateral heterogeneity is present, the changes in energy distribution over the frequency band and in attenuation pattern from both the locations would finally lead to different dispersion curves.

Checking results using parts of the array

Another task to be considered for checking the lateral heterogeneity is the generation of dispersion curves using different portions of the receiver array. For example, in case the data has been acquired with 48 receivers, the dispersion curves can be constructed for receiver numbers 1–24 and then for 25–48. If the dispersion curves are quite similar for both cases, it ensures that lateral homogeneity is there at the location of the data acquisition. If they are quite different, it implies that the medium has lateral heterogeneity (Foti et al., 2018).

Multiple shots and stacking together

A single MASW shot contains a remarkably high amount of noise and adequate resolution cannot be achieved in the required frequency band. If multiple shots are taken and then stacked together, it can significantly improve the signal-to-noise ratio (SNR). Vertical stacking can improve the SNR by the square root of the number of shots (Foti et al., 2014). Therefore, in MASW, it is suggested to take multiple shots and then stack them together for use in the analysis, especially at high noise locations. Also, vertical stacking in the f–k domain is suggested instead of the time domain (Foti et al., 2018). If the length of the receiver array increases, and/or the ambient noise increases, a higher number of shots should be used for stacking. The number of shots to be stacked together can be selected when the SNR remains the same even after adding more shots for stacking (Ivanov & Brohammer, 2008). Another thing to be considered is that after taking each shot, its waveform should be observed visually and the shots containing very high noise or having abnormal waveforms should be removed. Also, to prevent the data from getting affected by the noise, the test should be carried out when the traffic due to vehicles can be avoided.

Multiple shots and mean and standard deviation curve to curb data measurement uncertainty

The experimental dispersion curve of an MASW test suffers from uncertainty due to the noise present at the site. Therefore, rather than using a single dispersion curve to represent a site, it is suggested to generate multiple dispersion curves at the same location and prepare an ensemble of a mean and $\pm$ standard deviation curve. This would take care of the data measurement uncertainty. Section 2.2 provides more details about this.

Overview of the parameters of data acquisition for active MASW test

The parameters discussed above for the active MASW data acquisition have been presented in a tabular format in Tables 1 and 2. Table 1 provides guidelines for any general condition. Table 2 gives guidelines depending on the stiffness of the site (Vs30 value). It is suggested to use Table 1 guideline initially, carry out MASW test,

Table 1 Parameters for data acquisition: active MASW (Foti et al., 2018)

Parameter	Notation	Suggested values	Theoretical implications
Geophone spacing	Δx	1–4 m	Aliasing: usual minimum measurable wavelength $\lambda_{min} = 2\Delta x$ Minimum near-surface layer thickness/resolved depth $P_{min} = \lambda_{min}/3$ to $\lambda_{min}/2$
Array length	L	23–96 m	Maximum wavelength $\lambda_{max} = L$ Expected maximum investigation depth $P_{max} = \lambda_{max}/3$ to $\lambda_{max}/2$
Number of geophones	N	24 or 48	Quality of dispersion image
Distance between source and first geophone	X_1	5–20 m	Near-field and far-field effects Multiple shot locations strongly recommended
Sampling interval	Δt	0.5 ms	Nyquist/Shannon frequency $f_{max} = 1/2\Delta t = 1000$ Hz
Sampling Frequency	$f_s = 1/\Delta t$	2000 Hz	Nyquist/Shannon frequency $f_{max} = f_s/2 = 1000$ Hz
Post-trigger recording length (time window)	T	2 s	Record the whole surface wave-train
Pre-trigger recording length		0.1–0.2 s	Mitigating leakage during processing

Table 2 Parameters for data acquisition: active MASW (Penumadu & Park, 2005)

Vs30 (m/s)	X_1(m)	Δx(m)	L(m)	Optimum geophone (Hz)	Optimum source* (kg)	Recording time (s)	Sampling interval (ms)
<100	1–5	0.25–0.5	≤ 20	4.5	≥5	1	1
100–300	5–10	0.5–1	≤ 30	4.5	≥5	1	1
200–500	10–20	1–2	≤50	4.5–10	≥5	0.5	0.5
>500	20–40	2–5	≤100	4.5–40	≥5	0.5	0.5

*Weight of sledgehammer

and make a preliminary assessment of the stiffness (V_s profile) of the site. Then, based on the stiffness of the site, the guidelines provided in Table 2 can be used. However, still, these guidelines are just to give an overall idea of how to carry out the test. Based on site-specific conditions and the purpose of the test, adapted values of the parameters should be selected.

In Table 1, X_1, Δx, and L refer to the distance between the source and the first geophone, inter-geophone spacing, and the array length, respectively.

3.2 Passive Test

In the passive tests, the ambient vibrations are recorded and used for V_s profiling rather than the use of active sources. The ambient vibrations can be due to natural phenomena such as the earth's vibrations, sea waves, wind, or anthropogenic activities such as traffic and machinery. Usually, the natural phenomena generate lower frequency waves and human activities produce higher frequency waves. The advantage of passive tests over the active test is that they allow getting the dispersion curve data at lower frequencies compared to the active test. Thus, they help in obtaining V_s profiles up to higher depths. Typically, dispersion curve data from the lower (0.2–5 Hz) to intermediate (10–30 Hz) range of frequencies can be obtained using passive surveys. This range depends on factors such as the shape and size of the array, V_s and attenuation properties of the site, and the equipment used (Foti et al., 2018). Also, the passive sources have the advantage of being cheaper and no requirement of deployment and mobilization of a heavy source such as the active sources.

Selection of test parameters and their effects on the uncertainties

Similar to active testing, passive MASW testing is also highly dependent on the selection of the data acquisition parameters. The various test parameters and their influence on the passive MASW testing have been explained below.

Array setup

The passive tests can be carried out using a linear receiver array or 2D arrays. The method using a 1D linear array is called refraction microtremor (ReMi), proposed by Louie (2001). In this, the geophones are set up in the same way as the active MASW test, but the ambient vibrations are recorded and processed rather than those from an active source. The guidelines and pitfalls of the ReMi method have also been provided by Louie et al. (2021). The 2D receiver arrays can be deployed in various configurations such as circular, triangular, L-shape, and T-shape (Foti et al., 2018). Zywicki (1999) provided an in-depth discussion on passive surface wave testing using 2D arrays and found that the uniformly spaced circular arrays can give the best results under a majority of the circumstances. However, in the passive surface wave measurements using linear arrays, the wavefield comes from several directions, which makes the whole analysis extremely complicated and significantly increases the uncertainties in the results (Cox & Beekman, 2011). Therefore, it is highly suggested to avoid the use of a 1D linear array for passive surface wave measurements and to use only the 2D array for the passive test (Foti et al., 2018). However, these arrays require larger areas and are challenging to be placed. Also, there should be sufficient passive surface wave energy in the required frequency range near the array.

Depth of investigation

The maximum depth of investigation is controlled by the maximum retrieved wavelength (λ_{max}) and the resolution at shallow depths is controlled by the minimum

retrieved wavelength (λ_{min}). λ_{max} and λ_{min} primarily depend on the array aperture (maximum distance between 2 receivers) and the minimum spacing between 2 receivers, respectively. The V_s structure of the site and the processing technique can also affect them. Approximately, it is suggested to keep the minimum receiver spacing equal to the desired minimum thickness of the topmost layer and the array aperture at least equal to or 2 times the desired depth of investigation (Foti et al., 2018). Wathelet et al. (2008) provide another criterion, viz., theoretical array resolution limit ($k_{min}/2$) and aliasing limit (k_{max}) to define the frequency limits of the dispersion curve obtained from the passive test array, where k is the wavenumber. Also, when it is important to resolve the shallow layers properly, the passive surveys should be accompanied by the active test to get good high-frequency data.

Number of sensors

The choice of the number of sensors depends on the desired investigation depth. Even though only 4 receivers can provide results, a higher number of receivers would be required to produce better results. A smaller array may cause an overestimation of phase velocity due to poor wavenumber resolution (Yoon, 2005; Jiang et al., 2015). Therefore, it is suggested to keep the number of receivers as high as possible, especially at locations having low ambient vibrations. However, they are generally limited by the available equipment and space.

Recording duration and sampling frequency

The recording time of passive tests is usually suggested as 30–120 min. When the level of ambient vibrations is low, it is suggested to keep a long recording time. Sometimes, if the required frequency band is high, several hours of recordings may be required. After that, these recordings are divided into different time windows which may range from 1 to 5 min approximately. The average of all these time windows is calculated and then used for further processing. The sampling frequency in passive tests is kept lower than in the active tests. This is because the recording time is longer in passive tests. Usually, the sampling frequency is kept at 100–200 Hz.

Natural frequency of sensors

Regarding the natural frequency of the geophones, if the data is required only up to the upper tens of meters of soil, 4.5 Hz geophones are sufficient. If it is required to unravel the deeper soil layers, velocimeters/seismometers having natural periods of 1, 5, or 30 s should be used whose sensitivity is higher compared to geophones. The vertical component geophones provide the data to generate Rayleigh wave dispersion curves. If 3-component sensors are used, they help in generating a horizontal-to-vertical spectral ratio (HVSR) curve, which can help in generating an even deeper V_s profile. More details about the HVSR methods have been provided in Sect. 5.4. All the types of geophones and velocimeters/seismometers require proper installation, coupling with the soil, and leveling while putting them for the recording. Foti et al. (2018) have provided in-depth information about the specifications for the setup/installation of the geophones/velocimeters/seismometers in the field.

Check on the recorded ambient vibrations

To evaluate the ambient vibration level at the site, the models of reference levels of ambient vibrations are available: (1) Low noise model (NLNM); (2) High noise model (NHNM) (Peterson, 1993) which also includes instrumental self-noise. By comparing the recorded waveforms with these models, the user can verify whether the ambient vibration level at the site of acquisition is adequate or not. If the ambient vibration level at the site is not sufficient, it is required to increase the number of sensors, increase the recording time, make sure that the sensors are installed and leveled properly, and not affected by rain, wind, or temperature fluctuations.

3.3 Combined Active and Passive Test

As mentioned earlier, in the active MASW test, the waves generated contain more high-frequency content and lack sufficient low-frequency data. On the other hand, the passive MASW provides good low-frequency data because the ambient wavefield used in it contains primarily low-frequency waves. Therefore, it is imperative that if both of them are used collectively, a dispersion curve with a wide band of frequencies can be obtained. This serves two purposes: (1) Estimation of V_s profile up to higher depths, and (2) Getting high resolution at shallow depths. Also, taking such multiple acquisitions (active and passive) at a single site reaffirms the extraction of fundamental mode data (Martin et al., 2017) and thus improves confidence in the obtained results. It is quite common practice among researchers to use concentric circles as 2D arrays along with the active test to get good results (Wood et al., 2014; Foti et al., 2018). If 3-component seismometers are available, they can also provide a horizontal to vertical spectral ratio (HVSR) curve, which would help in V_s profile estimation at even deeper depths. More information about the HVSR curve and joint inversion using MASW and HVSR has been provided in Sect. 5.4. While carrying out combined active and passive tests, the arrays of both active and passive data acquisition should be placed at nearby locations. However, both the acquisitions must not be carried out together, because the wavefields of both would interfere with each other.

The use of combined active and passive data has been suggested and implemented by many researchers (Park et al., 2005; Tokimatsu 2005; Richwalski et al., 2007; Mahajan et al., 2011; Lontsi et al., 2016; Pamuk et al., 2017; Foti et al., 2018; Kamai et al., 2018; Senkaya et al., 2020). It can aid in getting data on a wide band of frequencies and help in understanding the modal nature of dispersion trends (Park et al., 2007).

4 Data Processing (Estimation of the Experimental Dispersion Curve)

The recorded data on the geophones in the time-offset domain (seismograms) are typically transformed into a dispersion image. Various algorithms/methods are available for this transformation which are discussed later in this section. From the dispersion image, by picking the energy peak at various values of frequencies (sampling), a dispersion curve is extracted. Usually, the dispersion curve is presented as a plot between Rayleigh wave phase velocity and frequency. There are also some other ways to present a dispersion curve, i.e., frequency–slowness and phase velocity–wavelength. Figure 8 shows a typical dispersion image along with the picked dispersion curve in which the X-axis data is on a logarithmic scale. The image generation and dispersion curve extraction were carried out using the software Geopsy (Wathelet, 2008) based on the frequency–wavenumber algorithm. Although the curve can be plotted on either a linear or a logarithmic scale, the logarithmic scale would present the data with better clarity, especially at lower frequencies. Also, before carrying out the inversion, it is suggested to sample the dispersion curve at equal logarithmic frequencies or wavelengths (Foti et al., 2018). The picking of the dispersion curve from a dispersion image may be automated or manual. However, it should be done with utmost care. The lower and upper bounds of the frequencies in the dispersion curve should be decided based on maximum and minimum wavelengths available (λ_{max} and λ_{min}), respectively. These are dependent on the length of the receiver array and inter-receiver spacing, respectively. Suppose the array length is L, then $\lambda_{max} =$ L. If the inter-receiver spacing is Δx, then $\lambda_{min} = 2\Delta x$. Based on these values, the

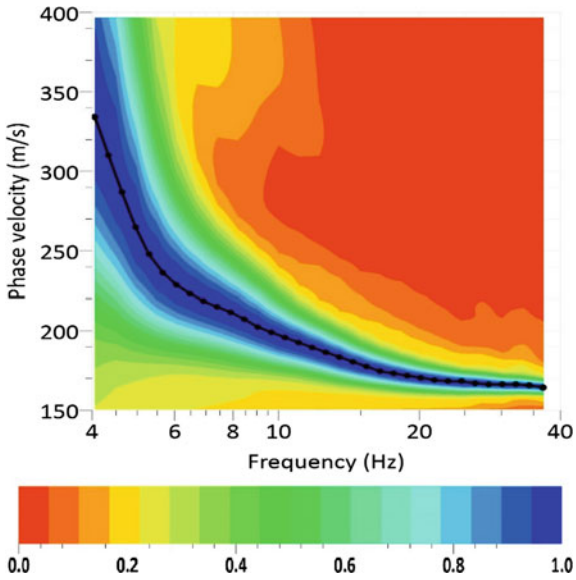

Fig. 8 Typical dispersion image and picked dispersion curve

range of frequencies in the dispersion curve to be extracted is decided. A dispersion curve showing data beyond this range becomes unreliable.

4.1 Methods of MASW Data Processing

Active MASW

There are many signal processing techniques for the active MASW, which include the frequency–wavenumber (f–k) (Capon, 1969; Lacoss et al., 1969; Nolet & Panza, 1976; Horike, 1985; Yilmaz, 1987), high-resolution f–k (Capon, 1969), frequency–slowness (f–p) (also referred as p–ω or τ–p) (McMechan & Yedlin, 1981), phase shift transform (Park et al., 1998), conventional frequency domain beamformer (Johnson & Dudgeon, 1993), cylindrical frequency domain beamformer (Zywicki, 1999), multi-offset phase analysis (MOPA) (Strobbia & Foti, 2006), multichannel nonlinear signal comparison (MNLSC) (Hu et al., 2019), etc.

Conventionally, the f–k and f–p methods have been utilized quite frequently by researchers (Foti, 2000; O'Neill, 2003). The f–k method is based on the 2D Fourier transform of the input time-offset data. The f–p method performs the slant stack transform and then the Fourier transform of the data. However, it was found that these methods underperform in getting adequate resolution dispersion curves when the number of receivers is small (Park et al., 1998). The phase shift method and cylindrical beamformer method were found to provide better resolution comparatively. The phase shift method involves Fourier transformation, amplitude normalization, and then retrieving of dispersion curve. It is quite effective in the decomposition of various modes and noise. The cylindrical beamformer uses the cylindrical wavefield as opposed to plane wavefield in other methods, which becomes handy in dealing with the near-field effects. Tran (2008) provides a detailed description of these four methods.

Various researchers have worked to assess the variability in results due to using different signal processing methods on common experimental data (Cornou et al., 2006a; Tran & Hiltunen, 2011; Cox et al., 2014; Garofalo et al., 2016). When the study location has a simple, normally dispersive V_s profile, these methods would yield reasonably matching results. However, for complex sites, the results of different methods can be different (Cox & Wood, 2011). Dal Moro et al. (2003) examined the three methods: f–k, τ–p, and phase shift methods. They found that the phase shift method can provide better results even with less number of geophones under most circumstances. On the other hand, the other two methods showed aliasing and reduction in quality, especially in the case of a smaller number of geophones. Tran (2015) found that cylindrical beamformer and phase shift transform better imaged the dispersion curve at lower frequencies (<15 Hz) compared to f–k and f–p methods. In a study by Tran and Hiltunen (2011), the spectrum obtained from the cylindrical beamformer provided the best resolution. This can be attributed to the fact that the f–k, f–p, and phase shift transforms treat the signal as a plane wavefield, while the

cylindrical beamformer uses the cylindrical wave equations to transform and identify Rayleigh waves. The assumption of the plane wavefield induces a near-field model incompatibility that may lead to problems in phase velocity estimation at low frequencies (Zywicki, 1999). Hence, a major advantage of the cylindrical beamformer is that it thwarts near-field effects because of using the cylindrical wave equations (no assumption of plane wavefield required). However, some studies have found that the cylindrical beamformer method showed lower phase velocities compared to the passive 2D arrays at lower frequencies. Therefore, the cylindrical beamformer is also not a completely effective method (Li, 2008; Jiang et al., 2015).

Passive MASW

1D geophone array

Louie (2001) developed the method termed refraction microtremor (ReMi) which uses ambient vibrations with a linear array. A 2D slowness–frequency (p–f) transform is applied to collect the Rayleigh waves and identify the true phase velocity. In active MASW tests, the waves have a specific propagation direction, i.e., along the geophone array, whereas passive waves arrive from any direction. ReMi was utilized by Pancha and Pullammanappallil (2011) and it was found that the higher modes of Rayleigh wave dispersion can be identified using this method. Spatial autocorrelation (SPAC) (and its modified versions MSPAC, ESPAC) (Aki, 1957; Ling, 1993; Bettig et al., 2001; Zhao & Li, 2010) has also been suggested to process passive surface waves' data recorded using a 1D linear array. Zhao (2011) has provided a brief explanation of the SPAC and f–k methods. The disadvantage of ReMi is that it requires manual picking, as this depends on subjective judgment, and sometimes influences the results. Also, this method assumes that passive source distribution is homogeneous and isotropic at the site or they are in line with the direction of the receiver array. This condition cannot be satisfied in the field most of the time. Overall, it is suggested to avoid the use of ReMi by many researchers because of a lot of shortcomings (Zywicki, 2007; Rosenblad & Li, 2009a, b; Foti et al., 2018). Instead, the use of 2D geophone arrays is encouraged for passive surface wave analysis.

2D geophone array

Park et al. (2004) introduced a data processing scheme, which is extended from the phase shift method (Park et al., 1998) applied for active MASW tests. Spatial autocorrelation (SPAC) and modified spatial autocorrelation (MSPAC) methods can also be employed for this. It was found that at lower frequencies, SPAC methods perform better than the f–k methods due to the limited resolution capability of f–k methods in treating wavefields coming from different directions (Horike, 1985; Okada, 2003; Cornou et al., 2006b; Wathelet et al., 2008). Zywicki (1999) provides detailed information about passive surface wave analysis using 2D arrays. Three different processing algorithms have been described there which are frequency domain beamformer (FDBF) for 2D arrays (Lacoss et al., 1969), minimum variance distortionless look (MVDL) (Capon, 1969), and multiple signal classification (MUSIC) (Schmidt & Franks, 1986). However, Jiang et al. (2015) found that FDBF

and MUSIC provided reasonably good results, but MVDL could not. The FBDF for 2D arrays is an extension of the beamformer method for the 1D linear receiver arrays. MVDL is a high-resolution method, which decreases the impact of waves coming from directions other than the active look direction. MVDL is also a high-resolution method, having its power estimate similar to the MVDL method.

5 Inversion

Inversion is the process of estimating the V_s profile of the site from the experimental dispersion curve. The process of inversion is not straightforward; it is non-unique and ill-posed, which induces inversion uncertainty. More information about the inversion uncertainty is provided in Sect. 2.3. Various algorithms/methods are available to carry out the inversion process. They are primarily of two types (Foti et al., 2018):

1. Local search algorithms: In this, in the beginning, an initial V_s profile is assumed, and its corresponding theoretical dispersion curve is generated. The misfit between this theoretical dispersion curve and the experimental dispersion curve is calculated. Then, in the next iteration, a modified V_s profile is generated such that the misfit value gets decreased. In this way, several iterations are carried out one after the other. When a point is reached when no noticeable change in the misfit occurs with more iterations (convergence), the process is stopped, and the V_s profile obtained at that time is considered as the final V_s profile. This whole process can be automated. In some software, it must be done manually, where the user can choose the V_s profile iteratively till he finds the best one (trial and error procedure).
2. Global search algorithms: In this, several V_s profiles are generated having an equivalent match with the experimental dispersion curve. The user is supposed to choose the parameterization, i.e., the expected values of the number of layers and the ranges of thickness, V_s, V_p, density, and Poisson's ratio of the layers.

Due to the various uncertainties associated with the MASW testing and its interpretations, the choice of a single V_s profile, i.e., the use of local search algorithms can involve significant errors. Also, in the local search algorithms, there is a possibility of getting caught in some local minima. The selection of the initial model also heavily affects the finally generated V_s profile. On the other hand, the consideration of a suite of V_s profiles, i.e., the use of global search algorithms would allow accounting for the uncertainties during the further analysis. Therefore, the use of global search algorithms is usually recommended for the inversion process. Poggi et al. (2012) have suggested a combined use of global and local search algorithms in which model space is searched and then the solution corresponding to the minimum value of misfit is picked out.

For carrying out the inversion, several methods are available, such as trial and error method (Stokoe et al., 1994), Occam's algorithm (Constable et al., 1987), least-squares technique (Xia et al., 1999), simulated annealing (Sen & Stoffa, 1991;

Martínez et al., 2000), genetic algorithm (Lomax & Snieder, 1994; Hunaidi, 1998), Monte Carlo method (Socco & Boiero, 2008), neighborhood algorithm (Sambridge, 1999; Wathelet, 2008), and mutation particle swarm optimization (MPSO) (Zarean et al., 2015). Some research has been carried out on how the use of different inversion methods by different analysts would influence the final V_s profile (Cox et al., 2014; Garofalo et al., 2016). Pelekis and Athanasopoulos (2011) provide a good description of the methods used for inversion and also propose a simplified inversion method (SIM).

While carrying out inversion, a theoretical dispersion curve has to be generated for each V_s profile from inversion, which is termed forward modeling. This theoretical dispersion is then compared with the experimental dispersion curve using the misfit value. For the forward modeling, various methods are available which are (a) Transfer matrix method proposed by Thomson (1950) and Haskell (1953), and subsequently modified by Knopoff (1964), Dunkin (1965), and Herrmann (1994). (b) Dynamic stiffness matrix method (Kausel & Roesset, 1981). (c) Propagator matrix method (Gilbert & Backus, 1966; Aki & Richards, 1980), etc.

5.1 Choice of the Depth of V_s Profile While Doing Inversion

The maximum depth of the V_s profile obtained from an MASW test is constrained due to various factors. It cannot be chosen randomly. It is unreliable if the software provides a V_s profile up to exceedingly high depth when the dispersion curve does not contain sufficient data at low frequencies (high wavelengths). Several researchers have found that the intra-analyst and inter-analyst uncertainties in the V_s profiles at large depths are much significant than those at shallow depths (Tran & Hiltunen, 2011; Cox et al., 2014; Garofalo et al., 2016). This implies that utmost care needs to be taken in deciding the maximum depth of V_s profile obtained from an MASW test. The maximum investigation depth is a function of the maximum available wavelength which mainly depends on these factors (Foti et al., 2018):

- The length/aperture of the receivers' array used for the test.
- The frequency content of the generated signals (depending upon the source and site attenuation).
- V_s profile of the soil.
- The receivers' frequency bandwidth.

Michaels (2011) presented a way to estimate the maximum frequency up to which the fundamental mode is dominant, based on Karl (1989). He also used eigenfunctions of frequencies to demonstrate how deep each frequency wave is penetrating which can be useful in knowing the usable frequency band for the MASW analysis.

Once the dispersion curve is generated from an MASW test, the values of the maximum wavelength (λ_{max}) and the minimum wavelength (λ_{min}) to be used for V_s profile generation must be fixed. It can be decided based on the minimum and

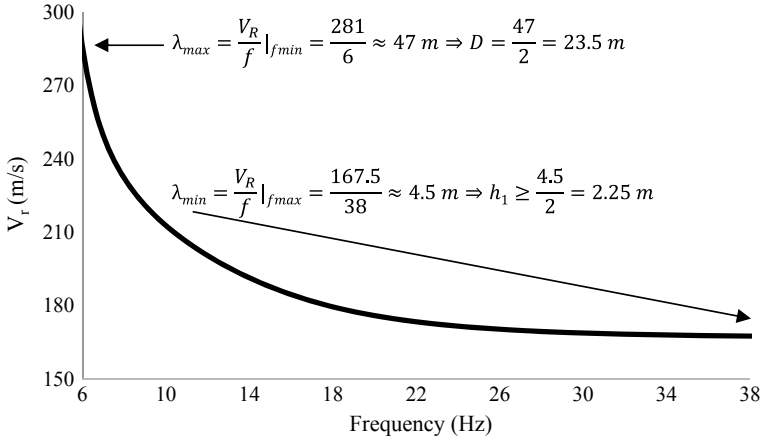

Fig. 9 Determination of maximum and minimum wavelengths available from the MASW test, which fixes the maximum depth of V_s profile and the minimum thickness of the top layer of the V_s profile that can be resolved, respectively

maximum frequencies obtained in the dispersion curve. This has been demonstrated in Fig. 9.

Figure 9 is a typical example of an experimental dispersion curve. As it is evident, λ_{max} is approximately 47 m. So, the maximum depth D up to which the V_s profile can be generated using this curve is $\lambda_{max}/2 = 23.5$ m. However, when it is required to be more conservative, this depth D should be kept limited to $\lambda_{max}/3$. Also, $\lambda_{min} = 4.5$ m indicates that the thickness of the topmost layer in the retrieved V_s profile should be at least 2.25 m. This means that, at this particular site, if there is a thin layer of less than 2.25 m thickness at the top, it is not possible to identify it using this experimental dispersion curve. In that case, another MASW test would be required to get the dispersion curve data at frequencies higher than 38 Hz which would help to resolve wavelengths less than 4.5 m.

5.2 Parameterization During Inversion

While carrying out the inversion process, it is required to choose a possible range of the parameters related to inversion. These parameters to be selected for each layer are the V_s, thickness (H) (except the half-space), V_p (compressional wave velocity), or Poisson's ratio (ν) and density (ρ). In some cases, the damping ratio (D) is also incorporated in the parameterization in case the attenuation is also considered in the model. Out of these parameters, V_s and H are the parameters having the highest impact on the dispersion curve. The values of ν and ρ can be given as a constant usually because they have negligible influence on the dispersion (Socco & Strobbia, 2004). They are chosen based on some available a priori data or some standard values

from the literature. However, the V_p is connected to V_s through ν. So, it is a good practice to give a range of ν which would allow a broad range of V_p and prevent it from getting trapped into unrealistic values. Also, in some cases, the water table can be present in the subsoil, due to which the values of ν and V_p become extremely high and subsequently affect the dispersion curve. In such cases, in inversion, if parameterization is given without the consideration of the water table, it can give substantially erroneous results. Therefore, it is required to have an estimate of the water table at the testing location and its consideration during inversion by providing a quite high value of ν and V_p (Foti & Strobbia, 2002). Regarding ρ, its increasing values with depth can provide results with better accuracy (Ivanov et al., 2009). The usually occurring values of ν and ρ for different soil conditions have been given by Foti et al. (2018).

The number of layers should be selected such that it is not too high which can be unrealistic. Also, it should be sufficient to properly resolve the soil profile. Di Giulio et al. (2012) have provided a method using multiple-model parameterization and Akaike's information criterion that can help in finding the adequate number of soil layers, and selecting the best class of models. Also, it is required to carry out multiple inversions with different parameterizations to find out the most appropriate V_s models. Methods to select appropriate parameterizations for different trials in the absence of any a priori data have been proposed by Cox and Teague (2016), and Vantassel and Cox (2021).

5.3 Special Considerations During Inversion: Inversely Dispersive Layers and Higher Modes

Before carrying out the inversion process, the experimental dispersion curve should be thoroughly perceived, which would hint at the V_s profile. If the V_r is continuously increasing with the decrease in the frequency, it is most likely that the profile has continuously increasing V_s with depth. If a kink is visible at some place in the dispersion curve, or the V_r remains constant with a change of frequency in a certain range, it can be a likely indication of a softer layer below a stiffer layer (Foti et al., 2018). Figure 10 shows an example where there is an unusual feature of a trough in the dispersion curve (approximately from 8 to 20 Hz). This type of shape is an indicative of inverse layering pattern (soft layer trapped between two stiff layers or stiffer layer trapped between two softer layers) in the V_s profile. In the InterPACIFIC project involving several analysts working on the same experimental dataset, a lower velocity layer in the top 50 m soil at a site at Mirandola was identified by only 5 of the total 12 teams (Garofalo et al., 2016). This clearly indicates that extra care should be taken in the visualization and interpretation of the dispersion curve before inversion, especially in the case of an inversely dispersive V_s profile.

In some cases, due to high impedance contrast between two layers or inverse layering, higher modes become dominant and the extracted dispersion curve from

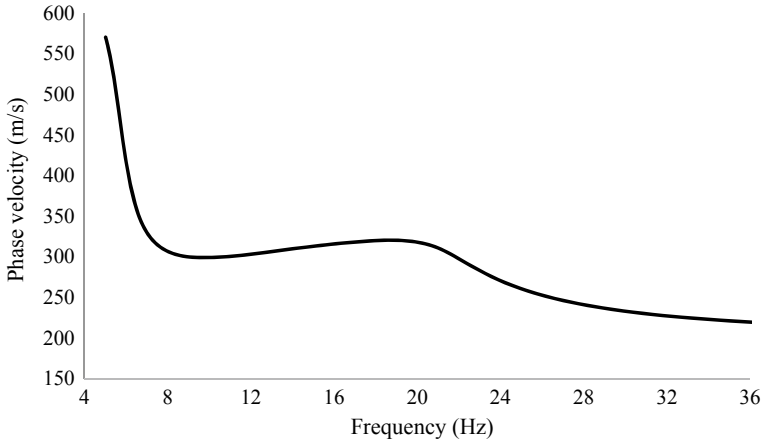

Fig. 10 A typical example of dispersion curve showing a trough between 8 and 20 Hz, indicating the presence of a softer layer below a stiffer layer at some depth

the dispersion image may be an apparent dispersion curve because of mode jumping. Figure 11 explains this phenomenon in which higher modes impede the extraction of the fundamental mode dispersion curve. If such an apparent curve is considered for further analysis, it would lead to completely different results from the real scenario. Therefore, dealing with higher modes requires some more effort compared to the normal analyses. Maraschini and Foti (2010) have proposed a way to deal with higher modes. Wood et al. (2014) have also shown a way to identify and deal with higher modes.

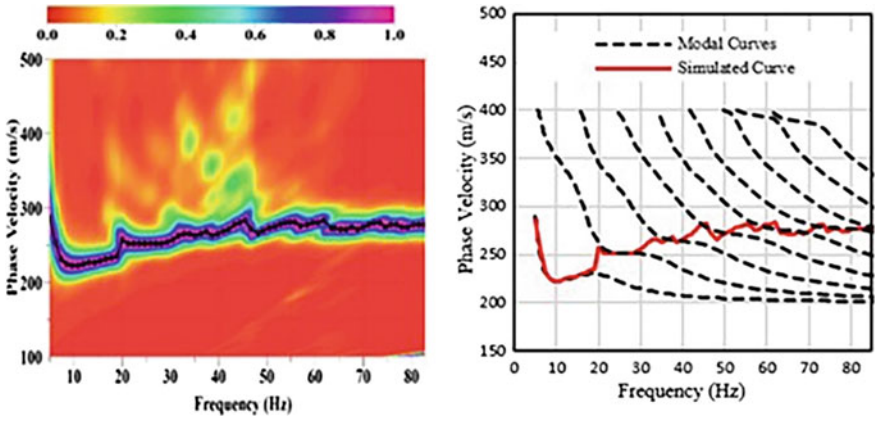

Fig. 11 A typical example of dispersion curve extraction affected by mode jumps, resulting in an apparent dispersion curve in place of the fundamental mode dispersion curve (Roy & Jakka, 2020)

5.4 Use of Horizontal to Vertical Spectral Ratio (HVSR) and Joint Inversion

The depth of investigation in an active MASW test using a sledgehammer can reach up to a maximum of 20–30 m approximately, as discussed earlier. In many cases, the data at a higher depth would be required. For that, the horizontal to vertical spectral ratio (HVSR) can become useful. The HVSR is the ratio of the Fourier spectra of horizontal and vertical velocity components of the ambient vibration recordings at a site. The horizontal one is the root mean square of the two orthogonal horizontal components. The technique which uses this ratio to estimate the V_s profile of soil is called the H/V technique, popularized by Nakamura (1989). The ambient vibrations may be due to the earth's vibrations, sea waves, wind, or human activities such as walking and driving vehicles. As these ambient vibrations are of low frequency, the HVSR method provides the data of higher depths of a V_s profile. The method is based on obtaining the curve between the H/V ratio and frequency at a site.

The field instrument used for this can be a single station 3-component sensor or an array of 3-component geophones which may be in the shape of a triangle, circle, L-shape, or any other. Figure 12 shows a single station 3-component sensor (Micromed, 2012). The signals are recorded for a particular duration and then divided into separate time windows. The H/V ratio is the average value obtained from all the time windows considered. The computed Fourier amplitude spectra can be smoothened using different ways. The method proposed by Konno and Ohmachi (1998) is a popular method for that currently. The peaks in any H/V curve correspond to an impedance contrast between 2 soil layers. Sometimes, a peak may be due to a velocity inversion or higher modes. To get a deeper and more accurate V_s profile at a site, the use of joint inversion using both the MASW and HVSR data has proven

Fig. 12 A single station 3-component ambient vibration recording sensor to obtain H/V spectral ratio curve

to be a particularly good technique (Scherbaum et al., 2003; Parolai et al., 2005; Arai & Tokimatsu, 2005; Castellaro & Mulargia, 2009). So, currently, such type of joint inversion is widely used worldwide. An important parameter obtained using the HVSR method is the fundamental frequency of the site (Haghshenas et al., 2008). Due to that, an advantage of HVSR is that it can help in constraining the bedrock depth (Wood et al., 2014). It is suggested to carry out HVSR investigations as per the guidelines provided by the SESAME project (SESAME Team, 2004). A thorough review of the application of the HVSR method has been presented by Molnar et al. (Molnar et al., 2018). The advantage of the joint inversion using the combined active MASW and HVSR is that the former provides good high-frequency data, enabling to get good resolution at shallow depths; and the latter provides good low-frequency data, enabling to get data up to deeper depths.

5.5 Use of a Priori Information

A lot of investigations by various researchers have been carried out to investigate how a priori information can help to produce better results in surface wave analysis. Cox and Wood (2011) compared the results of SASW, MASW, and ReMi methods. It was found that when a priori information about the water table (from P-wave refraction data) was used, the inter-method uncertainty reduced from 20–30% to less than 10%. Garofalo et al. (2016) found that a priori data in the form of borehole logs, P-wave refraction analysis, local geology, Rayleigh wave ellipticity, and HVSR can help in generating better results. Wood et al. (2015) found that for finding the V_s profile that reflects the actual soil layering, detailed subsurface investigations help in constraining the surface wave inversions. This becomes especially important for soils having high impedance contrasts and/or velocity reversals. The MASW results are typically used for seismic site response analysis which requires the knowledge of modulus reduction and damping ratio curves which depend on the soil type. The lack of knowledge of soil type can induce substantial uncertainties in the site response analysis results (Desai & Jakka, 2017). On the other hand, the availability of a priori data which includes the soil type from borehole logs can reduce the uncertainties in site response analysis significantly (Desai & Jakka, 2021; Desai et al., 2022). Overall, it is imperative that any a priori information in the form of borehole logs, water table estimation, etc. should be used as complementary data along with the MASW test to produce results with higher confidence and fewer uncertainties. A typical example of how a priori information can affect the results of MASW inversion has been shown in Fig. 13. The a priori information that has been included during the inversion is the thickness of the soil layers and the number of soil layers. While going from Fig. 13a to Fig. 13b, it is visible that V_s profiles are becoming highly constrained with the use of a priori information. Also, Fig. 13c shows that the standard deviation of the natural logarithm of V_s ($\sigma_{\ln V_s}$) is significantly decreased in the case of inversion with the a priori information.

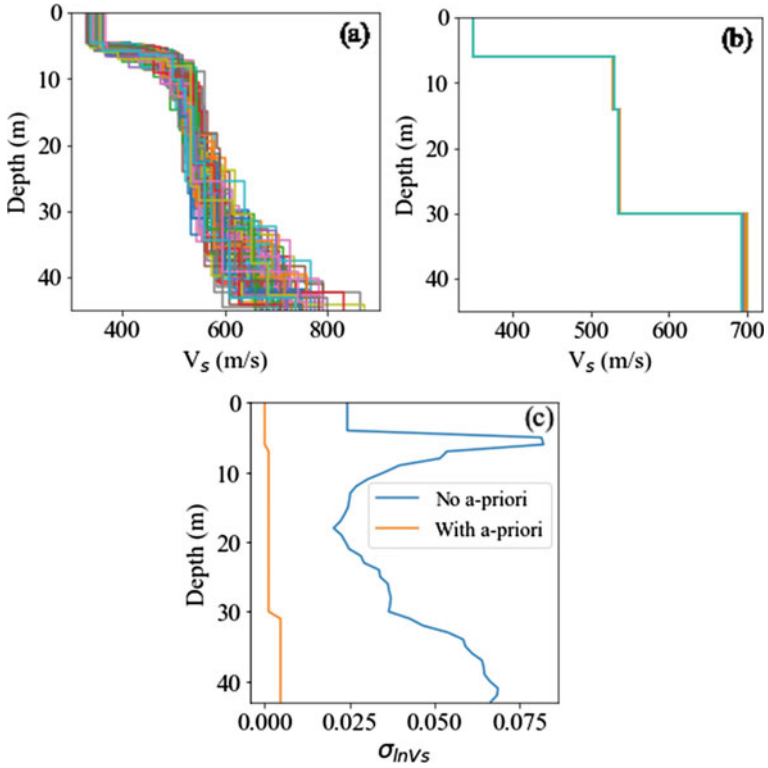

Fig. 13 V_S profiles after inversion considering **a** No a priori information; **b** a priori information; and **c** Influence of a priori information on the variability of V_S

6 Concluding Remarks

The MASW is the most common test currently for seismic site characterization and subsequent applications. Although its usage is quite extensive across the globe, the meticulous specifications associated with the complete method are not known to many practitioners. Due to the lack of awareness about the uncertainties in MASW, the practice of using MASW without following necessary rules is still prevalent. To explain these rules, on the whole, a comprehensive list of references has been presented in this article. Also, some results from the work carried out by us have been presented and used for necessary inferences. This also enabled us to cover all the different aspects of the MASW testing in depth. Subsequently, an attempt has been made to assemble and present a set of recommendations that are to be followed for a reliable practice of MASW testing. There are specifications for all three steps of the MASW, i.e., data acquisition, processing, and inversion. Primarily, the specifications are related to the source to first receiver distance, inter-receiver spacing, receiver array length, sampling frequency, choice of MASW source, boundaries of the generated

dispersion curve and the maximum depth of V_s profile that can be extracted, use of a priori information, joint inversion with HVSR method, etc. Discussions are also made on how the choice of these parameters influences the uncertainties in the MASW test and how these uncertainties can be minimized. Because the MASW method suffers from several uncertainties, while using this method, there must be a goal to restrict these uncertainties to the minimum level and/or account for them in further analyses. The suggestions presented in this study come from a large set of references. So, they would be helpful for people working in academics/industry in the fields of geophysical investigations, seismic hazard assessment, and many others as the MASW test has plenty of applications in various domains. Also, there is a dire need for a code that deals with the specifications for seismic surface wave testing because of its popularity and wide usage across the world. The summary of this article in the form of guidelines is presented below, which would help to minimize the uncertainties and increase the reliability of MASW testing.

Guidelines at a glance for a reliable estimation of shear wave velocity profile:

- The distance between the source and the first geophone (source offset) should be kept at approximately 5–20 m. However, if a source such as Vibroseis is used, the source offset can be kept higher.
- The inter-geophone spacing should be kept at approximately 1–4 m.
- The length of the geophone array should be kept at approximately 23–96 m.
- The number of geophones should be kept 24 or 48. If fewer geophones are used, the test should be repeated with different inter-geophone spacing to get good resolution.
- The sampling frequency should be kept at 500–2000 Hz. A higher sampling frequency would enable better resolution for very stiff top layers (e.g., pavement systems).
- The recording time and pre-trigger time are suggested as 2 s and 0.1–0.2 s, respectively. Also, the raw recorded waveform should be observed visually, and it should be made sure that full wave-train is captured on each geophone.
- The natural frequency of geophones is usually recommended as 4.5 Hz. If the depth of investigation required is quite shallow and/or high resolution is required at extremely shallow depths, then geophones of higher natural frequency can be used. If the information up to very high depth is required, then geophones of lower natural frequency should be used.
- The mass of the sledgehammer should be at least 5 kg. However, a heavier sledgehammer enables the acquisition of V_s profiles up to higher depths.
- With a single acquisition layout, around 5–20 shots should be taken (till the signal-to-noise ratio becomes acceptable), stacked, and then used to generate a dispersion curve.
- Taking forward and reverse shots (keeping the source on either side of the array) is recommended to tackle the effect of lateral heterogeneity.
- If any a priori information from some other test is used, the MASW test location should be kept near the location of the other test. Also, the V_s profile from MASW should correlate with the other field tests.

- The dispersion curves obtained from the MASW testing should be further analyzed along with the HVSR curves obtained from ambient vibrations or small earthquakes using the joint inversion technique, which enables to extend the shear wave velocity profiles up to bedrock and also helps in the estimation of bedrock depth, bedrock velocity, and site fundamental frequency.
- Whenever a researcher is carrying out the MASW test for the first time or a new methodology for the interpretation of MASW is suggested, it is suggested to validate their results using a comprehensive surface wave database by Passeri et al. (2021) which is an excellent source to be used as a reference benchmark.

Acknowledgements The authors wish to thank Science and Engineering Research Board (SERB), Department of Science and Technology (DST), Government of India, for providing financial support for carrying out the current research (Project Grant Code No. SB/FTP/ETA-164-2014).

References

Aki, K. (1957). Space and time spectra of stationary stochastic waves, with special reference to micro-tremors. *Bulletin. Earthquake Research Institute, University of Tokyo, 35*, 415–456.

Aki, K., & Richards, P. G. (1980). *Quantitative seismology: Theory and methods*. W. H. Freeman & Co.

Anbazhagan, P., & Sitharam, T. G. (2008). Site characterization and site response studies using shear wave velocity. *Journal Seismol Earthquake Engineering, 10*(2), 53–67.

Andrus, R. D., & Stokoe, K. H., II. (2000). Liquefaction resistance of soils from shear-wave velocity. *Journal Geotech Geoenvironmental Engineering, 126*(11), 1015–1025.

Arai, H., & Tokimatsu, K. (2005). S-wave velocity profiling by joint inversion of microtremor dispersion curve and horizontal-to-vertical (H/V) spectrum. *Bulletin of the Seismological Society of America, 95*(5), 1766–1778.

Asten, M. W., Askan, A., Ekincioglu, E. E., Sisman, F. N., & Ugurhan, B. (2014). Site characterisation in north-western Turkey based on SPAC and HVSR analysis of microtremor noise. *Exploration Geophysics, 45*(2), 74–85.

Ayolabi, E. A., & Adegbola, R. B. (2014). Application of MASW in road failure investigation. *Arabian Journal of Geosciences, 7*, 4335–4341.

Bergamo, P., Dashwood, B., Uhlemann, S., Swift, R., Chambers, J. E., Gunn, D. A., & Donohue, S. (2016). Time-lapse monitoring of climate effects on earthworks using surface waves. *Geophysics, 81*(2), EN1–EN15.

Bettig, B., Bard, P. Y., Scherbaum, F., Riepl, J., Cotton, F., Cornou, C., & Hatzfeld, D. (2001). Analysis of dense array noise measurements using the modified spatial auto-correlation method (SPAC): Application to the Grenoble area. *Bollettino Di Geofisica Teorica Ed Application, 42*(3–4), 281–304.

Boaga, J., Vignoli, G., & Cassiani, G. (2011). Shear wave profiles from surface wave inversion: The impact of uncertainty on seismic site response analysis. *Journal of Geophysics and Engineering, 8*(2), 162–174.

Bodet, L., Abraham, O., & Clorennec, D. (2009). Near-offset effects on Rayleigh-wave dispersion measurements: Physical modeling. *Journal of Applied Geophysics, 68*, 95–103.

Bozorgnia, Y., Abrahamson, N. A., Al, L., Ancheta, T. D., Atkinson, G. M., Baker, J. W., Baltay, A., Boore, D. M., Campbell, K. W., Chiou, B. S. J., et al. (2014). NGA-West2 research project. *Earthquake Spectra, 30*(3), 973–987.

Caielli, G., de Franco, R., Di Fiore, V., Albarello, D., Catalano, S., Pergalani, F., Cavuoto, G., Cercato, M., Compagnoni, M., Facciorusso, J., et al. (2020). Extensive surface geophysical prospecting for seismic microzonation. *Bulletin of Earthquake Engineering, 18*, 5475–5502.

Capon, J. (1969). *High-Resolution Frequency-Wavenumber Spectrum Analysis. Proceedings IEEE, 57*(8), 1408–1418.

Castellaro, S., & Mulargia, F. (2009). Vs30 estimates using constrained H/V measurements. *Bulletin of the Seismological Society of America, 99*(2A), 761–773.

Connolly, D. P., Kouroussis, G., Woodward, P. K., Alves Costa, P., Verlinden, O., & Forde, M. C. (2014). Field testing and analysis of high speed rail vibrations. *Soil Dynamics and Earthquake Engineering, 67*, 102–118.

Constable, S. C., Parker, R. L., & Constable, C. G. (1987). Occam's inversion: A practical algorithm for generating smooth models from electromagnetic sounding data. *Geophysics, 52*(3), 289–300.

Cornou, C., Ohrnberger, M., Boore, D. M., Kudo, K., & Bard, P.-Y. (2006a). Derivation of structural models from ambient vibration array recordings: results from an international blind test. In P. Y. Bard, E. Chaljub, C. Cornou, F. Cotton, & P. Guéguen (Eds.), *Proceedings of the 3rd International Symposium on the Effects of Surface Geology on Seismic Motion*; Aug 30-Sep 1; Grenoble, France; LCPC Editions.

Cornou, C., Ohrnberger, M., Boore, D. M., Kudo, K., & Bard, P.-Y. (2006b). Using ambient noise array techniques for site characterisation: Results from an international benchmark. In P. Y. Bard, E. Chaljub, C. Cornou, F. Cotton, & P. Guéguen (Eds.), *Proceedings of the 3rd International Symposium on the Effects of Surface Geology on Seismic Motion*; Aug 30-Sep 1; Grenoble, France; LCPC Editions.

Cox, B. R., & Beekman, A. N. (2011). Intramethod variability in ReMi dispersion measurements and Vs estimates at shallow bedrock sites. *Journal Geotechnical Geoenvironmental Engineering, 137*(4), 354–362.

Cox, B. R., & Teague, D. P. (2016). Layering ratios: A systematic approach to the inversion of surface wave data in the absence of a priori information. *Geophysical Journal International, 207*(1), 422–438.

Cox, B. R., & Wood, C. M. (2010). A comparison of linear-array surface wave methods at a soft soil site in the Mississippi embayment. In *GeoFlorida 2010 Adv Anal Model Des*, pp. 1369–1378.

Cox, B. R., & Wood, C. M. (2011). Surface wave benchmarking exercise: Methodologies, results and uncertainties. In *GeoRisk 2011 Risk Assess Management*, Jun 26–28; Atlanta (GA), pp. 845–852.

Cox, B. R., Wood, C. M., & Teague, D. P. (2014). Synthesis of the UTexas1 surface wave dataset blind-analysis study: Inter-analyst dispersion and shear wave velocity uncertainty. In *Geo-Congress 2014 Geo-Characterization Model Sustain.* Feb 23–26; Atlanta (GA), pp. 850–859.

Crice, D. (2005). MASW, the wave of the future. *Journal of Environmental and Engineering Geophysics, 10*(2), 77–79.

Cubrinovski, M., Green, R. A., Allen, J., Ashford, S., Bowman, E., Brendon, B., Cox, B., Hutchinson, T., Kavazanjian, E., et al. (2010). Geotechnical reconnaissance of the 2010 Darfield (Canterbury) earthquake. *Bulletin New Zealand Society Earthquake Engineering, 43*(4), 243–320.

Dal Moro, G., Pipan, M., Forte, E., & Finetti, I. (2003). Determination of rayleigh wave dispersion curves for near surface applications in unconsolidated sediments. In *SEG Technical Program Expanded Abstracts,* pp. 1247–1250.

Desai, A., & Jakka, R. S. (2017). Effect of uncertainty in soil type on seismic site response. In *Proceedings Indian Geotechnial Conference 2017 (IGC-2017)*, GeoNEst, December 14–16, 2017, IIT Guwahati, India, pp. 1–4.

Desai, A., & Jakka, R. S. (2021). Impact of A-priori Information on Data Measurement Uncertainty in MASW Testing. In *Proceedings Research Conclave 2021, December 4–5, 2021, IIT Roorkee, India*. IGS Local and Student Chapter Roorkee, paper no. TH-IV-31, pp. 1–4.

Desai, A., Kranthikumar, A., & Jakka, R. S. (2022). Role of borehole information in minimizing uncertainties in surface wave testing. In T. G. Sitharam, S. Kolathayar, & R. S. Jakka (Eds.), *Earthquake Geotechnics*. Lect Notes Civ Eng. Vol. 187. Springer, Singapore, pp. 55–65.

Desai, A., Roy, N., Jakka, R. S., Narayan, J. P., & Kranthikumar, A. (2019). Influence of source characteristics on the uncertainties in MASW survey. In F. Silvestri & N. Moraci (Eds.), *Earthq Geotech Eng Prot Dev Environ Constr Proc 7th Int Conf Earthq Geotech Eng 2019* (pp. 2068–2075). Italy.

Diaz-Segura, E. G. (2015). Effect of MASW field configuration on estimation of shear wave propagation velocity in sloped terrain. *Geotechnical Letter, 5*, 21–27.

Dunkin, J. W. (1965). Computations of modal solutions in layered elastic media at high frequencies. *Bulletin of the Seismological Society of America, 55*(2), 335–358.

Dwivedi, V. K., Dubey, R. K., Pancholi, V., Rout, M. M., Singh, P., Sairam, B., Chopra, S., & Rastogi, B. K. (2020). Multi criteria study for seismic hazard assessment of UNESCO world heritage Ahmedabad City, Gujarat. *Western India. Bulletin Engineering Geology Environment, 79*, 1721–1733.

Ebrahimian, H., Jalayer, F., Forte, G., Convertito, V., Licata, V., D'Onofrio, A., Santo, A., Silvestri, F., & Manfredi, G. (2019). Site-specific probabilistic seismic hazard analysis for the western area of Naples. *Italy. Bulletin Earthquake Engineering, 17*(9), 4743–4796.

Foti, S. (2000). Multistation methods for geotechnical characterization using surface waves. [dissertation]: Politecnico di Torino, Italy.

Foti, S., Comina, C., Boiero, D., & Socco, L. V. (2009). Non-uniqueness in surface-wave inversion and consequences on seismic site response analyses. *Soil Dynamics and Earthquake Engineering, 29*(6), 982–993.

Foti, S., Hollender, F., Garofalo, F., Albarello, D., Asten, M., Bard, P. Y., Comina, C., Cornou, C., Cox, B., Di Giulio, G., et al. (2018). Guidelines for the good practice of surface wave analysis: A product of the InterPACIFIC project. *Bulletin of Earthquake Engineering, 16*, 2367–2420.

Foti, S., Lai, C., Rix, G. J., & Strobbia, C. (2014). *Surface wave methods for near-surface site characterization.* CRC Press.

Foti, S., Parolai, S., Albarello, D., & Picozzi, M. (2011a). Application of surface-wave methods for seismic site characterization. *Surveys in Geophysics, 32*(6), 777–825.

Foti, S., Parolai, S., Bergamo, P., Di, G. G., Maraschini, M., Milana, G., Picozzi, M., & Puglia, R. (2011b). Surface wave surveys for seismic site characterization of accelerometric stations in ITACA. *Bulletin of Earthquake Engineering, 9*, 1797–1820.

Foti, S., & Strobbia, C. (2002). Some notes on model parameters for surface wave data inversion. In *15th EEGS Sympsium Application Geophysics to Engineering Environmental Probl*, pp. cp-191–00064.

Garofalo, F., Foti, S., Hollender, F., Bard, P. Y., Cornou, C., Cox, B. R., Ohrnberger, M., Sicilia, D., Asten, M., Di Giulio, G., et al. (2016). InterPACIFIC project: Comparison of invasive and non-invasive methods for seismic site characterization. Part I: Intra-comparison of surface wave methods. *Soil Dynamics and Earthquake Engineering, 82*, 222–240.

Gilbert, F., & Backus, G. E. (1966). Propagator matrices in elastic wave and vibration problems. *Geophysics, 31*(2), 326–332.

Giulio Di, G., Savvaidis, A., Ohrnberger, M., Wathelet, M., Cornou, C., Knapmeyer-Endrun, B., Renalier, F., Theodoulidis, N., & Bard, P. Y. (2012). Exploring the model space and ranking a best class of models in surface-wave dispersion inversion: Application at European strong-motion sites. *Geophysics, 77*(3), B147–B166.

Griffiths, S. C., Cox, B. R., Rathje, E. M., & Teague, D. P. (2016). Mapping dispersion misfit and uncertainty in vs profiles to variability in site response estimates. *Journal Geotechnical Geoenvironmental Engineering, 142*(11), 04016062.

Haghshenas, E., Bard, P. Y., Theodulidis, N., Atakan, K., Cara, F., Cornou, C., Cultrera, G., Di Giulio, G., Dimitriu, P., Fäh, D., et al. (2008). Empirical evaluation of microtremor H/V spectral ratio. *Bulletin of Earthquake Engineering, 6*, 75–108.

Haskell, N. A. (1953). The dispersion of surface waves on multilayered media. *Bulletin of the Seismological Society of America, 43*(1), 17–34.

Hebeler, G. L., & Rix, G. J. (2001). Site characterization in Shelby county, Tennessee using advanced surface wave methods. MAE Center CD Release 06–02, Georgia Institute of Technology, USA.

Heisey, J. S., Stokoe, K. H., II., & Meyer, A. H. (1982). Moduli of pavement systems from spectral analysis of surface waves. *Transportation Research Record, 852*, 22–31.

Herrmann, R. B. (1994). *Computer programs in seismology* (Vol. IV). Louis University.

Hobiger, M., Bergamo, P., Imperatori, W., Panzera, F., Lontsi, A. M., Perron, V., Michel, C., Burjánek, J., & Fäh, D. (2021). Site characterization of swiss strong-motion stations: The benefit of advanced processing algorithms. *Bulletin of the Seismological Society of America, 111*(4), 1713–1739.

Horike, M. (1985). Inversion of phase velocity of long-period microtremors to the S-wave-velocity structure down to the basement in urbanized areas. *Journal of Physics of the Earth, 33*, 59–96.

Hu, H., Senkaya, M., & Zheng, Y. (2019). A novel measurement of the surface wave dispersion with high and adjustable resolution: Multi-channel nonlinear signal comparison. *Journal of Applied Geophysics, 160*, 236–241.

Hunaidi, O. (1998). Evolution-based genetic algorithms for analysis of non-destructive surface wave tests on pavements. *NDT E Int., 31*(4), 273–280.

Ivanov, J., & Brohammer, M. (2008). Surfseis: active and passive MASW—User's Manual Version 2.0 Supplemental.

Ivanov, J., Park, C. B., Miller, R. D., & Xia, J. (2005). Analyzing and filtering surface-wave energy by muting shot gathers. *Journal of Environmental and Engineering Geophysics, 10*(3), 307–322.

Ivanov, J., Tsoflias, G., Miller, R. D., & Xia, J. (2009). Practical aspects of MASW inversion using varying density. In *Proceedings Sympsium Application Geophyics to Engineering Environment Problem SAGEEP*, pp. 171–177.

Jakka, R. S., Roy, N., & Wason, H. R. (2014). Implications of surface wave data measurement uncertainty on seismic ground response analysis. *Soil Dynamics and Earthquake Engineering, 61–62*, 239–245.

Jeong, J.-H., & Kim, J.-H. (2012). Comparison of signal powers generated with different shapes of hammer plates. *Journal of the Korean Earth Science Society, 33*(5), 395–400.

Jiang, P., Tran, K. T., Hiltunen, D. R., & Hudyma, N. (2015). An appraisal of a new generation of surface wave techniques at a test site in Florida. In *IFCEE 2015*, pp. 1981–1992.

Joh, S. H., Park, D. S., Magno, K., & Lee, J. H. (2019). Stress-based velocity correction for evaluating the shear-wave velocity of the earth core of a rockfill dam. *Soil Dynamics and Earthquake Engineering, 126*, 105785.

Johnson, D. H., & Dudgeon, D. E. (1993). *Array signal processing*. PTR Prentice Hall, Inc.

Jones, R. (1958). In-situ measurement of the dynamic properties of soil by vibration methods. *Geotechnique, 8*(1), 1–21.

Kamai, R., Darvasi, Y., Peleg, Y., & Yagoda-Biran, G. (2018). Measurement and interpretation uncertainty in site response of nine seismic network stations in Israel. *Seismological Research Letters, 89*(5), 1796–1806.

Karl, J. H. (1989). *An introduction to digital signal processing*. Academic Press.

Kausel, E., & Roesset, J. M. (1981). Stiffness matrices for layered soils. *Bulletin of the Seismological Society of America, 71*(6), 1743–1761.

Kayen, R., Asten, M. W., & Boore, D. M. (2005). The spectral analysis of surface waves measured at William Street Park , San Jose, California , using swept-sine harmonic waves. USGS Open-File Report 2005–1169.

Kayen, R., Moss, R. E. S., Thompson, E. M., Seed, R. B., Cetin, K. O., Der, K. A., Tanaka, Y., & Tokimatsu, K. (2013). Shear-wave velocity–based probabilistic and deterministic assessment of seismic soil lique-faction potential. *Journal Geotechnical Geoenvironmental Engineering, 139*(3), 407–419.

Keiswetter, D., & Steeples, D. (1994). Practical modifications to improve the sledgehammer seismic source. *Geophysical Research Letters, 21*(20), 2203–2206.

Keiswetter, D. A., & Steeples, D. W. (1995). A field investigation of source parameters for the sledgehammer. *Geophysics, 60*(4), 1051–1057.

Khan, S., & Khan, M. A. (2018). Seismic microzonation of Islamabad-Rawalpindi metropolitan area. *Pakistan. Pure Application Geophysics, 175*, 149–164.

Kim, J.-H., & Lee, Y.-H. (2011). Comparison of signal powers generated with metal hammer plate and plastic hammer plate. *Geophysics Geophysics Exploration, 14*(4), 282–288.

Kim, J. T., Kim, D. S., Park, H. J., Bang, E. S., & Kim, S. W. (2010). Evaluation of the applicability of the surface wave method to rock fill dams. *Exploration Geophysics, 41*(1), 9–23.

Knopoff, L. (1964). A matrix method for elastic wave problems. *Bulletin of the Seismological Society of America, 54*(1), 431–438.

Konno, K., & Ohmachi, T. (1998). Ground-motion characteristics estimated from spectral ratio between horizontal and vertical components of microtremor. *Bulletin of the Seismological Society of America, 88*(1), 228–241.

Kumar, J., & Rakaraddi, P. G. (2013). Effect of source energy for SASW testing on geological sites. *Geotechnical and Geological Engineering, 31*, 47–66.

Lacoss, R. T., Kelly, E. J., & Toksoz, M. N. (1969). Estimation of seismic noise structure using arrays. *Geophysics, 34*(1), 21–38.

Lai, C. G., Foti, S., & Rix, G. J. (2005). Propagation of data uncertainty in surface wave inversion. *Journal of Environmental and Engineering Geophysics, 10*(2), 219–228.

Lei, Y., Shen, H., Xie, S., & Li, Y. (2018). Rayleigh wave dispersion curve inversion combining with GA and DSL. *Journal of Seismic Exploration, 27*, 151–165.

Leyton, F., Leopold, A., Hurtado, G., Pastén, C., Ruiz, S., Montalva, G., & Saéz, E. (2018). Geophysical characterization of the Chilean seismological stations: First results. *Seismological Research Letters, 89*(2A), 519–525.

Li, J. (2008). Study of surface wave methods for deep shear wave velocity profiling applied to the deep sediments of the Mississippi embayment. [dissertation]: University of Missouri, USA.

Li, J., & Rosenblad, B. (2011). Experimental study of near-field effects in multichannel array-based surface wave velocity measurements. *Near Surface Geophysics, 9*(4), 357–366.

Lin, C. H., & Lin, C. P. (2012). Metamorphosing the SASW method by 2D wavefield transformation. *Journal Geotechnical Geoenvironmental Engineering, 138*(8), 1027–1032.

Lin, C. P., Chang, C. C., & Chang, T. S. (2004). The use of MASW method in the assessment of soil liquefaction potential. *Soil Dynamics and Earthquake Engineering, 24*, 689–698.

Ling, S. (1993). An extended use of the spatial autocorrelation method for the estimation of geological structure using microtremors. 1993. In *Proceedings of the 89th SEGJ Conference*, pp. 44–48.

Lomax, A., & Snieder, R. (1994). Finding sets of acceptable solutions with a genetic algorithm with application to surface wave group dispersion in Europe. *Geophysical Research Letters, 21*(24), 2617–2620.

Long, M., & Donohue, S. (2007). In situ shear wave velocity from multichannel analysis of surface waves (MASW) tests at eight Norwegian research sites. *Canadian Geotechnical Journal, 44*(5), 533–544.

Lontsi, A. M., Ohrnberger, M., & Krüger, F. (2016). Shear wave velocity profile estimation by integrated analysis of active and passive seismic data from small aperture arrays. *Journal of Applied Geophysics, 130*, 37–52.

Louie, J. N. (2001). Faster, better: Shear-wave velocity to 100 meters depth from refraction microtremor arrays. *Bulletin of the Seismological Society of America, 91*(2), 347–364.

Louie JN, Pancha A, Kissane B. 2021. Guidelines and pitfalls of refraction microtremor surveys. *Journal Seismology*. https://doi.org/10.1007/s10950-021-10020-5.

Madun, A., Jefferson, I., Foo, K. Y., Chapman, D. N., Culshaw, M. G., & Atkins, P. R. (2012). Characterization and quality control of stone columns using surface wave testing. *Canadian Geotechnical Journal, 49*(12), 1357–1368.

Mahajan, A. K., Galiana, J. J., Lindholm, C., Arora, B. R., Mundepi, A. K., Rai, N., & Chauhan, N. (2011). Characterization of the sedimentary cover at the Himalayan foothills using active and passive seismic techniques. *Journal of Applied Geophysics, 73*, 196–206.

Mahvelati, S. (2019). Advancements in surface wave testing: Numerical, laboratory, and field investigations regarding the effects of input source and survey parameters on Rayleigh and Love waves. [dissertation]: Temple University, USA.

Mahvelati, S., Coe, J. T., & Asabere, P. (2020). Field investigation on the effects of base plate material on experimental surface wave data with MASW. *Journal of Environmental and Engineering Geophysics, 25*(2), 255–274.

Maklad, M., Yokoi, T., Hayashida, T., ElGabry, M. N., Hassan, H. M., Hussein, H. M., Fattah, T. A., & Rashed, M. (2020). Site characterization in Ismailia, Egypt using seismic ambient vibration array. *Engineering Geology, 279*, 105874.

Maraschini, M., & Foti, S. (2010). A Monte Carlo multimodal inversion of surface waves. *Geophysical Journal International, 182*(3), 1557–1566.

Marosi, K. T., & Hiltunen, D. R. (2004a). Characterization of spectral analysis of surface waves shear wave velocity measurement uncertainty. *Journal Geotech Geoenvironmental Engineering, 130*(10), 1034–1041.

Marosi, K. T., & Hiltunen, D. R. (2004b). Characterization of SASW phase angle and phase velocity measurement uncertainty. *Geotechnical Testing Journal, 27*(2), 205–213.

Martin, A., Yong, A., Stephenson, W., Boatwright, J., & Diehl, J. (2017). Geophysical characterization of seismic station sites in the United States—The importance of a flexible, multi-method approach. In *16th World Conference Earthquack Engineering.* Santiago, Chile.

Martínez-, P., Navarro, M., Pérez-Cuevas, J., Alcalá, F. J., García-Jerez, A., & Sandoval, S. (2014). Shear-wave velocity based seismic microzonation of Lorca city (SE Spain) from MASW analysis. *Near Surface Geophysics, 12*(6), 739–749.

Martínez, M. D., Lana, X., Olarte, J., Badal, J., & Canas, J. A. (2000). Inversion of Rayleigh wave phase and group velocities by simulated annealing. *Physics of the Earth and Planetary Interiors, 122*(1–2), 3–17.

Mase, L. Z., Likitlersuang, S., Tobita, T., Chaiprakaikeow, S., & Soralump, S. (2020). Local site investigation of liquefied Soils Caused by Earthquake in Northern Thailand. *Journal Earthquake Engineering, 24*(7), 1181–1204.

McMechan, G. A., & Yedlin, M. J. (1981). Analysis of dispersive waves by wave-field transformation. *Geophysics, 46*(6), 869–874.

Mereu, R. F., Uffen, R. J., & Beck, A. E. (1963). The use of a coupler in the conversion of impact energy into seismic energy. *Geophysics, 28*(4), 531–546.

Michaels, P. (2011). Establishing confidence in surface wave determined soil profiles. In *GeoRisk 2011 Risk Assess Manage*ment, Jun 26–28; Atlanta (GA), pp. 837–844.

Michel, C., Edwards, B., Poggi, V., Burjánek, J., Roten, D., Cauzzi, C., & Fäh, D. (2014). Assessment of site effects in alpine regions through systematic site characterization of seismic stations. *Bulletin of the Seismological Society of America, 104*(6), 2809–2826.

Micromed, S. P. A. (2012). *Tromino user's manual*. Micromed S.p.A., Treviso, Italy.

Molnar, S., Cassidy, J. F., Castellaro, S., Cornou, C., Crow, H., Hunter, J. A., Matsushima, S., Sánchez-, F. J., & Yong, A. (2018). Application of microtremor horizontal-to-vertical spectral ratio (MHVSR) analysis for site characterization: State of the art. *Surveys in Geophysics, 39*, 613–631.

Morton, S. L. C., Ivanov, J., & Miller, R. D. (2015). A modified F-K filter for removing the effects of higher-mode dispersion patterns from surface wave data. In *28th Sympsium Application Geophysics to Engineering Environment Problems 2015*, SAGEEP 2015, pp. 445–451.

Mugesh, A., Desai, A., Jakka, R. S., & Kamal. (2022). Local site effects influence on earthquake early warning parameters. In T. G. Sitharam, S. Kolathayar, R. S. Jakka (Eds.), *Earthquake Geotechnics*. Lect Notes Civ Eng. Vol. 187. Springer, Singapore, pp. 119–127.

Nakamura, Y. (1989). A method for dynamic characteristics estimation of subsurface using microtremor on the ground surface. *Q Reports Railway Technical Research Institute, 30*(1), 25–33.

Nazarian, S. (2012). Shear wave velocity profiling with surface wave methods. In *Geotechnical Engineering State Art Pract Keynote Lect from GeoCongress*, pp. 221–240.

Nazarian, S., Stokoe, K. H., II., & Hudson, W. R. (1983). Use of spectral analysis of surface waves method for determination of moduli and thicknesses of pavement systems. *Transportation Research Record, 930*, 38–45.

Nolet, G., & Panza, G. F. (1976). Array analysis of seismic surface waves: Limits and possibilities. *Pure and Applied Geophysics, 114*, 775–790.

Noorlandt, R., Kruiver, P. P., de Kleine, M. P. E., Karaoulis, M., de Lange, G., Di Matteo, A., von Ketelhodt, J., Ruigrok, E., Edwards, B., Rodriguez-Marek, A., et al. (2018). Characterisation of ground motion recording stations in the Groningen gas field. *Journal of Seismology, 22*, 605–623.

O'Neill, A. (2003). Full-waveform reflectivity for modelling, inversion and appraisal of seismic surface wave dispersion in shallow site investigations. [dissertation]: University of Western Australia.

Odum, J. K., Stephenson, W. J., Williams, R. A., & von Hillebrandt, C. (2013). Vs30 and spectral response from collocated shallow, active, and passive-source Vs data at 27 sites in Puerto Rico. *Bulletin of the Seismological Society of America, 103*(5), 2709–2728.

Okada, H. (2003). The microtremor survey method. Society of Exploration Geophysicists of Japan, Translated by Koya Suto, Geophysical Monograph Series, No. 12, Society of Exploration Geophysicists, Tulsa.

Omar, M. N., Abbiss, C. P., & Mohd. (2011). Prediction of long-term settlement on soft clay using shear wave velocity and damping characteristics. *Engineering Geology, 123*(4), 259–270.

Pamuk, E., Cevdet, Ö., Özyal, Ş, & Akgün, M. (2017). Soil characterization of Tınaztepe region (Izmir/Turkey) using surface wave methods and nakamura (HVSR) technique. *Earthquake Engineering and Engineering Vibration, 16*(2), 447–458.

Pancha, A., Pullammanappallil. (2011). Analysis and interpretation of the Texas A&M University benchmark data using the refraction microtremor technique. In *GeoRisk 2011 Risk Assess Management,* Jun 26–28; Atlanta (GA), pp. 867–874.

Pandey, B., Jakka, R. S., & Kumar, A. (2016a). Influence of local site conditions on strong ground motion characteristics at Tarai region of Uttarakhand. *India. Natural Hazards, 81*, 1073–1089.

Pandey, B., Jakka, R. S., Kumar, A., & Mittal, H. (2016b). Site characterization of strong-motion recording stations of Delhi using joint inversion of phase velocity dispersion and H/V curve. *Bulletin of the Seismological Society of America, 106*(3), 1254–1266.

Panzera, F., D'Amico, S., Galea, P., Lombardo, G., Gallipoli, M. R., & Pace, S. (2013). Geophysical measurements for site response investigation: Preliminary results on the island of Malta. *Boll Di Geofis Theoretical Ed Application, 54*(2), 111–128.

Park, C. B., & Carnevale, M. (2010). Optimum MASW survey—Revisit after a decade of use. In: *GeoFlorida 2010 Advances Analysis Model Design*, pp. 1303–1312.

Park, C. B., Miller, R., Laflen, D., Neb, C., Ivanov, J., Bennett, B., & Geological, K. (2004). Imaging dispersion curves of passive surface waves. In *Expanded Abstracts74th Annual Meeting Soc Exploration Geophysics Proceeding CD ROM*.

Park, C. B., Miller, R. D., & Miura, H. (2002). Optimum field parameters of an MASW survey. *Proceedings Society Exploration Geophysics Japan Tokyo.*

Park, C. B., Miller, R. D., Ryden, N., Xia, J., & Ivanov, J. (2005). Combined use of active and passive surface waves. *Journal of Environmental and Engineering Geophysics, 10*(3), 323–334.

Park, C. B., Miller, R. D., & Xia, J. (1998). Imaging dispersion curves of surface waves on multi-channel record. In *SEG Technical Program Expanded Abstracts: Society of Exploration Geophysicists*.

Park, C. B., Miller, R. D., & Xia, J. (1999). Multichannel analysis of surface waves. *Geophysics, 64*(3), 800–808.

Park, C. B., Miller, R. D., Xia, J., & Ivanov, J. (2007). Multichannel analysis of surface waves (MASW)—Active and passive methods. *The Leading Edge, 26*(1), 60–64.

Park, C. B., & Ryden, N. (2007). Historical overview of the surface wave method. In *20th EEGS Sympium Application Geophysics to Engineering Environmental Problem Euroupe Association Geosciences Engineering: Society of Exploration Geophysicists*, pp. 897–909.

Parolai, S., Picozzi, M., Richwalski, S. M., & Milkereit, C. (2005). Joint inversion of phase velocity dispersion and H/V ratio curves from seismic noise recordings using a genetic algorithm, considering higher modes. *Geophysical Research Letters, 32*(1), L01303.

Passeri, F., Comina, C., Foti, S., & Socco, L. V. (2021). The Polito Surface Wave flat-file Database (PSWD): Statistical properties of test results and some inter-method comparisons. *Bulletin of Earthquake Engineering, 19*(6), 2343–2370.

Pelekis, P. C., & Athanasopoulos, G. A. (2011). An overview of surface wave methods and a reliability study of a simplified inversion technique. *Soil Dynamics and Earthquake Engineering, 31*(12), 1654–1668.

Penumadu, D., & Park, C. B. (2005). Multichannel analysis of surface wave (MASW) method for geotechnical site characterization. In *Geo-Frontiers Congress 2005 Earthquake Engineering Soil Dynamics*, pp. 1–10.

Peterson, J. (1993). Observations and modeling of seismic background noise. U.S. Geological Survey, Open-File Report, 93–322.

Poggi, V., Fäh, D., Burjanek, J., & Giardini, D. (2012). The use of Rayleigh-wave ellipticity for site-specific hazard assessment and microzonation: Application to the city of Lucerne. *Switzerland. Geophysical Journal International, 188*(3), 1154–1172.

Rahman, M. Z., Siddiqua, S., & Kamal, A. S. M. M. (2016). Shear wave velocity estimation of the near-surface materials of Chittagong City, Bangladesh for seismic site characterization. *Journal of Applied Geophysics, 134*, 210–225.

Rahnema, H., Mirassi, S., & Dal Moro, G. (2021). Cavity effect on Rayleigh wave dispersion and P-wave refraction. *Earthquake Engineering and Engineering Vibration, 20*(1), 79–88.

Rastogi, B. K., Singh, A. P., Sairam, B., Jain, S. K., Kaneko, F., Segawa, S., & Matsuo, J. (2011). The possibility of site effects: The Anjar case, following past earthquakes in Gujarat. *India. Seismological Research Letter, 82*(1), 59–68.

Rehman, F., El-Hady, S. M., Atef, A. H., & Harbi, H. M. (2016). Multichannel analysis of surface waves (MASW) for seismic site characterization using 2D genetic algorithm at Bahrah area, Wadi Fatima. *Saudi Arabia. Arab Journal Geosciences, 9*, 519.

Richwalski, S. M., Picozzi, M., Parolai, S., Milkereit, C., Baliva, F., Albarello, D., Roy-Chowdhury, K., Van Meer, H., & Zschau, J. (2007). Rayleigh wave dispersion curves from seismological and engineering- geotechnical methods: A comparison at the Bornheim test site (Germany). *Journal of Geophysics and Engineering, 4*, 349–361.

Rix, G. J., Hebeler, G. L., & Orozco, M. C. (2002). Near-surface Vs profing in the New Madrid seismic zone using surface-wave methods. *Seismological Research Letters, 73*(3), 380–392.

Rosenblad, B. L., & Li, J. (2009a). Comparative study of refraction microtremor (ReMi) and active source methods for developing low-frequency surface wave dispersion curves. *Journal of Environmental and Engineering Geophysics, 14*(3), 101–113.

Rosenblad, B. L., & Li, J. (2009b). Performance of active and passive methods for measuring low-frequency surface wave dispersion curves. *Journal Geotechnical Geoenvironmental Engineering, 135*(10), 1419–1428.

Rosenblad, B. L., Stokoe, K. H. II, Li, J., Wilder, B., & Menq, F.-Y. (2008). Deep shear wave velocity profiling of poorly characterized soils using the NEES low-frequency vibrator. In *Geotechnical Earthquake Engineering Soil Dynamics IV*, pp. 1–10.

Roy, N. (2015). Uncertainty in site characterization using surface wave technique. [dissertation]: Indian Institute of Technology, Roorkee, India.

Roy, N., Desai, A., & Jakka, R. S. (2020). Surface wave dispersion in a layered medium for varying subsurface scenarios. *International Journal Geotechnical Earthquake Engineering, 11*(2), 26–49.

Roy, N., & Jakka, R. S. (2017). Near-field effects on site characterization using MASW technique. *Soil Dynamics and Earthquake Engineering, 97*, 289–303.

Roy, N., & Jakka, R. S. (2018). Effect of data uncertainty and inversion non-uniqueness of surface wave tests on Vs, 30 estimation. *Soil Dynamics and Earthquake Engineering, 113*, 87–100.

Roy, N., & Jakka, R. S. (2020). Mapping surface wave dispersion uncertainty in Vs Profiles to Vs, 30 and site response analysis. *Soil Dynamics and Earthquake Engineering, 138*, 106298.

Roy, N., Jakka, R. S., & Wason, H. R. (2013). Effect of surface wave inversion non-uniqueness on 1D seismic ground response analysis. *Natural Hazards, 68*(2), 1141–1153.

Saifuddin, Y. H., & Chimoto, K. (2018). Variability of shallow soil amplification from surface-wave inversion using the Markov-chain Monte Carlo method. *Soil Dynamics and Earthquake Engineering, 107*, 141–151.

Salas-Romero, S., Malehmir, A., Snowball, I., & Brodic, B. (2021). Geotechnical site characterization using multichannel analysis of surface waves: A case study of an area prone to quick-clay landslides in southwest Sweden. *Near Surface Geophysics*, 1–17.

Sambridge, M. (1999). Geophysical inversion with a neighbourhood algorithm— I. Searching a parameter space. *Geophysical Journal International, 138*, 479–494.

Sandikkaya, M. A., Yilmaz, M. T., Bakir, B. S., & Yilmaz, Ö. (2010). Site classification of Turkish national strong-motion stations. *Journal of Seismology, 14*, 543–563.

Scherbaum, F., Hinzen, K. G., & Ohrnberger, M. (2003). Determination of shallow shear wave velocity profiles in the cologne, Germany area using ambient vibrations. *Geophysical Journal International, 152*(3), 597–612.

Schmidt, R. O., & Franks, R. E. (1986). Multiple source DF signal processing: An experimental system. *Adapt Antennas Wireless Communication, 34*(3), 281–290.

Sen, M. K., & Stoffa, P. L. (1991). Nonlinear one-dimensional seismic waveform inversion using simulated annealing. *Geophysics, 56*(10), 1624–1636.

Socco, L. V., & Boiero, D. (2008). Improved Monte Carlo inversion of surface wave data. *Geophysical Prospecting, 56*(3), 357–371.

Socco, L. V., Comina, C., & Anjom, F. K. (2017). Time-average velocity estimation through surface-wave analysis: Part 1-S-wave velocity. *Geophysics, 82*(3), U49–U59.

Socco, L. V., Foti, S., & Boiero, D. (2010). Surface-wave analysis for building near-surface velocity models—Established approaches and new perspectives. *Geophysics, 75*(5), 75A83–75A102.

Socco, L. V., & Strobbia, C. (2004). Surface-wave method for near-surface characterization: A tutorial. *Near Surface Geophysics, 2*, 165–185.

Stanko, D., Markušić, S., Strelec, S., & Gazdek, M. (2017). HVSR analysis of seismic site effects and soil-structure resonance in Varaždin city (North Croatia). *Soil Dynamics and Earthquake Engineering, 92*, 666–677.

Stokoe, K. H., II., Cox, B. R., Clayton, P. M., & Menq, F. (2020). NHERI@ UTexas experimental facility with large-scale mobile shakers for field studies. *Frontiers Built Environment, 6*, 575973.

Stokoe, K. H. II, & Nazarian, S. (1983). Effectiveness of ground improvement from spectral analysis of surface waves. In *Proceedings of the 8th European Conference on Soil Mechanics and Foundation Engineering*.

Stokoe, K. H. II, Nazarian, S., Rix, G. J., Sanchez-Salinero, I., Sheu, J. C., & Mok, Y. J. (1988). In situ seismic testing of hard-to-sample soils by surface wave method. In *Proceedings (Earthquake Engineering and Soil Dynamics II—Recent Advances in Ground-motion Evaluation) of Geotechnical Engineering Division of the American Society of Civil Engineers (ASCE)*, Park City, Utah, 27–30 June 1988, Geotechnical Special Publication No. 20, pp. 264–278.

Stokoe, K H. II, Rathje, E. M., Wilson, C. R., & Rosenblad, B. L. (2004). Development of the NEES large-scale mobile shakers and associated instrumentation for in situ evaluation of nonlinear characteristics and liquefaction resistance of soils. In *13th World Conference Earthquake Engeering*. Vancouver, Canada.

Stokoe, K. H. II, Wright, S. G., Bay, J. A., Roesset, & J. M. (1994). Characterization of geotechnical sites by SASW method. In R. D. Woods (Ed.), *Geophysical characterization of sites: New York*. International Science Publisher, pp. 15–26.

Strobbia, C., & Foti, S. (2006). Multi-offset phase analysis of surface wave data (MOPA). *Journal of Applied Geophysics, 59*, 300–313.

Suto, K. (2013). MASW surveys in landfill sites in Australia. *The Leading Edge, 32*(6), 674–678.

Taipodia, J., Ram, B., Baglari, D., Krishna, M., & Dey, A. (2014). Geophysical investigations for identification of subsurface stratigraphy at IIT Guwahati. *Indian Geotech Conf (IGC 2014)* (pp. 219–226). Kakinada.

Teague, D. P., & Cox, B. R. (2016). Site response implications associated with using non-unique Vs profiles from surface wave inversion in comparison with other commonly used methods of accounting for Vs uncertainty. *Soil Dynamics and Earthquake Engineering, 91*, 87–103.

SESAME team. (2004). Guidelines for the implementation of the H/V spectral ratio technique on ambient vibrations-measurements, processing and interpretations. (Deliverable No. D23.12), WP12. SESAME European research project.

Thomson, W. T. (1950). Transmission of elastic waves through a stratified solid medium. *Journal of Applied Physics, 21*, 89–93.

Tokimatsu, K. (1995). Geotechnical site characterization using surface waves. In *Proceedings of the First International Conference on Earthquake Geotechnical Engineering, IS-Tokyo 1995*, Japanese Geotechnical Society, Balkema; pp. 1333–1368.

Tran, K. (2008). An appraisal of surface wave methods for soil characterization. [master's thesis]:, University of Florida.

Tran, K. T., & Hiltunen, D. R. (2011). An assessment of surface wave techniques at the Texas A&M national geotechnical experimentation site. In: GeoRisk 2011 Risk Assess Manag.; Jun 26–28; Atlanta (GA), pp. 859–866.

Senkaya, G., Senkaya, M., Karsli, H., & Güney, R. (2020). Integrated shallow seismic imaging of a settlement located in a historical landslide area. *Bulletin of Engineering Geology and the Environment, 79*, 1781–1796.

Vantassel, J. P., & Cox, B. R. (2021). SWinvert: A workflow for performing rigorous 1-D surface wave inversions. *Geophysical Journal International, 224*(2), 1141–1156.

Watabe, Y., & Sassa, S. (2008). Application of MASW technology to identification of tidal flat stratigraphy and its geoenvironmental interpretation. *Marine Geology, 252*(3–4), 79–88.

Wathelet, M. (2008). An improved neighborhood algorithm : Parameter conditions and dynamic scaling. *Geophysical Research Letters, 35*, L09301.

Wathelet, M., Jongmans, D., Ohrnberger, M., & Bonnefoy-Claudet, S. (2008). Array performances for ambient vibrations on a shallow structure and consequences over Vs inversion. *Journal of Seismology, 12*, 1–19.

Wong, I. G., Stokoe, K. H., II., Cox, B. R., Yuan, J., Knudsen, K. L., Terra, F., Okubo, P., & Lin, Y. C. (2011). Shear-wave velocity characterization of the USGS Hawaiian strong-motion network on the Island of Hawaii and development of an NEHRP site-class map. *Bulletin of the Seismological Society of America, 101*(5), 2252–2269.

Wood, C. M., & Cox, B. R. (2012). A comparison of MASW dispersion uncertainty and bias for impact and harmonic sources. In *GeoCongress 2012 State Art Practice Geotechnical Engineering*, pp. 2756–2765.

Wood, C. M., Ellis, T. B., Teague, D. P., & Cox, B. R. (2014). Comprehensive analysis of the UTexas1 surface wave dataset. In *Geo-Congress 2014 Geo-Characterization Model Sustain*, Feb 23–26; Atlanta (GA); p. 820–829.

Wood, C. M., Wotherspoon, L. M., & Cox, B. R. (2015). Influence of a-priori subsurface layering data on the development of realistic shear wave velocity profiles from surface wave inversion. In *6th International Conference Earthquake Geotechnical Eng*ieering. Christchurch, New Zealand.

Xia, K., Hilterman, F., & Hu, H. (2018). Unsupervised machine learning algorithm for detecting and outlining surface waves on seismic shot gathers. *Journal of Applied Geophysics, 157*, 73–86.

Xia, J., Miller, R. D., & Park, C. B. (1999). Estimation of near-surface shear-wave velocity by inversion of Rayleigh waves. *Geophysics, 64*(3), 691–700.

Xu, Y., Xia, J., & Miller, R. D. (2006). Quantitative estimation of minimum offset for multichannel surface-wave survey with actively exciting source. *Journal of Applied Geophysics, 59*, 117–125.

Yamanaka, H., Chimoto, K., Ozel, O., Ozmen, O., Arslan, S., Yalcinkaya, E., Tun, M., Pekkan, E., Tsuno, S., & Kaplan, O. et al. (2020). Microtremor explorarions for shallow S-wave velocity profiles at strong motion stations in Turkey. In *17th World Conference Earthquake Eng*ineering Sendai, Japan, pp. 1–9.

Yilmaz, O. (1987). *Seismic data processing*. Society of Exploration Geophysics.

Yokota, T., Jinguuji, M., Yamanaka, Y., & Murata, K. (2017). S-wave reflection and surface wave surveys in liquefaction affected areas: A case study of the Hinode area, Itako, Ibaraki. *Japan. Exploration Geophysics, 48*, 1–15.

Yoon, S. (2005). Array-based measurements of surface wave dispersion and attenuation using frequency-wavenumber analysis. [dissertation]: Georgia Institute of Technology, USA.

Yoon, S., & Rix, G. J. (2009). Near-field effects on array-based surface wave methods with active sources. *Journal Geotechnical Geoenvironmental Engineering, 135*(3), 399–406.

Yordkayhun, S., Sujitapan, C., & Chalermyanont, T. (2015). Shear wave velocity mapping of Hat Yai district, southern Thailand: Implication for seismic site classification. *Journal of Geophysics and Engineering, 12*(1), 57–69.

Zarean, A., Mirzaei, N., & Mirzaei, M. (2015). Applying MPSO for building shear wave velocity models from microtremor Rayleigh-wave dispersion curves. *Journal of Seismic Exploration, 24*, 51–82.

Zekkos, D., Sahadewa, A., Woods, R. D., & Stokoe, K. H., II. (2014). Development of model for shear-wave velocity of municipal solid waste. *Journal Geotechnical Geoenvironmental Engineering, 140*(3), 04013030.

Zeng, C., Xia, J., Miller, R. D., Tsoflias, G. P., & Wang, Z. (2012). Numerical investigation of MASW applications in presence of surface topography. *Journal of Applied Geophysics, 84*, 52–60.

Zhang, S. X., Chan, L. S., & Xia, J. (2004). The selection of field acquisition parameters for dispersion images from multichannel surface wave data. *Pure and Applied Geophysics, 161*, 185–201.

Zhao, D. (2011). Analysis of surface wave benchmarking data. In *GeoRisk 2011 Risk Assessitance Management*, Jun 26–28; Atlanta (GA), pp. 853–858.

Zhao, D., & Li, V. (2010). Comparison of FK and SPAC methods in determining dispersion curves from passive surface waves. In *23rd EEGS Sympsium Application Geophysics to Engineering Environmental Problems*, pp. 536–542.

Zywicki, D. J. (1999). Advanced signal processing methods applied to engineering analysis of seismic surface waves. [dissertation]: Georgia Institute of Technology, USA.

Zywicki, D. J. (2007). The impact of seismic wavefield and source properties on ReMi estimates. In *Geo-Denver 2007 New Peaks Geotechnical*, pp. 1–10.

Zywicki, D. J., & Rix, G. J. (2005). Mitigation of near-field effects for seismic surface wave velocity estimation with cylindrical beamformers. *Journal Geotechnical Geoenvironmental Engineering, 131*(8), 970–977.